FACULTY
OF MATHEMATICS
AND PHYSICS
Charles University

DOCTORAL THESIS

Orsolya Molnárová

Advanced aluminium alloys prepared by powder metallurgy and spark plasma sintering

Department of Physics of Materials

Supervisor of the doctoral thesis: doc. RNDr. Přemysl Málek, CSc.

Study programme: Physics

Specialization: Physics of Condensed Matter and Materials Research

Prague 2018

I declare that I carried out this doctoral thesis independently, and only with the cited sources, literature and other professional sources.

I understand that my work relates to the rights and obligations under the Act No. 121/2000 Coll., the Copyright Act, as amended, in particular the fact that the Charles University has the right to conclude a license agreement on the use of this work as a school work pursuant to Section 60 paragraph 1 of the Copyright Act.

In…..... date..... signature

I would like to express my gratitude to my supervisor doc. RNDr. Přemysl Málek, CSc. for his guidance, sustain and good advice. My thanks must go also to Ing. Jakub Cinert and Ing. Filip Průša Ph.D. for the preparation of experimental materials, to RNDr. František Lukáč, Ph.D. for X-ray diffraction experiments, and to my colleagues RNDr. Peter Minárik, Ph.D. for preparation of lamellae, to Mgr. Jozef Veselý, Ph.D. for transmission electron microscopy, to Ing. Jana Kálalová and Marta Čepová for their help in preparation of samples for microstructural studies. Last but not the least important, I owe more than tanks to my family members for their encouragement throughout my life. Without their support it would be impossible to finish my studies.

Title: Advanced aluminium alloys prepared by powder metallurgy and spark plasma sintering

Author: Orsolya Molnárová

Department / Institute: Department of Physics of Materials

Supervisor of the doctoral thesis: doc. RNDr. Přemysl Málek, CSc., Department of Physics of Materials, Charles University

Abstract:

Mechanical properties of aluminium alloys highly depend on their phase composition and microstructure. High strength can be achieved among others by introduction of a high volume fraction of fine, homogeneously distributed second phase particles and by a refinement of the grain size. Powder metallurgy allows to prepare fine grained materials with increased solid solubility which are favourable precursors for further precipitation strengthening. Gas atomization was used for the preparation of powders of the commercial Al7075 alloy and its modification containing 1 wt% Zr. A part of gas atomized powders was mechanically milled at different conditions. Mechanical milling reduced the grain size down to the nano-size range and the corresponding microhardness exceeded the value of 300 HV. Powders were consolidated by the spark plasma sintering method to nearly fully dense compacts. Due to a short time and relatively low temperature of sintering the favourable microstructure can be preserved in the bulk material. The grain size of compacts prepared from milled powder was retained in the submicrocrystalline range and the microhardness close to 200 HV exceeded that of the specially heat treated ingot metallurgical counterparts. The prepared compacts retained their fine grained structure and high microhardness during their exposition to the temperature of 425 °C.

Keywords: aluminium alloys, powder metallurgy, gas atomization, mechanical milling, spark plasma sintering

Contents

Introduction

The growth of natural resource's scarcity presents an endlessly increasing problem in our continuously developing world industry. The difficulty made by limited resources should be faced and the material and energy efficiency have to be improved. A reduction in environmental impact can be managed using recyclable materials and reducing mechanical part's weight by using lightweight materials. Aluminium-based alloys represent an appropriate candidate, due to their properties as low density, high specific strength and oxidation resistance. Therefore, they can be utilized in long-life applications. Moreover, aluminium is highly suitable for recycling. It is reported to be almost infinitely recyclable [1] and the recycling process requires only 5% of the energy of primary Al production [2, 3].

High purity aluminium is a soft material with the ultimate strength of approximately 10 MPa [4], which limits its usability in industrial applications. In order to compete other constructional materials, the strength of Al-based materials has to be significantly increased. There are several ways how to increase the strength of metallic materials: alloying by adequate elements, introduction of appropriate strengthening particles, plastic deformation or grain size reduction. At present, the strongest commercially available Al alloy is an Al7068 alloy whose yield and ultimate tensile strength can be increased up to 683 and 710 MPa applying special heat treatment [5]. Using special processing technologies, the yield strength of Al alloys can be increased up to 1 GPa, as it was shown for a nanostructured Al7075 alloy processed by high pressure torsion [6].

A serious drawback of Al alloys is a drop of their strength at elevated temperatures. In case of age-hardenable Al alloys, the high temperature exposition usually leads to coarsening or dissolution of strengthening second phase particles. In case of wrought Al alloys, the deformation energy stored in the material during its processing is released by recovery or recrystallization processes occurring at elevated temperatures. Finally, the high temperature exposition can also result in grain coarsening. All above mentioned structural changes generally result in a decrease in strength. The solution of this problem represents one of the most important tasks in the production of modern Al-based materials.

As the efficiency of traditional processing routes for the development of high strength Al-based alloys is rather limited, alternative methods of material's processing are sought. In the 70th and 80th of the last century, rapid solidification (RS) processes were intensively studied and used for the preparation of materials with an improved microstructure. Due to cooling rates reaching even 10^6 Ks^{-1} the solid solubility can be strongly enhanced [7]. The supersaturated solid solution is a perfect precursor for the precipitation of a sufficiently high volume fraction of appropriately dispersed very fine second phase particles. Simultaneously, a fine-grained microstructure (grain size usually close to 1 μm) is typical for rapidly solidified materials [8, 9]. Both these aspects might contribute to a strength enhancement.

Rapid solidification represents a basis for processing routes such as melt spinning, atomization or a variety of deposition techniques [7]. In all these methods, at least one dimension of the product has to be minimized in order to ensure a sufficiently rapid heat transfer so that no bulk material suitable for further commercial utilization can be produced. Especially the atomized powder represents a good precursor for further treatment. The powder can be mechanically milled which can result in further microstructural changes (e.g. dissolution of second phase particles, grain size refinement deeply below 1 μm) [10, 11]. Nevertheless, for their commercial use the powders have to be consolidated into a bulk material. This can be performed using different methods. To minimize the porosity of resulting bulk materials, classical consolidation methods as hot isostatic pressing [7] require a high temperature and a long time of sintering. Unfortunately, this prolonged exposure to high temperatures usually results in a degradation of benefits from RS or milling.

From the 90th of the last century, severe plastic deformation (SPD) methods as e.g. equal channel angular pressing [12, 13] were widely used for processing of Al-based materials. The resulting bulk material usually does not contain any porosity and its strength is increased predominantly by a large amount of stored deformation energy and by a distinctive reduction in the grain size (typically below 1 μm). On the other side, these methods allow only a limited variation of mechanical properties by changes in phase composition.

In the last decade, the material research turned back to powder metallurgical (PM) routes and improved/ developed new methods for powder's consolidation, for example microwave sintering or spark plasma sintering (SPS). These consolidation

methods are capable of producing nearly full-density compacts at relatively low temperatures and short heat exposure times [14]. Additionally, the microstructure is influenced predominantly in the vicinity of contact points of powder particles [15]. Therefore, the benefits of RS or mechanical milling can be better maintained in the powder particle interior. In our research, a combination of rapid solidification, mechanical milling, and spark plasma sintering was chosen for the preparation of two aluminium alloys and investigation of their microstructure and properties.

The thesis is divided into 5 chapters. After sections Introduction and the Aims of the thesis Chapter 1 is describing the strengthening mechanisms in metallic materials followed by the high temperature stability of the second phase particles and grain structure. Further, it brings description and a short literature review of processing methods and studied Al alloys. Chapter 2 brings the experimental procedures employed during the materials preparation and experimental methods used for characterization of materials. Chapter 3 presents the results of the experimental work, which are discussed in Chapter 4. Chapter 5 lists the main conclusions of the research work and gives suggestions for the future work regarding the recent work's subject.

This thesis is based upon the experimental work carried out at the Department of Physics of Materials on Charles University (Prague, Czech Republic). Part of the works, the sintering and the X-ray diffraction measurements were carried out at the Institute of Plasma Physics, Czech Academy of Sciences (Prague, Czech Republic) under the common project GACR 15-15609S. Some samples were sintered by Hanka Becker at Bergakademie Freiberg, Germany.

Aims of the thesis

The principal task of the present thesis was to verify the possibility of producing advanced aluminium alloys via the PM route using a new combination of gas atomization, mechanical milling of powders, and SPS as a consolidation technique. Gas atomization was used to get powders with a non-equilibrium phase composition and fine-grained microstructure. A part of these powders was mechanically milled with the aim to change their phase composition, especially to refine or even dissolve the second phase particles, to introduce a high deformation energy into the material, and to refine the grain size. Milling was carried out with different parameters in order to study the impact of various parameters on powders final microstructure. The powders were then sintered by SPS to get dense compacts with otherwise minimized influence of sintering on powder's initial microstructure. Further, the compacts were heat treated at various temperatures to study their microstructural and mechanical high temperature stability.

Two Al-based alloys (Al7075 alloy and Al7075+ 1 wt% Zr alloy) were selected for this research with the main aim to increase their strength both at room and elevated temperatures. The influence of different stages of processing on the microstructure, phase composition, and mechanical properties of these alloys was investigated using a variety of experimental methods - light microscopy (LM), scanning electron microscopy (SEM), electron backscatter diffraction (EBSD), transmission electron microscopy (TEM), scanning transmission electron microscopy (STEM), energy dispersive spectroscopy (EDS), X-ray diffraction (XRD) and microhardness (HV) measurements.

To verify the efficiency of the processing technology, the well-known commercial Al7075 alloy was investigated. This choice of material enabled us to compare the achieved results with the huge amount of data reported by other authors on this alloy prepared by a variety of processing routes, especially with values reported for the Al7075 alloy after special thermal treatment aimed to reach the highest strength [16-18]. As the phase composition of this alloy highly alters with temperature, the investigation of its high temperature behaviour was more focused on the microstructure stability with a goal to increase the material's strength by a stable fine grain size.

In order to improve the microstructural stability, 1 wt% of Zr was added to the Al7075 alloy. It is believed that very fine particles of the Al_3Zr phase can pin the grain boundaries and retard their migration which otherwise would result in a grain growth [19]. The positive influence of Zr on the microstructure stability was reported previously both at materials prepared through rapid solidification techniques [20] and severe plastic deformation [21].

The experimental results obtained during this research should open a new way to the development of high temperature Al alloys which would retain their high strength up to the temperatures of about 400 °C.

1. Theoretical background

1.1. Introduction

There have been long lasting efforts to improve the strength of metallic materials. The influence of composition and microstructure on mechanical properties of materials was widely studied. There are several reviews and books dealing with strengthening mechanisms of metals, e.g. [22-24]. Nevertheless, the theory of individual strengthening mechanisms, their superposition and interaction is rather difficult and requires a deep knowledge of mathematics, mechanics and chemistry. The detailed elucidation of those mechanisms was not the aim of the present thesis and, therefore, only a short, mostly qualitative introduction into strengthening mechanisms of metallic materials will be given in the following sections.

1.2. Strengthening mechanisms in metals

The slip of dislocations is considered to be the most important deformation mechanism in a majority of metallic materials. Material strength is then connected with interactions of moving dislocations with obstacles opposing their slip. Any object in the crystal lattice which creates its own strain field will interact with dislocations. The degree of hardening by an obstacle is then determined by the type and magnitude of interaction between the strain fields of dislocation and obstacle [25].

There are several possibilities how to increase the strength of metallic materials – by dislocations, foreign atoms dissolved in the matrix, second phase particles, and grain boundaries. The basic strengthening mechanisms therefore are [24]:

- Work hardening,
- Solid solution strengthening,
- Precipitation and dispersion strengthening,
- Grain boundary strengthening.

The materials strength then results from a superposition of individual strengthening mechanisms.

Materials strength can be characterized also by its hardness; however, it is not an intrinsic property of materials. Nevertheless, the ultimate tensile strength (σ_{UTS}) for a number of metals was shown to be related to the microhardness (HV) as [26-28]:

$$HV \approx 3\sigma_{UTS}. \quad (1)$$

This relationship was found by Zhang et al. to hold for micron-grained, ultrafine-grained and also nanocrystalline materials [27].

1.2.1. Work hardening

Work hardening – also called strain hardening or deformation strengthening – is a strengthening method often used in materials whose strength cannot be increased by heat treatment, e.g. by changes in their phase composition.

Work hardening is a consequence of plastic deformation, which introduces deformation energy into the material. The deformation energy is mainly increased due to the introduction of dislocations during plastic deformation. By heavy straining, the dislocation density of metals can be increased from 10^7-10^{11} m^{-2} (characteristic for annealed material) to 10^{13}-10^{14} m^{-2} [29]. Beside dislocations also other defects, as stacking faults or anti-phase boundaries can be introduced into the material during deformation, all representing obstacles for the movement of dislocations.

As obstacles resist movement of dislocations, further movement of dislocation on a given slip system can appear first after increasing stress above the critical resolved shear stress, τ_C, whose value depends upon the resisting mechanisms [25]. A short list of the most common mechanisms resisting dislocation motion follows.

The basic mechanism acting against each moving dislocation is the difference in the atomic spacing at dislocation's core and around it. The resulting, so called Peierls-Nabarro stress for an isolated edge dislocation in an otherwise perfect crystal can be expressed as [24, 25]:

$$\tau_{PN} = \frac{2G}{1-\nu} e^{-\frac{2\pi w}{b}}, \quad (2)$$

where G is the shear modulus, ν the Poisson ratio, b the magnitude of Burgers vector and w the distance around the dislocation where atomic arrangement differs from that in a perfect crystal. However, this equation is inaccurate for dislocations with complex structures.

Further, dislocations can interact with each other. In case they are in the same slip plane, they will either repel (if they have the same sign) or attract and annihilate (if they have Burgers vectors with opposite signs). If a dislocation glide is blocked by an obstacle, the dislocations will create pile-ups at that obstacle. The resulting strengthening effect from the pile-up dislocations, $\tau_{pile\text{-}up}$ can be expressed as [25]:

$$\tau_{pile-up} = N\tau, \quad (3)$$

where N is the number of dislocations in the pile-up and τ is the shear stress for a single dislocation.

In case, a gliding dislocation interacts with dislocations intersecting its slip plane, also called forest dislocations, the cutting process can be very complex. Nevertheless, the resulting strengthening from forest dislocations (τ_f) can be expressed as [24, 28]:

$$\tau_f = \alpha G b \sqrt{\rho_f}, \quad (4)$$

where ρ_f is the forest dislocation density, α is a constant connected with the strength of actual interaction force, G is the shear modulus, and b the magnitude of the Burgers vector.

Dislocation motion can be accelerated by temperature elevation, as dislocations can overcome obstacles by thermally activated processes [25]. At sufficiently high temperatures, recovery of deformed structure can occur. During recovery the dislocations annihilate and rearrange in order to minimize the stored deformation energy. Alternatively, a recrystallization process can occur, when new defect-free grains nucleate and grow at the expense of the deformed structure.

1.2.2. Solid solution strengthening

Atoms of different elements dissolved in the matrix phase can lead to its strengthening by solid solution strengthening. These impurity atoms, either in substitutional or interstitial positions, impose lattice strains on surrounding atoms resulting in a lattice strain field. Interactions of these strain fields with dislocation distortion field affects the dislocation movement.

There is a variety of interactions existing between solutes and lattice dislocations. Considering only the elastic ones, two main types can be distinguished - the size effect and the modulus effect. The first one stems from the size misfit of the solute and matrix atoms, the other from the difference in the shear modulus. Both differences lead to a variation in the local stress field around the solute atom in a different manner leading to restriction of dislocation movement.

The strengthening effect of obstacles (solute atoms) ($\Delta\tau$), which need to be bypassed by dislocations was originally described by Orowan in the form [24]:

$$\Delta\tau = \frac{F_0}{bL}, \quad (5)$$

where F_0 is the obstacle strength, b the magnitude of the Burgers vector, and L the obstacle average spacing. This obstacle spacing is usually expressed in two forms. Assuming a straight dislocation line, it is $L = \frac{b}{c}$, for a flexible dislocation line $L = \frac{b}{\sqrt{c}}$, where c is the concentration of solutes.

The equation (5) can be rewritten (through substitution for F_0 and L) to express the strengthening effect from the difference in size and/or modulus of solutes at 0 K as [24, 28]:

$$\Delta\tau = G f^n c^m, \tag{6}$$

where G is the shear modulus, f a measure of the obstacle strength, c the solute concentration, n resp. m varies assuming different nature of obstacles resp. on the average obstacle spacing.

According to the assumed nature of obstacles, the average obstacle spacing and the dislocation flexibility, there are several models describing the dislocation-obstacle interaction. There are two main statistics, the Mott-Labusch statistics for a dense distribution of weak obstacles and Friedel statistics for a dilute solution of strong obstacles. Flexible dislocation lines in Friedel-Fleischer approximation of a dilute solution of strong obstacles leads to n = 3/2 and m = 1/2 [24, 30, 31]. In Mott-Labusch approximation of dense distribution of weak obstacles the strengthening effect of a random array of obstacles is characterized by n = 4/3 and m = 2/3 [24, 32].

At temperatures above 0 K the dislocations can overpass obstacles also by thermally activated processes. Moreover, at temperatures, when the solute atoms become mobile, the solutes diffuse to dislocations and form atmospheres around them. As a result, the dislocations can be pinned by solute atoms and an increased stress has to be applied in order to unpin the dislocations.

1.2.3. Precipitation and dispersion strengthening

Second phase particles present further type of obstacles for dislocation movement. The presence of a second phase particle represents a distortion in the matrix lattice. Therefore, the obstacles which hinder the dislocation motion are either the strain field around second phase particles or the second phase particles itself or both [33]. A short description of this problematics follows.

The particle-matrix interface gives rise to interfacial energy, whose magnitude depends on the interface properties. Therefore, the interaction between dislocations

and second phase particles depends on the type of the interface. According to the matching up of matrix and second phase lattices, three types of interfaces can be distinguished. In coherent interfaces, where the crystal structure and atomic arrangement of second phase and matrix match up on the boundary, the interfacial energy, normally consisting of chemical and structural contribution, has only the chemical part. In semi-coherent interfaces, where the failure in periodicity is solved by the introduction of misfit dislocations, the structural contribution of the interfacial energy appears. In incoherent interfaces, there is a large atomic misfit between the second phase and matrix lattices which results in a huge increase in interfacial energy.

Beside the particle-matrix interface, whose matching leads to so called coherency hardening, the second phase particles strengthening effect depends also on the particles internal structure and properties. In case, the dislocation cuts the particle, there are further contributions to precipitation hardening:

- modulus strengthening,
- strengthening from difference in stacking fault energy,
- strengthening by anti-phase boundaries,
- strengthening from new interfaces.

The second phase particles are formed by foreign atoms in combination with the matrix atoms and usually have a different structure than the matrix. Therefore, they usually have shear modulus different from that of the matrix. This leads to a change in the dislocation line tension when it enters the particle. Moreover, the particle and matrix can also differ in their stacking fault energy, which can mean a change in the flow stress to cross the particle by a dislocation. In case of an ordered particle, its crossing by a perfect dislocation can lead to generation of an anti-phase boundary, leading to strengthening. Further, dislocation cutting produces new ledges on the particle, which is a new interface between the particle and matrix, therefore it increases the interfacial energy.

The main strengthening effect of second phase particles is usually expressed by Labusch theory as [24]:

$$\Delta\tau \sim f_w^{\frac{2}{3}} R^{\frac{1}{3}} (\eta, \delta, \gamma_{AF}, \gamma_{\Delta SFE}, \gamma_{\alpha\beta})^{\frac{4}{3}}, \tag{7.1}$$

or by Friedel theory as [24]:

$$\Delta\tau \sim f_w^{\frac{1}{2}} R^{\frac{1}{2}} (\eta, \delta, \gamma_{AF}, \gamma_{\Delta SFE}, \gamma_{\alpha\beta})^{\frac{3}{2}} \tag{7.2}$$

where f_w is the weight fraction of second phase particles, R is the radius of second phase particles, η and δ denotes the relative change of shear modulus and lattice parameter, γ_{AF} denotes the anti-phase energy, $\gamma_{\Delta SFE}$ is the difference of stacking-fault energy in particle and matrix, $\gamma_{\alpha\beta}$ denotes the particle-matrix interface energy.

The second mechanism, when dislocations can by-pass second phase particles, is Orowan dislocation looping. The strengthening effect connected with dislocation bending needed in this process can be expressed as [28]:

$$\Delta\tau = \frac{Gb}{L-2R} \tag{8}$$

where G is the shear modulus, b the magnitude of the Burgers vector, L is the average obstacle distance, R is the radius of the second phase particles.

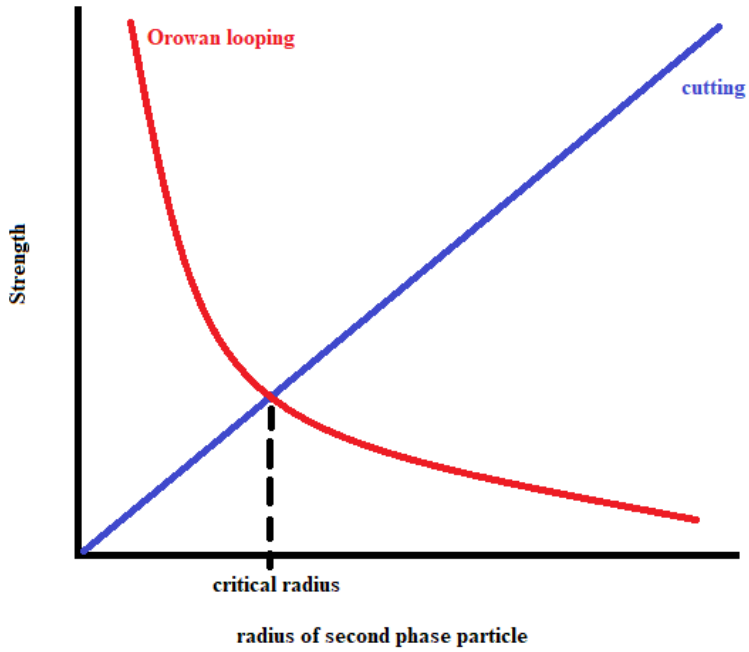

Figure 1. The scheme of dependence of the strength needed to cut through a second phase particle by a dislocation or to bypass it by Orowan looping on the radius of the second phase particle.

Consequently, the strength needed to cut through or bow the dislocations around the particle selects the active mechanism. However, as remarkable from Eq. (7.1) or (7.2) and (8), the active mechanism largely depends on the radius of the obstacles. Figure 1 shows the dependence of both mechanisms on the precipitate radii (with coherent boundary). It can be seen, that dislocations should cut the smallest

second phase particles, but above a critical radius, they should bypass them by Orowan looping [24].

In case of particles with semi- or incoherent boundaries, the value $\Delta\tau$ in Eq. (8) is not changed, but the value $\Delta\tau$ in Eq. (7) is increased. Therefore, the critical radius decreases. Consequently, maximum strengthening effect can be achieved by precipitates with coherent boundaries and with radius equal to the critical one, where the values of $\Delta\tau$ derived from Eq. (7) and (8) are equal.

At elevated temperatures, the dislocations are thermally activated, and bypassing particles becomes easier. Therefore, the strengthening effect of second phase particles decreases. Further, high temperatures can result in particle coarsening which leads to a decrease of their strengthening effect. At certain temperatures the second phase particles can dissolve, reducing thus the materials' strength, however, dissolution of second phase particles leads to solid solution strengthening.

1.2.4. Grain boundary strengthening

Grain boundaries represent an important obstacle for moving dislocations in polycrystalline materials. The strengthening due to grain boundaries has been found to be expressible by the Hall-Petch relation for both pure metals and alloys over a large range of grain sizes as [24, 28]:

$$\sigma_y = \sigma_0 + kd^{-\frac{1}{2}}, \qquad (9)$$

where σ_y is the yield stress, σ_0 is the contribution of other strengthening mechanisms, d is the grain size, and k is a constant individual for each material. This constant characterizes the shear stress required to release accumulated dislocations. Reducing the grain size, the density of grain boundaries and their strengthening effect increases. Therefore, grain boundary strengthening is the most essential strengthening mechanism in ultrafine-grained materials.

The Hall-Petch relation is applicable only in case of materials with a grain size above a critical value. When the grain size decreases below the critical value and becomes unable to support dislocation pile-ups, weakening mechanisms as viscous flow occurs and leads to a decrease in strength with decreasing grain size [34]. This critical grain size is below 10 nm for most metals [34, 35].

At higher temperatures or in materials containing non-equilibrium grain boundaries (as in heavily strained materials), dislocations can be trapped by grain

boundaries and annihilate there. In materials with high volume fraction of grain boundaries this mechanism leads to remarkable softening. Moreover, with decreasing grain size, other deformation mechanisms like grain boundary sliding occur, leading to a break-down of the Hall-Petch relation.

1.3. High temperature stability of strength

A brief overview of strengthening mechanisms given in previous paragraphs shows that temperature strongly influences the materials' strength especially through phase composition and microstructural changes. In order to maintain high material strength also at elevated temperatures, the stability of second phase particles and grain structure is required. Both these aspects will be discussed below.

1.3.1. Stability of strengthening particles

Due to the temperature dependence of the equilibrium solid solubility of solutes in solvents, the content of second phase particles varies with varying temperature. Changing the temperature, the decreasing equilibrium solid solubility leads to formation of second phase particles, whereas increasing equilibrium solid solubility results in their dissolution.

Beside processes induced by altering the temperature, second phase particles can evolve also at a constant temperature. The material containing second phase particles can reduce its energy among others by lowering the surface to volume ratio of second phase particles, i.e. by a growth of larger particles at the expense of smaller ones. The kinetics of this process, also called Ostwald ripening, is controlled by volume diffusion of solute atoms from shrinking second phase particles to growing ones.

As showed by Lifshitz, Slyozov and Wagner [36-38] for coarsening of particles in binary alloys, the average particle radius $\langle R \rangle$ increases with time t as follows:

$$\langle R(t) \rangle^3 - \langle R(t=0) \rangle^3 = k_r t, \qquad (10)$$

where $\langle R(t) \rangle$ is the average particle radius at time t, $\langle R(t=0) \rangle$ means the average particle radius at the beginning of coarsening and k_r is the rate constant, which can be related to properties of system as:

$$k_r \propto D c_e \sigma, \qquad (11)$$

where D is diffusivity of alloying element, c_e is the equilibrium solid solubility of the alloying element and σ is the matrix-precipitate interfacial energy [38].

In order to maintain the strengthening effect of second phase particles also at elevated temperatures, their size has to be stabilized, i.e. Ostwald ripening has to be prevented. Hence, it is essential to choose proper alloying elements. According to Eq. 10 and 11, elements with low diffusion coefficient and low equilibrium solid solubility in matrix, which form second phase particles with a low interfacial energy (low misfit) to the matrix phase should minimize the coarsening rate of second phase particles.

1.3.2. Stability of grain structure

It has been shown in paragraph 1.2.4. that grain boundaries represent obstacles to dislocation movement and contribute thus to materials' strength. In order to retain its contribution to strength, the grain size has to be stabilized. However, a high amount of energy connected with grain boundaries especially in fine grained materials represents a large driving force for total energy reduction through grain coarsening [39].

Grain coarsening occurs usually through a migration of grain boundaries into neighbouring grains. The velocity of grain boundary migration (v) during grain coarsening can be expressed as [39, 40]:

$$v = MP = M_0 e^{-\frac{Q_m}{RT}} \frac{2\gamma_b}{r}, \qquad (12)$$

where M is the grain boundary mobility, P denotes the driving force for grain growth, M_0 is the grain boundary mobility constant, Q_m is the activation energy for grain boundary migration, γ_b is the grain boundary free energy per unit area, and r the radius of grain boundary curvature.

There are two possibilities how to reduce the velocity of grain boundary migration: a thermodynamic and a kinetic way. The thermodynamic way of grain size stabilization is based on the reduction of activation energy for grain boundary migration (Q_m), which is often done by doping boundaries with solutes having large atomic size mismatch with the matrix atoms [41]. The kinetic approach relies on the reduction of grain boundary mobility, M [39, 42]. This is performed especially through second phase particles and inclusions, dispersed in matrix, which can apply pinning pressure on grain boundaries (Zener drag mechanism), which counteract driving force

of grain boundaries movement. The pinning pressure (P_Z) exerted by particles on unit area of grain boundary can be expressed as [43]:

$$P_Z = \frac{3f_p \gamma_b}{2r_p}, \quad (13)$$

where f_p is the volume fraction of randomly distributed spherical precipitates, r_p is their diameter and γ_b is the specific grain boundary free energy.

If the driving force of grain growth (P) becomes balanced by Zener pinning, the grain coarsening stops. The materials final average grain size $\langle D_f \rangle$ then can be expressed as [44]:

$$\langle D_f \rangle = \alpha_g \frac{4}{3} \frac{\langle r \rangle}{\langle f \rangle}, \quad (14)$$

where $\langle r \rangle$ denotes the average radius and $\langle f \rangle$ is an average volume fraction of spherical second phase particles, and α_g is a constant. According to Eq. 14, introduction of a high volume fraction of fine second phase particles can enhance the Zener pinning on grain boundaries and a fine grain size can be retained.

Coarsening of second phase particles at elevated temperatures results not only in a reduction of their strengthening effect (as mentioned in the previous paragraph) but also in a drop of the Zener drag and a higher grain boundary mobility. Moreover, in case of extreme temperatures, the kinetic way of grain size stabilization becomes impractical, since the mobility of grain boundaries follows an Arrhenius type function. Under these conditions the thermodynamic way of stabilization becomes more important as the grain boundary energy is only slightly dependent on temperature [45].

1.4. Theory of processing methods

As mentioned in the introduction, the development of modern materials with unique properties requires usually alternative processing routes. In the current thesis a PM route was chosen. Both its parts, i.e. the powder production and its consolidation will be discussed below separately.

1.4.1. Powder production techniques

Fine grained powders can be processed by a wide variety of techniques, as listed in [7] or [46]. The three main powder production methods are:

- physical methods as rapid solidification,

- mechanical methods: crushing, grinding, mechanical alloying, milling,
- chemical methods: electrolytic deposition, precipitation from liquid or gas etc.

Rapid solidification and milling, used in the current research, will be further described in detail.

1.4.1.1. Rapid solidification

Rapid solidification techniques enable a rapid extraction of thermal energy from the molten metal. Cooling rates up to 10^6 Ks^{-1} can be achieved, whereas conventional casting is characterized by cooling rates below 10^2 Ks^{-1} [8, 47]. The high cooling rate of RS leads to undercooling of the melt by 100 K or more [7, 8]. This technique therefore offers advantages in comparison to conventional casting techniques, like:

- extended solid solubility,
- suppression of precipitation or refinement of precipitates,
- formation of non-equilibrium phases, quasicrystals,
- grain size reduction.

The solidification microstructure is influenced by the rate of the solid-liquid interface movement (solidification velocity, V_s) and the temperature gradient (G_T), resulting from the melt undercooling and the recalescence. Beside these thermal effects also the kinetic effects have to be considered. The solidification kinetics is mainly influenced by solute segregation and interface energy [8].

Undercooling of the melt to a high degree can lead to extreme temperature gradient and formation of a single phase metastable solid solution, to a segregation free microstructure. The resulting material then exhibits a compositional uniformity, and the supersaturated solid solution can serve as a basis for controlled precipitation. However, this is attainable only at a specific undercooling - varying with the concentration of solute - where the free energy per unit volume of the liquid and the solid solution is the same [47].

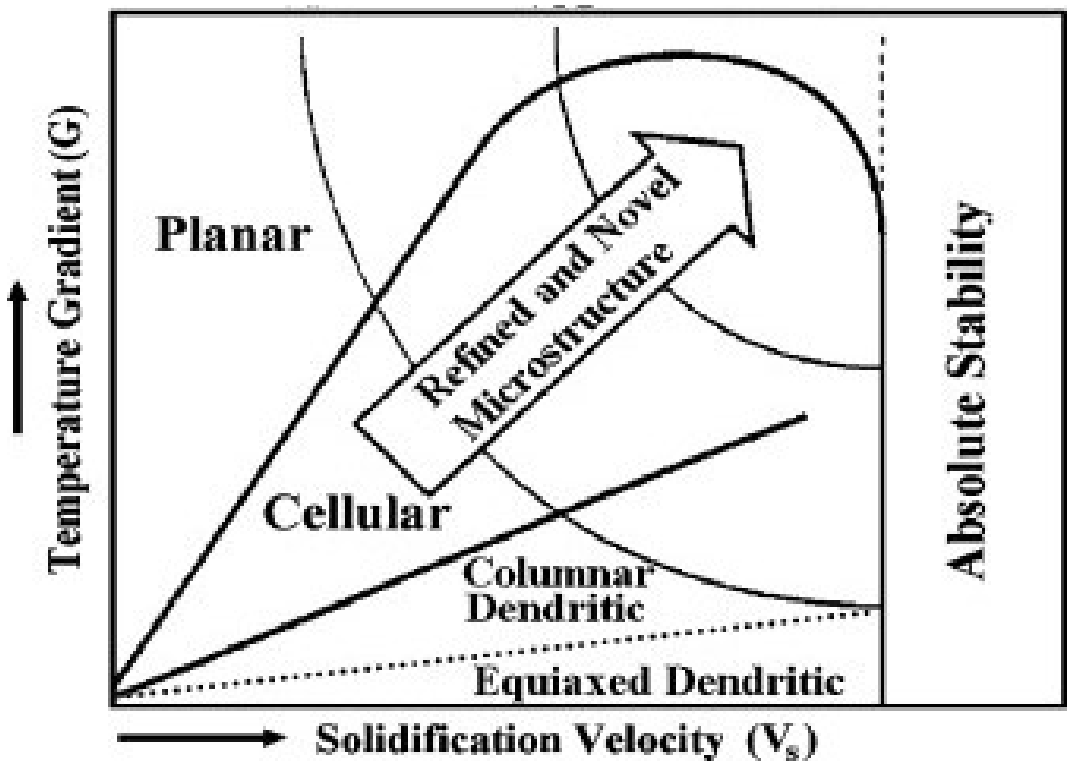

Figure 2. Schematic representation of the dependence of solidification microstructure on the temperature gradient and solidification velocity during solidification of alloys, taken from [48].

During solidification of alloys, solute atoms usually are unable to diffuse away from the fast moving solid-liquid interface to maintain a uniform composition in liquid, which leads to a constitutional undercooling of the melt along the interface. The resulting thermal gradient can destabilize the planar growth front. Nevertheless, at higher growth rates the interface energy has a stabilizing effect, resulting in a planar growth. However, as the solidification front velocity slows down or the temperature gradient decreases a transition from planar to cellular, or from cellular to dendritic growth mode can appear [8, 47], as illustrated in Figure 2.

The high degree of undercooling leads also to a high nucleation-rate and thus, to a fine grain size [8]. However, extreme cooling rates in small volumes of material can result in an insufficient time to more than one nucleation event leading to single crystalline powder particles [49].

The broad spectrum of rapid solidification techniques can be divided into two basic groups. In the first group, the RS is achieved by a high rate of heat extraction. The melt spinning is a typical representative of these so called chilling methods. In the

second group, the melt is undercooled before nucleation, which is typical for so called atomization methods [50].

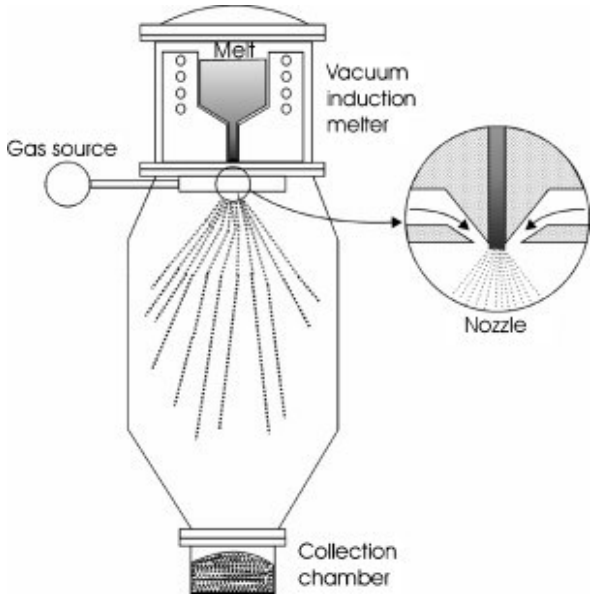

Figure 3. The scheme of the gas atomization method [51].

During atomization, the molten liquid metal is broken up into droplets which then solidify into a metal powder. Three different types of atomization processes can be distinguished according to the processes disintegrating the molten metal - explosion of liquid metal, fragmentation by centrifugal acceleration or impingement by an atomizing media. In the first case, for example during vacuum atomization, the molten metal is exploded into droplets after its exposition to vacuum. Centrifugal atomization forms droplets of metal by rotating a molten metal electrode. In the last case, the liquid metal stream is impinged into droplets by a high pressure gas or liquid stream serving as the cooling media (see Figure 3).

Powders of metallic materials are frequently prepared by gas atomization using inert gases like N_2, He or Ar. The inert atmosphere helps to avoid moisture absorption on the powder surface and the degassing step prior to consolidation is not needed [47].

The disintegration of molten metal during gas atomization can be divided into 5 steps [8]:

- unstable wavy melt stream after its contact with the atomizing gas,
- formation of ligaments or wave fragments,
- the decomposition of ligaments/wave fragments into droplets/primary fragments,
- further disintegration of droplets/primary fragments,

• collision and coalescence between the droplets/primary fragments.

The size distribution and shape of resulting powder particles depend on a range of variables, like nozzle design, type of atomizing gas, gas flow rate, molten material flow rate, type of metal and its temperature [7, 8]. Depending on the cooling rate and the surface tension of the cooled material the atomized powder shape changes from spherical through coalescence spheroids to coalescence membrane product (with decreasing surface tension and increasing cooling rate).

1.4.1.2. High energy milling

As mentioned above, RS extends solute solubility and refines grain size. Further microstructural refinement can be achieved by mechanical milling of the rapidly solidified powder. Simultaneously, mechanical milling can extend solid solubility compared to RS [11].

There are two different terms denoting the processing of powder particles in high-energy mills. Mechanical alloying is used for processes where mixtures of dissimilar powders are milled together [11]. The goal is to obtain a homogeneous alloy through material transfer. Milling of frequently pre-alloyed powders, where the material transfer is not the primary goal, is denoted as mechanical milling [11]. Mechanical milling is a widely used PM method developed for powders grain refinement and producing dispersion strengthened alloys with a uniform distribution of fine second phase particles.

Mechanical milling can improve the material strength as follows:

• the high density of dislocations leads to work hardening (Eq.4),

• the refined grain size raises the strength according to Eq. 9,

• milling usually extends solid solubility enhancing solid solution strengthening (Eq.6),

• second phase particles, dispersoids or precipitates, introduced into the material or evolved during milling contribute to dispersion or precipitation strengthening, Eq. 7.1, 7.2 and 8.

From the macroscopic point of view, the powders evolve through repeated deformation, fracture and welding of powder particles [11]. On a microscopic scale, at early stages of milling the deformation is localized in shear bands. After reaching a certain strain level the dislocations recombine or annihilate leading to a formation of

small angle boundaries. In this stage nanometer sized crystallites can be formed. Further milling leads to a steady state grain size distribution with randomly oriented grains divided by high angle boundaries [11].

The minimum grain size obtainable by milling is determined by a balance between the dislocation generation induced hardening rate and the recovery rate from dislocation annihilation and recombination. The model developed by Mohamed [52] predicts that the minimum grain size scales inversely with hardness, proportionally with stacking fault energy and exponentially with recovery activation energy. Fcc (face centred cubic) metals were long claimed to be too soft for effective energy storage from milling and, thus, for grain size reduction due to their high recovery rate. Nevertheless as shown first by Eckert et al. in [35], choosing proper conditions even nanocrystalline fcc metals can be prepared.

During milling, impurities can be introduced into the milled powder from the milling media, as balls, jar or atmosphere. For example, milling of Al powders is carried out usually in a stainless steel media. Contamination of Al powder by Fe during MM was reported to be very low, since Fe content in milled Al powders was reported to be 0.04 at% after 20 h of milling [35] resp. 0.12 wt% after 8 h of milling [53], which is below the impurity level of Fe in most commercial Al alloys [54]. The milling atmosphere can be diffused or entrapped into powder particles during milling or it can form various second phase particles with the powders matrix. Nitrogen or ammonia can be used to produce nitrides; hydrogen atmosphere contributes to formation of hydrides. Further, milling in air leads to formation of oxides [55]. To avoid this contamination, the milling area should be evacuated or filled with inert gases, especially in the case of reactive elements, as Al [10, 11]. Nevertheless, the introduced solutes, oxides, nitrides or other phases can play a significant role in materials microstructural stabilization through solute drag [56] and Zener pinning [57, 58]. Zener pinning of grain boundaries by AlN and Al_2O_3 particles was shown to suppress grain coarsening during consolidation of cryomilled Al5083 powders [58].

Beside fracturing, also cold welding of powder particles can occur during milling. Cold welding occurs also between powder particles and milling balls or milling jar. This process diminishes the production efficiency of mechanical milling as a significant amount of the powder remains stacked to the milling balls or jar. Removing of these stacked powder particles is very complicated and if the same milling balls and jar are used for further milling the new powder can be partially

contaminated by residuals from previous millings. A process control agent (PCA), which absorbs on the powder particle surface and reduces the surface energy prevents excessive agglomeration and mediates cold welding [59]. In case of Al alloys stearic acid is usually used, but ethanol, toluene or methanol were also reported as PCA for ball milled Al [10]. PCA is also a source of hydrogen, oxygen and carbon [60, 61]. Therefore, it is suggested to degas the milled powders before consolidation to remove volatile contaminants, since after powders consolidation the dissolved and trapped gases can result in porosity and degrade final mechanical properties [60]. On the other side, PCA also can lead to dispersion strengthening of material by oxides and carbides derived from the agent.

Beside the PCA, cold welding can be suppressed also by lowering the milling temperature [11]. This accelerates fracture processes and helps to attain the steady state conditions more rapidly. Cryomilling (milling at cryogenic temperatures) offers the following advantages compared to milling at room temperature [62-64]:

- suppresses agglomeration and welding of the milling media,
- suppresses solid redistribution, recovery or recrystallization,
- contributes to further grain refinement, frequently up to a nanocrystalline range,
- reduces the milling time required to form a nanocrystalline structure due to a suppression of dislocation annihilation,
- reduces oxidation under the protective nitrogen or argon atmosphere.

Beside the milling temperature, there are also other variables which determine the resulting microstructure of milled powders. These variables, like type of the mill, material of milling balls and jar, size of balls, ball to powder weight ratio, filling, milling time, and milling rate have then a pronounced effect on powders final microstructure and properties [10, 11].

There are several types of ball mills differing in their setup, arrangement for cooling, atmosphere control and efficiency of milling. The planetary ball mill and attritor belong to the most commonly used mills in production of fine grained Al powders [10, 11].

Planetary ball mills get balls into stirring motion by a rotation of the hollow cylindrical milling jar about its axis with a concurrent rotation of the milling jar system in the opposite direction resulting in a planet-like motion. The scheme of a planetary ball mill with the marked rotation directions is presented in Figure 4a. Since the

individual jars and the jar system rotate in opposite direction the centrifugal forces act in like and opposite directions [10]. This causes the milling balls to run down the wall of the jar and keep on grinding the powder [11].

Attritor (Figure 4b) consists of a stationary cylindrical grinding chamber and a drive shaft with multiple impellers set at right angles to each other and perpendicular to the shafts axis. This rotating shaft puts the milling media and powder into stirring motion. It energizes the milling balls, causing impact between balls, charge, shaft, impellers and container wall. The attritor tanks are jacketed allowing thus a more precise temperature control compared to usual planetary ball mills. Flowing water between the milling jar and its jacket cools the tank vessel and helps to suppress heat generation during milling, which could lead to massive solid reorganisation, recovery and recrystallization of the powder material.

As different mills differ in setup, temperature and atmosphere control etc., their efficiency of milling differs. According to [10] the milling efficiency of attritor is above that of the planetary ball mills.

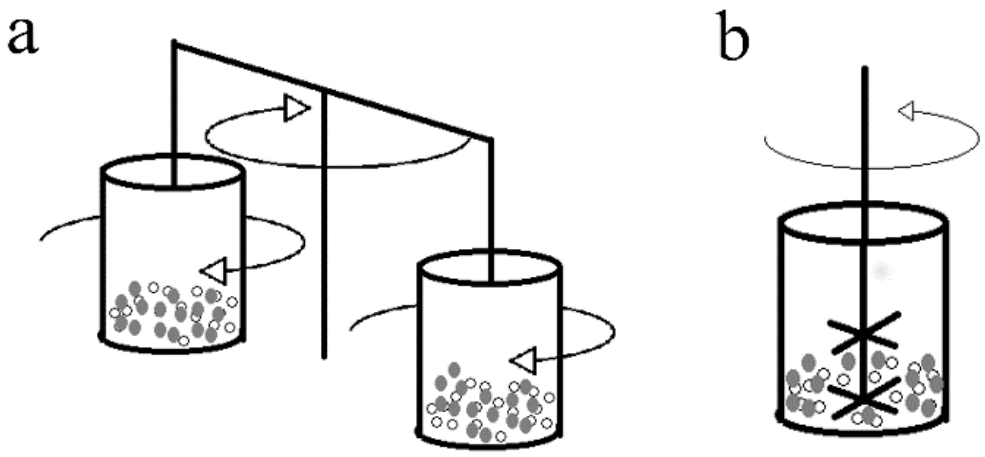

Figure 4. The scheme of the most commonly used mills in production of fine grained Al powders: a) planetary ball mill and b) attritor.

During ball milling, powder is altered through the high energy collisions by the milling jar and milling balls. The energy introduced into the powder material depends also on the characteristics of the milling jar and balls. Milling jars and balls are usually made of steel, tungsten carbide, alumina or zirconium oxide. Using WC or Zr_2O, diffusion and abrasion resulting in contamination can be minimized at the expense of the higher cost [10]. The size and density of balls influences the grain refinement rate,

since balls of higher specific gravity provide higher impact energy events resulting in a higher transferred energy [11].

Increasing ball-to-powder (BTP) ratio increases the number of collisions per unit time and thus the energy transferred to powder particles. However, this also leads to a possible increase in generated heat. Filling depends on the mill type used, usually it is about 50% to ensure enough space for the motion of milling media and powder [11].

Increasing milling time reduces the grain size exponentially up to a certain stationary value [11]. However, prolonged milling can lead to undesired contamination or formation of unwanted phases. Increase in milling rate characterized by revolutions per minute (RPM), usually increases milling intensity leading to quicker attainment of the steady state. However, there is an upper limit as the balls should not be pinned to the walls of the milling jar (in case of moving jars). Furthermore, a very high RPM can lead to undesirable temperature increase which might negatively influence the microstructure of the milled powder [11].

1.4.2. Powder consolidation methods

The small size of powder particles limits their engineering applicability. Therefore, they have to be compacted into bigger parts using suitable techniques. These techniques should lead to full density compacts and, simultaneously, have a minimum influence on the powders favourable properties in order to retain them in the compact. Solid state consolidation of powders is completed through a thermally activated mass transport driven by a surface and grain boundary energy reduction. Most consolidation methods - as cold pressing (CP), cold isostatic pressing (CIP), hot pressing (HP) and hot isostatic pressing (HIP) - use pressure (and in case of HP and HIP also elevated temperatures) to produce bulk samples. Others, like SPS use additional sintering mechanisms in order to get full density at temperatures lower than those used during HP and HIP [15].

1.4.2.1. Cold pressing, cold isostatic pressing, hot pressing, hot isostatic pressing

Bulk samples can be prepared from powders using pressure-less and pressure assisted forming operations, with or without external heating [10, 65, 66]. To the pressure-less sintering technologies belong methods as slip casting or microwave sintering. During sintering by these technologies, the powder is filled into a mould with or without a convenient liquid. Further, the mould is trimmed and led to dry or is heated by microwave heating [67].

During pressure assisted forming methods, the powder is filled into a closed die and the pressure is applied using punches or isostatically by a bath. According to the measure of external heating, these methods are divided into cold and hot compaction methods.

In cold compaction methods, the temperature does not exceed the level, above which typical high temperature deformation mechanisms like dislocation or diffusional creep occur [10, 46]. During cold compaction the densification proceeds due to rearrangement of powder particles, their plastic deformation and formation of mechanical bonds at inter-particle interfaces [46].

The most widely used cold compaction methods are CP and CIP. During CP, the pressure is applied uniaxially, using one or two punches. The friction at the die wall and the nature of the load distribution inside the die leads to heterogeneous density of the green sample [46]. CP is usually used to prepare a desired shape compact from the powder, with a density around 80% [68]. During CIP, the pressure is applied simultaneously and equally in all directions using a pressure transmitting fluid or powder bed, whereas the powder is sealed in elastomer container shaped for the application. The absence of wall friction enables homogeneous density distribution [46]. Material processed by CIP can reach 95-98% of the theoretical density [66, 69].

Higher density compacts can be obtained by sintering at elevated temperatures, where additional densification mechanisms occur. Temperatures above half of the melting point of given material lead to thermal activation of material and to sufficient mass transport between powder particles. The activated densification mechanisms are plastic yielding, power-law creep, diffusional creep and grain boundary sliding [46]. HP and HIP belong to the most used hot compaction methods. Similar to CP, HP uses axial pressure whereas during HIP the pressure is applied isostatically, as during CIP.

Due to the elevated temperature the porosity is reduced by necks' growth, plastic deformation of powders, creep and mass diffusion, leading to samples with improved density (when compared with CP and CIP samples) [66]. HP was reported to lead to densities up to 99.5% of theoretical density in an Al-Cu sample, but the sample was processed at 450 °C under 300 MPa within a long period, 2h, which led to extensive grain growth [70]. HIP was reported to lead to density up to 98.9% in an Al-Cu-Mg alloy using 580 °C and 130 MPa for 3h and the high temperature was reported to lead to localized melting [71].

The conventional consolidation methods as CP, CIP, HP, and HIP, are usually followed by secondary processing as extrusion, forging or rolling [72-75]. These are used to change the shape of the final part, to further raise the density and to break the oxide layer present on the surface of powder particles of some alloys. Oxide layers, due to low diffusion rates through the oxide layer, hinder solid state sintering [76]. But using secondary processing techniques these oxide layers can be destroyed and a metal-metal contact between powder particles can be achieved.

Although these methods, CP, CIP, HP and HIP, make possible to attain a high density compact and complex shaped samples, they are regarded to require specialized and costly instruments which operate at high pressures and have sample size restrictions which present serious prohibitions in significant upscaling [10]. Another issue is connected with the relatively slow heating rate (around 16 C°/min [77]) which also varies with the sintered part's volume. The slow heating rate to desired temperature means prolonged heat exposure. As already mentioned, powders processed by RS or mechanical milling are usually in a non-equilibrium state with a high level of supersaturation, metastable phases, high dislocation density (just in case of mechanically milled powder) and small grain size. Such materials will tend to their equilibrium during long exposition to elevated temperatures [78]. Prolonged heat influence could lead to solid redistribution, transformation of metastable phases to the stable ones, dislocation rearrangement and annihilation during recovery and recrystallization. Further, grain coarsening can occur along with precipitation of phases from the solid solution. Therefore, the powder should be exposed to the lowest possible temperature for the shortest time at which it is still possible to achieve a full density material. Compaction methods capable to produce high density products with a short exposition to the lowest possible sintering temperature have to be sought.

1.4.2.2. Spark plasma sintering

Spark plasma sintering, also called pulsed electric current sintering or plasma assisted sintering combines uniaxial pressure with heating by a direct pulsed electrical current [15, 79].

The current enables direct heating through Joule heat, with heating rates up to 1000 °C/min, which helps to limit the heat exposure time of the powder. Further advantages of SPS are the lower sintering temperature compared to conventional sintering techniques, no need of pre-compaction of powders and the possibility to produce compacts with nearly theoretical density [15].

Figure 5 shows the scheme of an SPS device and a typical scheme of the SPS process. During SPS, the powder is placed in a die, vacuum is set and a low initial load is applied to ensure the contact between the loosely packed powder particles. The powder is heated with a defined heating rate to the chosen sintering temperature, and a pressure is simultaneously applied (Figure 5b). Both the mechanical load and electric current can be maintained constant during the sintering cycle or they can vary during the sintering process. The pressure may increase gradually during the sintering and an on-off pulse pattern with a 1-300 ms pulse duration can be applied. The temperature is usually controlled through axial pyrometers placed in a hole in the punch or by radial pyrometer placed in a hole in the die, or with a radial pyrometer focusing on the outside of the die. After sintering the sample is unloaded and cooled.

The sintering is usually reported to occur in the following steps: [80]

- rearrangement of powder particles
- powders activation
- sintering neck formation
- sintering neck growth
- plastic deformation

In case of conductive powders, powders activation is reported to be promoted by the spark discharge, which removes surface oxides and increases powder surface leading to neck formation by evaporation, condensation and diffusion. The third and fourth steps are promoted by current, which flows through necks leading to Joule heat and therefore fast densification. The plastic deformation in the last step is enhanced by the applied pressure at high temperature [80].

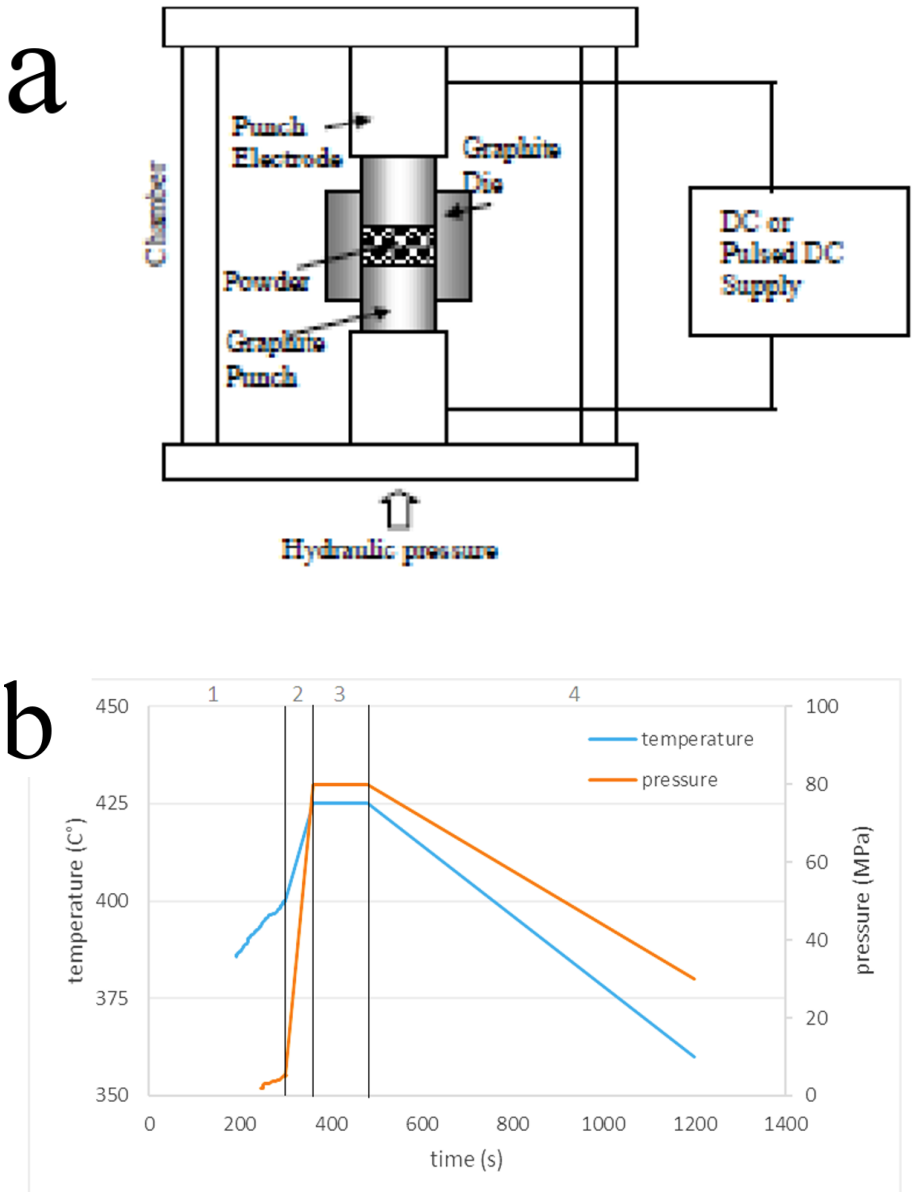

Figure 5. The typical scheme of an a) SPS device [15] and b) of the SPS process.

In conductive powders, the energy is dissipated within the sample and conductive parts of the SPS tooling. Thus, the Joule heat makes possible to reduce beside the duration also the energy costs of sintering [15]. In non-conductive powders, conductive tooling need to be used and the Joule heat generated in the SPS tooling is transmitted to the powder.

The maximum used load is between 50 and 250 kN depending on the SPS tooling material [81]. The process can be carried out under vacuum or in a protective inert gas atmosphere. Samples after sintering are free cooled, alternatively cooling rates up to 150 °C/min can be achieved due to the water cooling of the chamber, or a cooling rate of 400 °C/min can be attained with additional tooling [81].

In order to choose the proper sintering parameters, the processes taking place during SPS should be discussed.

Mechanical aspects

Applying pressure during powder sintering was shown to promote densification [82]. The pressure breaks up the powder particle agglomerates, changes the amount and quality of contacts between powder particles. This way, it helps to reduce sintering temperatures and to shorten sintering times without a negative influence on the density and grain size of sintered compacts [81].

The effect of pressure changes with temperature. If the sintering pressure is applied already at low temperatures (at the beginning of sintering), it is below the yield strength of the powder and no plastic deformation occurs. If the same pressure is applied at high temperatures, plastic deformation of powder particles can occur, as the increasing temperature leads to a drop in the yield strength of most metallic powders. Therefore, in conventional pressure assisted consolidation processes the pressure is applied preferably at elevated temperatures, where the pores can effectively collapse leading to higher density [83]. Guillard et al. reported about sintering of SiC particles by SPS [84]. They demonstrated, that application of pressure at the temperature of SPS helped removing closed porosity and led to improved densification, compared with the sample at which the pressure was applied at temperature below the SPS temperature. On the other side, pressure applied already at temperatures below the SPS temperature led to a slightly higher density in low temperature (250-300 °C) SPS compacts from milled Al powder [85]. The discrepancy can be explained by the behaviour of materials. Whereas SiC particles are hard at lower sintering temperatures, Al exhibits plastic flow which limits formation of closed pores.

Thermal aspects

During SPS, the sample is heated directly by Joule heating, which in conductive powders leads to high heating rates. It enhances densification diffusion processes and reduces the time and the temperature needed to attain full density compared to conventional sintering methods as HP or HIP, where the powder is heated by conduction [15, 86].

The rapid heating makes possible to reduce the influence of prolonged, high temperature exposition. Among others, it limits the grain growth. Sintering of alumina was presented to lead to a finer grain size if higher heating rates were used [87]. Munir et al. concluded the same inverse proportion between the heating rate and resultant grain size [88].

Beside the heating rate, the cooling rate can also have a pronounced effect on the samples final microstructure. Cooling rates of 1.6 to 6.9 Ks^{-1} were achieved by gas quenching after SPS of Ti6Al4V alloy and led to an increase in materials ultimate compressive strength and ductility and to the formation of nanocrystalline intermetallic phases [89]. A rapid cooling from sintering temperature can avoid further inconvenient processes as grain coarsening or undesirable coarsening of second phase particles.

The non-uniform arrangement of powder prior to sintering can lead to non-uniform heating. Further, the non-homogeneous current path can lead to high local temperature gradients, local melting, which is more remarkable at larger sintered sample sizes and complex shapes [81, 90]. The non-uniform temperature field can create thermal stresses which contribute to the deformation of powder particles during sintering through dislocation creep.

Electrical aspects

Due to the non-homogeneity of the packed powder particles mass, the current flows at the beginning of sintering through powders contact points making percolation current paths. This asymmetric distribution of current leads to changing magnetic flux in each grain, which then become individual heat sources. The Joule heat generated along the current path leads to neck formation, where the electric resistivity falls, and high current density appears leading to high heating rate. The temperature at these places can highly exceed the set one, which can lead to local melting or solid-state recrystallization. However, the electric resistivity of the hot spots increases, consequently the current flow is diverted to other contact points forming further necks at various places, leading to a more uniform sintering. The presence of localized high current density, along with localized high temperature and stress at contact point of particles was revealed by finite element modelling [91]. These mechanisms were

considered to be responsible for a bimodal microstructure of an SPS consolidated cryomilled Al5083 powder [91].

As the material of the SPS tooling is different from that of the sintered powder the Peltier effect can appear. The discontinuity of the Peltier coefficient leads to differences in the tooling and powders temperature, which in case of conductive powder can be neglected [81].

Although usually only the thermal effects of the current are discussed, the current has also non-thermal effects. The electrical fields present in the sintering die influence the mass transport. The contact of different SPS tooling and powder materials causes also electrochemical reactions and electromigration [88, 92].

The presence of current leads to electroplastic effect. It means, that under the effect of electric field, metallic materials exhibit lower yield strength than in the absence of the field [15].

Further, electrical current can cause nucleation of second phase particles [88]. Increased current density can decrease incubation time and increase the growth rate of second phase particles, as it enhances mobility and defect concentration [93-95].

Generation of electrical discharge and spark plasma between the powder particles was discussed by many researchers, however, their presence was not yet unambiguously demonstrated. They are proposed to clean surface of powder particles leading to enhanced sintering. However, the low values of applied voltage in SPS does not fulfil the basic principle for plasma generation between gaps of powder particles as stated in [96]. Some researches confirmed, some refused their generation during SPS. Ozaki showed, that during SPS of Al powder no discharge was present when graphite die was used [97]. Tokita reported neck formation due to presence of plasma, but his research was declined by others [88]. Yanagisawa reported sparks between some particular Cu powder particles subjected to single pulse discharges, but it had no apparent influence on the neck formation [98]. A research conducted to understand SPS mechanisms by Zhang et al. [99] showed the occurrence of spark discharges during sintering by direct visual observation. In contrast, Hulbert et al. [100] utilized acoustic emission spectroscopy and ultrafast in-situ voltage measurement beside direct visual observation of SPS process on various powders and concluded, that no plasma was present during sintering.

Material aspects

SPS is widely used for consolidation of a large variety of both novel and traditional materials. SPS was reported to produce biomaterials, catalysts, glassy materials, nanostructures, piezo and pyroelectrics etc. [88]. Moreover, it was meny times shown to enhance the properties of the final samples, compared to samples prepared by traditional routes. SPS led for example to appearance of superplasticity in ceramics [101], improved magnetic properties [102], improved bonding quality [88] etc.

Sintering parameters of different materials differ due to the intrinsic and extrinsic characteristics of the sintered powders. As SPS is a solid state sintering technology, the sintering temperature is below the melting point of the sintered powder. Nevertheless, ceramics need high temperatures and pressure for densification as they have covalent bonding and low self-diffusion coefficient [81]. Metallic materials have to be sintered at temperatures, where grain boundary and volume diffusion are present. Nanostructured materials have to be sintered with short holding times and large pressure to avoid undesirable coarsening [103].

The effect of the sintered powder size on the samples final mechanical properties was studied among others by Diouf et al. on a Cu gas atomized powder [104]. He showed, that the compacts final density decreases with increasing particle size. Similarly, sintering of sieved Mg powder led to higher density compact when powder with finer particle size was compacted [105]. Similar effect was observed for several Al alloys prepared by SPS [85, 106].

1.4.2.3. Comparison of consolidation methods

During SPS, the direct Joule heating of the conductive powder and the high heating rate enhance densification processes, compared to other consolidation methods (as e.g. HIP). Further, the densification mechanisms activated by pressure, thermal and electrical effects promote to attain a high density compact.

Several studies compared the influence of different sintering techniques. Ni nanopowders were compacted by HIP and SPS by Gubicza et al. [86]. SPS was shown to lead to dense samples already at lower temperatures than HIP and with limited grain

growth. Similarly, Bousinina et al. sintered Ni nanopowder by SPS and HIP and concluded that the grain coarsening was more limited in case of SPS process [107].

Zadra et al. performed experiments on pure Al sintered by SPS technology in two modes. They sintered samples in contact with SPS punches through a conductive graphite foil or placing a non-conductive alumina spacer between the sample and the powder. In the second case the sample was heated non-directly as in case of HP. Zadra showed that the direct Joule heating led to a more uniform sintering [108]. Similar experiment was performed by Kellogg et al. Using insulating die, no high density sample could be processed from atomized Al5083 powder [109]. SPS of cryomilled Al5083 powder led to bulk compacts using both, insulating or conductive die, but there were found differences in their fracture morphology and hardness [109, 110].

Khalil sintered an Al6061 alloy with HIP, microwave sintering, furnace sintering and SPS, and found that the highest density was obtained for SPS samples [111]. Eldesouky et al. reported enhanced mechanical properties of SPS processed micro- and nano-sized Al2124 powder compared to the HP counterpart [77]. Similar enhancement of mechanical properties of an SPS sintered Al alloy compared to the material prepared by HP was reported in [112].

Due to the economic and technological advantages of the SPS technique like enhanced heating rate, relatively low sintering temperature, shorter holding time, not necessary pre-compaction, no need of sintering agents, applicability to hard-to-sinter materials, cleaning effect on boundaries and enhanced final properties along with the retention of powders initial microstructure, this technology offers a lot of advantages compared to conventional sintering technologies.

1.5. Aluminium alloys

Aluminium is denoted as the most abundant metallic element in Earth's crust, however, due to its high chemical activity it never exists in its pure form. Al is present in the form of compounds almost in all minerals, vegetation and animals. Al is about three times lighter than iron or copper and is an excellent conductor of heat and electricity. Furthermore, a tough inert oxide film is immediately formed on its surface when exposed to air, leading to its high corrosion resistance. Therefore, Al is widely used in transportation, building materials, consumer durables or chemical and food processing equipment.

Pure aluminium (99.996%) is soft and weak with an ultimate strength of approximately 10 MPa [4]. Al of commercial purity (99-99.6%) becomes harder and stronger due to the presence of impurities, especially of Si and Fe. Further strength increase can be achieved in Al-based alloys. According to the main alloying elements (e.g. Cu, Mn, Si, Mg, Mg+Si, Zn), the aluminium alloys are divided by the Aluminium Association system into 9 families (Al1xxx to Al9xxx). Some alloying elements (for example Mg) exhibit a relatively high solid solubility in Al already at room temperature and solid solution strengthening is typical for such alloys [113]. The strength of these alloys cannot be significantly influenced by thermal treatment and thus these alloys are non-heat treatable. On the other side, Al alloys containing alloying elements with limited solid solubility at room temperature and with a strong temperature dependence of solid solubility (for example Cu) can be strengthened by a suitable thermal treatment. Appropriate precipitates can be introduced into the alloy during this thermal treatment improving thus its strength. Such alloys are called heat treatable. The strength of heat treated commercial Al alloys exceeds 550 MPa [4, 5].

Grain refinement to sub-microcrystalline or even nanocrystalline range can further improve the materials' strength. Methods of severe plastic deformation (especially the method of equal-channel angular pressing) were frequently used for these purposes. However, it is difficult to combine SPD techniques with heat treatment. Formation of precipitates of strengthening phases prior to SPD usually limits deformability of the material and results in cracking during SPD. This is especially true for most Al7xxx type Al alloys containing Zn as the main alloying element [114, 115], where strengthening phases form rapidly after quenching, limiting thus the time for the following SPD. This limitation was overcome by pre-aging treatment, however it led to overaging connected with remarkable strength loss [116].

Powder metallurgy represents an alternative processing route which could combine the contribution of several strengthening mechanisms. The following sections provide an overview of results obtained at various PM Al alloys, especially on those with composition similar to materials investigated in our research.

1.5.1. Powder metallurgy of aluminium alloys

Powder metallurgy is widely used in the production of Al alloys. Materials with desirable properties, not attainable through conventional metal working processes, can

be produced through PM. Moreover, PM processing route is characterized by a large flexibility in material selection and design. PM route is currently extensively used to produce high strength and/or creep resistant Al alloys with properties beyond the levels of ingot metallurgy. The best green material for such applications is a powder with fine, supersaturated microstructure, or with a dense distribution of fine strengthening particles which are resistant to coarsening and dissolution. Such microstructure is usually achieved by rapid solidification, mechanical milling and alloying.

Gas atomization belongs to the most widely used rapid solidification methods for the preparation of PM Al alloys. Atomization processes were reported to produce generally spherical powder particles with a wide size range. Varying the medium of atomization or the process parameters, the resulting particle size can be tailored. Since the solidification rate of the powder particle is determined primarily by the size of the solidifying droplet, the actual powder particle size also influences its microstructure [117]. Atomized powder particles were reported to exhibit segregation free, cellular or dendritic microstructures [49, 118-124]. An increasing solidification velocity and temperature gradient alter the microstructure from dendritic through cellular to segregation free. Therefore, the largest powder particles - characterized by the slowest solidification rate - exhibit dendritic microstructure [125]. Faster solidification leads to cellular microstructure. Increasing cooling rate leads also to a refinement of cells and dendrites [49, 121, 122, 124]. The highest solidification rates suppress formation of intermetallic particles, and can lead to formation of amorphous phases as it was shown for an Al-Ni based alloy in [122].

Atomized powders are characterized by grain sizes from a few micrometres up to several tens of micrometres [118, 124]. The rapid cooling during gas atomization influences also the alloys phase composition. Metastable phases and extended solid solution is widely reported to occur in atomized powders [49]. All these characteristics, the fine grain size, presence of metastable phases, and extended solid solubility can lead to relatively high microhardness of these powders.

Further microstructural refinement can be achieved by mechanical milling of powders. The actual measure of refinement depends on the alloys properties and milling parameters. Milling usually leads to a remarkable refinement of microstructure.

Fcc metals, as Al, were for a long time considered to have a limited ability to grain size reduction through milling, claiming they are too soft for effective storage of

deformation energy. Nevertheless, appropriate milling times were reported to lead to grain sizes in the nanocrystalline range in Al-based materials [10]. Several authors reported about remarkable grain size refinement using different mills and milling parameters (see Table 1).

Material	Parameters of milling	Final grain size	Reference
Pure Al	Shaker mill, 22 h	22 nm	[35]
Pure Al	20 h	39 nm	[126]
Pure Al	100 h	25 nm	[127]
Pure Al	32 h	21 nm	[128]
Pure Al	Cryomilling, 8 h	26 nm	[129]
Al6061	20 h	30 nm	[130]
Al2124	60 h	18 nm	[77]
Al-Cu	4 h	60 nm	[131]
Al-Ti	60 h	21 nm	[132]
Al-Ti	Cryomilling, 60 h	16 nm	[132]
Al-Fe	150 h	26 nm	[61]
Al-Mg	Cryomilling, 7 h	29 nm	[133]
Al-Mg	Cryomilling, 8 h	26 nm	[63]
Al-Mg	Cryomilling, 8 h	20-200 nm	[60]
Al50Mg50	76 h	2 nm	[134]

Table 1. The final grain sizes of Al alloys reached by mechanical milling with different parameters.

The minimum ever achieved grain size reported for any Al alloy was 2 nm. Such grain size was achieved by mechanical alloying of Al and Mg powders with a composition corresponding to Al50Mg50 for 76 h in an in-house built mill [10, 134].

Beside the grain size reduction, mechanical milling refines/dissolves second phase particles and enhances solid solubility. Mechanical alloying of Al-5 at% Fe powder led to dissolution of 3.3 at% Fe [61]. An enormous enhancement of the solubility of Fe in Al up to 4.5 at% was reported in [135] (the maximum equilibrium solid solubility of Fe in Al is 0.025 at% at 655 °C [4]). In an Al-15 at% Cu alloy, mechanical milling was reported to enhance solid solubility of Cu in Al to 5.6 at% [136], whereas maximum equilibrium solid solubility of Cu in Al is 2.48 at% at 550 °C

[4]. The solid solubility of Mg was reported to be enhanced to 18 at% in an Al70Mg30 and up to 45 at% in an Al50Mg50 alloy [134], although the equilibrium solid solubility of Mg in Al is 1.2 at% at RT, maximum is 16.26 at% at 450 °C [4]. Mechanical milling was shown to enhance solid solubility of Ti in Al to 7.5 wt% [137], however, it has a maximum equilibrium solid solubility of 0.57 at% at 665 °C [4]. After 90h of mechanical alloying, 3 at% of Zr were reported to be successfully dissolved in Al, although, the maximum equilibrium solid solubility of Zr in Al is 0.085 at% at 660 °C [4, 138]. Mendis et al. dissolved up 1 at% of Zr in Al-Fe alloy after 90h of milling [139].

Powder consolidation is probably the most serious problem of powder metallurgy of Al alloys. There are several problematic issues connected with it. Al powders usually need degassing prior to consolidation. The attainment of high density compact requires generally high pressure and/or temperatures and long times of sintering. The hard oxide layer on the Al powders surface hinders attainment of a good metal-metal contact. A brief review concerning these issues follows.

Aluminium powders are usually degassed before their consolidation to remove the trapped contaminants which can contribute to porosity and material degradation [140]. This is usually performed at temperatures between 400 °C and 525 °C for several hours [72-75]. This long exposition to elevated temperatures can lead to degradation of powders properties [60].

There are several low and high temperature consolidation methods widely used in PM of Al-alloy powders. Low temperature consolidation methods as CP and CIP use high pressure to enhance plastic flow and to consolidate powders to compacts. CP of air atomized Al powder using 165 MPa led to porosity around 10% [141]. Similar porosity was attained in another Al compact prepared using 200 MPa [142]. Higher density samples can be achieved by increasing the value of pressure. Ball milled nanocrystalline pure Al powder was reported to be compacted by CP using up to 1 GPa pressure to 95-98% of theoretical density [128]. CP of ball milled Al-Cu sample required extreme pressure, above 7 GPa to attain full density [131]. However, achievement of such high pressures requires costly tooling and limits the sample size.

High final density samples can be attained also using high temperature consolidation methods as HP or HIP. Hot pressing (450 °C, 30 MPa, 90 min) of a water atomized Al alloy powder was reported to lead to 90.2% density. An Al-Fe-Zr alloy was reported to attain 97% density when compacted by HP at 400-480 °C with 445

MPa for 10 min [138]. Further, 94% density was reported for an AlCrCuFeNiZn sample hot pressed at 600 °C with 650 MPa for 15 min [143].

Further problem during consolidation of Al alloys powders is connected with the presence of hard, thermodynamically stable oxide layers on the surface of powder particles. These layers cannot be simply broken by pressure or removed by heat, thus they usually remain between the powder particles in PM samples. These layers reduce the quality of interparticle bonding in prepared compacts. The poor quality of the interparticle contacts deteriorates mechanical properties of consolidated materials [112, 144, 145]. Therefore, Al powders compacted by isostatic deformation processes as CIP [72, 75] or HIP [73, 74] have a reduced ductility. Therefore, usually post processing in form of extrusion, rolling or forging is applied in order to break up and disperse the oxide boundaries by shear stress [64]. Moreover, these post processing methods also help to reduce remaining porosity increasing thus the materials final mechanical properties [72]. Nevertheless, these post processing methods are usually carried out at elevated temperatures, which can completely change the microstructure and phase composition and degrade the samples final properties.

In summary, the attainment of low porosity Al-based compacts with conventional consolidation methods needs extremely high pressure and/or high temperatures [46]. Extended heat exposition can also help to increase the samples density. Further reduction of porosity can be achieved through post processing. The long exposition to high temperatures during powder consolidation or during post processing can have an undesirable effect on the compacts final microstructure. Therefore, the powder consolidation method has to be chosen carefully. It should have a minimized heat influence on the powder and be capable to enhance the bonding quality of powders. Choosing SPS as the consolidation method should ensure a limited high temperature exposition of powder and a direct metal-metal contact of sintered powder particles. A short literature review concerning the Al powders sintered by SPS follows.

Contrary to problems connected with conventional consolidation methods, as listed above, SPS was many times reported to sinter Al powders to high density compacts during a short period at relatively low sintering temperatures. SPS was severely times used to prepare bulk samples from pure Al powders [108, 144-147], Al alloys [14, 106, 123, 145, 148, 149] to mechanically milled Al and mechanically alloyed Al composite powders [61, 85, 91, 121, 130, 138, 139, 150-157]. The rapid

internal heating through Joule heat allows minimizing the sintering time which consequently reduces the heat influence. SPS was also reported to be capable to break surface oxide layer during sintering and lead to metal-metal contact [106, 112, 144, 145, 147].

A limited grain size increment in case of both atomized and milled powders was reported by several authors [121, 130, 139, 147, 150, 151, 154]. It was explained by a pinning effect of Al oxide particles and impurities introduced into the matrix during milling and by a rapid heating.

Mechanical properties of SPS compacts of Al alloys prepared with different parameters were found to be similar or improved compared to the wrought or thermo-mechanically treated Al alloys counterpart by several researchers [61, 91, 106, 108, 123, 130, 138, 144-146, 148, 151-153, 155, 156]. The improved properties were explained by a high-quality metallurgical bonding of powder particles, large fraction of submicron or nanometer-sized grains, bimodal microstructure, fine precipitates, and high content of intermetallic particles [61, 123, 130, 138, 148, 149, 155, 156].

1.5.2. High temperature aluminium alloys

As mentioned in the introduction, a poor thermal stability of Al alloys represents a serious drawback in their application field. The high strength of commercial Al alloys is usually achieved through precipitation strengthening. Fine grain size, i.e. a large number of grain boundaries, can contribute to further strengthening. Unfortunately, it is very difficult to retain the adequate phase composition and microstructure during exposition of Al alloys to elevated temperatures, usually above 200 °C [158]. Due to the temperature dependence of the solid solubility of alloying elements in Al matrix some precipitates can dissolve. A tendency to lower the internal energy and enhanced diffusion at elevated temperatures contributes also to coarsening of remaining precipitates. Additionally, they reduce also the pinning effect of precipitates. All these effects result in a degradation of strength of Al alloys during their exposition to elevated temperatures.

In order to maintain the high strength of Al alloys despite of their exposition to elevated temperatures, all above mentioned processes have to be avoided or at least minimized. A theoretical background of the high temperature stabilization is given in section 1.3. As stated in that section, proper choice of alloying elements represents the

way how to fulfil the theoretical requirements. The stabilization of the second phase particle content and of the grain size will be described separately.

In order to maintain a sufficient fraction of second phase particles, the alloying elements have to be selected carefully. They should have a low solid solubility and a low diffusivity in Al both at room and at elevated temperatures. Moreover, they should form such intermetallic phase with the matrix atoms, which has a low mismatch with the Al matrix. This way, the second phase particles dissolution and ripening can be suppressed and a persistent second phase particle content can be maintained.

The most widely used commercial high temperature Al alloys contain elements as Fe, Cr, Mo, Ti etc. These elements form in the Al matrix second phase particles with a high temperature stability and appropriate morphology to serve as dispersion hardener and improve the high temperature stability of grain size as grain boundary pinners [159, 160].

Another group of high temperature Al alloys contains Zr, Sc, Ti, Hf, V etc. which have a very low diffusion coefficient at RT and elevated temperatures and a low equilibrium solid solubility [4, 161]. Moreover, they are able to form with Al particles of trialuminides which have a low mismatch with the Al matrix, especially when they are present with $L1_2$ structure. This structure is typical only for the Al_3Sc phase, however, other elements as Zr, Ti, Hf or V can form trialuminides with $L1_2$ structure as a metastable phase. These trialuminides fulfil all requirements to suppress effectively Ostwald ripening.

Zr has a special position among elements used for production of high temperature Al alloys, since Zr has the slowest diffusion rate [162], its equilibrium solid solubility in Al is very low (with a maximum of 0.28 wt% (0.083 at.%) at 660 °C [163]). It forms the Al_3Zr phase, which appears in two modifications. The formation of stable phase with the structure DO_{23} is preceded by a metastable phase of $L1_2$ structure, see Figure 6.

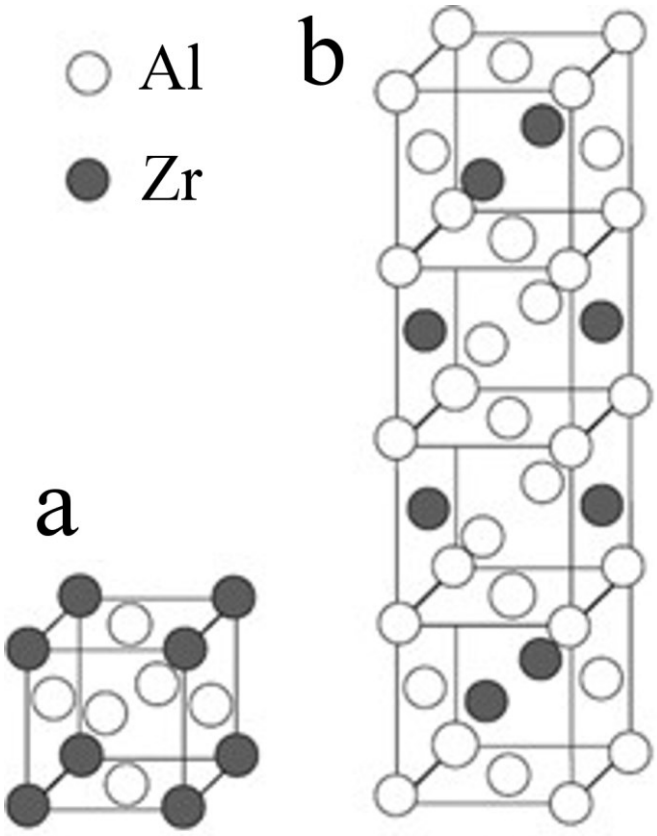

Figure 6. The scheme of unit cells of the Al_3Zr phase: a) metastable $L1_2$ modification, b) stable DO_{23} modification.

The $L1_2$ structure metastable phase has a lower lattice mismatch with Al matrix (about 0.7% [164, 165]) compared to the stable phase (about 2.9% [164]). This reduced mismatch, according to the theory of the diffusion controlled particle coarsening, leads to increased thermal stability of these second phase particles.

Transition of the metastable phase to the stable structure occurs at relatively high temperatures after prolonged times. No transition to the stable phase was found to occur after aging of an Al-Zr (0.2 at%) alloy at 425 °C for 1600h by Knipling et al. [166]. The absence of transition of the $L1_2$ structure to the stable one was found after aging for 100h at 500 °C [167]. Only aging for more than 20h at temperatures above 550 °C resulted in a transition to the DO_{23} structure.

For effective strengthening a homogeneous, dense precipitation of fine particles is needed. In Al-Zr alloys, coarse particles were found only at low solidification rates of the order of 10 Ks^{-1}, higher solidification rates suppressed their formation even at high Zr contents [168]. Thus, RS methods can lead to convenient

microstructure for precipitation of appropriate second phase particles during the materials following treatment.

1.5.3. The Al-Zn-Mg-Cu system

The Al-Zn-Mg-Cu alloy system belongs to the Al7xxx group, whose main alloying element is Zn, the most used minor alloying elements are Mg and Cu. These Al alloys are traditionally used for aerospace and transportation applications thanks to their high strength and heat treatability [4].

According to the existing literature the Al-Zn-Mg-Cu alloy system forms four major intermetallic phases: η ($Mg(Zn,Cu,Al)_2$), T ($Mg_3Zn_3Al_2$), S (Al_2CuMg) and θ (Al_2Cu) [163, 169, 170]. The main intermetallic phase present in a given Al-Zn-Mg-Cu alloy depends on the alloys exact elementary composition. In case the Zn:Mg ratio is over 2.5, η phase is preferentially formed, whereas lower ratios lead to formation of T phase [171]. Cu with a concentration up to 1 wt% remains in solid solution or substitutes Zn atoms in η and T phases and decelerates their coarsening [172]. Above this concentration, S phase is formed through heat treatment above 175 °C. In case of much higher concentration of Cu this S phase can form already during alloys solidification [163, 172].

The strength of the Al-Zn-Mg-Cu alloy is connected predominantly with the evolution of η phase. The precipitation treatment has to be preceded by rapid quenching from a sufficiently high solution temperature. The precipitation process starts with the formation of solute (Zn, Mg, Cu) and vacancy-rich solute clusters. These clusters are precursors for Guinier-Preston (GP) zones. GP zones are coherent, metastable precipitates with a diameter of a few nanometers [173, 174].

Two types of GP zones were found and described in an aged Al-Zn-Mg alloy [175]. GP(I) type is reported to form from solute-rich zones at temperatures between RT and 150 °C [176-178]. They are formed by ordered layers of Zn and Mg/Al in {100} Al plane and exhibit spherical morphology. GP(II) type forms after quenching from temperatures above 450 °C and aging above 70 °C from vacancy-rich clusters [175, 178] on {111} Al planes with plate like morphology [175].

During further aging the GP zones are replaced by metastable semi-coherent, η’ phase with a hexagonal structure [175, 178, 179]. The main hardening effect is

attributed to this hexagonal phase [175]. The typical size of these plate-like precipitates is 3-4 nm in thickness and 5-10 nm in width.

At higher aging temperatures and longer aging times incoherent equilibrium hexagonal η phase forms, which has slightly different cell parameters than the metastable form. The η phase precipitates are preferentially located at grain boundaries and have generally a larger size (>50 nm) [17, 175, 178-181].

Cu atoms have an overall hardening effect in Al-Zn-Mg-Cu alloy as it strongly influences the evolution of the η ($Mg(Zn,Cu,Al)_2$) phase. Cu promotes early clustering processes due to strong interaction with vacancies and solute atoms. Cu decelerates dissolution of GP(I) zone at 150 °C, which without Cu would dissolve completely [171, 182]. Further, it stimulates formation of GP(II) zones and its transformation to η' phase [182]. Cu also retards formation of η phase and decelerates thus overaging [182].

The materials final mechanical properties depend beside the size and type of precipitates also on their displacement. This was reported to be affected by material's dislocation structure, grain boundaries or heating characteristics.

Dislocations and grain boundaries represent sinks for vacancies and solute atoms, thus they can reduce solute concentration and limit following precipitation [178, 183]. A lower density of precipitates formed in extruded ultrafine-grained Al-Zn-Mg-Cu alloy compared to coarse grained counterpart was presented in [183]. Nevertheless, grain boundaries also serve as heterogeneous nucleation centres. The solute-vacancy complexes diffuse to and decompose at grain boundaries and leave segregates behind. These segregates then can act as nuclei for GP zones, η' and η particles leading to their discontinuous distribution [124, 183-186]. Moreover, dislocations and grain boundaries enhance coarsening kinetics as they present easy-route for diffusional processes [186, 187].

The high volume fraction of grain boundaries in UFG alloys hinders homogeneous nucleation of precipitates during aging [183, 188]. The precipitation at grain boundaries, connected with the formation of precipitation free zones in the vicinity of boundaries, leading to stress corrosion cracking is characteristic for highly alloyed Al-Zn-Mg-Cu alloys [18, 171].

The parameters of thermal treatment can markedly affect the resulting microstructure. Proper solid solution treatment prior to aging can dissolve most of the precipitates present in the material. A slow quenching rate can lead to heterogeneous

nucleation and precipitates coarsening, on the other side, rapid quenching rates promote homogeneous nucleation of phases. Low heating rates to the aging temperature were reported to lead to formation of η phase along dislocations and η' phase in the matrix, resulting in higher peak strength in pre-deformed sample compared to un-deformed ones [187]. High heating rates to the aging temperature resulted in a lower number of GP zones and η' particles and led to precipitation-free zones along with coarse precipitates on dislocations.

One representative of the Al7xxx group is the high strength Al7075 alloy. The Al7075 alloy has a strength comparable to many steels: The yield and ultimate strength of annealed alloy (so called O-temper) are about 105 and 230 MPa [189], but precipitation strengthening can highly increase these values.

The strengthening of Al7075 alloy through heat treatment is caused by a high number of GP zones and η' precipitates [175, 185, 190]. The highest strength of the Al7075 alloy is achievable by a peak ageing treatment (so called T6-temper), consisting of solution heat treatment at temperatures between 450 and 490 °C followed by artificial aging at 120 °C for several hours [18, 184, 185, 191]. The development of GP zones with a diameter of 2-4 nm and a fine dispersion of the η' phase inside grains and along grain boundaries leads to a yield resp. ultimate strength of 505 MPa resp. 580 MPa [189, 191]. Further strength increase of Al7075 alloy can be achieved also through work hardening and grain size refinement.

Cryorolling of an Al7075 alloy led to nanocrystalline grains and a yield strength of 550 MPa, higher than those of commercial Al7075-T6 counterpart (505 MPa) [16, 189]. Low temperature aging of the sample increased the materials yield strength to 615 MPa [16]. Ultrafine-grained Al7075 alloy (grain size 400 nm) prepared by ECAP exhibited a yield and tensile strength of 650 and 720 MPa [115]. An extremely high yield strength (1 GPa) was reported for an Al7075 alloy produced by HPT at RT [6]. The remarkable strength was explained by nanograins and nanometric intergranular clusters.

Another way in processing fine grained sample from the Al-Zn-Mg-Cu, particularly Al7075 alloy, is the PM route. Al7075 compacts were prepared by HIP and extrusion of a gas atomized powder with a final grain size around 1 μm [183]. The samples yield and ultimate tensile strength were 283 and 436 MPa. Ultrafine-grained samples, with grain sizes of 150-300 nm, were prepared by cryomilling of gas atomized powder followed by HIP and extrusion [17]. The yield and ultimate tensile

strength of the resulting sample was 583 and 631 MPa, higher than that of commercial Al7075-T6 [17]. This was attributed to strengthening by grain boundaries. Nanocrystalline grains with a size of 32 nm were reported for a milled and hot pressed (400 °C, 500 MPa, 1h) Al7075 alloy [192]. The compact was reported to have a high, 288 HV microhardness. Prealloyed Al7075 powder was cold compacted and hot forged at different temperatures [193]. The forged sample showed a density of 99.6% and a slight anisotropy of hardness. The compacts microhardness was low, around 55 HV.

Other samples from the Al7075 alloy were processed by a combination of gas atomization and high pressure cold deposition; however, the sample exhibited a remarkable inhomogeneity along the deposition direction [118]. Spray forming of Al7075 powders followed by extrusion led to porosity up to 20 vol% [194]. Atomized Al7075 powders were sintered by SPS to study corrosion properties by Tian et al. [124].

Further, also composite materials were prepared using the Al7075 alloy as a matrix. Mechanically alloyed Al7075 powder was milled with different amounts of graphite. The milled powder was cold pressed and hot extruded [195]. The mechanical properties of the composite material were found to be considerably higher than those of plain Al7075 alloy. Another composite sample was prepared by hot extrusion from mixed pure Al and Al7075 powders [196]. Decreasing amount of pure Al powder led to a change of fracture mode from ductile to nearly brittle. A composite of Al7075 alloy with carbon-coated silver nanoparticles was prepared by mechanical milling [197]. The nanoparticles with a content up to 2 wt% were shown to enhance microhardness by 80 HV. Nanocrystalline Al7075 alloy reinforced by Al_2O_3 was mechanically milled and hot pressed [198]. The hardness of the composite sample increased with increasing amount of Al_2O_3 particles up to 204 HV.

Addition of Zr to the Al7075 alloy was reported to improve alloys properties. First of all, Zr can form relatively coarse Al_3Zr particles at the beginning of solidification, which then serve as heterogeneous nuclei for Al grains, thus leading to a grain size refinement. This effect of Zr was demonstrated for example in [166, 199]. Moreover, fine Al_3Zr particles can also serve as grain boundary pinners. This was confirmed for example in [200, 201].

A combination of gas atomization and semi-solid rolling was tested at the Al-Zn-Mg-Cu-Zr alloy [202]. A sample with 91% density and 158 HV was prepared. The

effect of Zr addition was not discussed. Another Al-Zn-Mg-Cu-Zr alloy modified by the addition of Zr was processed by atomization followed by extrusion. The fine-grained microstructure (grain size around 1 μm) was retained during the high temperature exposition due to the developed Al_3Zr particles [203]. Zr addition and rolling of PM (gas atomization+ hot extrusion) sample was show to lead to superplasticity at relatively high strain rates as a consequence of significant grain refinement [20]. Zr addition led to continuous recrystallization during deformation since it effectively hindered redistribution of dislocations and motion of grain boundaries.

2. Materials preparation and experimental procedure

2.1. Materials preparation

In this thesis two Al alloys were studied. The widely studied Al7075 aluminium alloy and its modification, alloyed with 1 wt% of Zr (alloy further denoted as Al7075Zr) were investigated. The chemical composition of both alloys according to the manufacturer is presented in Table 2.

	Zn	Mg	Cu	Zr	Ti	Al
Al7075	6.6	2.3	1.7	-	-	balance
Al7075Zr	6.6	2.3	1.7	1.0	-	balance

Table 2. The chemical composition of investigated alloys, in wt%.

2.1.1. Gas atomization

The gas atomized powders with chemical composition presented in Table 1 were delivered by Nanoval GmbH & Co. KG, Berlin, Germany. The alloys were atomized by nitrogen and sieved down to 50 μm. The mass median diameter (the droplet size corresponding to 50% cumulative frequency) of Al7075 and Al7075Zr alloys' powder was stated by producer to be 22.6 μm and 20.9 μm.

2.1.2. High-energy milling

To alter and refine materials microstructure the gas atomized powders were high-energy milled in a Retsch PM 100 CM planetary ball mill (Retsch GmbH, Germany) or in an UNION HD01 Lab attritor (Union process Inc., USA) which enabled to decrease the milling temperature to cryogenic ones.

High-energy milling of gas atomized powders was carried out at room temperature in an inert Ar atmosphere or at cryogenic temperatures, in LN (liquid nitrogen), using stainless steel vessel and stainless steel balls with a BTP ratio of 32:1 (in case of attritor) resp. 40:1 (in case of planetary ball mill).

During milling in attritor the jacketed milling jar was cooled by flowing water. During cryomilling liquid nitrogen (boiling temperature 77 K) was continuously charged into the milling area in order to maintain a constant milling environment. The

evaporated nitrogen was removed through a blower equipped with a particle filter to filtrate the powder particles from the gas flow. After the milling process the vessel with the milled slurry was closed with a cover so that the powder was under the liquid nitrogen surface. After the evaporation of the liquid nitrogen the powder was separated from the milling balls.

During milling in the planetary mill, the process was interrupted for 30 min after every 30 min long milling period in order to restrict further heat generation and allow cooling.

The milled powders were stored in plastic bags without inert atmosphere.

The first choice of milling parameters was based on the previous experience in the research groups using the attritor and the planetary ball mill. The milling time, milling temperature, and RPM were then varied to optimize the microstructural refinement of milled materials. The exact milling parameters are listed in the section 3.2. separately for each studied material.

2.1.3. Spark plasma sintering

Both atomized and milled powders were sintered by the spark plasma sintering technology using the FCT SPS-HP25 (FCT Systeme GmbH, Effelder-Rauenstein, Germany) and SPS 10-4 (Thermal technology, USA) devices.

The powders were placed in a graphite die with an additional graphite foil between the die, punches and the powder in order to protect the die and punches from reaction with the powder material. Approximately 3 g of powder were sintered into cylindrical specimens with the dimensions approximately 20 mm in diameter and 5 mm in height. The sintering parameters were selected based on the previous experience in the research group [119]. All samples were sintered at 425 °C for 4 min under 80 MPa. At the beginning of sintering a 5 MPa initial load was applied to press the loosely packed powder in the die. Maintaining the pressure, the samples were free heated up to 400 °C with a heating rate of 80 °C/min. The sintering temperature of 425 °C was reached with a heating rate of 25 °C/min. Simultaneously, the uniaxial pressure was increased up to 80 MPa. After the 4 min holding time, the sample was unloaded and free-cooled.

2.1.4. Denotation of studied samples

In order to make the reading of this thesis easier and more comfortable, the following table (Table 3) was prepared in order to show the logic of the denotation used throughout the text. The exact denotation of each sample will be listed during the thesis in the related sections.

Description	Denotation	Example
Atomized **p**owder	_AP	Al7075_**AP**
Milled **p**owder, in attritor, at **RT**	_MP_RT	Al7075_**MP_RT**_3_180
Milled **p**owder, in attritor, in **LN**	_MP_LN	Al7075_**MP_LN**_3_180
Milled **p**owder, in **p**lanetary mill	_MP + P	Al7075_**MP**_RT_8_400**P**
Compact from **a**tomized powder	_AC	Al7075_**AC**
Compact from powder **m**illed in attritor	_MC	Al7075_**MC**_RT_3_180
Compact from powder **m**illed in planetary ball mill	_MC+P	Al7075_**MC**_RT_8_400**P**

Table 3. The logic of the denotation of samples and an example.

2.2. Experimental techniques

Light microscopy, scanning electron microscopy, transmission electron microscopy and scanning transmission electron microscopy were used to investigate the materials microstructure. The phase composition was studied using X-ray diffraction. Mechanical properties of powders and compacts were characterized by microhardness measurement.

Sample preparation

For microstructural investigation and microhardness measurements, powder particles were cold mounted into an acrylic resin. Alternatively, for scanning electron microscopy, they were hot mounted (180 °C, 2.5 min) by conductive resin with carbon filler. From the sintered compacts, thin samples with an area of 5 x 5 mm^2 were cut parallel to the direction of stress applied during SPS using a Struers Accutom-50 precision cut-off machine. Each sample was mechanically grinded and polished up to

1 μm diamond past, followed by chemical polishing with SiO_2 oxide polishing suspension.

Light microscopy

The morphology and microstructure of all powders was observed by light microscopy (LM) using a metallographic microscope Olympus GX51. Cold mounted and polished gas atomized powders were etched with Dix-Keller reagent for 10 s to reveal constituents.

Scanning electron microscopy

Scanning electron microscopy (SEM) was used for more detailed microstructural observations. SEM investigations, as secondary electron imaging (SE), backscattered electron imaging (BSE), electron backscattered diffraction (EBSD) and energy dispersive spectroscopy (EDS) were performed using a FEI Quanta 200F scanning electron microscope equipped with field emission cathode. SE and BSE imaging were performed to study the morphology and microstructure of samples. EBSD technique was used to determine the crystallographic orientations of grains. Information about the grain size and its distribution, misorientation of neighbouring grains, and type of grain boundaries was obtained from these measurements. EDS investigations showed the elemental composition of samples and the distribution of individual elements in the studied samples.

For EBSD measurement, the samples were further electro-polished by Lectropol-5 at -25 °C with 15 V for 5 s using 33% solution of nitric acid in methyl alcohol, in order to remove a thin surface layer, which could be deformed by polishing.

SE and BSE imaging were performed at 15 kV, whereas EBSD measurement was carried out at 10 kV in order to ensure a relatively low interaction volume of electrons with the studied sample. In order to make a reliable statistics of grain sizes several powder particles were tested in case of powdered material. In case of compacts an area of 50x50 μm^2 was tested in case of compacts from gas atomized powders, in case of compacts from milled powder an area of 30x30 μm^2 was tested. The EBSD mapping step size was chosen based on a small test mapping using a step size of 0.1 μm. With the help of this step map an approximate grain size of the sample was

estimated. Further EBSD mapping of the sample was performed with a step size which ensured to have at least 5 tested points in a grain. Thus, step size differed for different materials, from 0.2 to 0.01 μm. The orientation image maps from EBSD investigation were processed using OIM Analysis program. The average grain size (area) was stated by this program as number of points within a grain times the squared step size times a number characterising the scanning grid. The grain diameter was evaluated supposing circular grains. Grain disorientation was stated using the same program. Plots were generated using angles from 5 to 65º.

High-angle grain boundary (HAGB) was stated as boundary between 15 and180°, whereas boundaries 5-15° were considered as low-angle grain boundary (LAGB).

EDS analysis was performed using an acceleration voltage of 20 kV. Although, this high voltage increased the interaction volume of electrons with the material, enabled to make visible each element in the spectrum of investigated materials. The interaction volume can be determined to be around 2 μm [204].

Transmission electron microscopy

To monitor materials microstructure in more details transmission electron microscopy (TEM) investigation was carried out using a JEOL 2200FS microscope. Observations in bright field (BF), dark field (DF), and selected area electron diffraction (SAED) were performed at an acceleration voltage of 200 kV. Moreover, the scanning transmission electron microscopy (STEM) was used for the investigation of the finest microstructural details (carried out by JEOL 2200FS microscope in STEM mode). High quality figures were taken with HAADF (high-angle angular dark field) detector in STEM, showing mainly atomic number contrast.

Specimens for TEM observations were cut from powders embedded in a conductive resin using a focused ion beam (FIB) in Zeiss Auriga scanning electron microscope. Lamellae with a size of a few tens of microns were cut with Ga+ ions from the interior of a chosen powder particle. The lamellae were placed with the help of a micromanipulator on a Cu half-grid and fixed by platinum welding, where they were further thinned by ions to electron-transparency. Samples from compacts were grinded to the thickness of 0.1 mm and then electro-polished in Tenupol-2 under 15 V at −15 °C in 33% solution of nitric acid in methyl alcohol.

X-ray diffraction

The phase composition and structural changes were investigated by X-ray diffraction (XRD) using a vertical θ-θ diffractometer D8 Discover in Bragg-Brentano geometry with CuKα source and NiKβ radiation filter. Phase identification was done using Diffrac.Eva with accessed PDF-2 database of crystalline phases. Quantitative Rietveld analysis was performed by TOPAS V5 to determine the weight fraction of all identified phases [205]. X-ray diffraction measurement of powdered samples was carried out on non-mounted powders. Sintered samples were fully polished before XRD observation in order to remove their surface influenced by grinding. All XRD investigations and the data evaluation were performed at the Institute of Plasma Physics of the Czech Academy of Sciences within a common research project GACR 15-15609S.

Fundamental Parameters Approach was used for calculation of profile broadening because of instrumental effects. Sizes of coherently diffracting domains (CDD, or crystallite size) and microstrains were evaluated from the broadening of diffraction peaks assuming that small crystallites and microstrains contribute to broadening of Lorentzian and Gaussian components of pseudo-Voigt function, respectively [206].

Microhardness measurement

To evaluate the materials' ability to resist plastic deformation the Vickers microhardness testing was used. Microhardness (HV) was measured using a Qness Q10A+ automatic microhardness tester. Measurement was carried out on fully polished samples. The microhardness of powdered materials was measured at a load of 10 N. Each indent was applied to a different powder particle. At least 10 different powder particles were tested. The characteristic size of indents, in case of powdered material, was around 5-10 μm, therefore, microhardness test could be performed only on powder particles with a polished cross section of approximately 35 μm (according to the EN ISO 6507, in case of Al alloys the distance of indent from the samples edge has to be 3 times the indents diameter). The load of 50 N was used for compacts samples. In case of compacts at least 20 intents were applied with a distance of 200 μm between individual indents (according to the EN ISO 6507, in case of Al alloys the distance between indents has to be 6 times the indents diameter).

Heat treatment of samples

Compact samples were heat treated at 300 and 425 °C to study the thermal stability of their microstructure. The temperature 300 °C was chosen to overage the microstructure. Temperature 425 °C was chosen to be close to the dissolution temperature of η phase but below the temperature which according to the previous experiences of research group led to voids and blistering (450-475 °C).

Samples were put into ovens heated to the required temperature. After 1h of annealing they were removed from the oven and water quenched. As the Al7075 type alloys exhibit intensive natural aging a constant time of 1 week was maintained between quenching from annealing temperature and further sample investigation in all heat treated samples.

3. Experimental results

The commercial Al7075 alloy and its modification containing 1 wt% Zr were selected to verify the processing route consisting from gas atomization, mechanical milling, and spark plasma sintering and to study the influence of processing parameters on the microstructure, phase composition, and mechanical properties. The chemical composition of gas atomized powders stated by the manufacturer is given in section 2.1. (Table 2). The composition was also verified by X-ray fluorescence analysis which showed slightly higher contents of alloying elements. Both alloys were studied at different stages of their processing and the results are presented in the following sections.

3.1. Gas atomized powders

The method of LM revealed that the gas atomized powder particles of the Al7075 and Al7075 +1 wt% Zr alloys (further referred as Al7075_AP and Al7075Zr_AP) exhibited mostly a spherical shape, some particles were surrounded by satellites (Figure 7).

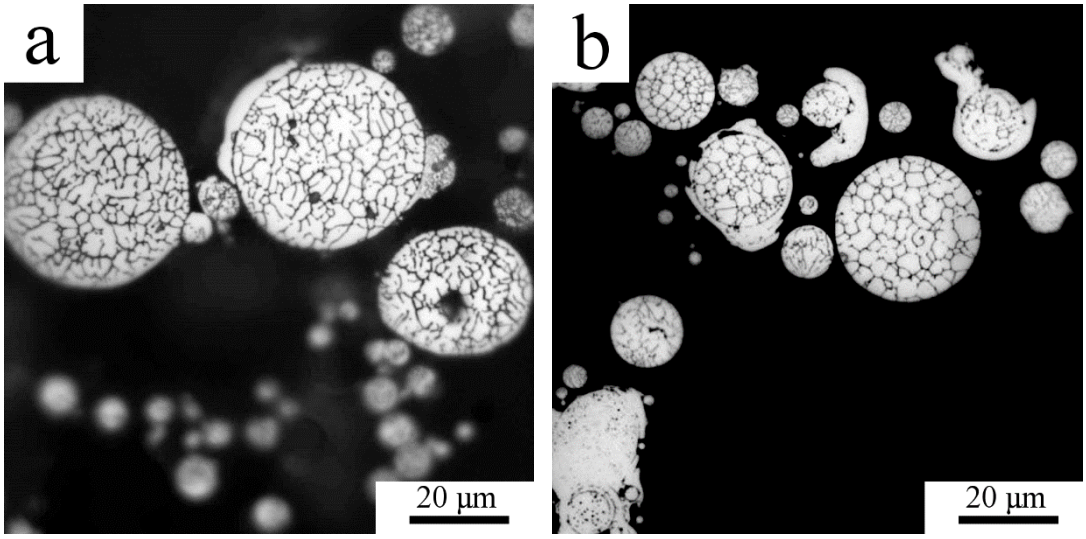

Figure 7. The morphology of gas atomized powder particles: a) Al7075_AP, b) Al7075Zr_AP, constituents revealed by etching with Dix-Keller solution, LM.

The powder material consisted of both coarser particles with the size up to several tens of µm and numerous much finer powder particles with the size one order finer as presented in Figure 8. This figure also shows that some initially spherical

liquid droplets collided during atomization process and solidified together to form powder particles of more complicated shapes. SEM investigation showed mostly a cellular microstructure in both powders (Figure 9). Higher magnification investigations revealed a segregation free microstructure in the smallest powder particles and in the satellite regions (Figure 10).

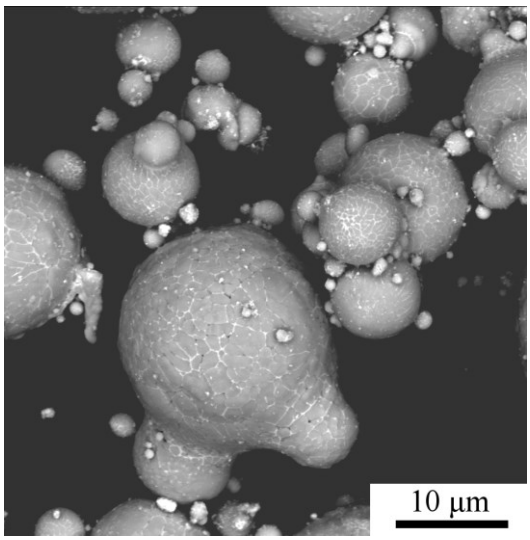

Figure 8. The size distribution of gas atomized powder particles demonstrated on the Al7075_AP powder, SEM-SE.

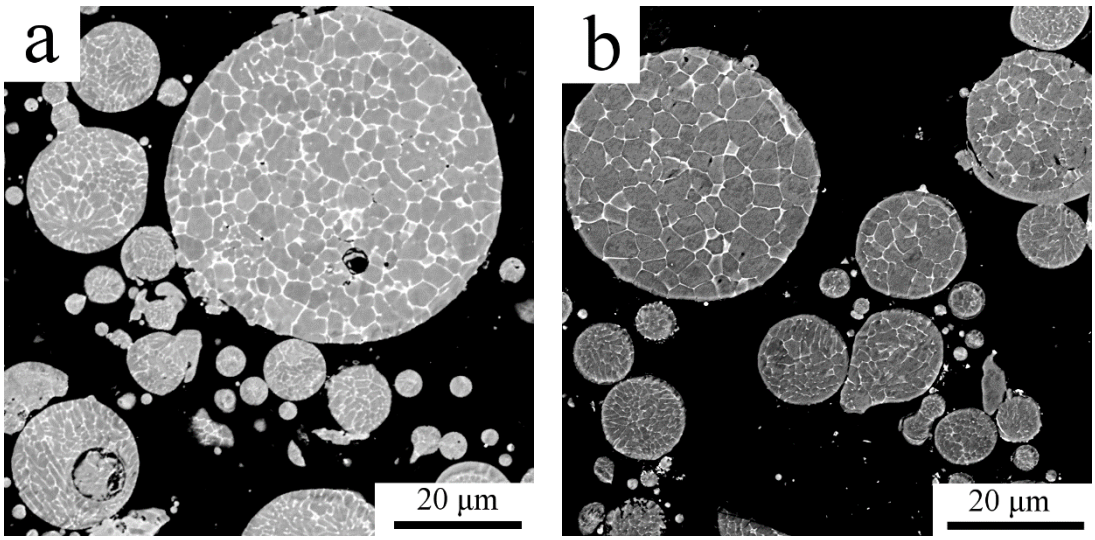

Figure 9. The cellular microstructure of gas atomized powder particles and variation of cell size with the powder particle size: a) Al7075_AP, b) Al7075Zr_AP, SEM-BSE.

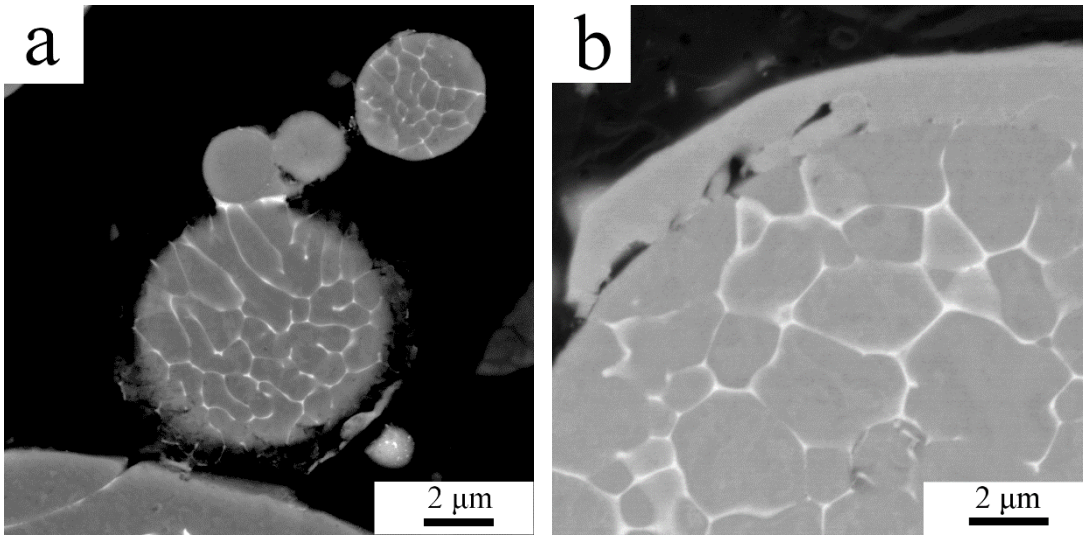

Figure 10. The segregation free microstructure: a) in the finest powder particles in the Al7075_AP powder, b) in satellites in the Al7075Zr_AP powder, SEM-BSE.

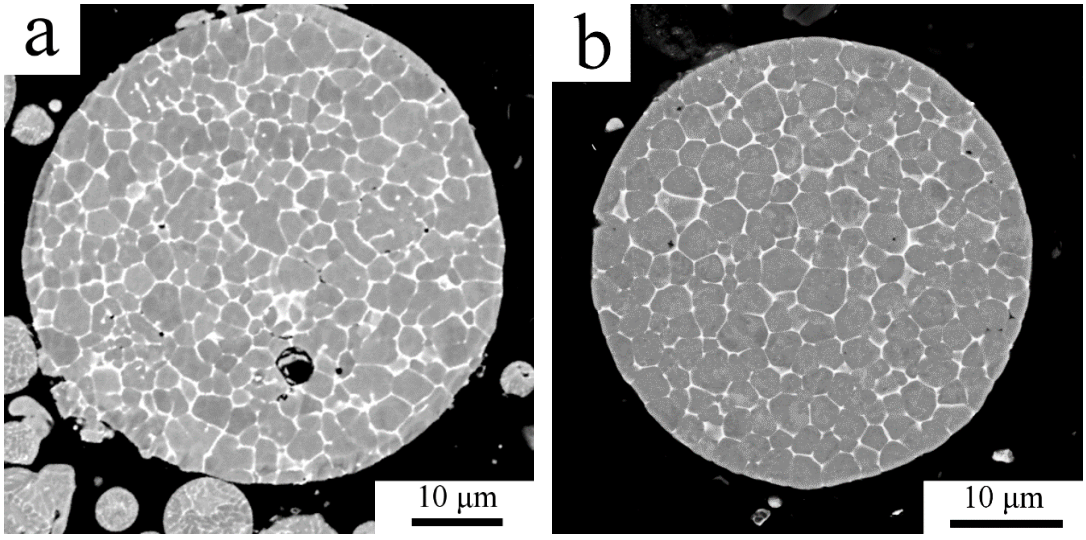

Figure 11. The microstructure of the largest powder particles found in both alloys: a) Al7075_AP, b) Al7075Zr_AP, SEM-BSE.

The typical cell size is in the order of µm in both materials, however, it is clearly dependent on the powder particle size, see Figure 9. Larger powder particles seemed to contain larger cells, whereas a finer microstructure was observed in smaller particles. Figure 9 shows the cross sections of powder particles, so that the true size of powder particles is unknown. However, especially the very small powder particles are very close to each other and it can be assumed, that the actual size of the cross sections is in a reasonable relation to the real size of powder particles. Figure 11 documents the microstructure of the largest powder particles found in both alloys and it can be concluded that their cell size is comparable.

The SEM-BSE micrographs in Figures 9-11 show mainly contrast induced by different atomic numbers of elements (Z contrast). Thus the cell interiors contain predominantly alloying elements with lower Z, whereas elements with higher Z are segregated along the cell boundaries. This was confirmed also by SEM-EDS mapping. The EDS maps for an Al7075Zr_AP powder particle revealed an increased content Mg and Cu in intercellular regions compared to matrix (Figure 12), whereas the content of Zn in intercellular region was only slightly higher than in the matrix. No places with enhanced concentration of Zr atoms were observed in the Al7075Zr_AP powder. A similar distribution of alloying elements was observed also in the Al7075_AP powder.

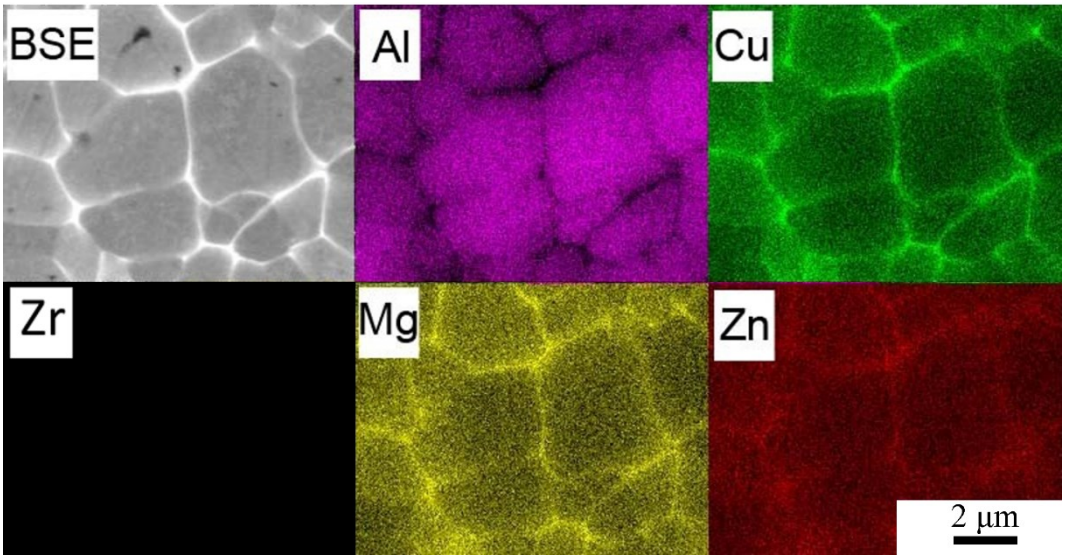

Figure 12. The element distribution in an Al7075Zr_AP powder particle, SEM-BSE figure and the corresponding SEM-EDS maps.

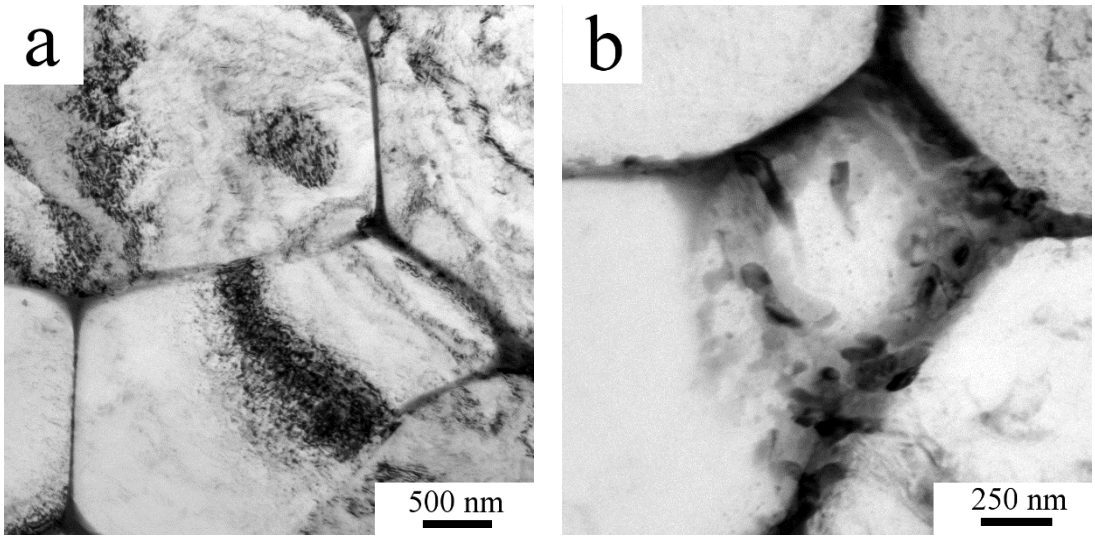

Figure 13. Microstructural details of intercellular areas in an Al7075Zr_AP powder particle: a) continuous-like intercellular phases, b) individual particles, TEM-BF.

The intercellular regions documented in SEM-BSE figures were studied in more details by TEM. As shown in Figure 13a, the intercellular segregations seem to be mostly continuous, however, there were rarely found also places where the intercellular regions were decorated by chains of individual particles (see Figure 13b).

Figure 14 brings the STEM-EDS maps obtained from an intercellular region of the Al7075Zr_AP powder particle. The intercellular region which seemed to be a continuous layer was found to consist of alternating grains of different intermetallic phases with a size around 100 nm. It is remarkable, that in this intercellular region an increased content of Cu can be correlated with an increased content of Al which suggests the presence of a phase containing these two elements. A weaker correlation can be found for Mg and Zn, both elements are evidently located also in the cell interiors. The intercellular parts contain also a notable amount of Ga. The most Ga is concentrated on places where also Mg exhibits an increased concentration.

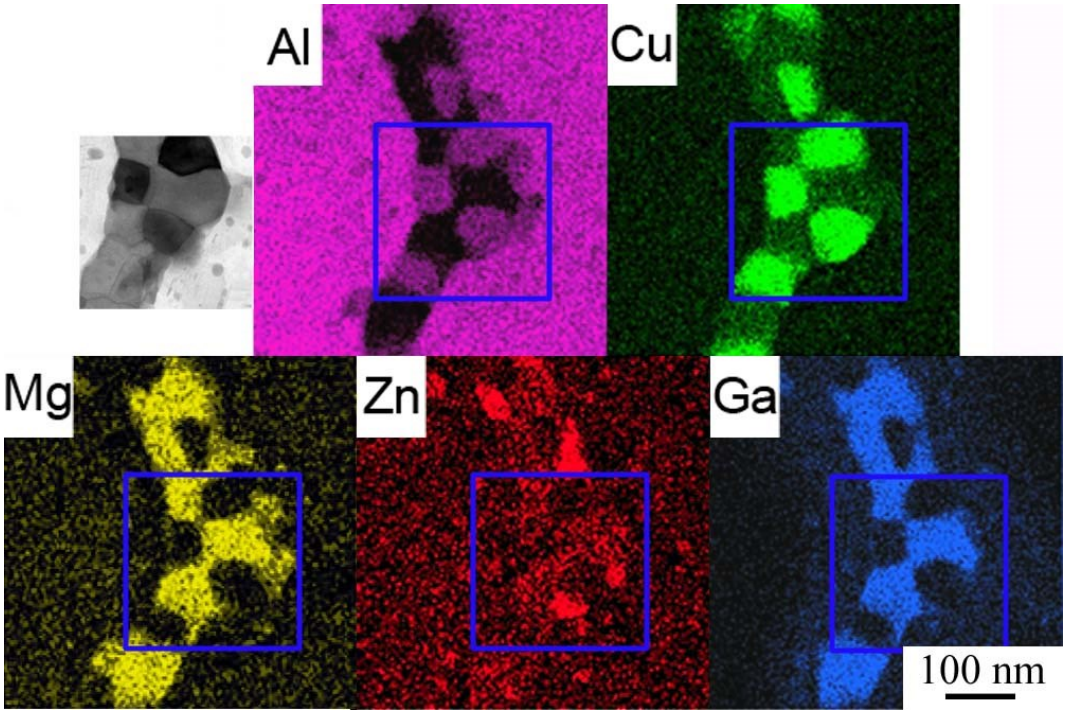

Figure 14. Cell boundary regions of an Al7075Zr_AP powder particle, STEM, and the corresponding STEM-EDS maps.

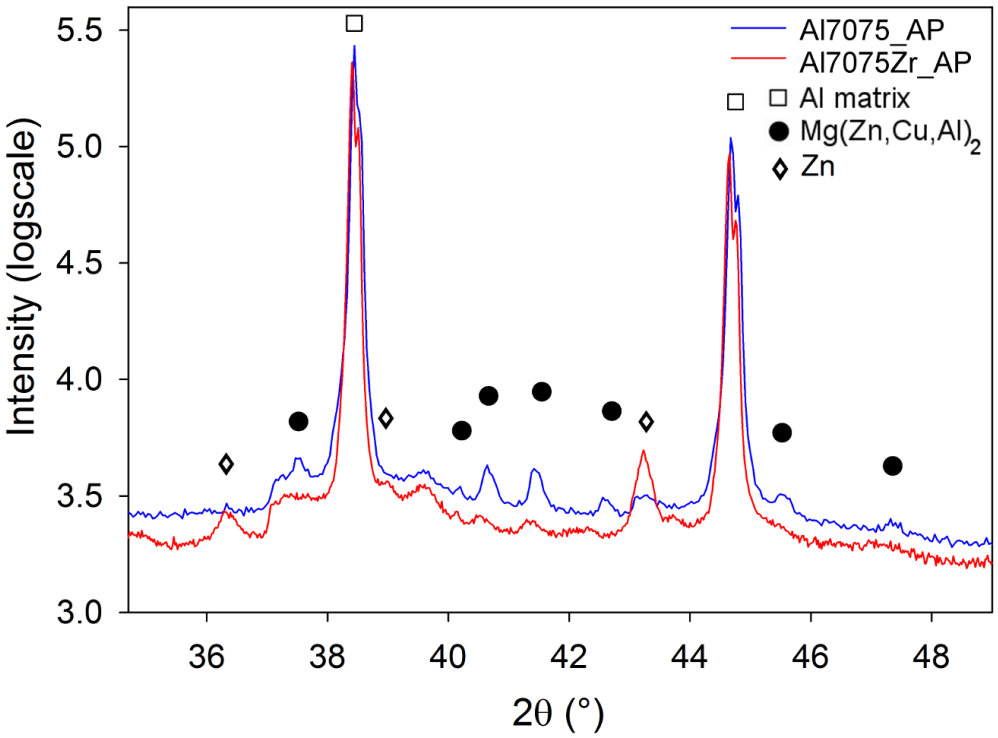

Figure 15. The XRD patterns of gas atomized powders, Al7075_AP and Al7075Zr_AP.

As mentioned in section 1.5.3., the η phase ($Mg(Zn,Cu,Al)_2$) is expected to be the main strengthening phase in the studied Al7075-based alloys. This phase was detected in the Al7075_AP powder by XRD (Figure 15). Other phases, which might also be present in this alloy, are below the detectability limit of the used method. In the Al7075Zr_AP powder the intensity of diffraction peaks of the $Mg(Zn,Cu,Al)_2$ phase is lower. Surprisingly peaks of pure Zn were detected. The weight fractions of detected phases were evaluated by Rietveld analysis. The Al7075_AP powder was found to contain 1.3 ± 0.1 wt% $Mg(Zn,Cu,Al)_2$ phase, whereas Al7075Zr_AP contained 1.1 ± 0.1 wt% of $Mg(Zn,Cu,Al)_2$ phase and 1.9 ± 0.2 wt% Zn phase (see Table 4). The weight fractions of intermetallic phases evaluated by the Rietveld analysis have to be handled very carefully. The limit of detection of any second phase particles using Cu radiation, is around 0.2 wt% [207]. Thus another phases with weight content below 0.2 wt%, not detected by XRD, can be also present. Further, quantification of phases with a fraction close to 1 wt% is connected with relative errors around 20% [207]. However, these values were stated using well crystallized phases and high accuracy measurement and analysis. Another error can be connected with the precision of background identification and size of intermetallic phases. In case the size

of intermetallic phases is small, the corresponding XRD peak is wide, and the choice of background can highly affect the integrated intensity of the peak (which gives the weight fraction of phases). Therefore, the inaccuracy of determination of wt% of phases can be actually much higher than that presented in all through the thesis as an experimental error.

The analysis of electron diffractograms obtained from TEM investigations revealed also the presence of the $Mg_2Cu_5Al_6$, Al_2Cu and Ga_2Mg phases. The Ga_2Mg intermetallic compound was found in the intercellular area presented in Figure 14. This Ga contamination is a result of lamella preparation by FIB.

The atomized powders' average grain sizes were determined by EBSD measurements. Several powder particles with different sizes were investigated for both alloys. The mean grain size was found to be around 6 μm in the Al7075_AP powder. Figure 16 shows a representative SEM-BSE figure and the corresponding orientation image micrograph of the Al7075_AP powder along with the distribution of grain boundaries. It is remarkable that cells observed in coarser powder particles correspond very well to grains and most intercellular segregations represent high-angle grain boundaries. Another situation can be seen in smaller powder particles. The grain size is mostly coarser than that observed in larger powder particles and the intercellular segregations do not correspond to grain boundaries. Some very small powder particles with cellular microstructure observed in their interior seem to be even single crystalline.

Slightly finer and more homogeneous microstructure was observed in the Al7075Zr_AP powder (Figure 17). The average gain size was stated to be around 4 μm. The grains are predominantly separated by high-angle boundaries, which mostly correspond to cell boundaries (Figure 17c).

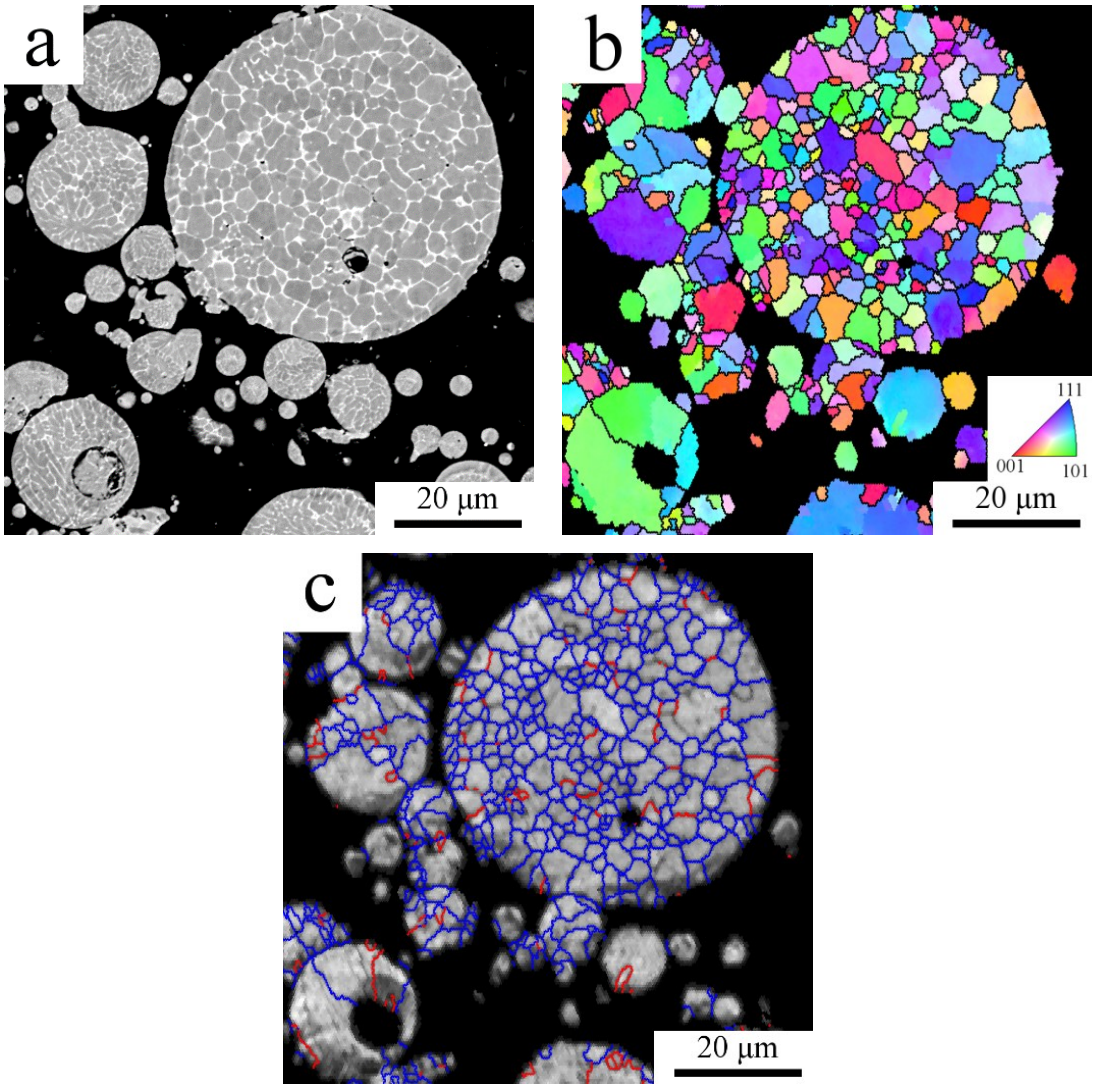

Figure 16. The microstructure of the Al7075_AP powder: a) SEM-BSE contrast micrograph, b) the corresponding orientation image micrograph with HAGBs in black and c) the distribution of grain boundaries, HAGBs in blue and LAGBs in red.

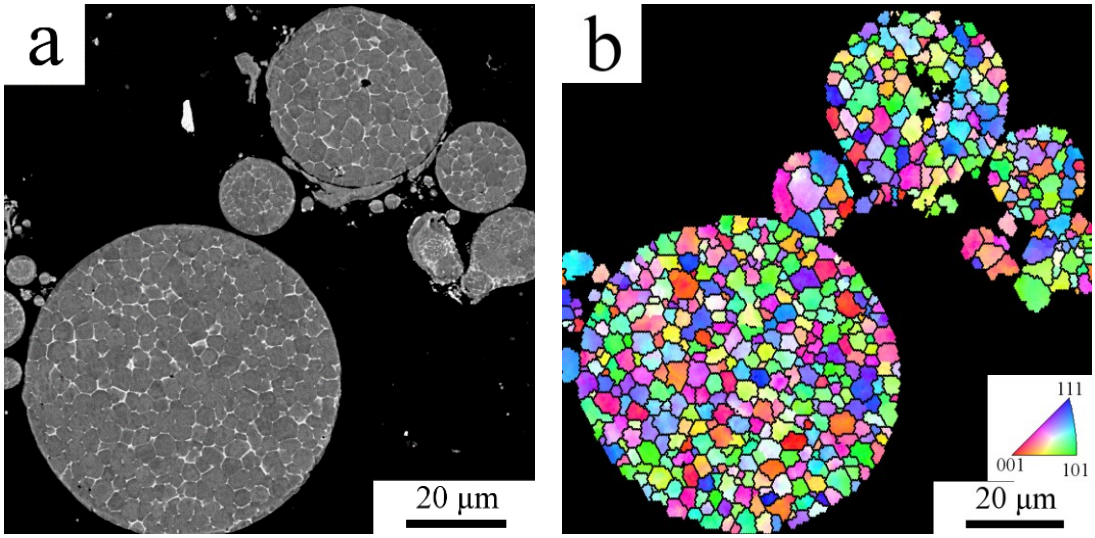

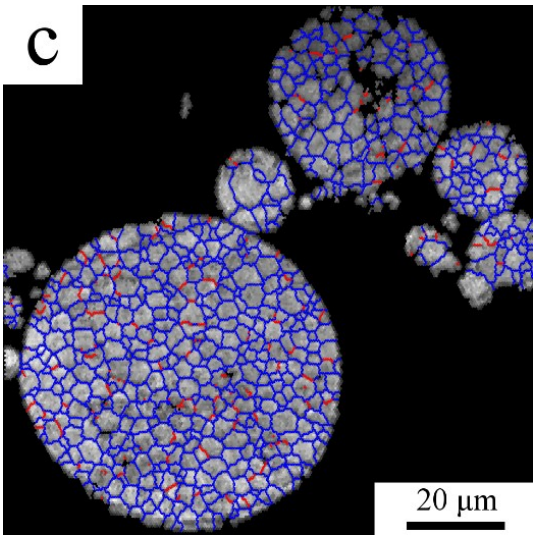

Figure 17. The microstructure of the Al7075Zr_AP powder: a) SEM-BSE contrast micrographs, b) the corresponding orientation image micrograph with HAGBs in black and c) the distribution of grain boundaries, HAGBs in blue and LAGBs in red.

The powders mechanical properties were characterized by microhardness. The microhardness of the Al7075_AP powder was stated to be 127 ± 41 HV, whereas the microhardness of the Al7075Zr_AP alloy was 97 ± 15 HV (see also Table 4). As mentioned in section 2.2, microhardness measurement could be performed only on powder particles with a sufficiently large cross section. Therefore, these values do not represent the microhardness of the finer powder particles with a finer internal microstructure or even segregation free microstructure.

Sample	$Mg(Zn,Cu,Al)_2$ [wt%]	Zn [wt%]	d [µm]	HV
Al7075_AP	1.3 ± 0.1		6	127 ± 41
Al7075Zr_AP	1.1 ± 0.1	1.9 ± 0.2	4	97 ± 15

Table 4. Comparison of the weight content of second phase particles, approximate grain size, and microhardness of gas atomized Al7075_AP and Al7075Zr_AP powders.

3.2. Milled powders

As a next step in our research, both gas atomized Al7075_AP and Al7075Zr_AP powders were mechanically milled in order to refine their microstructure (decrease the grain size, dissolve the alloying elements). As the

measure of microstructural refinement is expected to depend on the milling intensity, it was varied. The intensity of milling can be affected predominantly by the following parameters: milling time, RPM, and milling temperature. The influence of various milling parameters was tested on the Al7075_AP powder using an UNION HD01 Lab attritor using a BTP of 32:1. The list of used milling parameters is given in Table 5. The parameters, which led to the best results were used for milling of the Al7075Zr_AP powder.

Alloy	$t_{milling}$ [h]	RPM [min^{-1}]	Atmosphere	Temperature [°C]	Further designation
Al7075	3	180	Ar	RT	Al7075_MP_RT_3_180
Al7075	3	400	Ar	RT	Al7075_MP_RT_3_400
Al7075	8	400	Ar	RT	Al7075_MP_RT_8_400
Al7075	3	180	LN	77 K	Al7075_MP_LN_3_180
Al7075	3	400	LN	77 K	Al7075_MP_LN_3_400
Al7075Zr	3	400	Ar	RT	Al7075Zr_MP_RT_3_400

Table 5. The parameters of milling in attritor and the powders designation.

The morphology and size of milled powder particles was studied by LM. Figure 18 shows results of this investigation for selected milling parameters. The milled powder particles exhibited irregular shapes and their size was increased in comparison with gas atomized powders. Image analysis of LM micrographs showed an increase in the size of powder particles (more exactly of their cross sections) of about 2 times in case of the lowest milling intensity (Al7075_MP_RT_3_180). More intensive milling (Al7075_MP_RT_3_400) led to a powder particle size increase up to around 20 times (compare Figures 18a and b). Similar results were obtained for the milled Al7075Zr alloy (Al7075Zr_MP_RT_3_400). Milling at cryogenic temperatures led to much smaller increase in the powder particles size (2-5 times) (Figures 18c and d).

All milled powder particles exhibited areas of discontinuity (see darker areas in Figure 18b, inside the powder particles), which are pores induced by milling. All these changes, i.e. the irregular morphology, size increment, and porosity reflect repeated fracture and cold welding during the milling process.

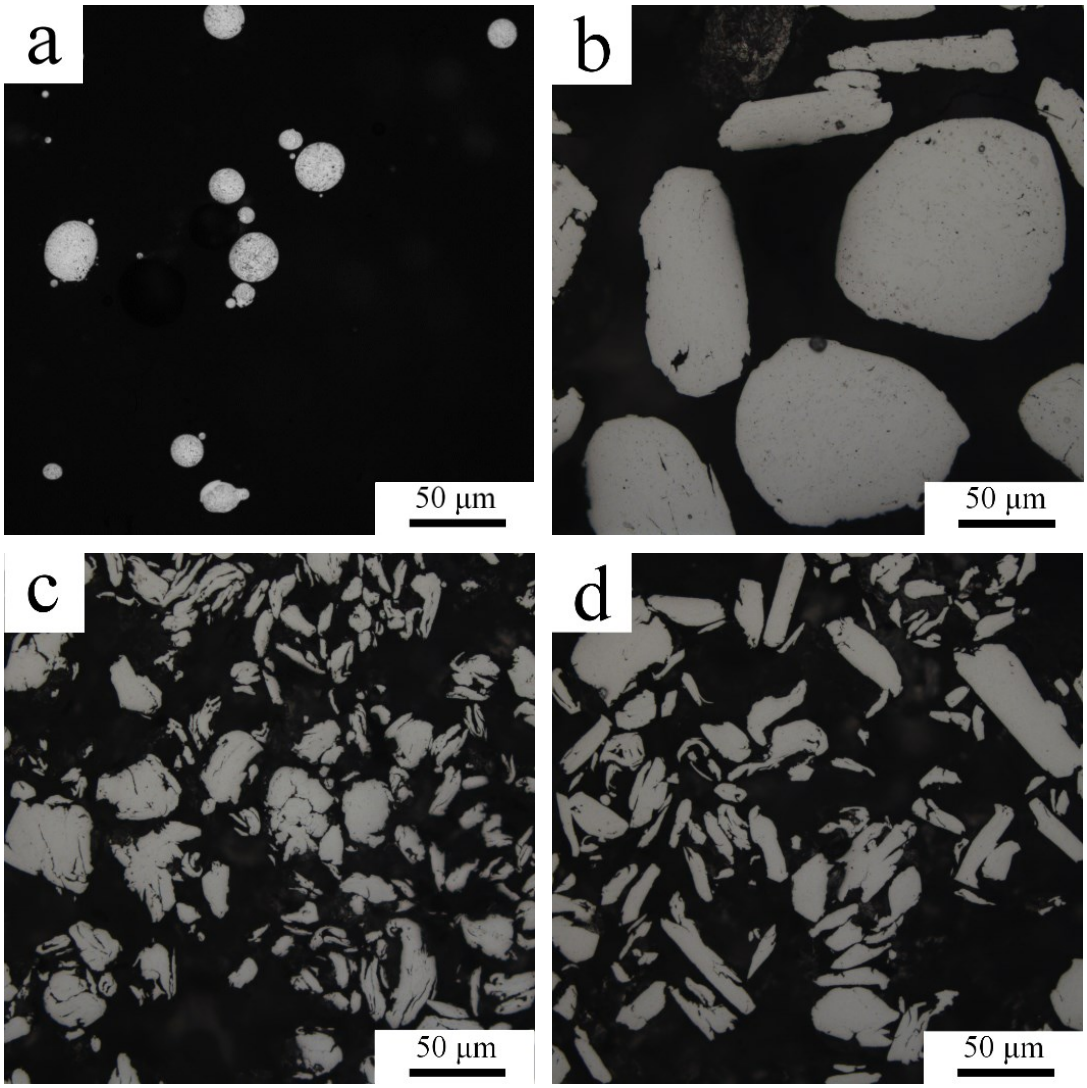

Figure 18. Comparison of the morphology and size of powder particles: a) Al7075_AP, b) Al7075_MP_RT_3_400, c) Al7075_MP_LN_3_180, d) Al7075_MP_LN_3_400, LM.

SEM revealed the microstructure of milled powder particles at higher magnification (Figure 19). In case of lower milling intensity (180 RPM for 3h at RT) the cellular microstructure of former gas atomized powder particles is still recognizable, see Figure 19a and Figure 19c (in higher magnification). More intensive milling, e. g. increased RPM or decreased milling temperature, resulted in a complete destruction of the initial microstructure (Figure 19b). However, places with increased concentration of higher atomic number atoms were recognized on SEM-BSE figures in all cases (see Figure 19d). Beside these areas also numerous pores (dark areas in Figures 19c,d inside the powder particles) are visible.

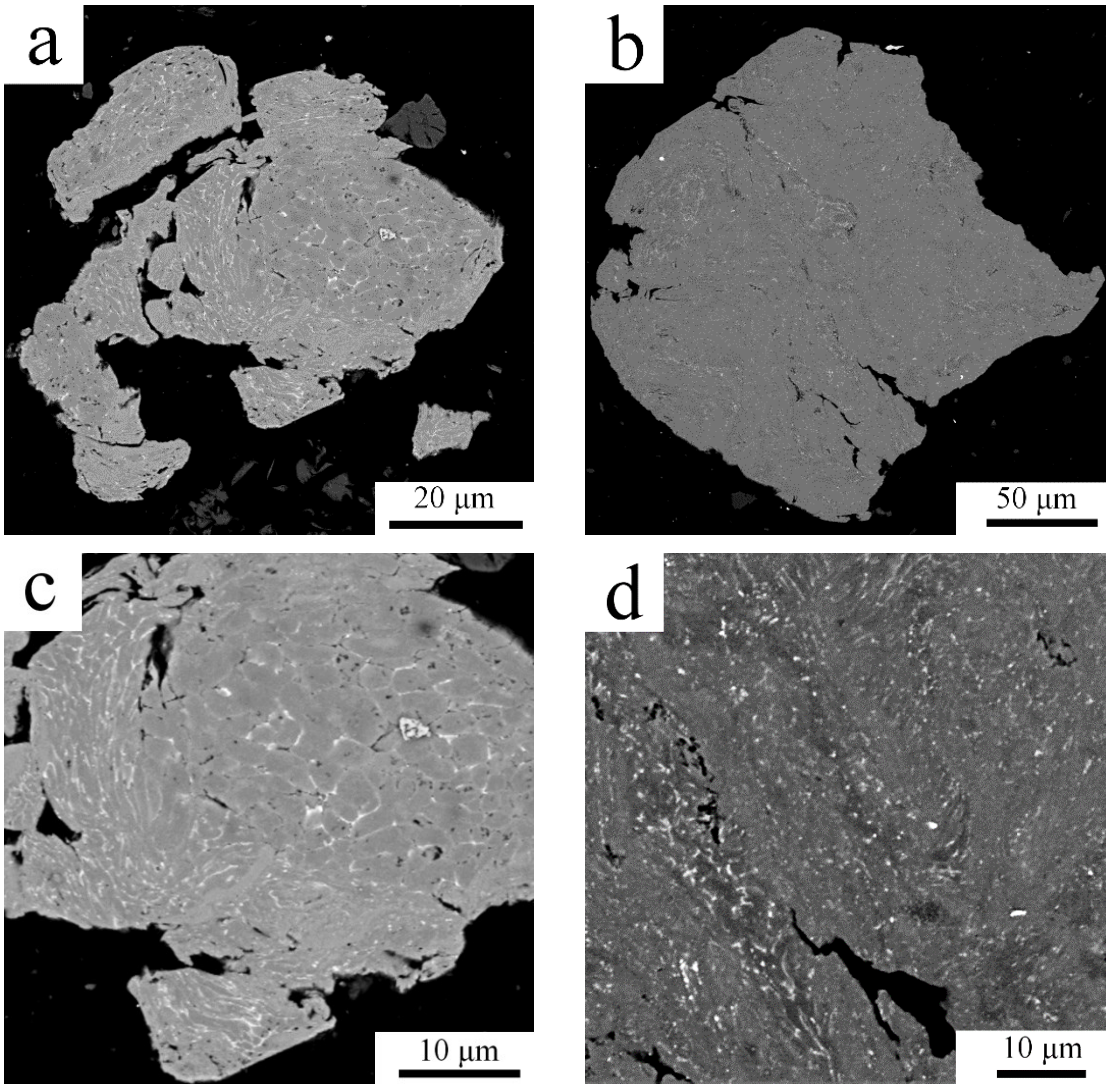

Figure 19. The typical microstructure of milled powder particles: a) Al7075_MP_RT_3_180, b) Al7075_MP_RT_3_400, and their details, c) Al7075_MP_RT_3_180, d) Al7075_MP_RT_3_400, SEM-BSE.

The evolution of phase composition with varying milling parameters was studied by XRD. The comparison of XRD patterns for a gas atomized Al7075_AP powder and one milled powder (Al7075_MP_RT_3_400) is presented in Figure 20a. A similar comparison of XRD pattern for a gas atomized and milled powder of the Zr-containing alloy is presented in Figure 21. Figure 20b presents the detail of the XRD pattern of Al7075_MP_RT_3_180 powder between the Al peaks.

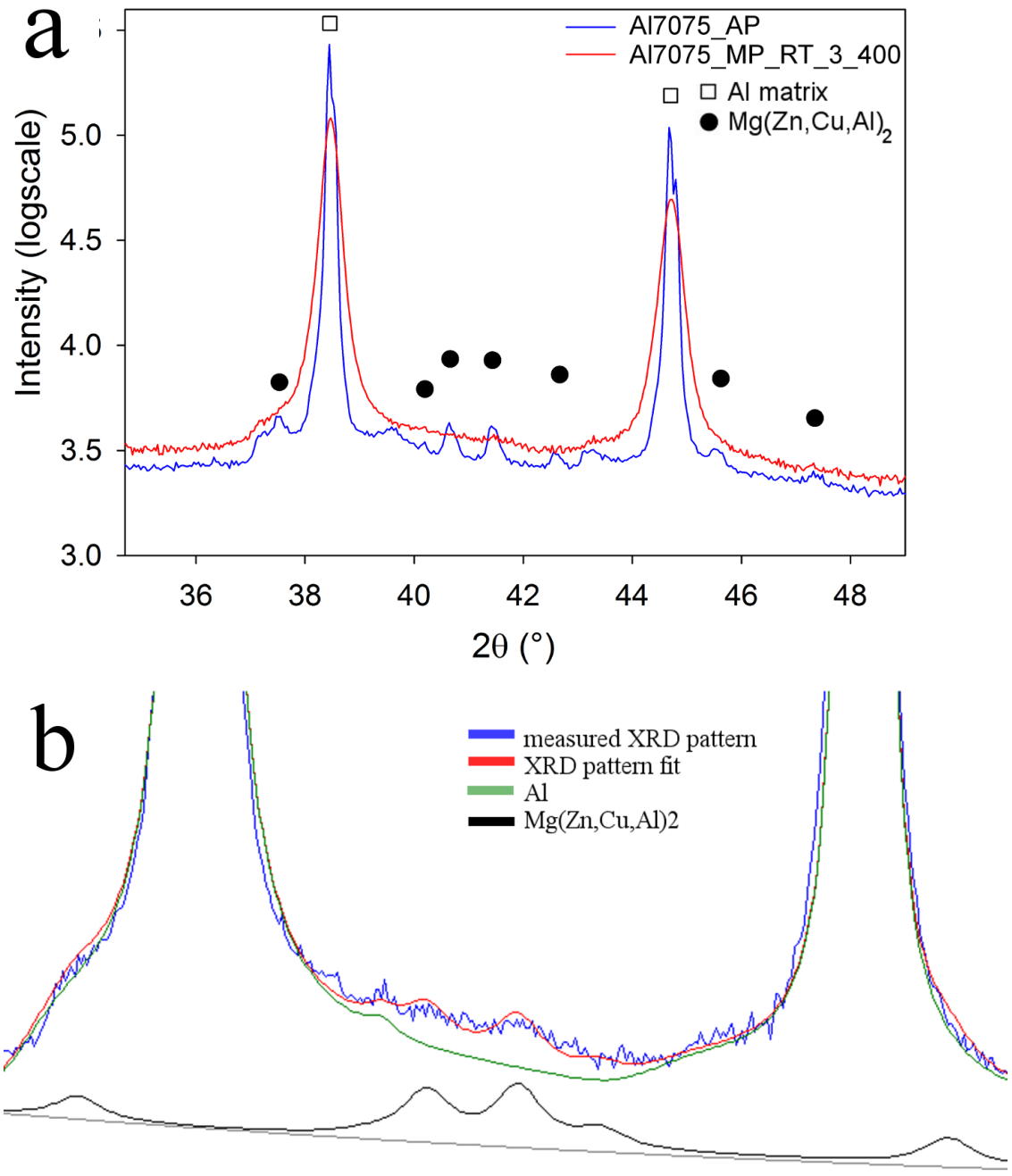

Figure 20. The result of XRD measurement a) comparison of XRD pattern of the gas atomized Al7075_AP powder and one milled powder (Al7075_MP_RT_3_400) of Al7075 alloy and b) detail of XRD pattern for another milled powder (Al7075_MP_RT_3_180).

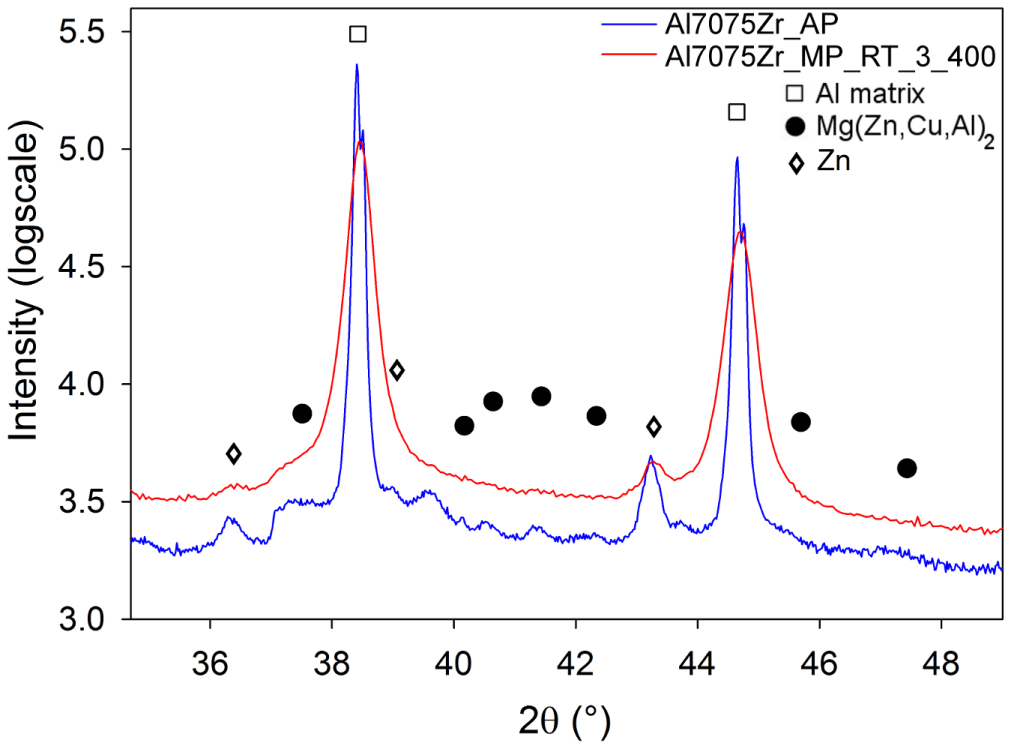

Figure 21. Comparison of XRD pattern of the gas atomized powder (Al7075Zr_AP) and one milled powder (Al7075Zr_MP_RT_3_400) of Al7075Zr alloy.

Figures 20 and 21 present a reduction/loss of XRD peaks of non-matrix phases induced by milling. Although the presence of η phase is not visible in the full height XRD patterns as Figure 20a, there are very small peaks corresponding to this phase (see Figure 20b). However, as these peaks are very low and wide, the fraction of this η phase is at the limit of detectability. This was the case in all milled powders of Al7075 alloy, therefore, their weight fraction was not evaluated. In Al7075Zr_MP_RT_3_400 a relatively low peak corresponding to pure Zn was found. Its content was evaluated by Rietveld analysis to be 0.9 ± 0.3 wt%, i.e. about half of that observed in the gas atomized Al7075Zr_AP powder. In case of the Zr-containing alloy, a slight shift of the Al XRD peaks to higher angles is also observable. Milling caused a remarkable broadening of diffraction peaks corresponding to the Al matrix. The results of Rietveld analysis of the Al diffraction line broadening were performed and the resulting sizes of crystallites in the matrix phase are listed in Table 6.

The evaluation of the grain size using EBSD method failed in all milled powders. No orientation image micrograph could be prepared from any powder milled in attritor, probably because of their too fine structure. Therefore, no direct information on the grain size of milled powders is available. In this case the evaluation of the CDD

from diffraction line broadening represents an alternative method. Such evaluation is possible only in case when the CDD is below about 400 nm [208]. This requirement was definitely not fulfilled in the gas atomized powders. The crystallite size evaluated for all milled powders is between 50 and 70 nm. Although the CDD size cannot be directly correlated with the grain size, the comparison of data obtained in gas atomized and milled powders shows a remarkable size refinement induced by milling.

Sample	CDD size [nm]	HV
Al7075_MP_RT_3_180	67 ± 10	136 ± 40
Al7075_MP_RT_3_400	55 ± 10	216 ± 20
Al7075_MP_RT_8_400	53 ± 10	229 ± 29
Al7075_MP_LN_3_180	71 ± 10	188 ± 21
Al7075_MP_LN_3_400	50 ± 10	220 ± 20
Al7075Zr_MP_RT_3_400	57 ± 10	219 ±20

Table 6. Comparison of crystallite sizes and microhardness of powders milled in attritor.

The average microhardness values with the corresponding standard deviations are listed in Table 6. It is clear that milling led to an increase in microhardness in all milled powders in comparison with the gas atomized counterparts. In case of milling at room temperature, the microhardness increased with increasing RPM. On the other side, the influence of milling time was less important. Cryomilling in liquid nitrogen accelerated the powder strengthening at low RPM, the influence of decreased milling temperature was negligible at higher RPM. The highest microhardness value of 229 HV was found in the Al7075_MP_RT_8_400 powder, however, samples Al7075_MP_RT_3_400 and Al7075_MP_LN_3_400 exhibited a microhardness very close to this value, 216 resp. 220 HV. The microhardness values measured in the milled Al7075Zr_MP_RT_3_400 powders were very close to those of the Al7075_MP_RT_3_400 powder.

Milling of both Al7075_AP and Al7075Zr_AP powders was alternatively carried out in a planetary ball mill. Milling was performed for 8 h with 400 RPM in Ar atmosphere with BTP 40:1. The planetary ball milled powders will be further referred as Al7075_MP_RT_8_400P and Al7075Zr_MP_RT_8_400P. LM

investigation revealed that milling led to irregularly shaped, in size increased powder particles (Figure 22, figures taken at the same magnitude as Figure 18). Image analysis of LM micrographs showed an increase in the size of powder particles induced by milling. The powder particles of Al7075_MP_RT_8_400P exhibited a size increase of about 30-times, whereas in case of Al7075Zr_MP_RT_8_400P powder the size increase was found to be around 15-times.

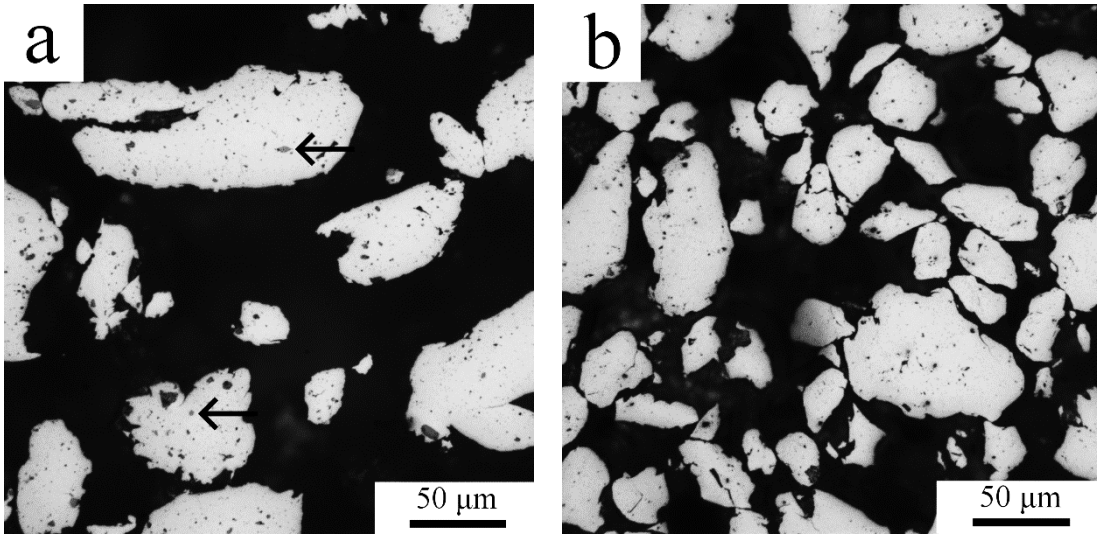

Figure 22. The morphology and size of planetary ball milled powder particles: a) Al7075_MP_RT_8_400P, b) Al7075Zr_MP_RT_8_400P, LM.

SEM-BSE investigations showed the presence of some particles with a size up to several µm with Z higher than that of the matrix around (Figure 23). Some of these particles (visible as black particles also in LM micrographs in Figure 22) are denoted by black arrows. As remarkable from Figure 23, the Al7075_MP_RT_8_400P powder contains much more of these particles than the Al7075Zr_MP_RT_8_400P powder. The elemental composition of these particles was studied by SEM-EDS measurement. The investigation showed that these particles contained Ni and Ti. They were implanted into the milled powder during the milling process from the vessel, where they were present as impurities from the preceding milling process. SEM-EDS mapping showed a homogeneous distribution of Zn, Mg, Cu, and Al (within the limit of resolution of the used technique) in both materials. This is presented in Figure 24 for the Al7075Zr_MP_RT_8_400P powder.

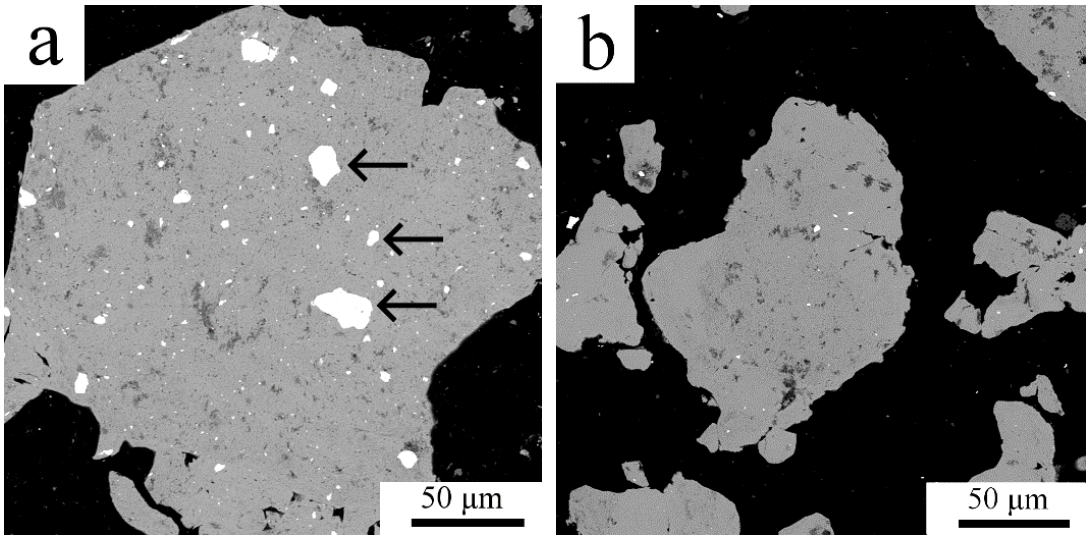

Figure 23. The microstructure of planetary ball milled powder particles:
a) Al7075_MP_RT_8_400P, b) Al7075Zr_MP_RT_8_400P powder, SEM-BSE.

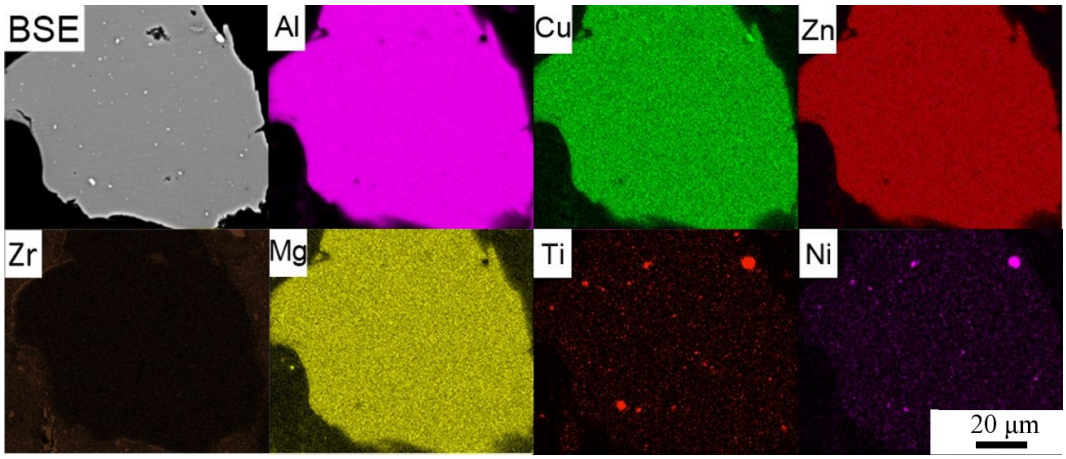

Figure 24. The contaminating particles in the milled Al7075Zr_MP_RT_8_400P powder, SEM-BSE and SEM-EDS.

As in case of powders milled in attritor, it was not possible to obtain orientation image maps and to determine the grain size by EBSD. Therefore, and due to non-visible Zn and Mg containing second phase particles in SEM-BSE/EDS figures, the TEM investigation of both planetary milled powders was performed. TEM investigation of the Al7075_MP_RT_8_400P powder revealed elongated 50 - 200 nm grains (Figure 25a). At even higher magnification, nanometer-sized second phase particles were found predominantly along grain boundaries (Figure 25b). According to STEM-EDS investigations, these particles were rich on Mg and Zn. TEM investigations of the milled Al7075Zr_MP_RT_8_400P powder showed also elongated grains, their size was even smaller - between 20 and 100 nm (Figure 26a).

No second phase particles were found between the grains (Figure 26b). The size of elongated grains stated from TEM is in a good agreement with the crystallite size 90 and 64 nm determined from the analysis of the XRD peaks broadening for both planetary ball milled powders (see Table 7).

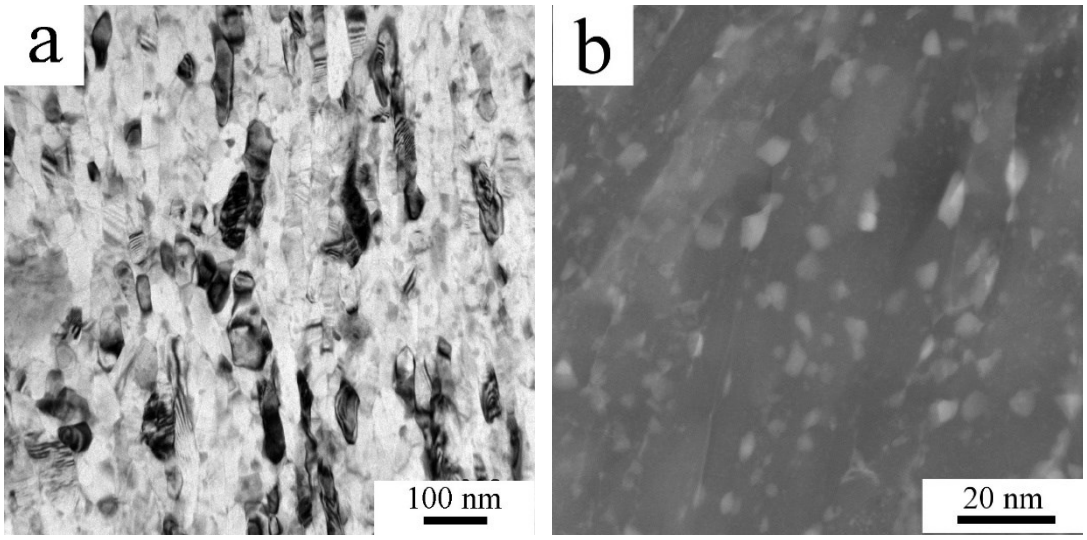

Figure 25. The microstructure of the Al7075_MP_RT_8_400P powder: a) elongated grains, TEM-BF, b) small second phase particles between the grains, HAADF-STEM.

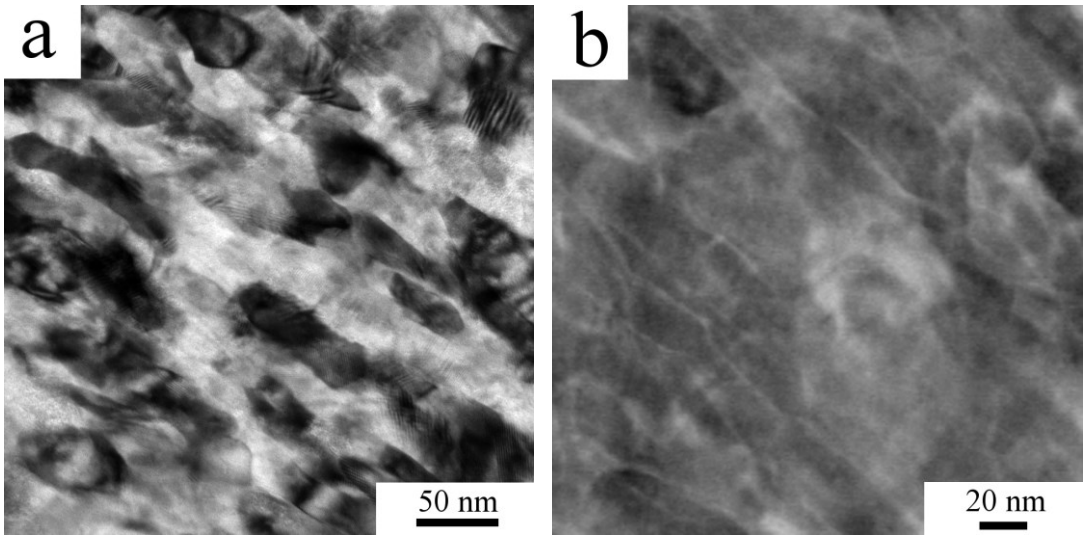

Figure 26. The microstructure of the Al7075Zr_MP_RT_8_400P powder: a) elongated grains, TEM-BF, b) the absence of small second phase particles between the grains, HAADF-STEM.

The powders phase composition was studied by XRD technique. Figures 27 and 28 present the changes induced by planetary ball milling of both alloys. Milling led to reduction or loss of non-matrix XRD peaks. The XRD peaks of η phase in the planetary milled Al7075 powder were at the limit of detectability, in the Zr-containing powder even below this limit. The weight fraction of the η phase was, therefore, not evaluated. XRD showed no peaks for Ni and Ti contaminating particles, their weight fraction is probably below the detectability limit. Similarly to powders milled in attritor, milling induced a remarkable broadening of XRD peaks of the Al-matrix in both powders. The CDD sizes evaluated from this broadening are below 100 nm and correspond very well to the grain sizes evaluated from TEM micrographs. In the Al7075Zr powder, planetary milling led also to a slight displacement of matrix XRD peaks to higher angles.

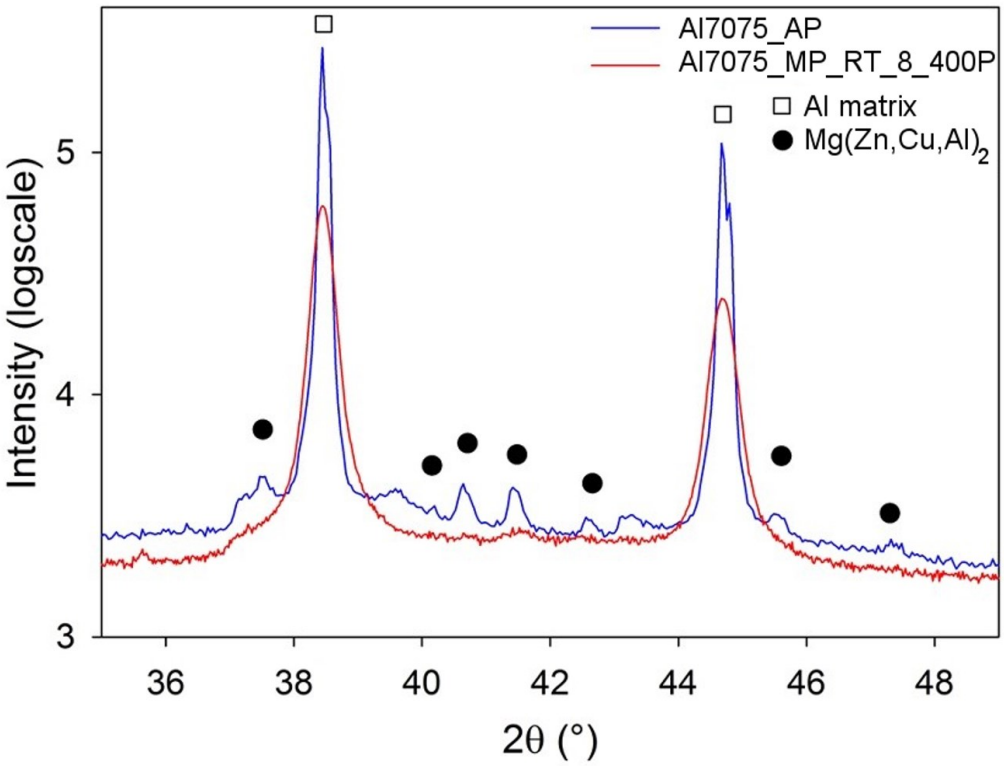

Figure 27. Comparison of XRD pattern of the gas atomized Al7075_AP powder and planetary ball milled Al7075_MP_RT_8_400P powder.

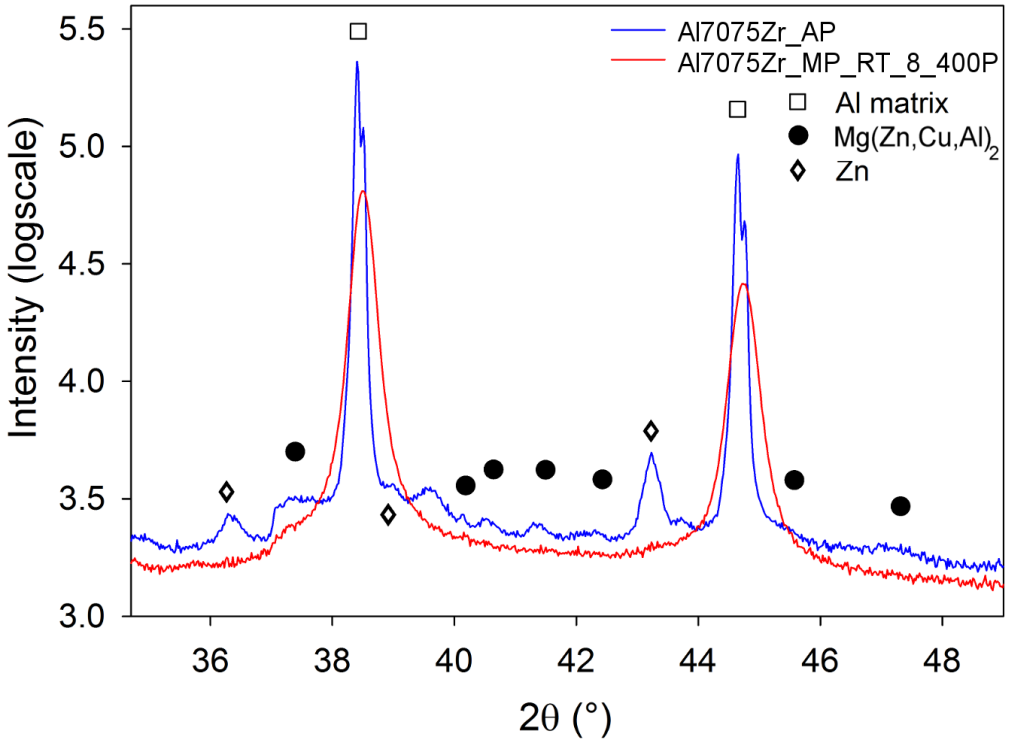

Figure 28. Comparison of XRD pattern of the gas atomized Al7075Zr_AP powder and planetary ball milled Al7075Zr_MP_RT_8_400P powder.

Both planetary ball milled powders were tested by microhardness measurement. The results are listed in Table 7. The microhardness of powders was found to be exceptionally high, above 300 HV in both alloys.

Sample	d [nm]	CDD size [nm]	HV
Al7075_MP_RT_8_400P	50 – 200	90 ± 10	327 ± 32
Al7075Zr_MP_RT_8_400P	20 - 100	64 ± 10	343 ± 25

Table 7. Comparison of the grain size evaluated by TEM, crystallite size of the Al matrix and microhardness of planetary ball milled powders of Al7075 and Al7075Zr alloys.

3.3. Spark plasma sintered compacts from gas atomized powders

SPS of gas atomized Al7075 and Al7075Zr alloys' powder was carried out at 425 °C for 4 min with 80 MPa using a FCT SPS-HP25 device. These sintering parameters were chosen based on previous experience of research group working with this SPS device, see [119]. Sintering led to nearly full density compacts which will be

further referred to as Al7075_AC and Al7075Zr_AC. The porosity of both compacts was determined from image analysis of SEM micrographs (taken on samples polished up to 1 μm) to be below 1 vol%.

The microstructure of both compacts is shown in Figures 29 and 30 in SEM-BSE contrast. Former powder particles are still recognisable in both compacts, to make this more apparent, some former powder particles are highlighted in Figure 29a by white curves. A comparison of Figures 29a and 30a makes visible a higher fraction of fine second phase particles in the Al7075_AC sample. Figures 29b and 30b show the boundary region of original gas atomized particles in higher magnification. The boundaries of former atomized powder particles of the Al7075 alloy become at some places decorated by precipitates with a size up to 1 μm (see blue arrows in Figure 29b). Further, the initially continuous layers of intermetallic phases inside the powder particles were rearranged into a semi-continuous network of second phase particles (see the chains of second phase particles in the lower half of Figure 29b). Such semi-continuous networks could be rarely seen in Al7075Zr alloys compact, in this sample the continuous layers of intermetallic phases were replaced by distinct second phase particles (Figure 30b).

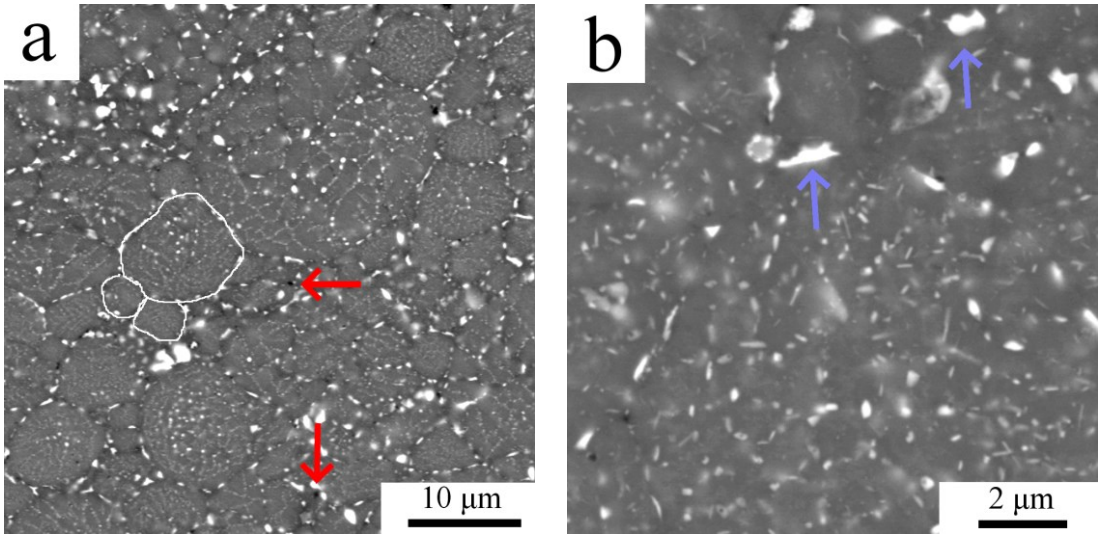

Figure 29. The microstructure of the Al7075_AC compact: a) the former powder particles, b) detail of powder particles boundary and chains of second phase particles, SEM-BSE.

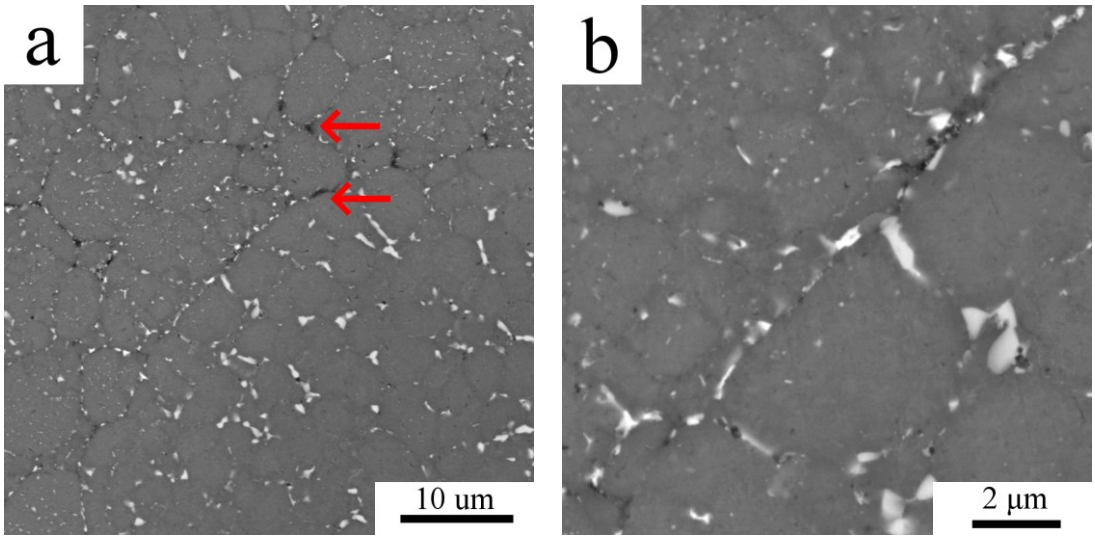

Figure 30. The microstructure of the Al7075Zr compacts: a) the former powder particles, b) detail of powder particles boundary and the second phase particles, SEM-BSE.

Some discontinuities in materials' matrix are visible in Figures 29a and 30a (some of them denoted by red arrows). These are not necessarily pores remained after incomplete sintering, they could be formed by pull-out of phases during materials final metallographic preparation with colloidal silica. This can be explained by the fact, that they are inside of the original powder particles, at the intercellular boundary (red arrows in Figure 29a).

A more detailed insight into the compacts' microstructure and phase composition was obtained using TEM. Figure 31 shows TEM micrographs of the Al7075_AC sample. Large precipitates up to 1 µm in size were found between former individual powder particles. These particles were identified by SAED as the η phase. One of these particles is in Figure 31a denoted by red arrow. Figure 31b shows a part of the chain like arrangement of various second phase particles with a size of several tens to hundreds nm. Moreover, also grains with a dense distribution of small nm sized second phase particles in their interior, and precipitation-free zone along grain boundaries were found (Figure 31c).

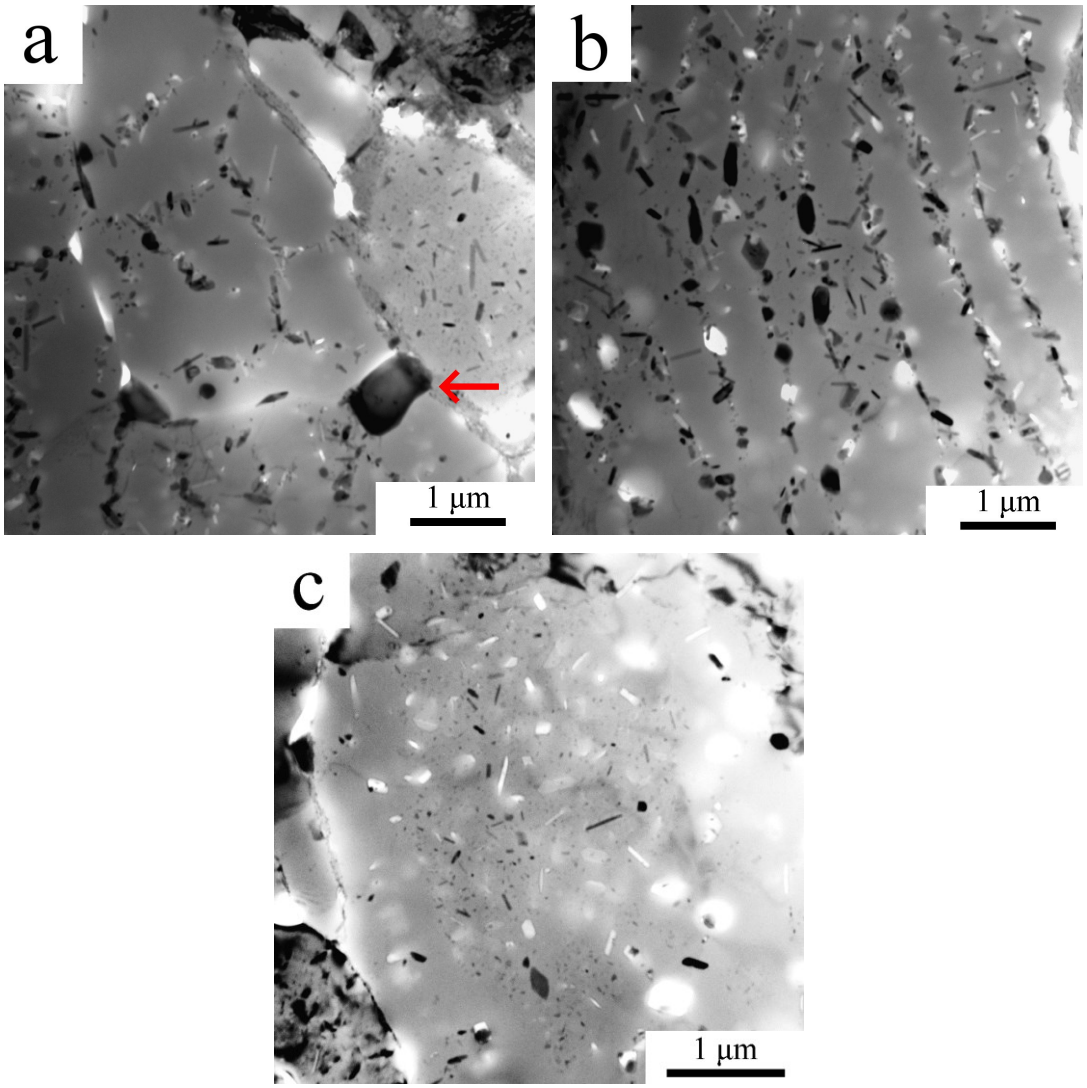

Figure 31. The microstructure of the Al7075_AC compact: a) coarse second phase particle, b) the chain like arrangement of second phase particles, c) dense distribution of fine second phase particles, TEM-BF.

Similar microstructure was observed also in the Al7075Zr_AC sample. Figure 32a shows a cell interior with several small second phase particles arranged into arrays. TEM-EDX analysis revealed an increased content of Mg, Cu, and more rarely also Zn in distinct particles. Thus it can be supposed that these second phase particles are of $Mg(Zn,Cu,Al)_2$ and Al_2CuMg type. A dense and homogeneous distribution of nm-sized Al_3Zr particles was found in some grains (see Figure 32b), however, at other places the Al_3Zr particles were found to be arranged into a fan-shape structure. Such a fan shape arrangement is presented in Figure 32c in dark fields contrast mode, which enabled better visibility of the structure. Electron diffraction analysis revealed that

these particles are formed by the metastable modification of the Al_3Zr phase with $L1_2$ structure.

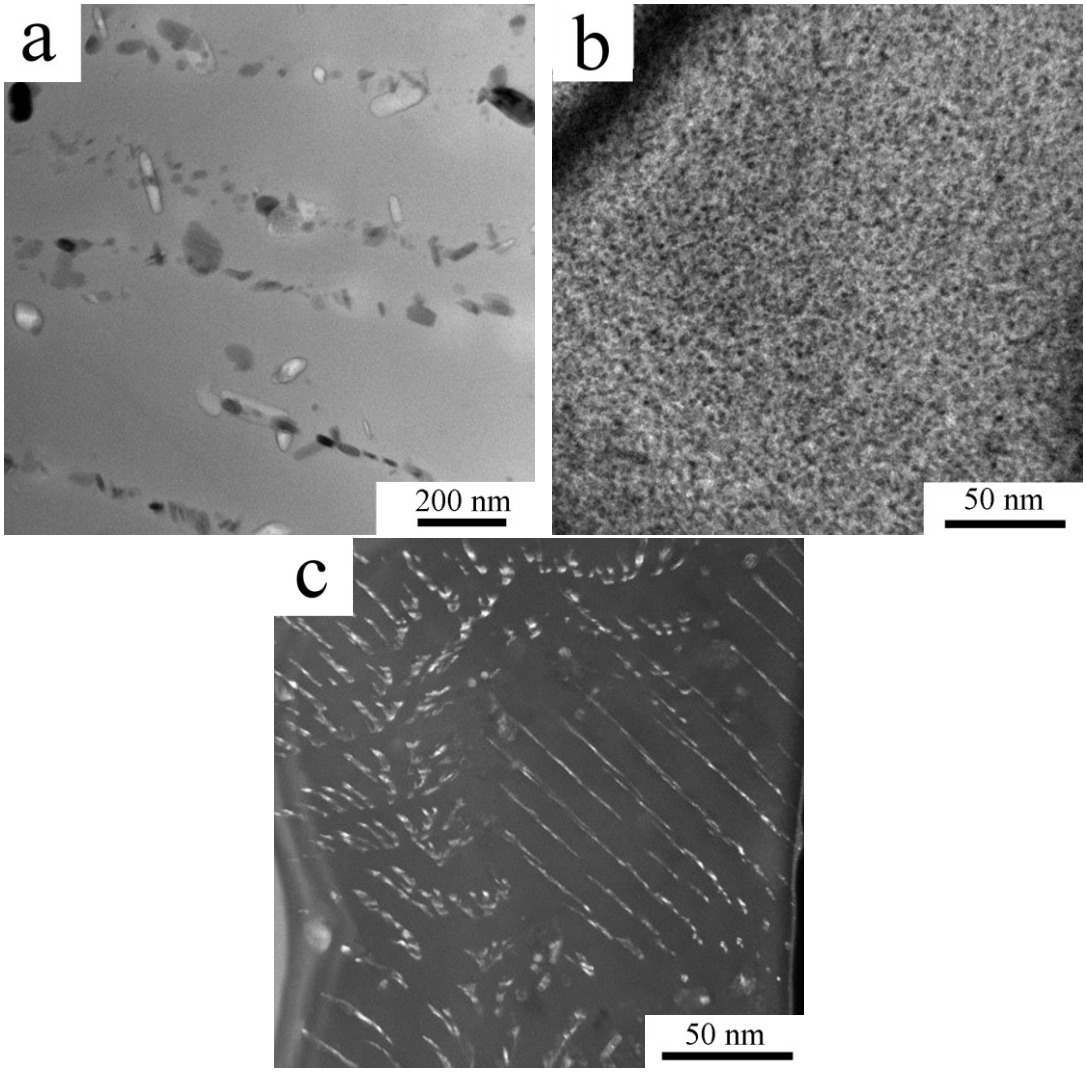

Figure 32. The microstructure of the Al7075Zr_AC compact: a) precipitates arranged into chains, b) homogeneous distribution of nm-sized Al_3Zr, TEM-BF, c) Al_3Zr particles arranged into a fan-shaped structure, TEM-DF.

The changes in phase composition induced by SPS were investigated by XRD. Figure 33 presents the comparison of XRD patterns for the gas atomized Al7075_AP powder and the corresponding Al7075_AC compact. Figure 34 shows the comparison of XRD patterns for the gas atomized Al7075Zr_AP powder and the corresponding Al7075Zr_AC compact. The SPS induced alteration of second phase particle content was evaluated from XRD pattern by Rietveld analysis, the results are listed in Table 8. SPS led to dissolution of Zn phase along with precipitation of η and S second phase particles.

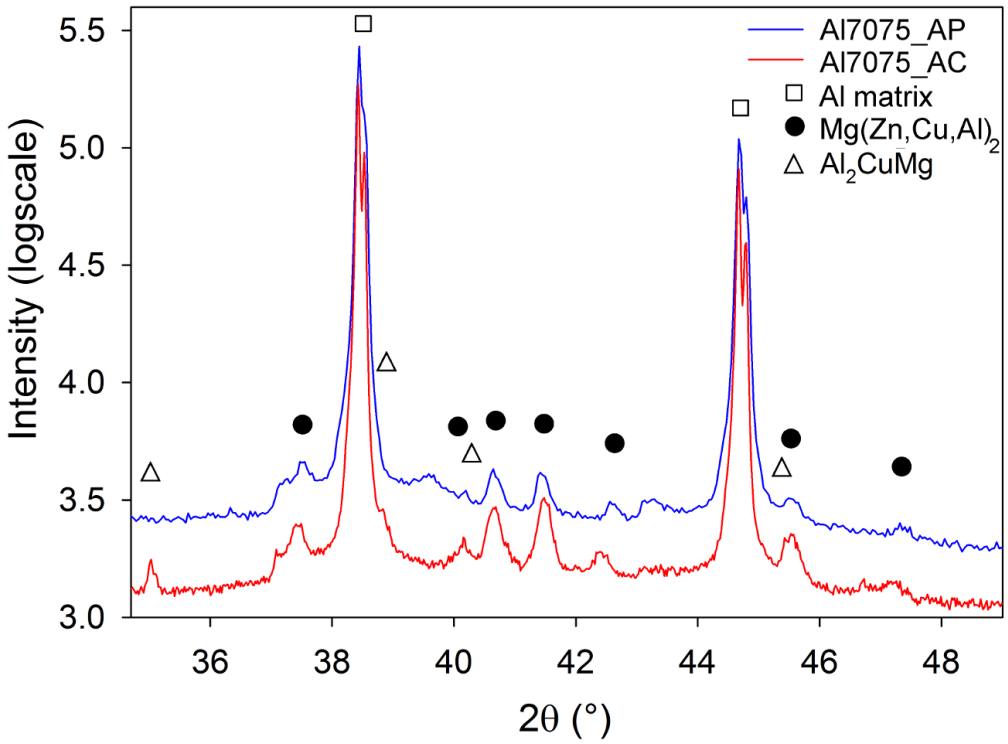

Figure 33. Comparison of XRD pattern of the Al7075_AC compact and the corresponding gas atomized Al7075_AP powder.

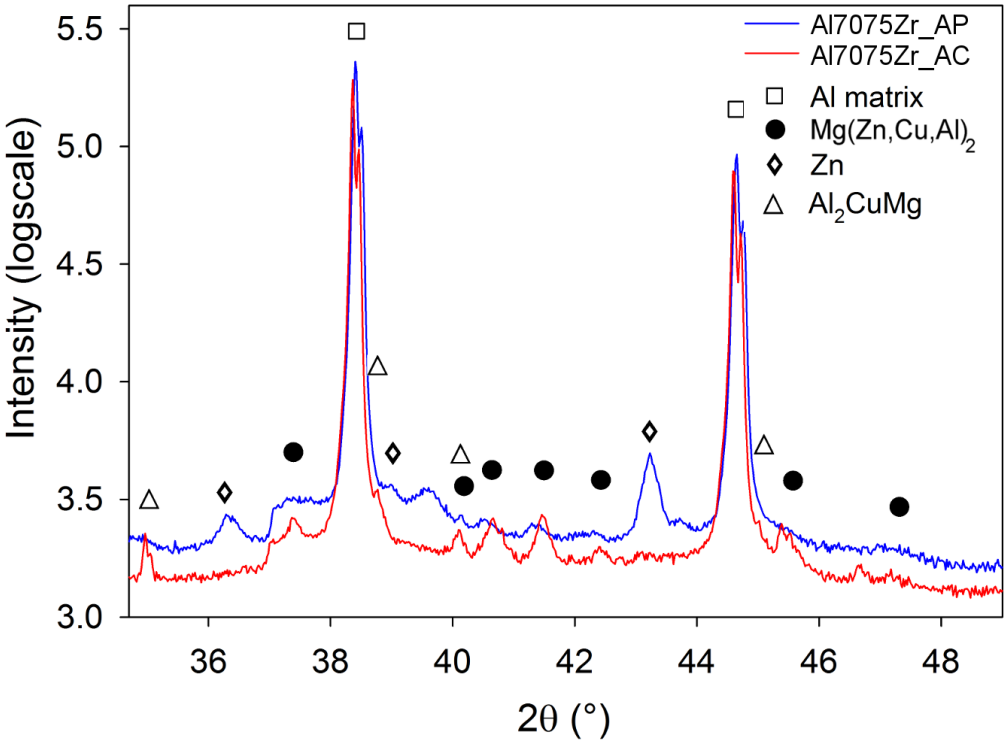

Figure 34. Comparison of XRD pattern of the Al7075Zr_AC compact and the corresponding gas atomized Al7075Zr_AP powder.

Sample	$Mg(Zn,Cu,Al)_2$ [wt%]	Al_2CuMg [wt%]	d [μm]	HV
Al7075_AC	4.2 ± 0.2	0.8 ± 0.2	5.2 ± 1.7	151 ± 3
Al7075Zr_AC	1.4 ± 0.1	1.1 ± 0.2	3.4 ± 1.1	171 ± 6

Table 8. Comparison of weight content of second phase particles, grain size, and microhardness of compacts prepared from gas atomized powders, samples Al7075_AC and Al7075Zr_AC.

The EBSD method was used for the evaluation of the grain size and of the character of grain boundaries. Figures 35a and 36a show the orientation image micrographs of the Al7075_AC and Al7075Zr_AC samples with HABGs in black. Black, i.e. non-diffracting regions correspond in both figures most probably to coarse precipitates of intermetallic phases observed by SEM-BSE. The EBSD data were used for the evaluation of the grain size distribution (Figure 37). It is apparent that the grain size is coarser and the distribution of grain sizes is broader and displaced to larger values in the Al7075_AC compact compared to the Al7075Zr_AC compact. Whereas the Al7075_AC compact exhibits a broad maximum of the grain size distribution between 4 and 10 μm, a high fraction of 2-4 μm sized grains was observed in the Al7075Zr_AC compact. The average grain sizes of 5.2 ± 1.7 μm and 3.4 ± 1.1 μm were evaluated for the Al7075_AC and Al7075Zr_AC compacts, respectively.

Figures 35b and 36b show the distribution of low- and high-angle grain boundaries in both samples, HAGBs in blue and LAGBs in red. These figures reveal clearly the original powder particles. The new boundaries formed during SPS at contact points of original powder particles are high-angle grain boundaries. Most grains inside these original particles are also separated by high-angle grain boundaries. Similarly to the gas atomized powder, some smaller original powder particles are composed of a small number of relatively coarse grains or are even single crystalline. On the other side, the finest grains were observed at places between original coarse powder particles (see red arrows in Figures 35b and 36b). The high fraction of HAGBs (close to 90%) is remarkable also from Figure 38, which presents the distribution of misorientation angles in both compacts. The distribution functions are nearly identical for both materials and agree well with the distribution function for random misorientation (when all relative orientations of neighbouring grains are equally

probable) of grains in cubic materials [209]. A small deflection from this Mackenzie distribution is present in the range of small angles.

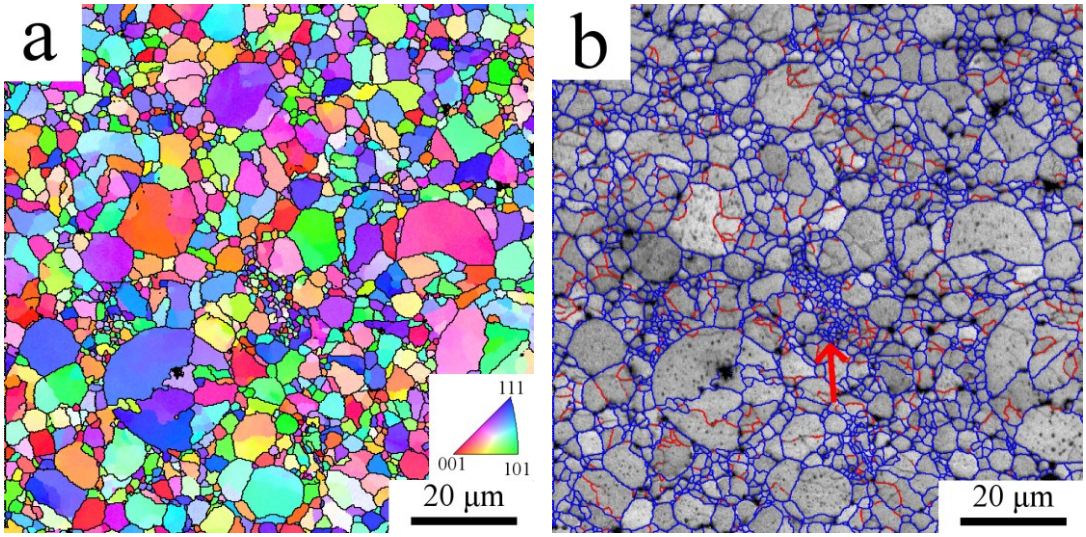

Figure 35. The results of EBSD investigation of the Al7075_AC compact: a) orientation image figure with HAGBs in black, b) the distribution of grain boundaries, HAGBs in blue and LAGBs in red.

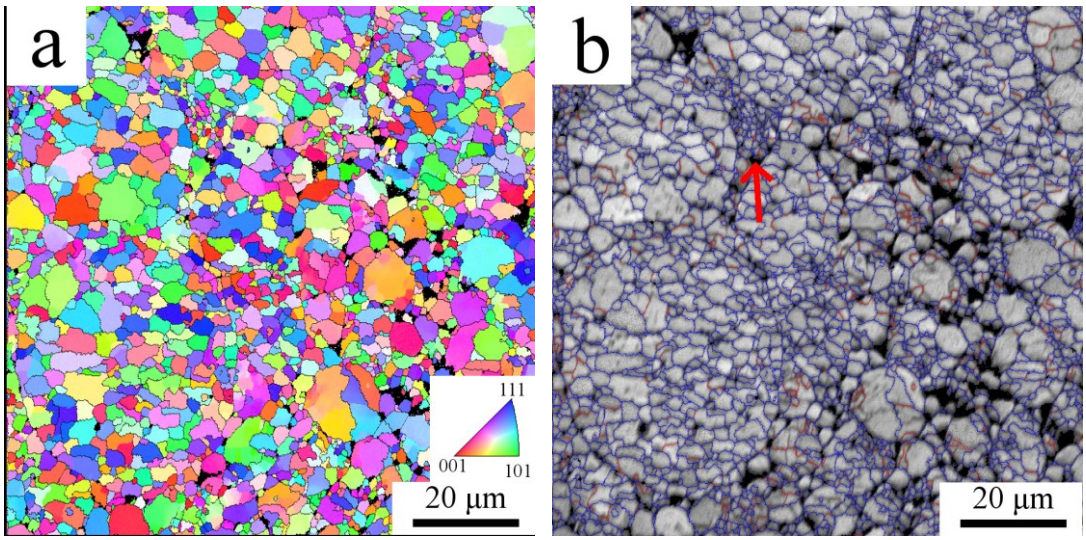

Figure 36. The results of EBSD investigation of the Al7075Zr_AC compact: a) orientation image figure with HAGBs in black, b) the distribution of grain boundaries, HAGBs in blue and LAGBs in red.

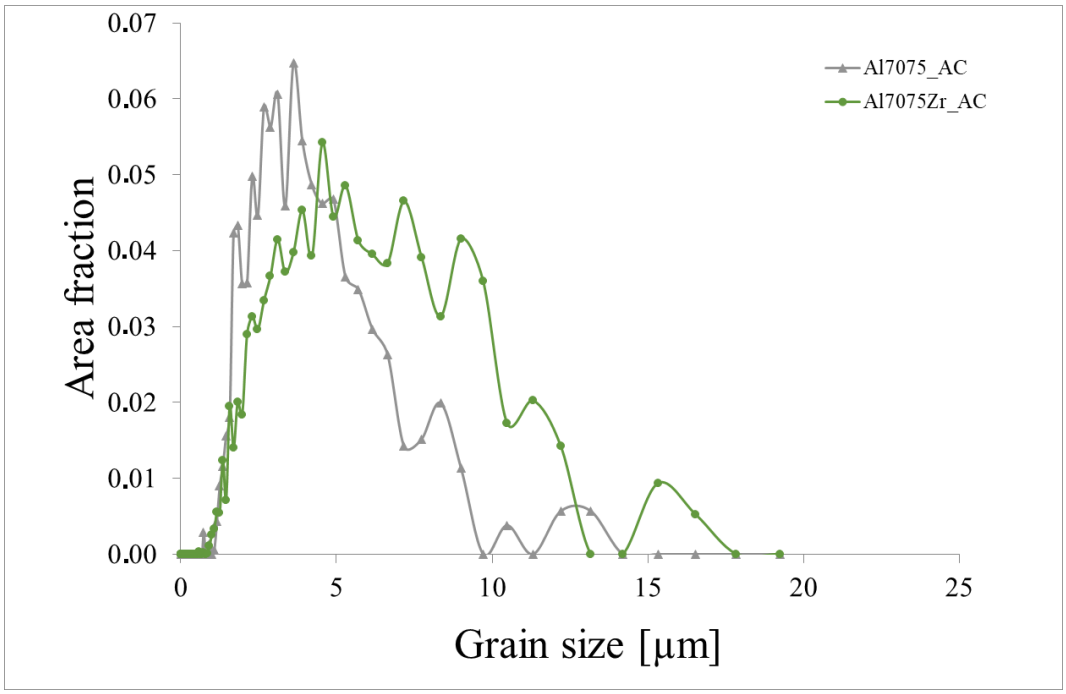

Figure 37. The distribution of grain sizes in compacts sintered from gas atomized powders.

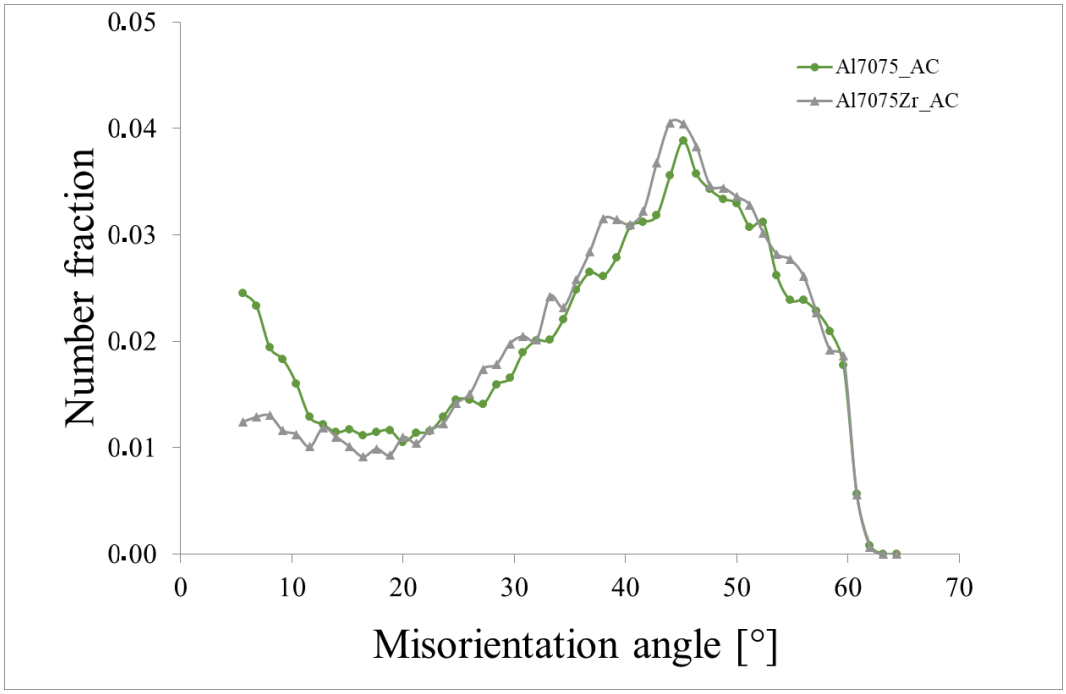

Figure 38. The distribution of misorientation angles in compacts sintered from gas atomized powders.

The microstructural changes caused by the SPS process were reflected also in the evolution of microhardness. The microhardness of both compacts was found to be higher compared to the values measured for the corresponding gas atomized powder,

151 ± 3 HV and 171 ± 6 HV for the Al7075_AC and Al7075Zr_AC compacts, respectively (see also Table 8).

3.4. Spark plasma sintered compacts from milled powders

Powders milled in attritor were compacted at 425 °C for 4 min with 80 MPa using a SPS 10-4 device, similar to that used to sinter the gas atomized powder. Compacts will be further denoted with a sign derived from the mark of powder material by changing the MP in their sign to MC. SPS led to dense compacts with a porosity below 1 vol% in each case as determined from image analysis of SEM micrographs (taken on samples polished up to 1 μm).

The microstructure of all compacts was investigated by SEM-BSE method and the materials milled for 3 hours were selected for comparison (Figure 39). The rests of original cellular microstructure observed in the powder milled at RT with 180 RPM were also retained in the Al7075_MC_RT_3_180 compact (Figure 39a). The boundaries of original powder particles are decorated by precipitates of the size of several hundreds of nm. Much finer precipitates are located in the interior of original powder particles. Figures 39b and c document an increasing fraction and size of precipitates in the Al7075_MC_LN_3_180 and Al7075_MC_RT_3_400 compacts, i.e. in materials previously milled at decreased temperature or at higher RPM. Curved strips containing finer precipitates are encompassed by larger second phase particles with a size close to 1 μm. The microstructure of the Zr-containing Al7075Zr_MC_RT_3_400 compact is much more homogeneous, curved strips of coarser precipitates can be rarely seen and the size of these coarser precipitates is slightly lower (around 0.5 μm) (Figure 39d).

The changes in phase composition induced by SPS were investigated by XRD. Only the presence of η and S phases in case of material without Zr addition was detected. The compacts sintered from milled Al7075Zr powder were found to contain beside η phase also Al_3Zr. The results of Rietveld analysis are summarized in Table 9. A remarkably increased weight fraction of the η particles up to nearly 6 wt% was observed. It seems that the weight fraction of this phase increases with increasing intensity of milling, i.e. especially with increasing RPM and decreasing milling temperature.

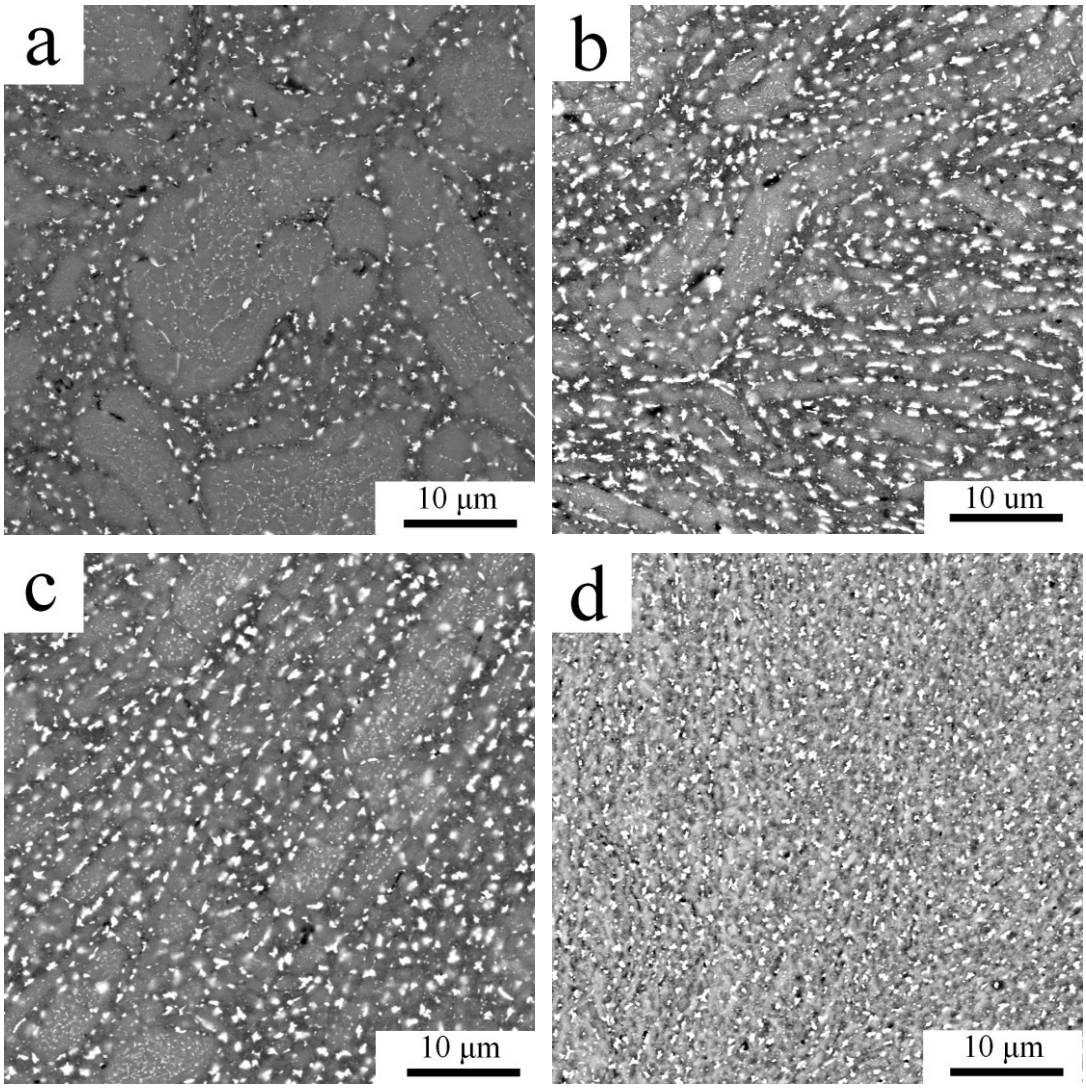

Figure 39. The microstructure of SPS compacts from powders milled in attritor at different parameters: a) Al7075_MC_RT_3_180, b) Al7075_MC_LN_3_180, c) Al7075_MC_RT_3_400, d) Al7075Zr_MC_RT_3_400, SEM-BSE.

Figures 40 and 41 compare XRD patterns of selected compacts prepared from attritor milled powders with those prepared from gas atomized powders. The figures present graphically the increased weight fraction of second phases in compacts prepared from milled powders.

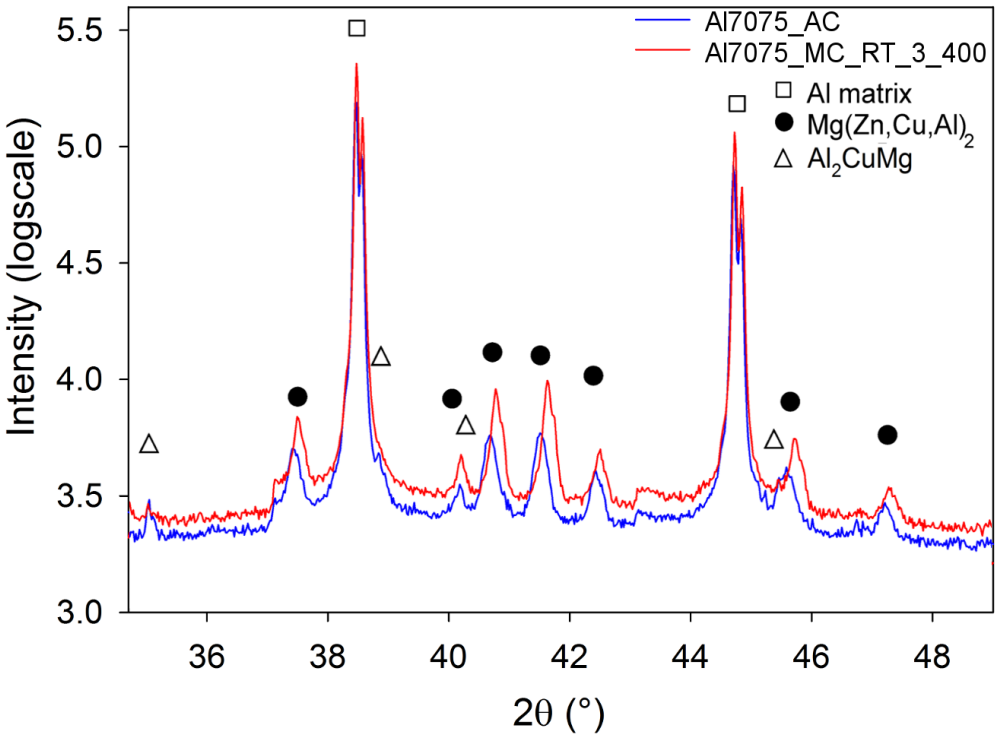

Figure 40. The comparison of XRD patterns of the Al7075_AC compact prepared from gas atomized powder and the Al7075_MC_RT_3_400 compact prepared from a powder milled in attritor.

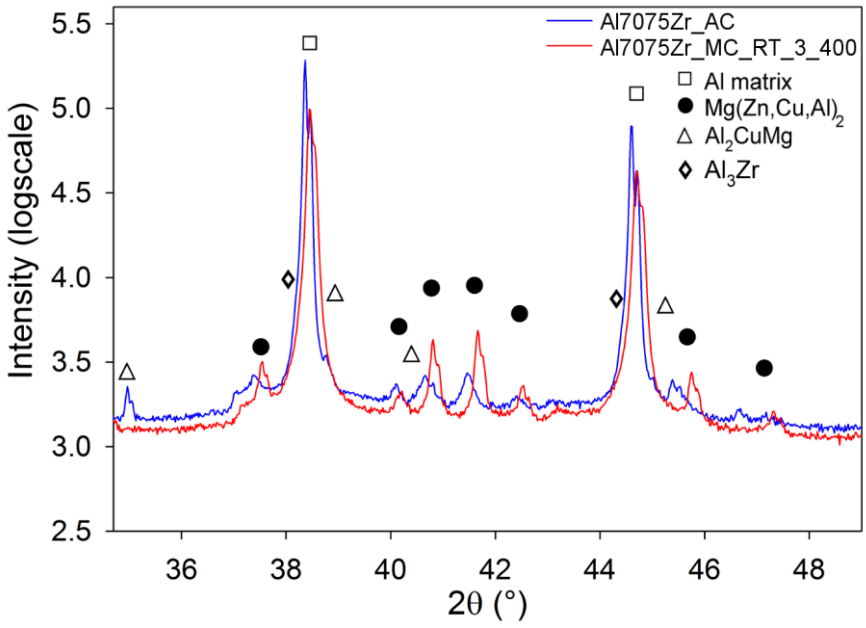

Figure 41. The comparison of XRD patterns of the Al7075Zr_AC compact prepared from gas atomized powder and the Al7075Zr_MC_RT_3_400 compact prepared from a powder milled in attritor.

The compacts' grain structure was studied by EBSD measurement. Figure 42 a-f shows the orientation image maps for the same SPS compacts as in Figure 39, i.e. for compacts prepared from powders milled for 3 hours at different conditions. The non-homogeneous microstructure of SPS compacts presented in Figure 39 is reflected also in the grain size distribution. The largest non-homogeneity was observed in the Al7075_MC_RT_3_180 compact prepared from the powder milled with the lowest intensity. The rests of original cellular microstructure are still recognizable, see the right upper corner of Figures 42a, where the size of some grains exceeds even 10 μm. Other places containing much finer grains of the size close to 1 μm were also observed. Increasing intensity of milling (lower milling temperature in Figure 42c or higher RPM in Figure 42e) results in the formation of curved strips of coarser grains with the size up to 5 μm encompassed by fine grained regions. The microstructure of the Zr-containing compact is very homogeneous with most grains of the size slightly below 1 μm. The average grain sizes evaluated from orientation image micrographs are summarized in Table 9. The differences among different compacts are relatively small, however, there are differences in the distribution of grain sizes (Figure 43). As already mentioned above the microstructure homogeneity increases with increasing intensity of milling. The Al7075_MC_RT_3_180 compact prepared from the powder milled with the lowest intensity exhibits a broad distribution of grain sizes and numerous coarser grains. Much narrower distribution and only very scarce larger grains were observed in the Al7075_MC_RT_8_400 compact prepared from the powder milled with the highest intensity. A positive influence of Zr can also be observed. The Al7075Zr_MC_RT_3_400 compact contains only fine grains with a size below 2 μm.

Figures 42 documents that most grains are divided by high-angle grain boundaries. The distributions of misorientation angles for all compacts prepared from powders milled in attritor are shown in Figure 44. It is evident that there are no significant differences in the distribution of misorientation angles in selected compacts. The distributions are almost identical with the distribution for random misorientation of grains in cubic materials [209], showing on no directionality caused by the pressure during SPS. The fraction of high-angle boundaries was determined to be between 92 and 95% in all studied compacts.

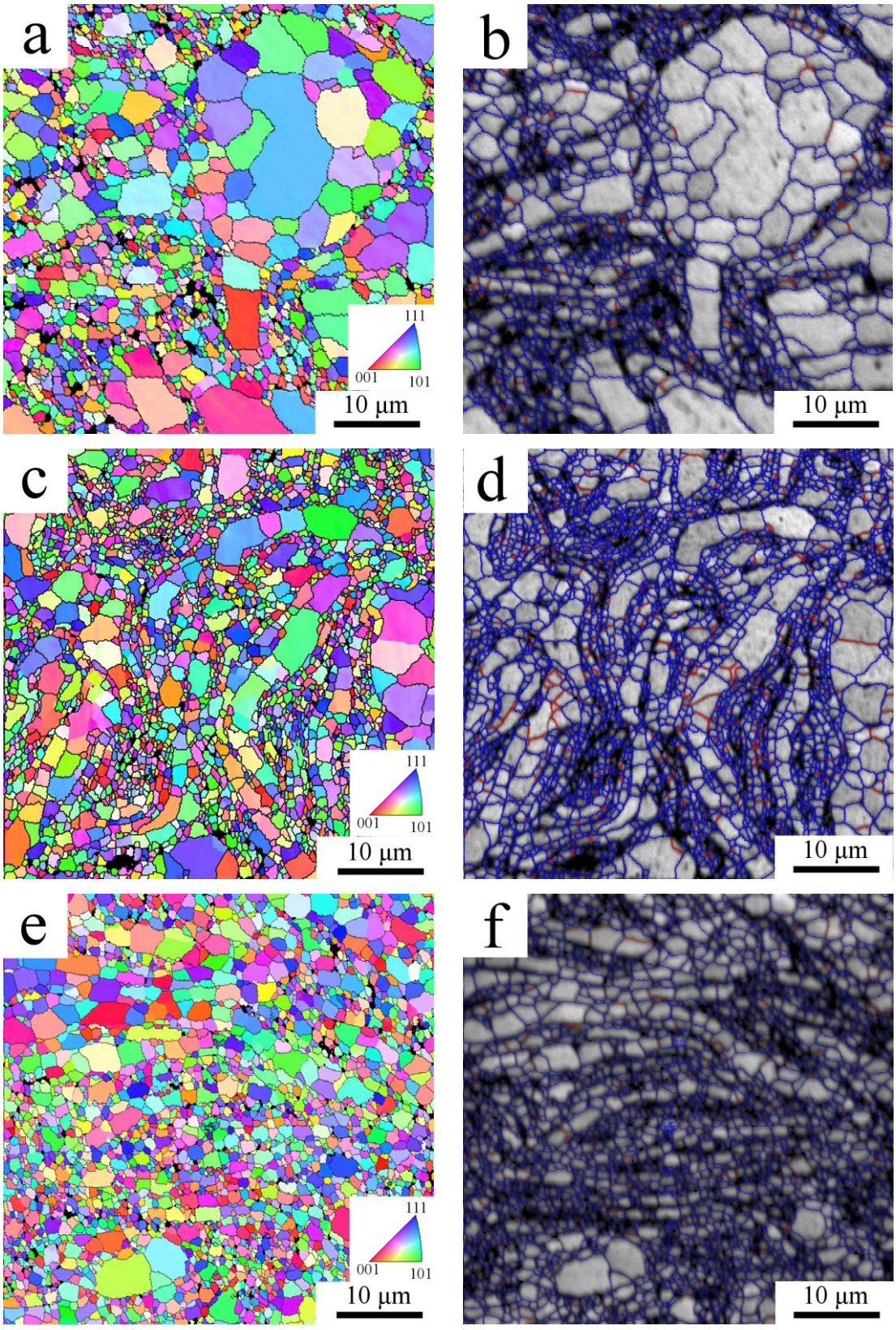
a
111
001
101
10 μm
b
10 μm
c
111
001
101
10 μm
d
10 μm
e
111
001
101
10 μm
f
10 μm

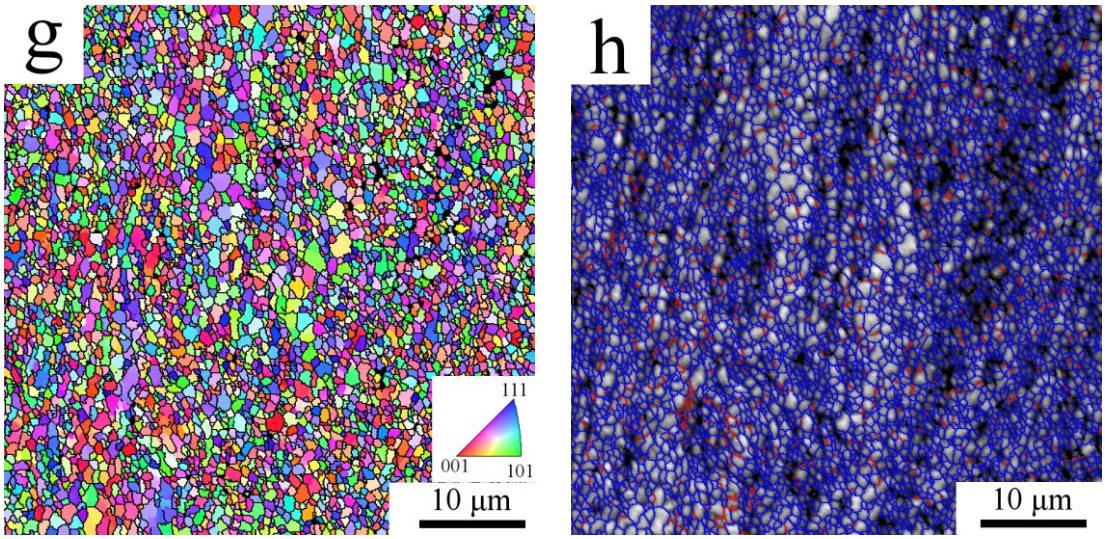

Figure 42. The orientation image micrographs and distribution of grain boundaries (HAGBs in blue and LAGBs in red) of SPS compacts from powders milled in attritor at different parameters: a,b) Al7075_MC_RT_3_180, c,d) Al7075_MC_LN_3_180, e,f) Al7075_MC_RT_3_400, g,h) Al7075Zr_MC_RT_3_400.

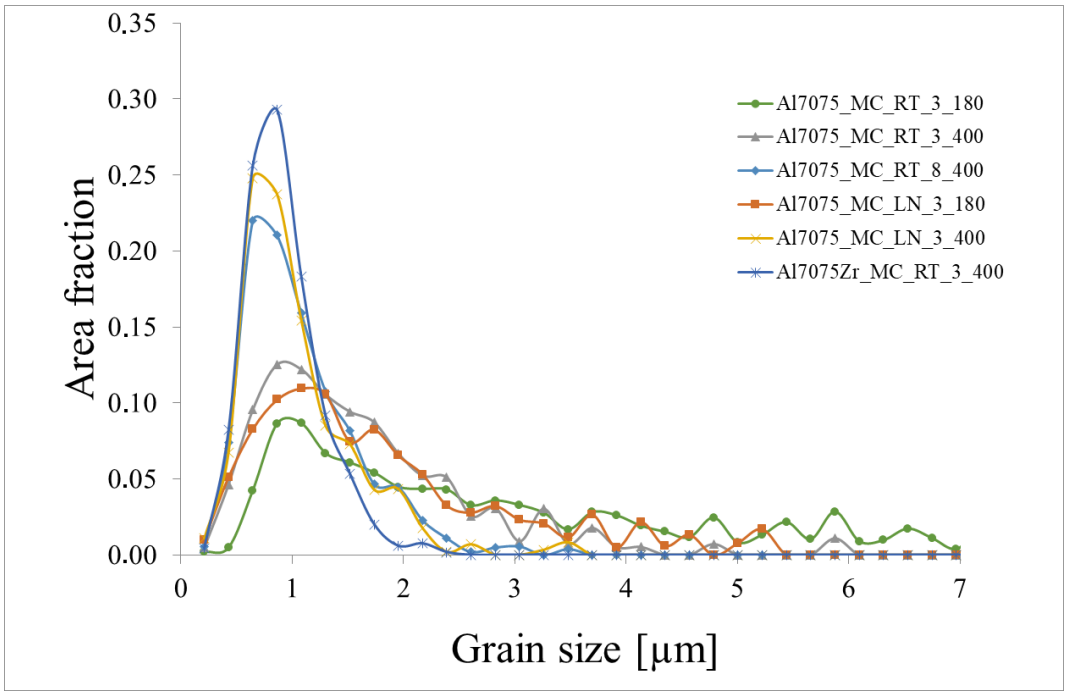

Figure 43. The distribution of grain sizes of compacts sintered from powders milled in attritor.

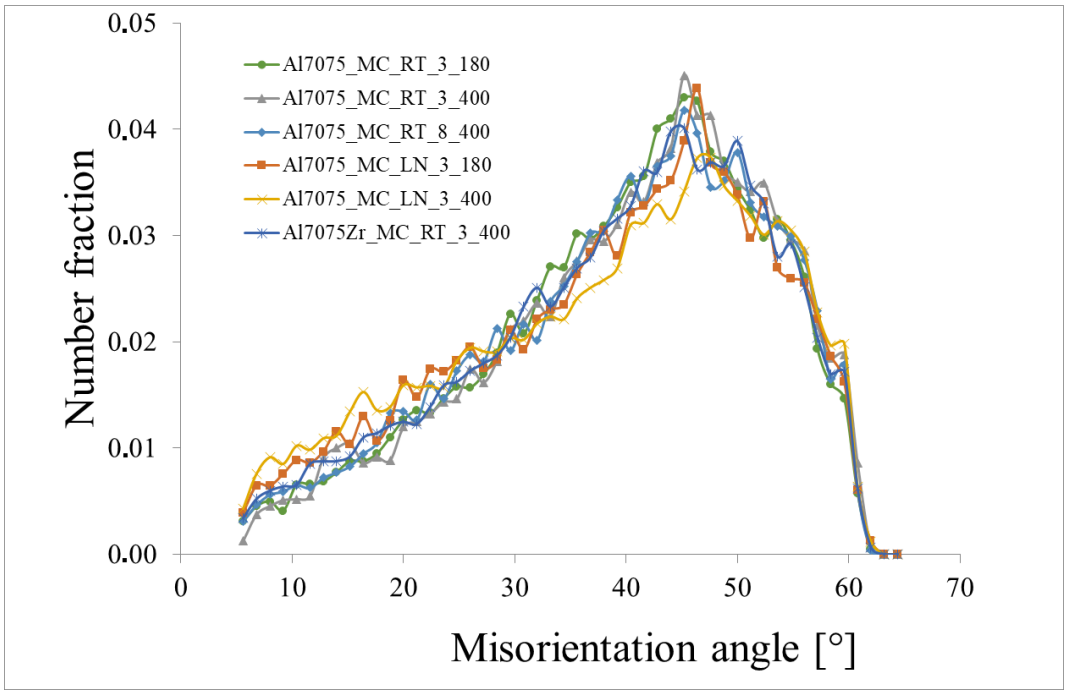

Figure 44. The distribution of misorientation angles of compacts sintered from powders milled in attritor.

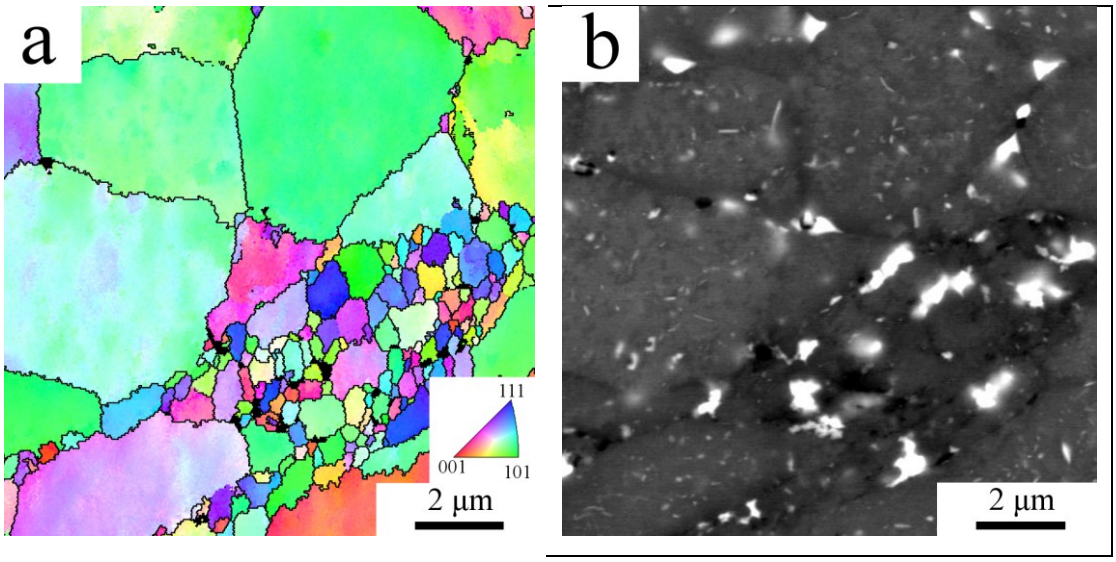

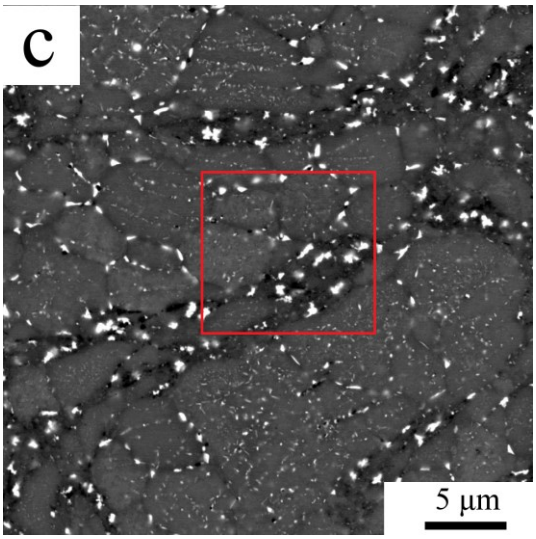

Figure 45. Correlation between the distribution of second phase particles and grains for sample Al7075_MC_RT_3_180: a) orientation image micrograph with HAGBs in black, b) the corresponding SEM-BSE figure, and c) the investigated area in lower magnification.

Due to the non-homogeneous distributions of second phase particles (Figure 39) and grain sizes (Figure 42) a new EBSD investigation was carried out to correlate the position of second phase particles and grains of different sizes. The Al7075_MC_RT_3_180 compact was chosen for this experiment. Figure 45a displays the orientation image micrograph of a selected area (Figure 45b). Figure 45c displays the investigated are in lower magnification, where it is highlighted by red square. A comparison of figures makes clear, that the large grains belong to cellular-like areas which seem to be remained from the slightly deformed gas atomized powder. The area with small grains can be correlated with the area of large irregularly shaped second phase particles. Similar distribution of small grains is expected to occur also in other compacts prepared from powder milled in attritor.

The results of microhardness measurements are summarized in Table 9. Values close to 120 HV were found in all compacts of Al7075 alloy, within the experimental error independent of the milling parameters. The microhardness of the Zr containing compact is higher – close to 140 HV. Comparison of microhardness values measured in SPS compacts with those for corresponding milled powders (Table 6) shows that SPS resulted in a drop of microhardness. This behaviour is opposite to compacts prepared from atomized powders where SPS resulted in an increase in microhardness (Table 4 and 8). Further, the microhardness measured for the compacts

prepared from the powders milled in attritor are below those measured in the compacts prepared from the gas atomized powders (Table 8).

	$Mg(Zn,Cu,Al)_2$ [wt%]	Al_3Zr [wt%]	Al_2CuMg [wt%]	d [μm]	HV
Al7075_MC_RT_3_180	3.6 ± 0.1			3.0 ± 0.9	125 ± 6
Al7075_MC_RT_3_400	5.0 ± 0.2			1.7 ± 0.5	122 ± 3
Al7075_MC_RT_8_400	5.6 ± 0.3			1.1 ± 0.4	118 ± 4
Al7075_MC_LN_3_180	4.0 ± 0.2		1.2 ± 0.1	1.9 ± 0.6	123 ± 6
Al7075_MC_LN_3_400	5.7 ± 0.3			1.1 ± 0.3	129 ± 5
Al7075Zr_MC_RT_3_400	3.6 ± 0.2	1.2 ± 0.1		0.9 ± 0.3	139 ±5

Table 9. Comparison of weight content of different second phases, average grain size, and microhardness of compacts prepared from powders milled in attritor.

Planetary ball milled powders, Al7075_MP_RT_8_400P and Al7075Zr_MP_RT_8_400P were compacted by SPS at 425 °C for 4 minutes with 80 MPa using a SPS 10-4 device. Both compacts exhibited extremely low porosity, 0.4 vol% in the Al7075_MC_RT_8_400P and 0.16 vol% in the Al7075Zr_MC_RT_8_400P compacts as determined by image analysis of SEM micrographs.

Figures 46 and 47 show the microstructure of both compacts in SEM-BSE contrast. The compacts microstructure is homogeneous, except the contaminating particles containing Ni and Ti (Figures 46a and 47a). As mentioned in Section 3.2., these Ni and Ti rich particles were introduced into the powder during its milling from the milling jar. At higher magnification (Figures 46b and 47b), precipitates of two size scales can be distinguished. Precipitates with a size up to 1 μm alternate with much smaller ones. SEM-EDS mapping, performed on the Al7075Zr_MC_RT_8_400P compact showed the presence of Zn, Mg and Cu in the larger precipitates (Figure 48). The composition of the smaller second phase particles could not be stated by SEM-EDS due to their small size.

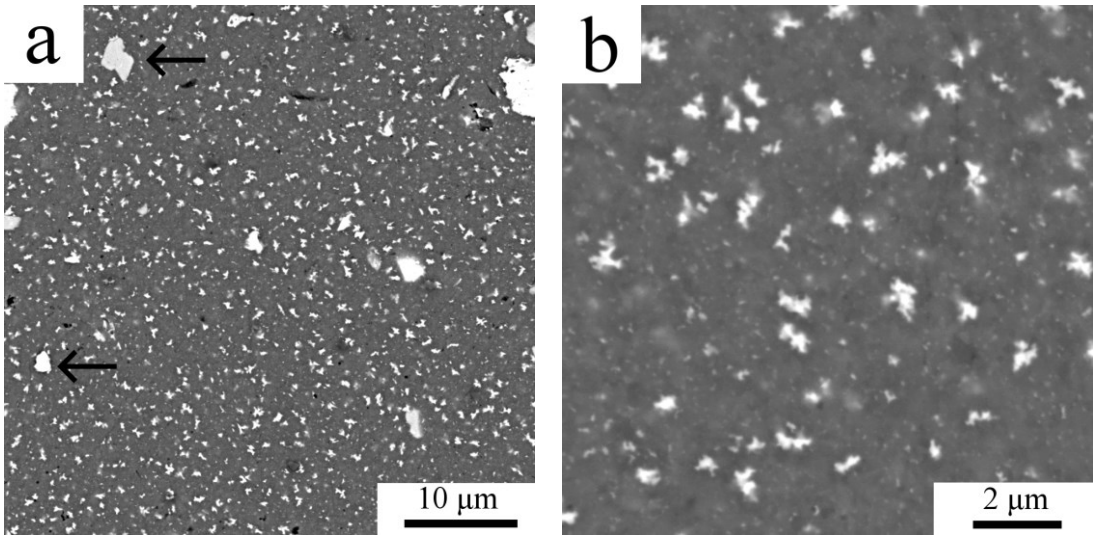

Figure 46. The microstructure of the Al7075_MC_RT_8_400P compact prepared from the planetary ball milled powder: a) overview, b) its detail, SEM-BSE.

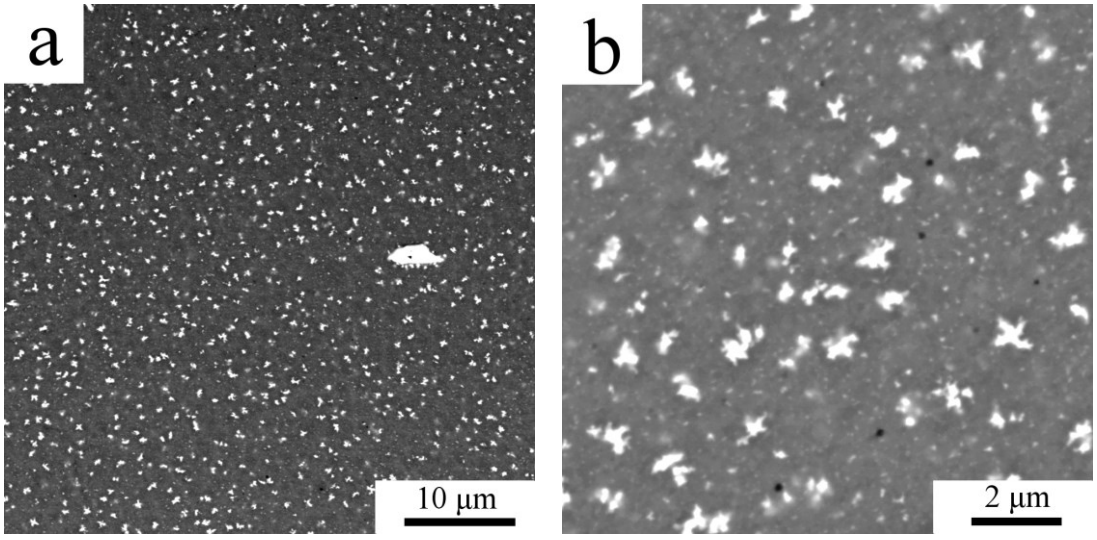

Figure 47. The microstructure of the Al7075Zr_MC_RT_8_400P compact prepared from the planetary ball milled powder: a) overview, b) its detail, SEM-BSE.

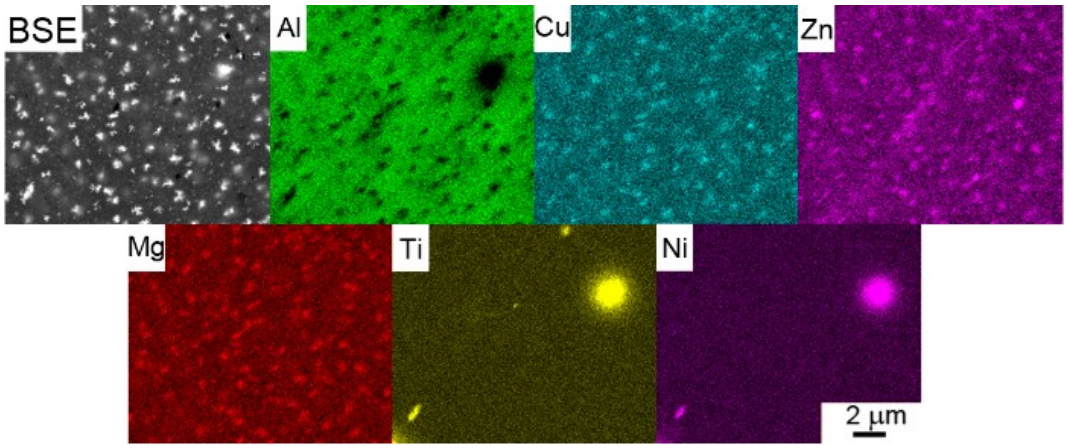

Figure 48. Element distribution in the Al7075Zr_MC_RT_8_400P compact, SEM-BSE figure and the corresponding SEM-EDS maps.

The microstructure was studied in more details by TEM. The microstructure of the Al7075_MC_RT_8_400P compact consists of fine equiaxed grains alternating with relatively large second phase particles between the individual grains (Figure 49a). The second phase particles become better visible in STEM-HAADF showing mainly Z contrast (Figure 49b). This investigation revealed, that beside the large, several hundred nm sized second phase particles along grain boundaries, also finer, several tens of nm sized second phase particles are present inside the grains.

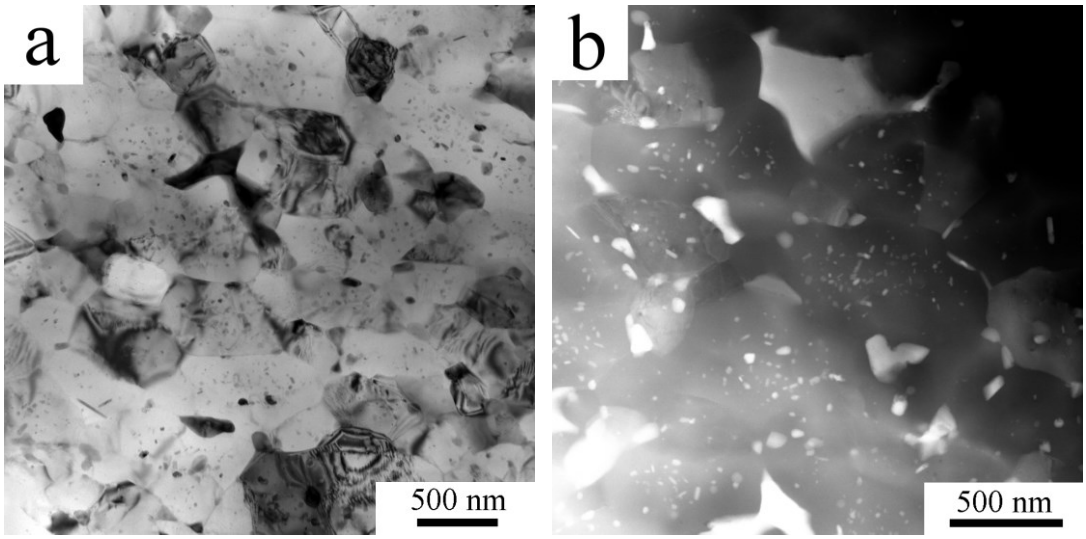

Figure 49. The microstructure of the Al7075_MC_RT_8_400P compact prepared from the planetary ball milled powder: a) TEM-BF, b) STEM-HAADF.

A homogeneous microstructure and fine equiaxed grain structure was observed in the Al7075Zr_MC_RT_8_400P compact (Figure 50a). Beside the large second

phase particles between the grains and the smaller ones inside the grains, also nm sized Al_3Zr particles with $L1_2$ structure (determined from electron diffraction – see the inset in Figure 50b) inside grains were found (Figure 50b). STEM investigation also revealed a semicontinuous MgO layer present along boundaries of former powder particles, as presented on STEM-EDS maps in Figure 51 for the Al7075Zr_MC_RT_8_400P compact. Precipitates, visible on the STEM figure on Figure 51 were identified by spot TEM-EDS measurement to be most probably Al_3Zr, $MgZn_2$ and Al_2CuMg phase.

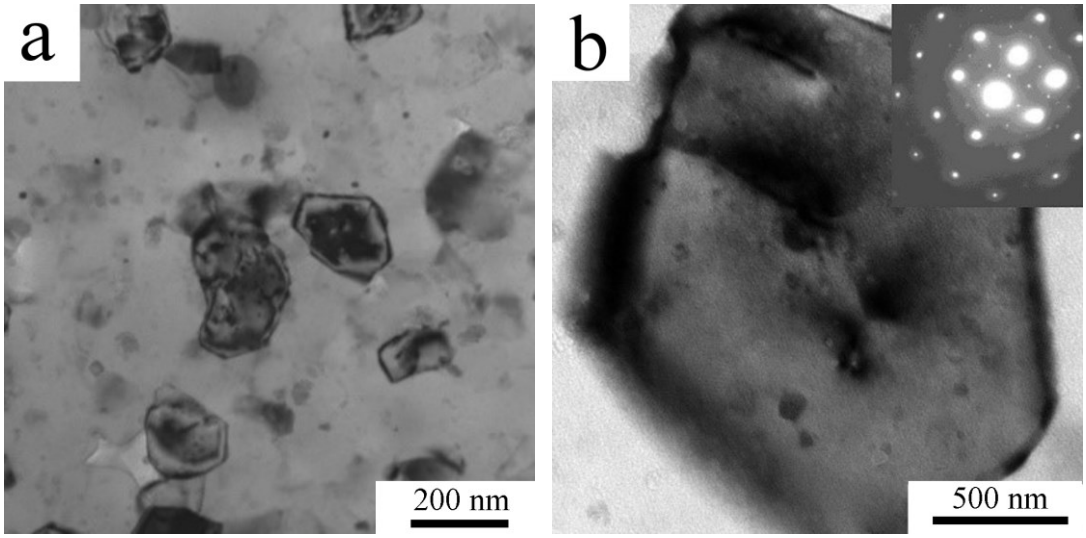

Figure 50. The microstructure of the Al7075Zr_MC_RT_8_400P compact prepared from the planetary ball milled powder: a) overview, b) its detail, TEM-BF.

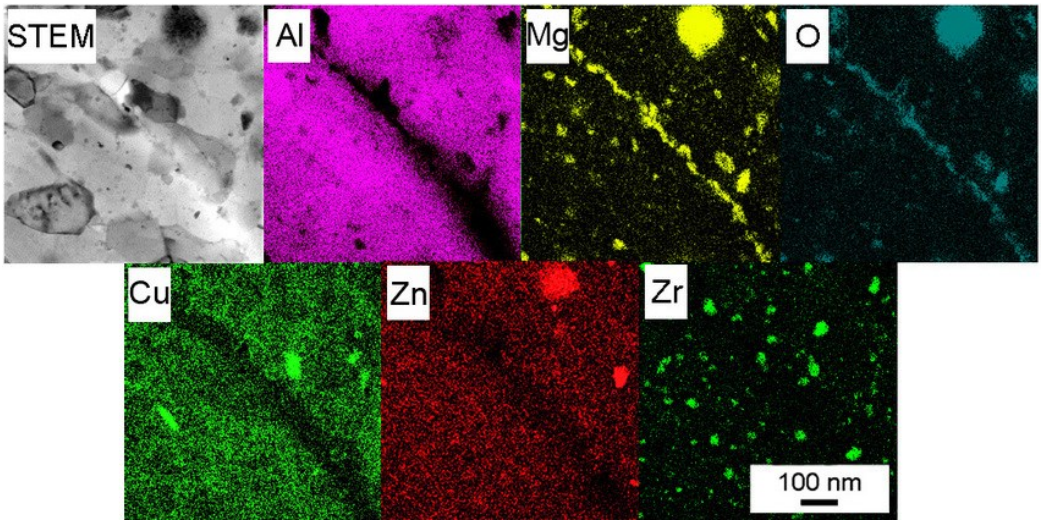

Figure 51. STEM image of the MgO layer observed in the Al7075Zr_MC_RT_8_400P compact and the corresponding STEM-EDS maps.

The phase composition of compacts prepared from planetary ball milled powders was studied by XRD. Similarly to compacts prepared from powders milled in attritor, an increase in wt% of the η phase was observed in comparison with the corresponding milled powders (Figures 52 and 53). Additionally, the S phase was detected in Al7075_MC_RT_8_400P compact and the Al_3Zr phase was found in the Zr-containing compact. Results of Rietveld analysis of XRD pattern are listed in Table 10.

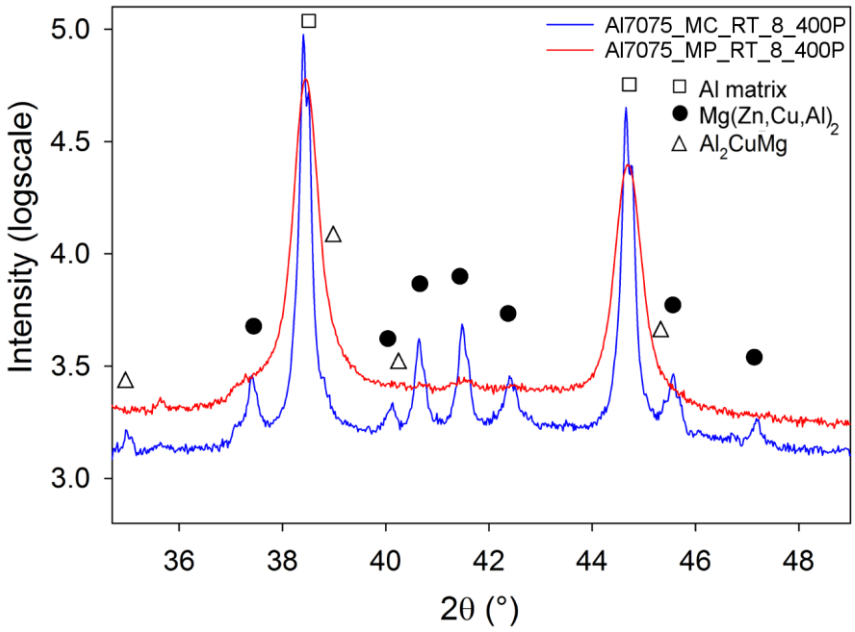

Figure 52. Comparison of XRD pattern of the Al7075_MC_RT_8_400P compact and the corresponding Al7075_MP_RT_8_400P powder.

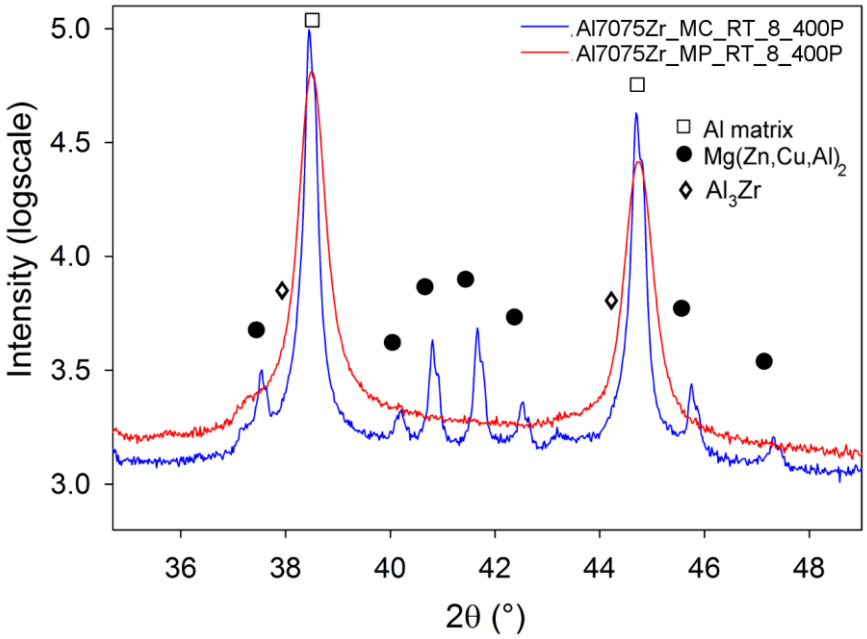

Figure 53. Comparison of XRD pattern of the Al7075Zr_MC_RT_8_400P compact and the corresponding Al7075Zr_MP_RT_8_400P powder.

The compacts' grain structure was studied by EBSD measurement. Figures 54 and 55 show very fine grain sizes in both compacts. The Zr-containing compact exhibits a smaller grain size (0.34 ± 0.09 μm) than the compact without Zr (0.55 ± 0.24 μm) (Table 10). Comparing to the grain sizes of the corresponding milled powders (Table 7) it is visible, that SPS resulted in grain coarsening. Nevertheless, the grain sizes determined for these compacts remain in the sub-microcrystalline range and are below those measured in compacts prepared from powders milled in attritor (Table 9) or gas atomized powders (Table 8). Figure 56 presents the distribution of grain sizes in both compacts prepared from planetary ball milled powders. This distribution is very narrow in both samples. No grains with the size exceeding 0.6 μm were detected in the selected field in the Zr-containing compact. Figures 54b show, that most grains are divided by high-angle grain boundaries. The fraction of HAGBs is around 90% in both compacts. Figure 57 shows, that the misorientation angles distribution is very similar in both compacts. Similarly to the compacts described previously, it is almost identical with the distribution function for random misorientation of grains in cubic materials [209], showing on no directionality caused by the pressure during SPS.

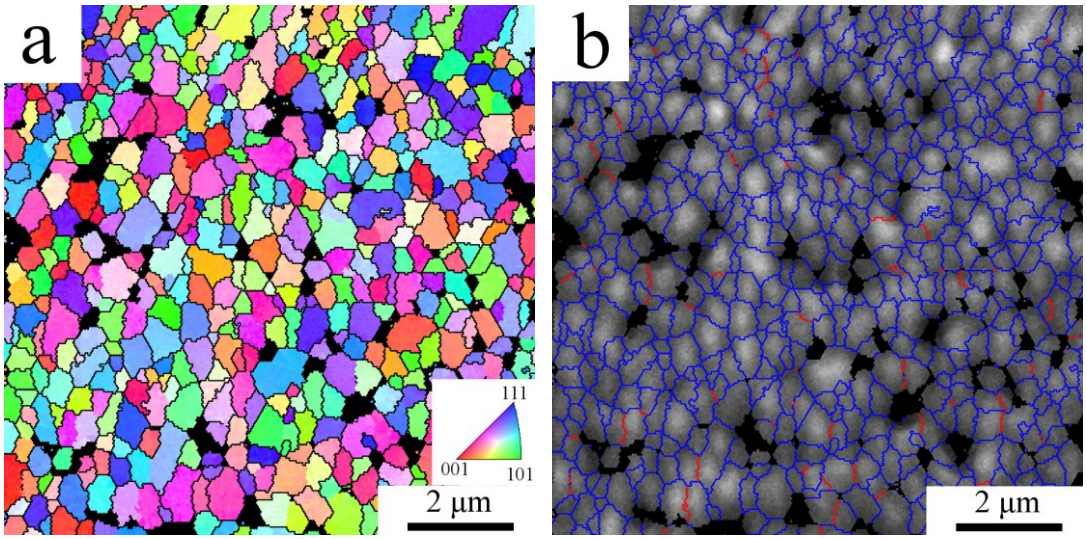

Figure 54. The results of EBSD investigation of the Al7075_MC_RT_8_400P compact: a) orientation image figure with HAGBs in black, b) the distribution of grain boundaries, HAGBs in blue and LAGBs in red.

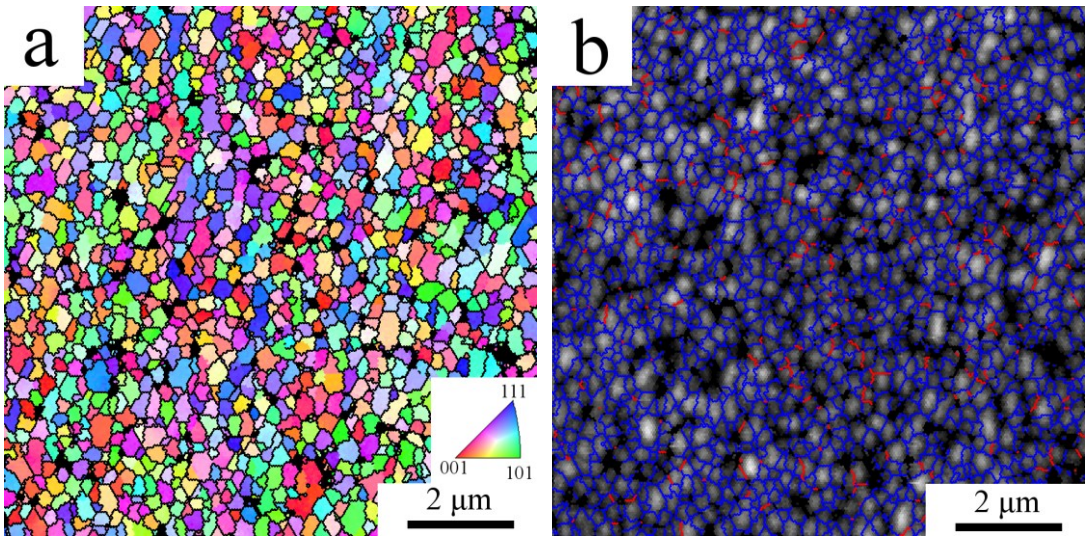

Figure 55. The results of EBSD investigation of the Al7075Zr_MC_RT_8_400P compact: a) orientation image figure with HAGBs in black, b) the distribution of grain boundaries, HAGBs in blue and LAGBs in red.

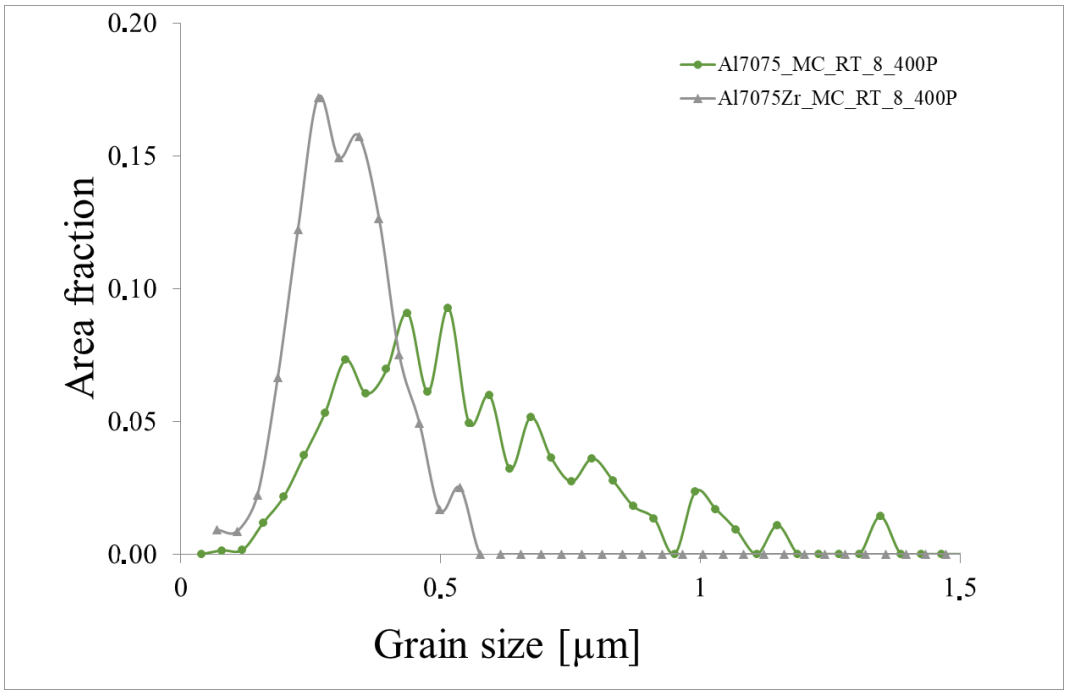

Figure 56. The distribution of grain sizes in compacts sintered from planetary ball milled powders.

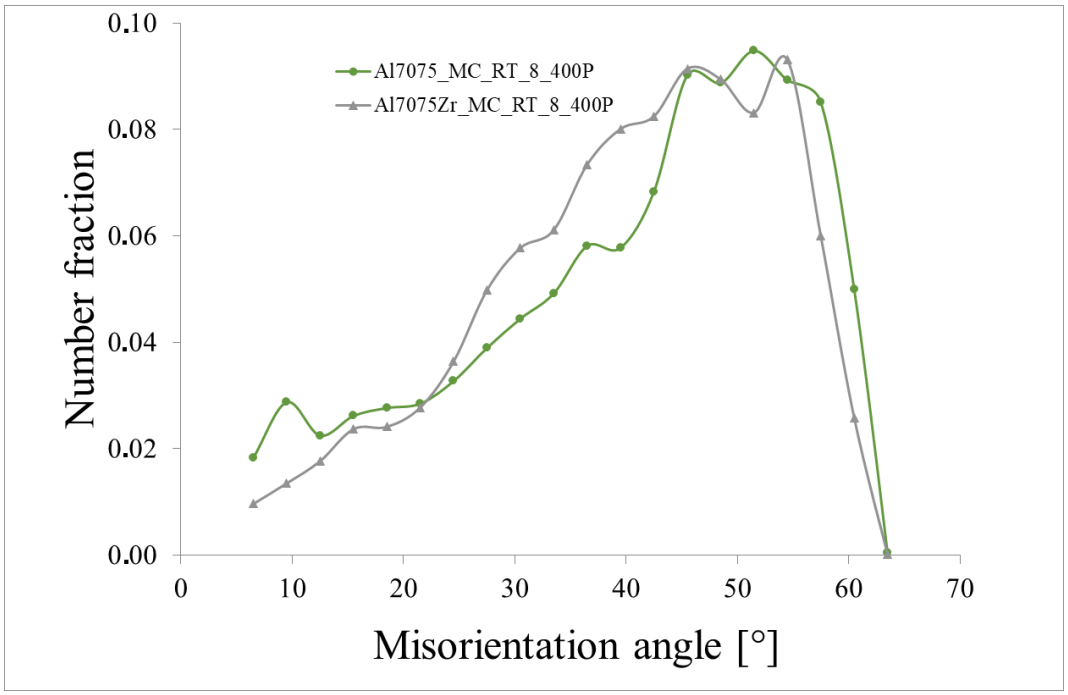

Figure 57. The distribution of misorientation angles in compacts sintered from planetary ball milled powders.

The microhardness exceeding 300 HV which was found in planetary ball milled powders decreased in SPS compacts to values below 200 HV (see Table 10).

Nevertheless, these values are still above those measured for the compact prepared from gas atomized powder or from powder milled in attritor.

	$Mg(Zn,Cu,Al)_2$ [wt%]	Al_2CuMg [wt%]	Al_3Zr [wt%]	d [μm]	HV
Al7075_MC_RT_8_400P	4.5 ± 0.6	1.6 ± 0.2		0.55 ± 0.24	161 ± 7
Al7075Zr_MC_RT_8_400P	3.6 ± 0.5		1.0 ± 0.1	0.34 ± 0.09	195 ± 8

Table 10. Comparison of weight content of second phases, average grain size, and microhardness of compacts prepared from planetary ball milled powders.

3.5. High temperature stability of compacts

As mentioned in the paragraph 1.5.3., exposition of Al7075-based alloys to elevated temperatures can significantly change their phase composition, the size and distribution of strengthening particles, the grain size, and thus also the strength characteristics. Especially a strength drop observed after exposition to temperatures above around 200 °C limits the commercial utilization of these alloys.

The stability of all compact was tested by isochronal annealing for 1 h at 300 and 425 °C followed by water quenching. These temperatures should correspond to regions of overageing (300 °C) and partial dissolution (425 °C). Figures 58 and 59 document the microstructure evolution in the Al7075_AC and Al7075Zr_AC compacts prepared from gas atomized powders due to their heat treatment. The microstructure changes in both compacts are similar. From the SEM-BSE figures it is remarkable, that annealing at 300 °C increased the content of second phase particles (Figures 58b, 59b), whereas annealing at 425 °C led to dissolution of most smaller precipitates and coarsening of some larger particles. A mixture of coarse second phase particles of several μm in size and smaller rod like particles was observed in both materials (Figure 58c, 59c).

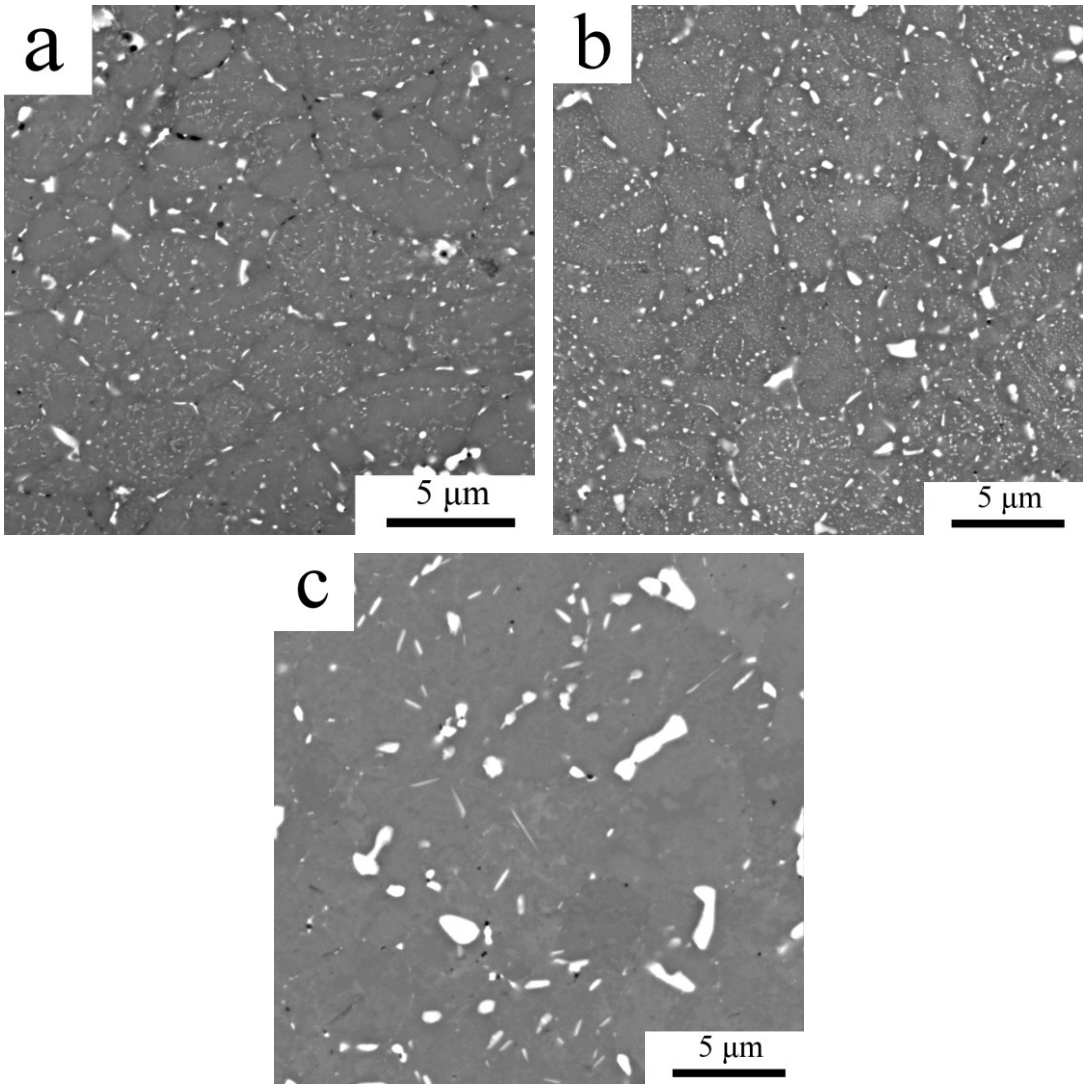

Figure 58. The microstructure of the Al7075_AC compact: a) naturally aged, non-annealed, b) annealed for 1h at 300 °C, c) annealed for 1h at 425 °C, SEM-BSE.

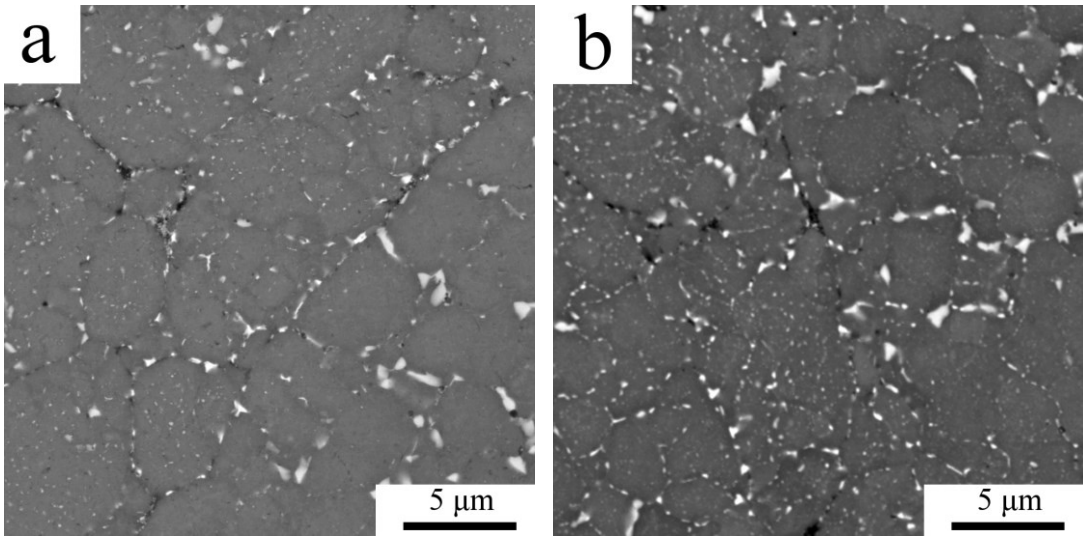

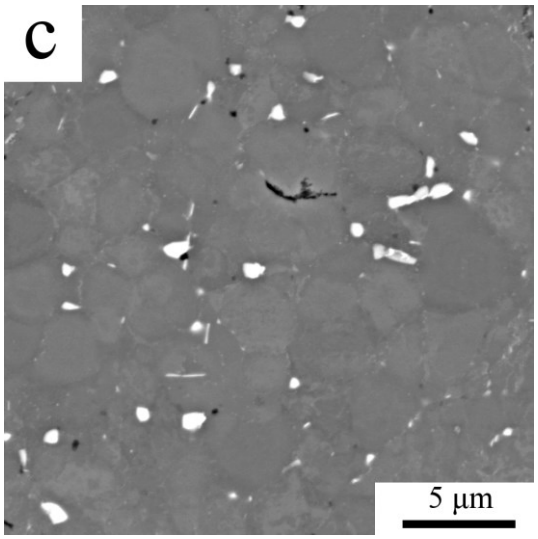

Figure 59. The microstructure of the Al7075Zr_AC compact: a) naturally aged, non-annealed, b) annealed for 1h at 300 °C, c) annealed for 1h at 425 °C, SEM-BSE.

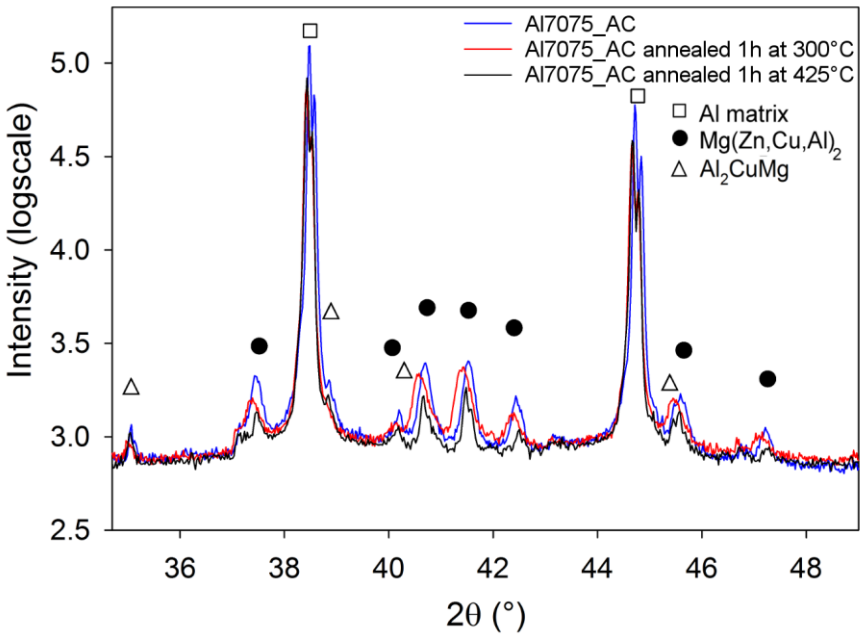

Figure 60. Comparison of XRD patterns of non-heat treated Al7075_AC compact with the patterns of Al7075_AC compact heat treated at 300 and 425 °C.

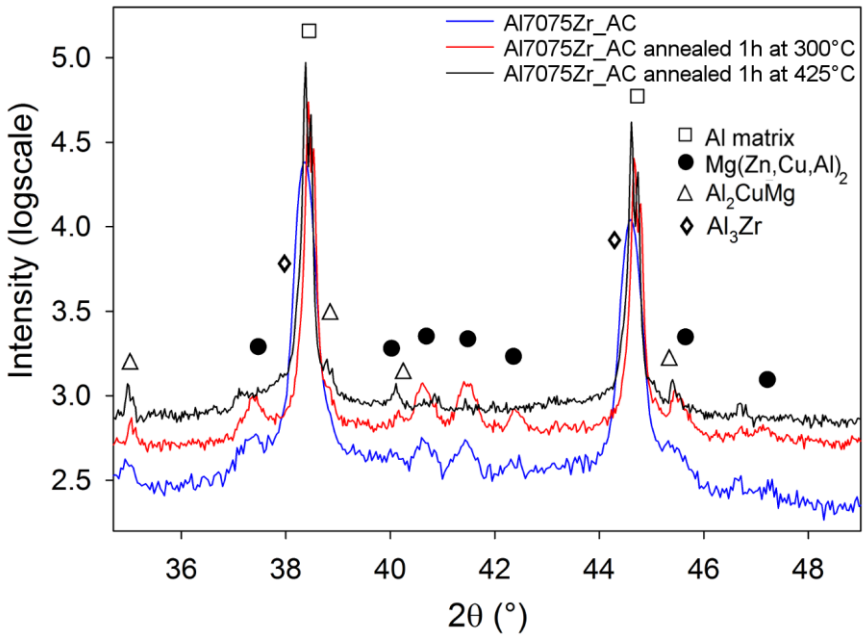

Figure 61. Comparison of XRD patterns of non-heat treated Al7075Zr_AC compact with the patterns of Al7075Zr_AC compact heat treated at 300 and 425 °C.

		$Mg(Zn,Cu,Al)_2$ [wt%]	Al_2CuMg [wt%]	d [μm]	HV
Al7075_AC	Non-annealed	3.7 ± 0.2	0.7 ± 0.2	5.2 ± 1.7	151 ± 3
	1h 300 °C	5.4 ± 0.3	0.9 ± 0.1	4.7 ± 1.5	82 ± 1
	1h 425 °C	1.7 ± 0.1	1.4 ± 0.1	6.1 ± 1.8	125 ± 2
Al7075Zr_AC	Non-annealed	1.4 ± 0.1	1.1 ± 0.2	3.4 ± 1.1	171 ± 6
	1h 300 °C	4.3 ± 0.2	1.2 ± 0.1	3.6 ± 1.2	114 ± 3
	1h 425 °C	0	1.5 ± 0.2	3.8 ± 1.2	172 ± 7

Table 11. The influence of heat treatment on the phase composition, average grain size, and microhardness of SPS compacts prepared from gas atomized powders.

The changes in the compacts phase composition induced by heat treatment were traced by XRD method (Figures 60, 61). The results of Rietveld analysis are listed in Table 11. The results confirmed an increase in the weight fraction of the η phase during annealing at 300 °C. Annealing at 425 °C led to a decrease of the content of η phase. Simultaneously a slight increase in the weight fraction of the S phase was

observed (Table 11). This table summarizes also the values of average grain size determined from orientation image micrographs. It can be seen that the grain size is stable (within a standard deviation) even during annealing at 425 °C. Heat treatment influences significantly the microhardness of both compacts. Relatively high values observed in the naturally aged, non-annealed compacts are reduced during annealing at 300 °C. On the other side, annealing at 425 °C results in a repeated increase in microhardness of both compacts. In the Zr-containing compact, the microhardness of the sample annealed at 425 °C reaches the one observed in the initial non-treated sample.

Based on the results given above, the compacts prepared from milled powders were annealed only at 425 °C in order to study the stability of their grain size and evolution of microhardness. The microstructural changes caused by annealing were very similar in all compacts prepared from powders milled in attritor, independently of the parameters of milling. Figure 62 documents the typical massive redistribution of higher atomic number alloying elements during annealing of the Al7075_MC_LN_3_180 compact prepared from the cryomilled powder. Similar changes can be seen on Figure 63 documenting the evolution of microstructure of Al7075Zr_MC_RT_3_400 sample. The smallest second phase particles seem to be dissolved, whereas the larger ones remained undissolved, some of them grew. XRD analysis (Figure 64 and 65) of annealed compacts was performed only for the two sample presented in Figures 62 and 63. Rietveld analysis showed a decreased content of η phase to values around 2 wt%, whereas S phase was formed in both compacts (content around 1.5 wt%). The wt% of Al_3Zr phase in Al7075Zr_MC_RT_3_400 was found not to be altered by heat treatment, it remained 1.2 wt%. XRD analysis of other heat treated samples was not performed as it can be supposed that the changes in phase composition will be similar to those observed in these compacts.

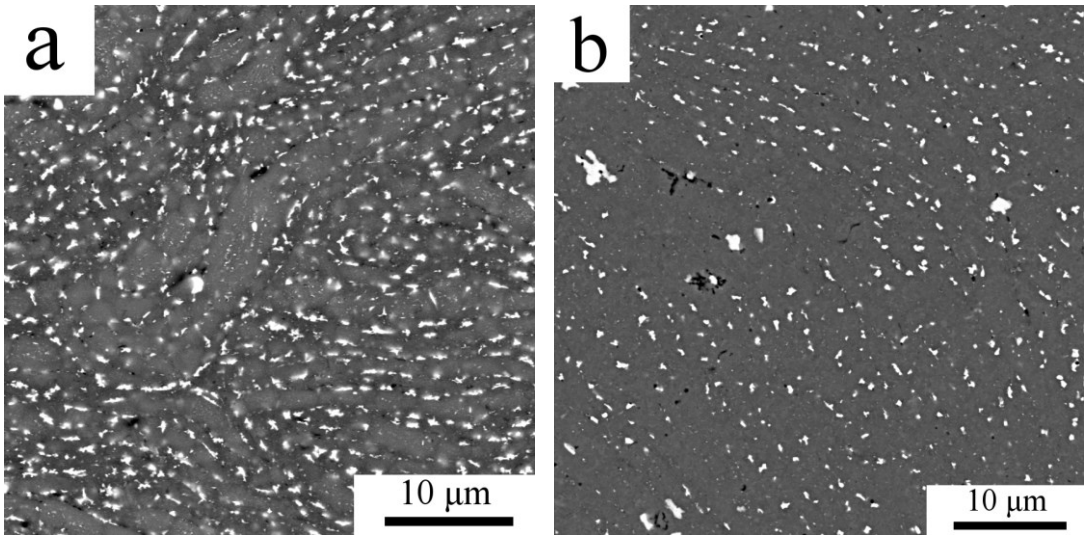

Figure 62. The microstructure of the Al7075_MC_LN_3_180 compact after heat treatment: a) non-annealed, b) annealed for 1h at 425 °C, SEM-BSE.

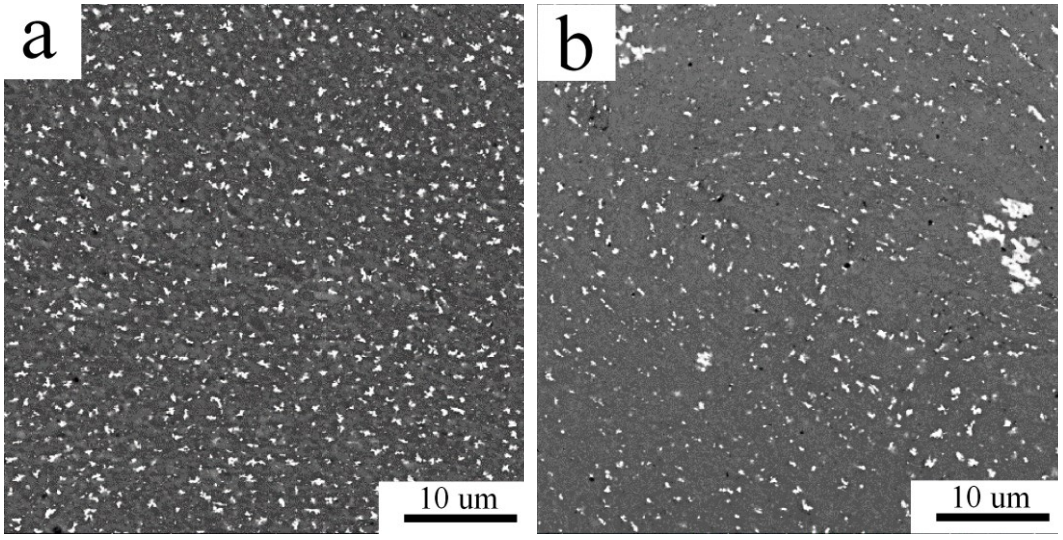

Figure 63. The microstructure of the Al7075Zr_MC_RT_3_400 compact after heat treatment: a) non-annealed, b) annealed for 1h at 425 °C, SEM-BSE.

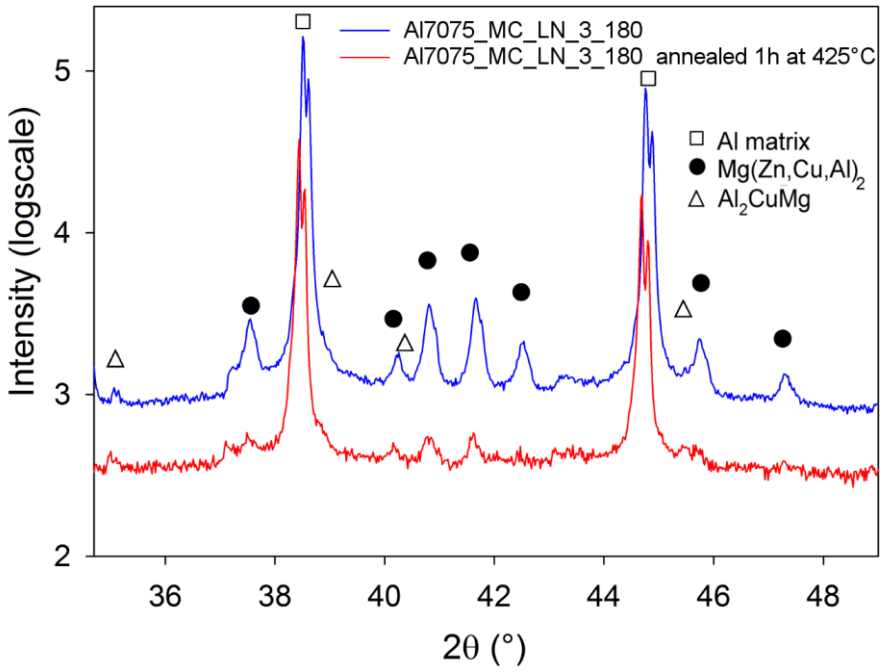

Figure 64. Comparison of XRD pattern of the non-heat treated and annealed (at 425 °C for 1h) Al7075_MC_LN_3_180 compact.

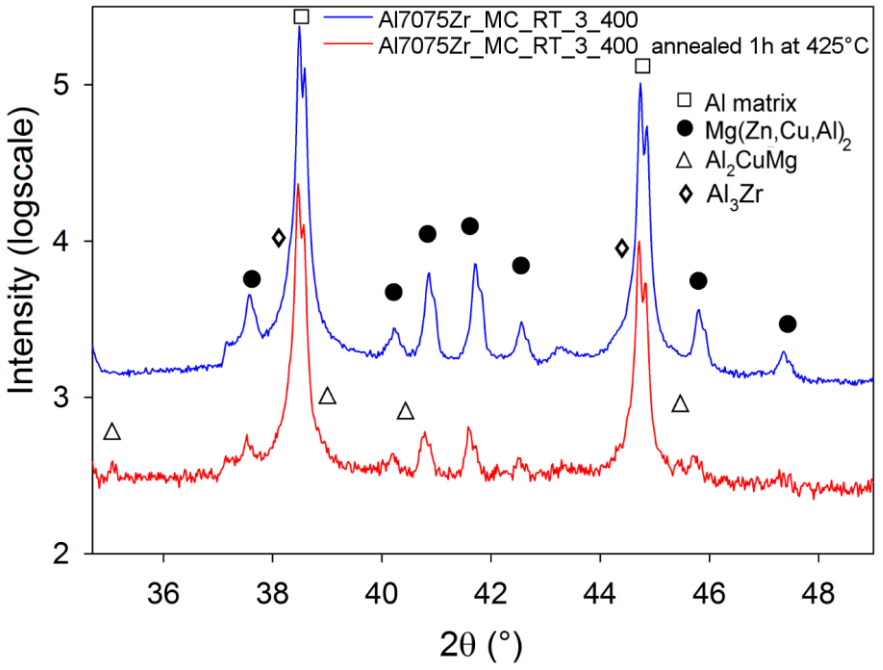

Figure 65. Comparison of XRD pattern of the non-heat treated and annealed (at 425 °C for 1h) Al7075Zr_MC_RT_3_400 compact.

Table 12 summarizes the values of the average grain size determined from EBSD investigation. It can be seen that annealing at 425 °C has no systematic

influence on the grain size and the microcrystalline structure is preserved. The microhardness values determined in compacts of Al7075 alloy annealed at 425 °C are within the standard deviation identical with those of non-annealed compacts.

		d [μm]	HV
Al7075_MC_RT_3_180	non-annealed	3.0 ± 0.9	125 ± 6
	1 h at 425 °C	3.6 ± 2.4	127 ± 4
Al7075_MC_RT_3_400	non-annealed	1.7 ± 0.5	122 ± 3
	1 h at 425 °C	2.0 ± 1.7	129 ± 2
Al7075_MC_RT_8_400	non-annealed	1.1 ± 0.4	118 ± 4
	1 h at 425 °C	1.6 ± 0.8	121 ± 5
Al7075_MC_LN_3_180	non-annealed	1.9 ± 0.6	123 ± 6
	1 h at 425 °C	1.4 ± 0.4	125 ± 3
Al7075_MC_LN_3_400	non-annealed	1.1 ± 0.3	129 ± 5
	1 h at 425 °C	1.3 ± 0.6	130 ± 7
Al7075Zr_MC_RT_3_400	non-annealed	0.9 ± 0.3	139 ±5
	1 h at 425 °C	1.2 ± 0.4	173 ± 4

Table 12. The influence of heat treatment on the average grain size and microhardness of SPS compacts prepared from powders milled in attritor.

The influence of annealing at 425 °C for 1 hour on the microstructure and phase composition of compacts prepared from planetary milled powders was very similar to other SPS compacts. Figures 66a,b and 67a,b document a partial dissolution of precipitates. This was confirmed also by XRD investigation (Figure 68, 69). The analysis of XRD pattern shows a reduction of the content of the η phase, the weight fraction of the S phase is not significantly influenced (Table 13). EBSD investigation revealed no changes in the grain sizes of compacts (Figures 66c,d and 67c,d). The grain size of both Al7075_MC_RT_8_400P and Al7075Zr_MC_RT_8_400P compacts remains stable, deeply below 1 μm. The microhardness values of both compacts are remarkably high and even slightly increased after annealing.

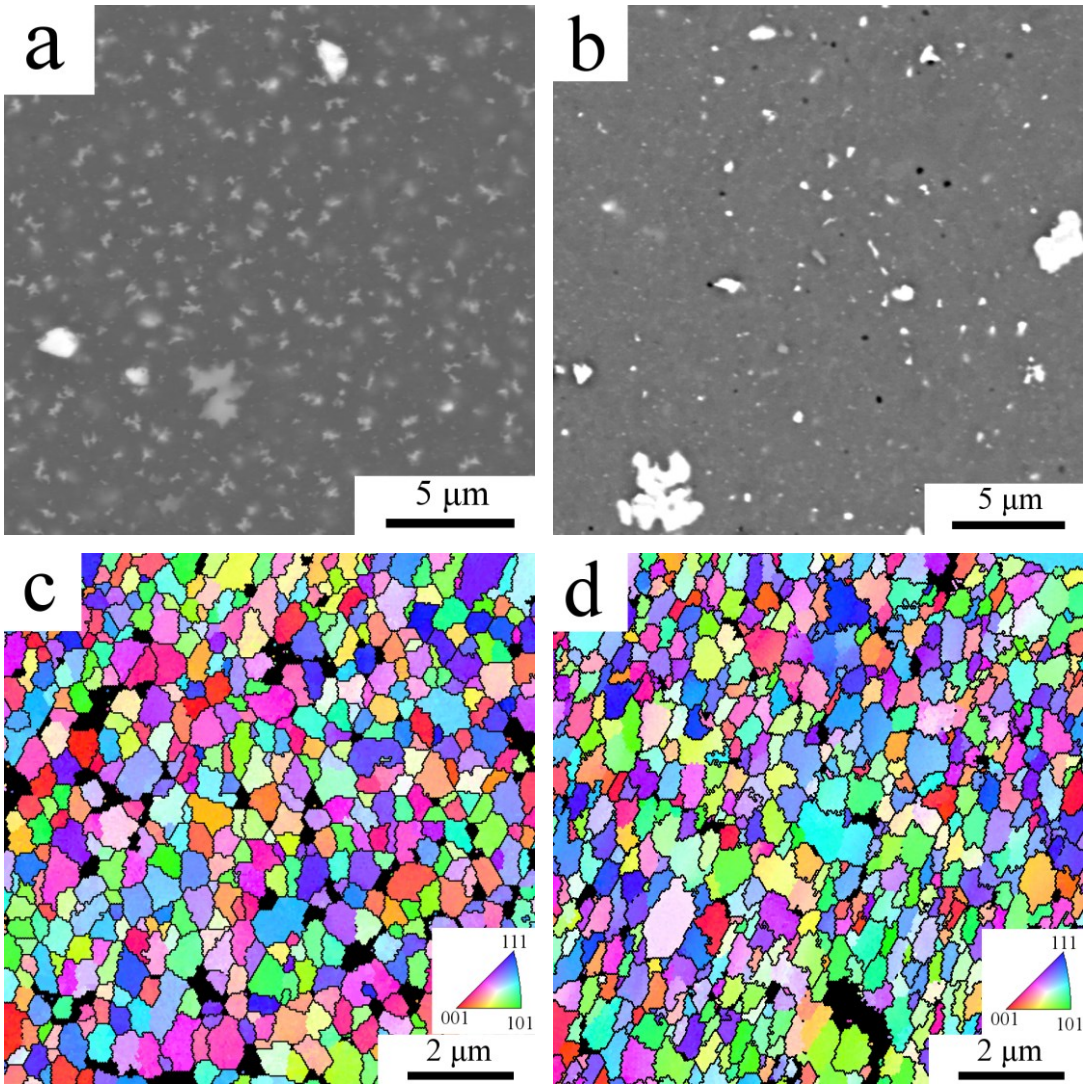

Figure 66. The microstructure of the Al7075_MC_RT_8_400P compact: a) non-annealed, b) annealed for 1 h at 425 °C, SEM-BSE, and the orientation image micrographs of samples with HAGBs in black: c) non-annealed, b) annealed for 1 h at 425 °C.

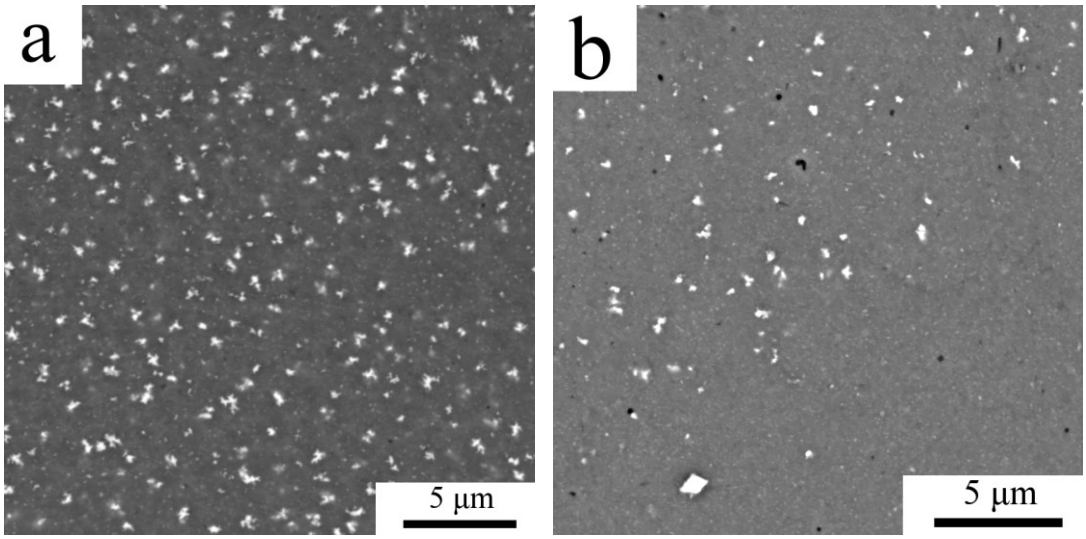

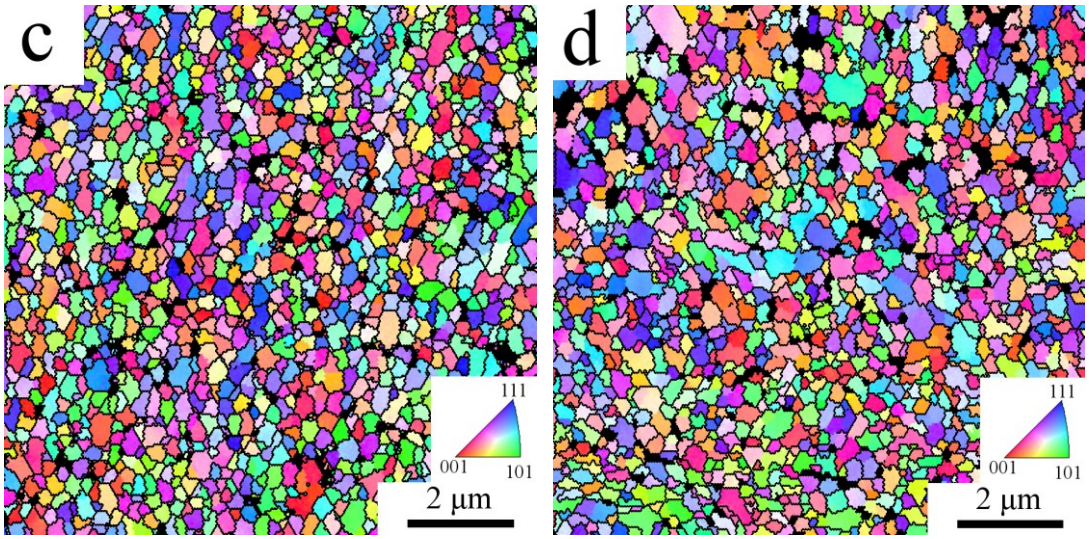

Figure 67. The microstructure of the Al7075Zr_MC_RT_8_400P compact: a) non-annealed, b) annealed for 1 h at 425 °C, SEM-BSE, and the orientation image micrographs of samples with HAGBs in black: c) non-annealed, b) annealed for 1 h at 425 °C.

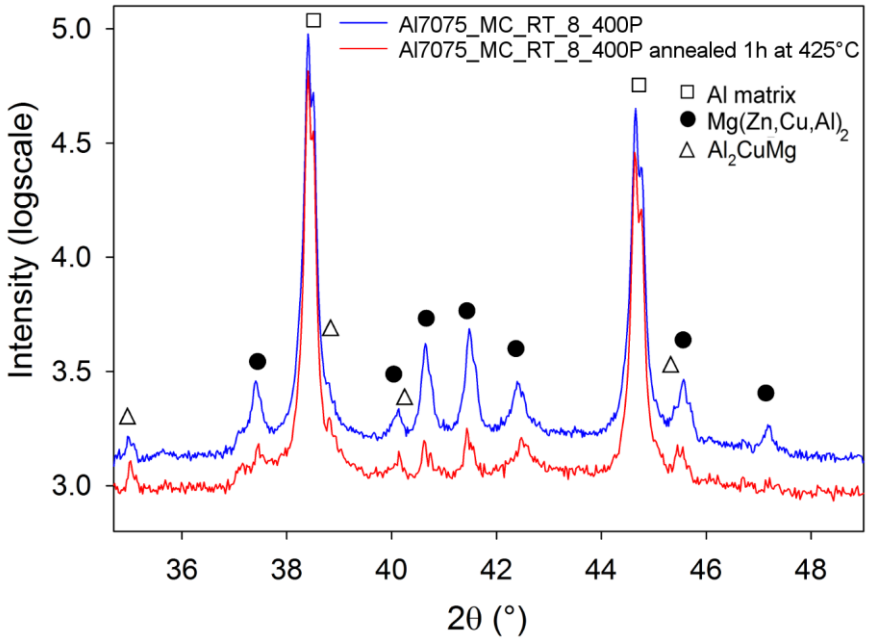

Figure 68. Comparison of XRD patterns of non-heat treated and annealed (at 425 °C) Al7075_MC_RT_8_400P compact.

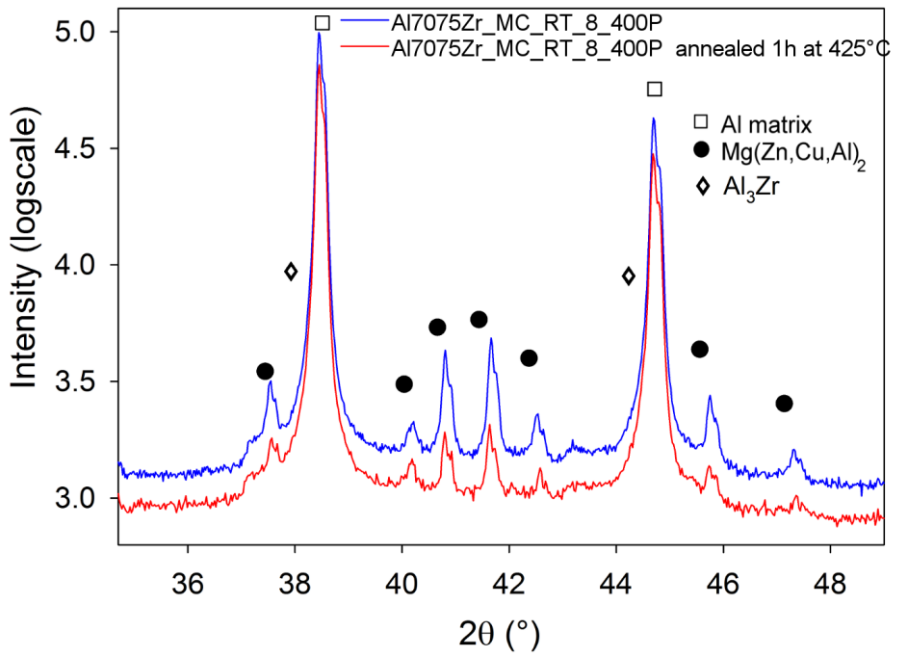

Figure 69. Comparison of XRD patterns of non-heat treated and annealed (at 425 °C) Al7075Zr_MC_RT_8_400P compact.

		$Mg(Zn,Cu,Al)_2$ [wt%]	Al_2CuMg [wt%]	Al_3Zr [wt%]	d [μm]	HV
Al7075_MC_RT_8_400P	Non-annealed	4.5 ± 0.6	1.6 ± 0.2		0.55 ± 0.24	161 ± 7
	1 h at 425 °C	1.4 ± 0.4	1.8 ± 0.3		0.57 ± 0.18	178 ± 5
Al7075Zr_MC_RT_8_400	Non-annealed	3.6 ± 0.5		1.0 ± 0.1	0.34 ± 0.09	195 ± 8
	1 h at 425 °C	1.4 ± 0.4		1.2 ± 0.1	0.34 ± 0.08	202 ± 5

Table 13. The influence of heat treatment on the phase composition, average grain size, and microhardness of SPS compacts prepared from planetary ball milled powder.

4. Discussion

The high strength of the Al7075 type alloys is mostly derived from the precipitation sequence either at room or at elevated temperatures after solution treatment. Additional strength increase can be achieved by strain hardening through plastic deformation. Finally, a reduction of grain size can further contribute to the materials strength. Whereas precipitation and strain hardening can be applied to materials prepared through traditional processing routes, substantial grain refinement requires a special attitude. The minimum grain size achievable in Al7075 type alloys by ingot metallurgy processing route is above 10 μm [210] which is not sufficient for a substantial strengthening. Various methods of severe plastic deformation made possible to reduce grain size down to a submicrocrystalline or even nanocrystalline region, however, it is difficult to combine them with precipitation strengthening. Precipitation strengthening cannot precede severe plastic deformation processing, for example equal-channel angular pressing (ECAP), as high strength of fully precipitated materials brings too strong requirements on the forming tools, and simultaneously such materials are frequently brittle. Furthermore, ECAP of Al7075 type alloys is usually performed in the temperature range where the precipitation strengthening intensifies. Thus also materials after solution treatment are excluded from ECAP processing as intensive precipitation of phases from the solid solution could occur already during the first ECAP cycle and the following cycles would be hindered by a high strength of the precipitate hardened material. Therefore, only materials in the initially overaged state are suitable for ECAP. Such materials are sufficiently soft and do not exhibit any precipitation strengthening during ECAP. On the other side, precipitation strengthening of previously severely deformed samples requires dissolution of coarse second phase particles present in the initially overaged material, i.e. annealing at temperatures at least of 470 °C. However, such temperatures are too high to retain the fine-grained structure produced by ECAP.

Powder metallurgy is an alternative way for processing fine grained materials with convenient green microstructure for further controlled precipitation. The high cooling rates of rapid solidification processes (exceeding 10^3 Ks^{-1}) lead to higher supersaturation as compared to mould cast techniques characterized by relatively low cooling rates [8, 199, 211].

4.1. Gas atomized powders

The Al7075_AP and Al7075Zr_AP powders used in our research contained mostly spherical powder particles, in some cases with satellites. The spherical shape is usual for gas atomized powders, as the most molten metal has large surface tension and low viscosity, which leads to instantaneous spheroidisation of droplets [7]. Satellite particles attached to other powder particles are produced by interparticle collisions during the droplets solidification. Such collisions are highly probable during atomization process, as the atomizing fluid flow leads to enormous turbulence in the atomization chamber [7].

The Al7075_AP and Al7075Zr_AP powders exhibit a broad particle size distribution. The exact cooling rate in various powder particles depends beside the atomizing medium mainly on the size of melt droplets [7, 211]. As the cooling rate is inversely proportional to the droplet size, the solidified powder particles exhibited various types of internal microstructure [212, 213]. The highest solidification rates are achieved in the finest powder particles [125]. The high temperature gradient and the high rate of solidification front movement results in a supersaturated, featureless microstructure. Such segregation-free microstructure was observed in some very small powder particles or in satellite particles (Figure 10a and b). Similar featureless microstructures were previously found e.g. on the surface of gun splat Al-Fe alloy [214] or at the cooled surface of rotating blade quenched Al-Fe-Ce-Ti and Al-Fe-V-Si alloys [215]. A segregation free microstructure was reported also in small rapidly solidified droplets and satellite particles of the gas atomized Al-Cr-Zr alloy [216] or Al-Fe-Nd alloy [217] or in the smallest powder particles of a spray formed Al-Ni alloy [218].

As the actual cooling rate decreases with increasing droplet size, the planar solidification front breaks down leading to first cellular and then dendritic microstructure [8, 47, 212]. Our powders were sieved and their mass median diameter (the average diameter by mass) was 20 μm, i.e. relatively fine, therefore, most powder particles exhibited a cellular microstructure. For comparison, a mixture of cellular and dendritic microstructure was observed in a gas atomized Al7075 alloy with a coarser mass median diameter, close to 50 μm [119, 219]. Similarly, Devaraj et al. reported on cellular microstructure in smaller and dendritic microstructure in larger powder particles of an atomized Al-4.5 wt% Cu alloy [123]. The same trend was reported to

occur in a spray formed Al-Ni alloy [218] and atomized Al-Si alloy [120]. Gas atomized Al-Fe powders of various Fe content also exhibited a transition from cellular to dendritic and eutectic microstructure, moreover, in case of the largest powder particles also primary intermetallic phases were observed [220, 221].

Figure 9 documents a decreasing cell size in both Al7075_AP and Al7075Zr_AP powders with decreasing powder particle size, i.e. with increasing cooling rate during atomization. This is a typical feature of rapidly solidified materials and was severely times reported in the literature [8]. In a spray formed Al-Ni powder the cell size was shown to decrease with decreasing powder particle size [218]. This was reported also for an atomized powder of Al-Si alloy [120]. Higher cooling rates at the cooled wheel side of melt spun Al-Zn-Mg-Cu-(Zr-Sc) ribbons led to finer microstructure than that at the free side [199]. Similarly, the dendrite arm spacing was reported to increase with decreasing solidification rates (i.e. with increasing powder particle size) in a gas atomized Al2024 alloy [222].

The main alloying elements present in the Al7075-type alloy (Zn, Mg, Cu) form an eutectic system with Al [4, 113]. This means, that the first solid formed during solidification should be the solute lean Al solid solution. During the non-equilibrium process of rapid solidification, the diffusional processes can be much slower than the movement of the solidification front, thus a fraction of alloying elements remains in the melt. This solute enriched melt solidifies at the end as a mixture of intermetallic phases. It was verified by EDS experiments that the main alloying elements present in our materials really segregated at intercellular boundaries. The intercellular regions seemed to be continuous layers containing above mentioned elements. However, a detailed investigation by STEM-EDS revealed a mixture of various intermetallic phases at these places. Such microstructure was reported to be formed in several alloys throughout the literature, e.g. [218]. EDS results yielded no information about displacement of Zr atoms. It can be supposed, that Zr remained dissolved in the gas atomized Al7075Zr_AP powder due to rapid solidification. Dissolution of Zr as consequence of rapid solidification of alloy was showed also in [223], where 0.5 wt% of Zr was dissolved in an Al-Zn-Mg-Cu alloy produced by melt spinning.

Both gas atomized powders were fine grained with grain sizes of a few μm. The grain size was found to slightly vary with the powder particle size (Figure 16 and 17). The number of nucleation centres was shown to decrease with increasing cooling rate [224]. As smallest powder particles are characterized by the largest cooling rates,

there will be a lower number of nucleation centres. Thus the smallest droplets can be even single-crystalline. Growing droplet size results in a lower cooling rate and more time is available for nucleation processes. More nucleation centres can be then in larger droplets which leads to a smaller grain size.

In the largest powder particles usually individual cells could be identified with individual grains. On the other side, in smaller powder particles the intercellular boundary could not be identified with grain boundary, one grain contained several cells. This can be explained considering the processes taking place during gas atomization. Nucleation centres of Al grains formed at several places inside the solidifying droplet. Each nucleated grain grew radially with a more or less planar solidification front, however, in some cases the moving liquid-solid interface become instable leading to cellular solidification microstructure (which according to Jacobson et al. can be explained as dendritic microstructure without secondary arms [47]). In case, that such a cellular microstructure is during metallographic preparation polished through the primary arms with intercellular segregation between them, the microstructure seems to be composed of cells, but these cells can belong to one individual grain. Such a structure can be clearly observed in Figure 16, in one smaller powder particle also in Figure 17. Similar microstructure, i.e. one grain containing several cells encompassed by intercellular segregation was reported also in [219] or [225]. Although the relationship between the solidification microstructure resp. grain size on powder particle size presents an interesting field, a thorough investigation of this problematics would require further analysis of this structure. As this problematic is beyond the scope of this thesis, no such detailed study of this microstructure was performed.

The Zr containing Al7075Zr_AP powder was found to exhibit a slightly finer grain size in comparison with the Al7075_AP powder. It was reported in [166] that coarse primary Al_3Zr particles which can be formed during solidification of the Al-Zr alloy as the first phase, can serve as nucleation centres for the Al matrix. Nevertheless, the presence of such coarse primary Al_3Zr particles was not confirmed by XRD neither by TEM. Despite of these findings, their presence cannot be excluded. Both experimental methods have their limitations. For XRD experiments, the weight fraction of these particles is probably below the limit of detectability. In case of TEM investigation, only a very small lamella with a size a few tens of μm and thickness below 100 nm was studied. The probability of the presence of a primary Al_3Zr particle

in this very small volume is very low. Thus the role of Zr alloying in the grain refinement cannot be verified experimentally.

The mechanical properties of powders were characterized by microhardness measurement. Due to the small size of the powders, this was the only available technique to directly compare mechanical properties of powders and compacts. Further, due to the powder particles small size only the largest powder particles could be tested, therefore the microhardness values should be considered carefully.

As the Al7075 type alloys are heat treatable, the microhardness of its atomized powder is determined predominantly by phase composition. The Al7xxx alloys are widely known to exhibit rapid natural aging at room temperature when prepared in supersaturated state, as diffusion rates of main alloying elements, Mg and Zn are sufficiently high at room temperature to enable redistribution of these solute atoms [4]. The atomized powders were stored at RT for a long period after their atomization, therefore they can be supposed to be already naturally aged and no additional remarkable hardening through further aging can be expected. The microhardness of both atomized powders (127 and 97 HV) was highly below that of a peak aged ingot metallurgical counterpart (170 HV [189]), which reflects the presence of coarse second phase particles in layers of intermetallic phases along cell boundaries. The value measured for the gas atomized powder is near to microhardness of solution treated cast Al7075 alloy (107HV) [226]. Similar values close to 100 HV, were reported for another gas atomized powder of the Al-Zn-Mg-Cu alloy in [219].

The difference in the microhardness of gas atomized Al7075_AP and Al7075Zr_AP powders cannot be explained by the grain size effect as the grain sizes of both powders were found similar - a few micrometers in size. Similarly, the effect of Zr addition can probably be neglected. Zr remained, most probably, dissolved in the gas atomized Al7075Zr_AP powder (as shown by XRD and TEM investigations) and it was reported in [199] for a melt spun Al-Zn-Mg-Cu ribbon that the dissolved Zr (1 wt%) has a low effect on resulting microhardness. The difference of microhardness should be explained based on different content of second phase particles and different content of elements in solid solution. Although the hardening effect of elements in solid solution could be easily quantified [4], the content of second phase particles is close to 1 wt% in both alloys, which is – as already discussed – connected with large errors. Thus neither the exact content of second phase particles nor the wt% of solutes

in solid solution can be evaluated, which makes impossible to estimate quantitatively the strengthening effects.

4.2. Milled powders

It is generally accepted that mechanical milling can modify both the microstructure and phase composition of materials (see section 1.4.1.2.). The influence of mechanical milling on initially gas atomized powders was investigated in our research and significant changes in the size and shape of powder particles, in their microstructure, in the content and distribution of second phase particles, grain size, and microhardness were observed.

The size and shape of milled powder particles results generally from a competition of repeated fracturing, flattening, and cold welding of powder particles. As reported e.g. in [11], intensive cold welding leading to an increase in powder particle size is characteristic for milling of ductile powders. Our experiments revealed a significant increase in the size of milled powder particles and their irregular shape. This suggests that cold welding played a decisive role during milling. Similar evolution of powder particle size was reported in literature [11]. Cold welding was present even at very low milling temperatures as presented on cryomilled powders, which agrees with the results presented in [63, 154] for cryomilled Al powders. Nevertheless, cryomilling of powders in attritor revealed a slower powder particle coarsening than it was detected to occur in powders milled at RT. This can be attributed to fracturing processes enhanced by the decreased temperature [227]. Mechanical milling altered also the continuity of powder particles. Cold welding does not occurred along the whole surface of colliding powder particles and some submicrometer voids were left behind (see Figure 18 and 19).

The changes in the phase composition and in the distribution of intermetallic phases caused by milling can be generally explained on the base of the following considerations. Severe plastic deformation during milling can break the second phase particles and reduce their size. Simultaneously, dislocations crossing the second phase particles destroy their ordering. The expected high dislocation density in the deformed powder particles along with elevated temperature arising from powder particle collisions enhance diffusional processes. Thus severe plastic deformation of powders can lead also to a partial/full dissolution of second phase particles and formation of a supersaturated solid solution.

The SEM-BSE investigation was used to follow the changes in the distribution of intermetallic phases. This observation revealed a gradual destruction of the cell microstructure with nearly continuous layers of intermetallic phases (rich in Cu, Mg, and partially Zn) located along cell boundaries which was typical for gas atomized powders. Rests of this microstructure were observed only in the Al7075_MP_RT_3_180 powder, i.e. at the lowest intensity of milling. No such structures were observed in more intensively milled powders, however, some places with bright contrast in SEM-BSE figures indicated an enhanced concentration of atoms with higher atomic numbers. The investigation of planetary ball milled powders revealed only the presence of coarse particles containing Ni or Ti which were introduced as contamination from the preceding milling in the same milling jar. No particles of intermetallic phases containing the main alloying elements (Zn, Mg, Cu) were observed by SEM-BSE. A homogeneous distribution of these alloying elements was confirmed by SEM-EDS experiments (Figure 24) within the resolution limit of this method. Similar microstructural changes caused by milling can be found e.g. in [53, 91, 154, 192, 228].

The SEM-BSE method documented disappearance of relatively coarse second phase particles during milling, however, it cannot distinguish whether the original second phases were completely/partially fractured, dissolved or replaced by much finer particles with the size below the detectability limit of this method. The XRD method was therefore applied. A reduction of peak area/loss of XRD peaks of non-matrix phases during milling is in agreement with SEM observations. Nevertheless, the absence of XRD peaks for non-matrix phases does not mean their absolute absence in the samples as this method has its limitation. Although each crystalline material with internal order contributes to corresponding XRD peaks, in case of low fraction of given phases, the XRD peaks of these phases can be hidden in the background and can become undetectable. Further, a reduction of size of second phase particles or reduction of their internal order leads to broadening of peaks, which again can lead to a decrement of peak height below the background level. Although the low XRD peaks does not allowed quantification of phases, it led information about their presence in all milled powder of Al7075 alloy.

The dissolution of intermetallic phases should result in a transport of alloying elements to the supersaturated matrix where they occupy interstitial or substitutional positions in the matrix phase lattice, change its elementary cell size, and displace the

matrix phase XRD peaks. Dissolution of elements with larger atomic radius than that of the solvent atom enhances the elementary cell size and displaces the XRD peaks to lower angles, whereas dissolution of lower atomic radius elements reduces the elementary cell size and displaces the XRD peaks to higher angles. The atomic radius of Al (0.143 nm) is higher than that of Cu (0.128 nm) and Zn (0.134 nm) but smaller compared to that of Mg (0.160 nm) [192]. Therefore, dissolution of phases containing predominantly Cu and Zn should lead to a peak displacement to higher angles, whereas dissolution of phases containing predominantly Mg should lead to a peak displacement to smaller angles. The phases present in the Al7075 alloy are usually complex and contain all above mentioned elements. Nevertheless, it was shown previously that dissolution of all alloying elements in an Al7075 alloy during milling leads to an XRD peak displacement to higher angles [192, 229]. Such displacement was also observed in our experiment which proves the process of dissolution of intermetallic phases during milling. Similar changes in the position of matrix XRD peaks were reported for a variety of Al-based milled materials – e.g. for a mechanically alloyed Al6063 alloy [230], mechanically alloyed Al-Zn-Mg-Cu-Zr alloy [231], mechanically alloyed Al7075 [229] or mechanically milled Al7075 alloys [192].

A complete dissolution of second phases of Al-Zn-Mg-Cu-Zr alloys was reported to occur after mechanical alloying for 40 h [231] resp. 80 h of milling [232]. In our case, such complete dissolution occurred in the Al7075Zr_MC_RT_8_400P compacts after 8 h of milling, in a much shorter term than reported for similar alloys in literature. The comparison of our result with literature data showed that the milling in our planetary mill resulted in the fastest and most intensive changes in the phase composition and microstructure.

The only direct confirmation of the presence/absence of second phase particles was obtained by TEM methods. The STEM method revealed numerous nanoparticles in the planetary milled Al7075_MP_RT_8_400P powder and the STEM-EDS method confirmed the presence of Mg and Zn in these nanoparticles. On the other side, no second phase particles were found in the lamella cut from a Al7075Zr_MP_RT_8_400P powder particle. However, it does not exclude presence/absence of intermetallic phases in other powder particles of planetary ball milled powders as the prepared lamellae could not be representative. This discrepancy between the microstructure of the two powders milled in planetary ball mill, Al7075_MP_RT_8_400P and Al7075Zr_MP_RT_8_400P can be explained also by

the non-controlled temperature during milling. In case of milling of Al7075_MP_RT_8_400P powder there could be a higher temperature increase which led to precipitation of fine second phase particles. Such temperature increase during milling was reported for example in [10, 233], where the temperature reached up to 200 °C in a planetary ball mill. However, there is no explanation why it happened in one case and not in other.

The grain size of gas atomized powders was in the range of units of μm. It is generally expected that mechanical milling should lead to a further grain size refinement, even to a nanocrystalline range. Whereas the grain size of gas atomized powders was estimated from EBSD investigation, this method failed at milled powders as it was not possible to obtain reasonable diffraction patterns even using the finest patterning and the best combination of spot size, accelerating voltage etc. According to [234] the minimum spatial resolution of the EBSD method for Al-based materials is approximately 60 nm using a tungsten filament and 20 to 30 nm using field emission cathode. It can be therefore expected that the grain size in our milled powders will be close to this limit. Additionally, an increased dislocation density can be expected in milled powders which can cause variations in crystallographic orientation inside individual grains and further complicate obtainment of reasonable diffraction patterns.

As mechanical milling destroys the cellular microstructure and SEM yields no contrast making possible to determine the grain size, TEM represents the only alternative, how to visualise the grains. As the preparation of specimens for TEM from very small powder particles is extremely complicated and time consuming it was not possible to investigate the microstructure of all milled powders and only those, milled in planetary mill were examined. Further complication connected with TEM examination is that the investigated volume is relatively small and there can be a doubt whether the investigated region represents fully the microstructure of the milled powders. Nevertheless, the results of TEM investigation confirm that the grain size of planetary milled powders really falls into the nanocrystalline range. The grain size of the Zr-containing alloy was found to be slightly lower than that without Zr. The width of elongated grains is close to 50 nm in the Al7075_MP_RT_8_400P powder and even 20 nm in the Al7075Zr_MP_RT_8_400P powder. This difference can be explained by the stabilizing effect of Zr on the grain size during milling. Dissolved Zr atoms were reported to lead to solute drag on dislocations and grain boundaries which hinder their motion, thus suppressing recovery and recrystallization [235].

The refinement of the grain size to a nanocrystalline range due to mechanical milling was reported for several Al-based alloys. The grain size of approximately 100 nm was found in the Al-Zn-Mg-Cu-Zr alloy after 80 h of planetary ball milling [232], milling of an Al7075 powder for 20 h (with toluene as PCA) reduced the grain size to 26 nm [192]. Similar grain size reduction to 28 nm was observed also after cryomilling of an Al-Zn-Mg-Cu powder for 10 h [154], cryomilling of the same alloy for 12 h led to the grain size of 46 nm [17]. The comparison of our results with literature data shows that the milling in our planetary mill was very intensive and similar grain size refinement was achieved after shorter milling times already at room temperature.

As mentioned above, TEM investigation was not performed at all milled powders and the grain sizes were not directly evaluated for powders milled in attritor either at RT or at cryo-temperatures. At these powders, only the sizes of coherently diffracting domains (crystallites) were evaluated from the broadening of XRD diffraction peaks. These values cannot be directly correlated with grain sizes, however, they confirm a very fine microstructure of milled powders. Table 6 shows a slight reduction of the crystallite size with increasing RPM both at RT and at cryo-temperatures. On the other side, the influence of increasing milling time or decreasing milling temperature seems to be negligible within the experimental error. Literature data on the influence of milling parameters on the grain size are rather controversial. According to [11, 63] the milling conditions do not affect the minimum achievable grain size, but they alter the rate of refinement. Usually the refinement of powder's microstructure can be enhanced by increased RPM or milling time. Increasing RPM up to reasonable values (not leading to attachment of milling balls to vessel) leads to an increased impact energy on powder particles which should enhance grain size reduction in milled powders [236]. However, according to [236] there is a threshold impact energy below which no significant structural refinement occurs during milling. Above this threshold value, an increased RPM results in a faster attainment of a fine grain size. The influence of RPM on milled powders properties was studied by Ahmed et al. during mechanical alloying of an Al6063 alloy. They showed, that an increase in RPM from 300 to 700 RPM led to attainment of steady state in 20 h instead of 40 h. Moreover, the powders grain size in the steady state was found to be finer when milled with higher a RPM [230]. Increasing milling time was reported first to refine powder's grain size following an exponential trend, whereas prolonged milling ends in a saturation of the grain size [11, 63].

Cryomilling is generally expected to lead to quicker grain refinement compared to milling at RT [11, 63]. However, the crystallite size evaluation used in our research does not confirm this expectation – the crystallite sizes are identical (within the experimental error) for powders milled at RT and at cryo-temperature. The minimum grain size achievable by milling has been discussed with respect to work hardening and recovery rates, which scale with the melting point [35]. The minimum grain size achievable in ball milling is thus determined by a balance between creation and annihilation of dislocations during milling. Cryomilling is therefore predicted to have a low impact on further grain size reduction in metals with low self-diffusion activation energies, like Al. As measurement of grain size from milled powder is difficult, usually only crystallite size data are reported in literature. Minimum crystallite sizes were found to be in good agreement when achieved by milling at room or cryogenic temperatures. Cryomilled Al exhibited a crystallite size of 26 nm [237] and 25 nm [129] while mechanical milling at RT led to crystallite sizes of 22 nm [35] and 25 nm [127], all in attritor.

The microstructure, phase composition and their changes can highly affect the samples mechanical properties. Mechanical milling generally introduces a large fraction of deformation energy into the powder material, causes a significant grain size refinement, reduces the size of second phases particles, and enhances the amount of alloying elements dissolved in the matrix phase. All these changes should enhance strength characteristics of milled powders compared to gas atomized powders. The results of microhardness measurements in our milled powders confirmed these expectations. Excluding the Al7075_MP_RT_3_180 powder, milled at the lowest intensity, the microhardness values of all powders milled in attritor are close or even exceeding the value of 200 HV. These values are clearly above that measured for a peak aged ingot metallurgical Al7075 alloy (170 HV), despite of the fact that no special thermal treatment was applied to these milled powder. Similar microhardness values were achieved in a melt spun Al-Zn-Mg-Cu-Zr ribbon after optimized thermal treatment (186 HV). Mechanically alloyed Al-Zn-Mg-Cu powder in a supersaturated state exhibited a microhardness around 220 HV and crystallite size around 35 nm [229]. On the other side, an Al-Zn-Mg-Cu mechanically alloyed powder in supersaturated state was reported to exhibit a microhardness of only 73 HV despite of a crystallite size of 76 nm [238]. Although our powders milled in attritor contained some coarser second phase particles and had a crystallite size between 50 and 70 nm,

their microhardness was relatively high, around 200 HV, thus higher than that reported by Shafei et al. [238] and comparable with that reported by Yazdian et al [229].

Much higher microhardness values exceeding 300 HV were found in both powders milled in a planetary mill. No such high values were till this time reported in literature. As widely known, milled powders can be strengthened beside grain size refinement or work hardening also by particles introduced into their matrix during milling [239, 240]. These introduced particles can stem from PCA or milling jar and balls or powder surface layers [11, 241]. In our planetary ball milled powders some particles containing Ni and Ti were found. These particles represent a contamination from powders milled previously in the same vessel. The Al7075_MP_RT_8_400P powder was the first milled Al-based powder and, therefore, the volume fraction of contaminating particles is higher than that in the later milled Al7075Zr_MP_RT_8_400P powder. Despite of a lower fraction of these contaminating particles in the Zr-containing powder, its microhardness was even higher. In order to exclude the influence of these contaminating particles, the milling of both gas atomized powders was repeated with the same milling parameters in a new non-contamined milling jar. The microhardness of these new milled powders was found to be very close what confirmed the absence of influence of the Ni and Ti particles on the microhardness values.

To explain much higher microhardness of planetary milled powders compared to that milled in attritor all strengthening mechanisms described in chapter 1.2. will be discussed. Both powders were highly deformed during milling so that the dislocation density was increased in comparison with the gas atomized powders. Although dislocation densities in powders milled in different mills were not studied it can be expected that they will be roughly equal and thus the contribution of work hardening will be comparable in both types of milled powders. The grain size of powders milled in attritor was not evaluated from direct microstructural investigations. However, XRD experiment showed a comparable or even slightly smaller crystallite size in the powder milled in attritor than in the planetary milled powders. That means that neither grain size can be responsible for the higher microhardness of planetary milled powders. Therefore, the difference in powders microhardness can be explained most probably by their different content, size, and distribution of second phase particles. In powders milled in attritor, either rests of cellular microstructure or relatively large regions (up to 1 μm) with increased concentration of higher atomic number atoms were observed

by SEM (Figures 19c,d). On the other side, no such microstructural features were observed in the planetary ball milled powders (Figure 23). Nanometer-sized second phase particles were observed in the Al7075_MP_RT_8_400P powder (Figure 25b). Such very small particles might be responsible for the abnormally high microhardness values. A complete dissolution of second phases was documented in Figure 26b for the Al7075Zr_MP_RT_8_400P powder. As mentioned above, the lamellae used for TEM observation represents a very limited area of the investigated material and the absence of very fine precipitates in this area does not mean an absolute absence of these particles in the whole volume of the Al7075Zr_MP_RT_8_400P powder. The highest microhardness (343 HV) found in this Al7075Zr_MP_RT_8_400P powder can also reflect solid solution hardening both by main alloying elements and by Zr atoms. No similarly high microhardness values can be found in literature. A supersaturated mechanically alloyed Al-Zn-Mg-Cu powder with the crystallite size around 35 nm exhibited microhardness around 220 HV [229].

4.3. Spark plasma sintered compacts

All powders were consolidated by spark plasma sintering. As mentioned in section 1.4.2.2. the main advantages of this sintering method are relatively low temperatures and very short times of sintering which help to preserve the benefits gained from rapid solidification or mechanical milling. The sintering temperature of 425 °C was selected on the base of previous experiments [119] where sintering temperatures between 425 and 550 °C were used. It was found that already the lowest used temperature leads to nearly full density compacts. The volume fractions of pores were found below 1 vol% in all sintered materials. These values were estimated by image analysis of SEM figures by ImageJ program. The evaluation error is estimated to be 0.1 vol%. The SEM figures used for porosity evaluation were taken on surfaces polished up to 1 μm polishing slurry to avoid etching of surface by the finest colloidal silica, however, even this polishing could lead to voids after fall-out of some second phase particles, thus the true porosity can be even smaller than 1 vol%.

The sintering temperature used in our research is lower than that usually used in production of high density Al alloys by SPS (450-600 °C) [10, 123, 147]. Lower sintering temperatures were usually reported to result in lower densities [85, 123]. The improvement in density in the current research can be prescribed to a higher applied

pressure (80 MPa) compared to the values used in literature (30-60 MPa) [61, 123, 130]. In some researches also higher pressures, as 100 MPa, were used in combination with lower sintering temperatures (300 °C) [85]. However, this temperature decrease was too large and led to samples with poor density (93-95% of the theoretical value).

Both gas atomized and milled powders were handled without an inert atmosphere. It is generally known that 5-15 nm thick oxide layers are formed in this case on the surface of Al-based powders. As mentioned in section 1.4.2., these oxide layers hinder solid state sintering, due to low diffusion rates through the oxide layer [76]. Conventional sintering techniques as e.g. HIP have to be followed by secondary processing methods, since they cannot break up the oxide layer in the absence of shear deformation. In case of SPS it is believed, that the local electric and magnetic fields can activate powders surface and help to break up and remove the oxide layer leading to enhanced thermal diffusion [99].

Moreover, addition of Mg to Al alloys is capable to deoxidize the oxide layer by forming MgO phase on the surface of powder particles. Such phase was found in our compacts at boundaries of original powder particles (see Figure 51). This layer helps sintering as shown e.g. in [147, 242].

During consolidation of milled Al powders precipitation of AlN and Al_2O_3 particles is reported to occur [58, 63, 129]. These particles were reported to have a size of 3-10 nm with a spacing around 10 nm, furthermore, they are incoherent, insoluble and have a high temperature stability. Thus, they might play a significant role in retarding grain growth [58, 63]. No such particles were found in the compacts studied in the present thesis. However, their presence cannot be excluded, as these particles are expected to be very small. The presence of such particles can be revealed only by methods of high-resolution transmission electron microscopy or atom probe field-ion microscopy. A classical TEM used in our research is not capable of revealing such extremely small particles. Moreover, the content of these phases is expected to be deeply below 1 wt%, thus their presence cannot be shown by XRD [58, 129].

As shown in sections 3.3. and 3.4., the microstructure evolution and properties of SPS compacts are different for compacts prepared from gas atomized and milled powders. These results are, therefore, discussed separately in the following paragraphs.

4.3.1. Spark plasma sintered compacts from gas atomized powders

One of the benefits of rapid solidification during gas atomization process is an extension of solid solubility. The high temperature exposition during SPS led to redistribution of solutes and to increment in weight fraction of second phase particles (Table 8).

The distribution of second phase particles both in powders and SPS compacts was studied predominantly by SEM-BSE method. The distribution of second phase particles in the gas atomized powder depended on the size of powder particles, i.e. on the solidification rate. In compacts prepared from gas atomized powders, the distribution of second phase particles is somewhat similar to that observed in gas atomized powders, however, some differences were also observed.

Coarse second phase particles of the η phase were formed at some contact points between original powder particles. As reported for the SPS technique, the temperature especially at these contact points can be much higher than the set one [15], and, additionally, enhanced diffusion of alloying elements occurs along the surface of original powder particles. A very fast diffusion at these places can then result in the formation of these coarse precipitates. Similar enhanced precipitation by formation of coarse second phase particles along boundaries of former powder particles was reported also in [154].

The continuous layers of intermetallic phases observed in gas atomized powders were replaced by individual separated particles in SPS compacts. According to literature data, dissolution of the η phase appears at 450-470 °C [185, 191]. Although the sintering temperature of 425 °C is slightly lower, a partial dissolution of this phase cannot be excluded. Places with locally enhanced temperature (exceeding the set one) definitely appear during SPS and dissolution of the η phase can occur there. Nevertheless, the relatively short holding time at relatively low sintering temperature limited dissolution of second phase particles present in intercellular regions of gas atomized powder particles and minimized diffusion of alloying elements to a long distance. Precipitates forming chain-like structures were thus formed (from partially dissolved former second phase particles or from solute present in solid solution) preferentially at places of former continuous layers (see the precipitation free zone along grain boundary in Figure 31c). Chain-like arrangement of second phase particles was found in parallel lines (Figure 31b, Figure 32a). This formation excludes,

that they were formed along former cell boundaries. More probably they were formed along grain boundaries and dislocations, as precipitation of second phase particles in Al7075 type alloy is reported to occur preferentially on grain boundaries and dislocations [124, 183-187]. A similar formation of chain-like precipitate arrangement from intercellular/dendritic segregations during SPS was reported e.g. in [119, 123, 219].

Numerous very small precipitates were found inside grains. Most of these precipitates could not been observed by SEM due to their very small size. The distribution of these precipitates was homogeneous (Figure 31c). The exact nature of these precipitates was not examined. As the Al7075-type alloys are capable of natural aging, it cannot be distinguished whether these small precipitates were formed already during SPS or during the following aging at room temperature. In the Zr-containing material, also extremely fine particles of the metastable Al_3Zr phase were observed (Figure 32). Precipitation of this phase occurred in some grains homogeneously, in other cases a fan-shape arrangement of these particles was formed. According to literature, such arrangement of Al_3Zr particles is generally found in Zr-containing Al alloys [168].

Whereas SEM-BSE investigation confirmed rearrangement of second phase particles, XRD showed changes in their weight fraction. The influence of enhanced temperature during SPS induced a growth in weight fraction of the the η phase, simultaneously the S phase appeared in both compacts prepared from gas atomized powders. It was discussed above that the sintering temperature of 425 °C is high enough to partially dissolve the phases present at cell boundaries of gas atomized droplets [243, 244]. Simultaneously, some other precipitates can coarsen and new precipitates can be formed from the supersaturated matrix phase. The precipitation process clearly predominates during sintering. These changes in weight fraction of second phases are in accordance with the literature [4]. Similar processes were observed e.g. during SPS of another Al-Zn-Mg-Cu alloy during SPS at 500 °C [119, 219].

As mentioned in Introduction, the large Joule heat generated during SPS at contact points leads to neck formation between adjacent powder particles. The temperature can highly exceed the set one at these places and even a local melting can occur. In this case a formation of new grains might be expected. No such effect was, however, observed in our SPS compacts prepared from gas atomized powders. The

SPS compacts retained the original grain structure of gas atomized powder particles. A relatively broad distribution of grain sizes reflects a similar distribution observed in gas atomized powder particles. The smaller grains observed in compacts stem predominantly from original larger powder particles, whereas coarse grains in compacts can be identified as the original smaller single crystalline droplets of atomized powders. As already discussed in chapter 4.1., it can be considered that this difference is connected with a different activation of nucleation centres in droplets with different sizes. A smaller mean grain size in the Al7075Zr_AC compact is in agreement with a smaller grain size in the Al7075Zr_AP powder in comparison with the materials not containing Zr. The mean grain sizes of both compacts are close to those measured for the corresponding gas atomized powders. This confirms that the short duration of SPS and the relatively low sintering temperature do not allow a grain growth.

Both interfaces present in SPS compacts, i.e. boundaries between grains and boundaries between original powder particles, have predominantly a high-angle character (Figures 35b and 36b). The distribution of misorientation angles shows on random distribution of grain orientation, i.e. on a low effect of SPS pressure on the compacts microstructure. Nevertheless, there is a slight deviation from the random distribution at low misorientation angles. This can be explained by the solidification microstructure of gas atomized powders, which was retained also in the compacts. Low-angle boundaries were found predominantly in Al7075_AC compact (see Figure 35 and 38), which stem from the cellular solidification microstructure observed in Al7075_AP powder (Figure 16).

As SPS led to precipitation of phases from the solid solution of atomized powders, it led also to changes in the materials microhardness. A significant microhardness increase was observed in SPS compacts prepared from gas atomized powders in comparison with corresponding powders. The precipitation of strengthening phases during SPS seems to be mostly responsible for this increased microhardness of these compacts as the grain size of compacts prepared from atomized powders was close to that of corresponding powders and it can be supposed that SPS does not introduce any significant work hardening because of enhanced temperature during SPS process. The measured microhardness values between 151 and 171 HV are close to that of peak aged ingot metallurgy Al7075 (170HV) [189], although no optimized thermal treatment was performed. The smaller grain size in the SPS

compacts can probably balance the deficit of precipitation strengthening. Cast Al-Zn-Mg-Cu alloy was reported to exhibit a microhardness around 100 HV [189]. Semi solid rolling of gas atomized Al-Zn-Mg-Cu alloy led to microhardness values between 90 and 150 HV depending on the rolling temperature [202]. ECAP elevated this value up to values around 200 HV. The high microhardness in these ECAP samples was reported to be caused by the small grain size in range 0.3-1 μm [245].

4.3.2. Spark plasma sintered compacts from milled powders

Whereas SPS led to only slight changes in weight fraction of second phase particles, in their size and distribution, and in the grain size in case of originally gas atomized material, large changes were observed in SPS compacts prepared from milled powders.

Precipitates of two size scales (the first one with the size around 1 μm and the second one about one order finer) were observed in SPS compacts prepared from milled powders by the SEM-BSE method. In the compact prepared from the powder milled in attritor at the lowest intensity the distribution of precipitates was not homogeneous and revealed the rests of original cellular structure (Figure 39a). It can be seen in this micrograph that the coarser precipitates are located predominantly at boundaries between original powder particles whereas the fine precipitates can be found in their interiors. The SEM-BSE micrograph taken in the same compact at a higher magnification and its comparison with the corresponding EBSD orientation image micrograph revealed, that larger second phase particles were located along grain boundaries, whereas the finer ones are inside grains (Figure 45). A similar distribution of precipitates can be seen also in compacts prepared from Al7075_MP powders milled at higher intensity, however, the distribution of larger precipitates is more homogeneous. This distribution of precipitates is in accordance with expectation, as boundaries are preferential diffusion paths and precipitation sites in one. Similar microstructure was observed in the cryomilled Al-Zn-Mg-Cu powder sintered by HIP+extrusion - the coarser irregularly shaped precipitates of η phase were located at boundaries between ultrafine-grains of the compact, whereas GP zones and nanometer sized η′ precipitates were found inside grains [183]. Very similar microstructure was reported also in [154] for a cryomilled Al-Zn-Mg-Cu alloy sintered by SPS where

relatively coarse, 400 nm η particles were found along grain boundaries and at contact points of former powder particles.

Both larger and finer precipitates were also found in SPS compacts prepared from planetary ball milled powders. In contrast to compacts prepared from powders milled in attritor an apparently random distribution of coarser precipitates was observed. This can be probably attributed to its more intensive milling and following precipitation of fine second phase particles. During SPS this homogeneous structure of the planetary milled powder led to a more homogeneous structure of corresponding compacts.

It was shown in section 3.2. and discussed in section 4.2. that milling resulted generally in a partial or full dissolution of second phase particles and increased the amount of alloying element dissolved in the matrix. The heat effect during SPS led to a massive precipitation and coarsening of phases. The weight fraction of the η phase increased from values below 1 wt% found in the milled powders to values between 3.6 and 5.7 wt% in the corresponding SPS compacts. Like in the compacts prepared from gas atomized powders, the S phase formed during SPS. Table 9 documents that the weight fraction of second phases increases generally with increasing intensity of milling (increasing milling time, increasing RPM, decreasing milling temperature). This can be explained by their differently deformed microstructure. First, the higher dislocation density and the higher fraction of boundaries enhance the number of preferable nucleation centres [183]. Second, both dislocations and grain boundaries represent routes of easy diffusion for Zn, Cu and Mg atoms, enhance the diffusion rate and promote coarsening of second phase particles even during the short term of SPS [183]. Consequently, a more pronounced precipitation can occur than in the compact prepared from gas atomized powders.

Our results are in accordance with the literature data dealing with precipitation occurring during sintering. SPS was reported to led to precipitation of η phase from the supersaturated solid solution of cryomilled Al-Zn-Mg-Cu powder [154]. HIP followed by extrusion led also to precipitation of η phase from cryomilled Al-Zn-Mg-Cu powders matrix [183]. Consolidation of mechanically alloyed Al-Zn-Mg-Cu-0.1Zr powder by HP at 350 °C led to precipitation of η phase from the supersaturated solid solution [231].

The energy introduced by milling into the powders of the Al7075Zr alloy influences also the precipitation of the Al_3Zr phase during SPS. Whereas the fraction

of this phase is under the detectability limit of the XRD method (and was detected only by TEM) in compacts prepared from gas atomized powders the weight fraction close to 1% was observed in compacts prepared from milled powders. The STEM-EDS map of the distribution of Zr in the Al7075Zr_MC_RT_8_400P compact in Figure 51 revealed even the presence of coarser Zr containing particles. The literature data on the precipitation of the Al_3Zr phase are controversial. Whereas no diffraction peaks of this phase were observed in a mechanically alloyed Al-Zn-Mg-Cu-(1 or 2 wt% Zr) powder sintered by HIP at 380 °C for 12 min despite of a high Zr content [232], precipitation of the Al_3Zr phase was reported to occur from supersaturated solid solution of cryorolled Al7075 alloy already after annealing at 250 °C for 1 h [226].

Contrary to the compacts prepared from atomized powders, SPS led to remarkable changes in the grain size of milled powders. In case of compacts prepared from powders milled in attritor there is no direct comparison with the microstructure of the milled powders. Only the size of coherently diffracting domains estimated from the XRD peak broadening is available for these powders. However, the measurements performed on planetary milled powders revealed that CDD size agrees well with the grain size determined from TEM micrographs. Therefore, it can be assumed that the grain size of powders milled in attritor will be also in the range up to 100 nm. On the other side, the grain size of the SPS compacts prepared from powders milled in attritor is mostly close or larger than 1 μm, so that a massive grain coarsening occurred. Severe plastic deformation introduced to the material during milling represents a strong driving force for recrystallization under heat influence. The elevated temperature during SPS led to recrystallization of deformed structure, despite of the very short heat exposition.

The grain structure of compacts prepared from powders milled in attritor is heterogeneous, and seems to be formed by stocked curved strips. This microstructure can be the result of the layering and cold welding of flattened former powder particles. The grain structure consists of areas of coarser grain size interchanging with regions of finer grain size making a bimodal microstructure. This wavy grain structure is not unique. A similar banded structure is frequently reported for severely deformed metals after annealing, and it was reported also for several SPS processed alloys. Xiong et al. reported about similar mixture of coarser and finer grains in an Al5083 alloy prepared by SPS of cryomilled powder [91]. Bimodal microstructure was shown to evolve also in a SPS compacted cryomilled Al 5083 powder [72, 151] and cryomilled Al-Mg

[246]. Beside Al alloys, similar banded grain structures with bimodal grain size distribution were found among others also in Fe-Al [247], Mg alloys [248] or ODS steels [249-251] processed by SPS. Nevertheless, the bimodal microstructure was reported also to occur also in compacts processed by other consolidation methods, for example by HIP [250, 251].

Several possible mechanisms of the formation of bimodal microstructure were reported. Boulnat et al. suggested that they arose from a heterogeneous spatial distribution of stored energy from milling, resulting in a non-homogeneous recrystallization [248, 251]. Alternatively, bimodal grain size distribution can stem from the elongated grains in the milled powder or some grains of powder material can also selectively grow, since grain boundary mobility and activation energy depend on its orientation [91]. In case of SPS, local differences in electric current leading to localized high temperature or stress increase can also result in stress-assisted grain growth [91]. Severe grain growth as possible explanation for bimodal grain structure was proposed by Koizumi et al [247]. Hu et al. explained the bimodal grain structure by grain or subgrain rotations caused by boundary diffusion processes until adjacent grains have a similar orientation. These grains then would coalescence into a larger grain. Zhou et al explained grain growth in cryomilled Al powder by coalescence of nano-sized grains to larger ones [53]. Moreover, coarse grain aggregates were reported to be formed by diffusional processes filling pores and crevices [73].

A finer and more homogeneous microstructure was found in the Al7075Zr_MC_RT_3_400 sample compared to Al7075_MC_RT_3_400 prepared with the same parameters. The milled powders showed similar crystallite size, however they contained different second phase particles in different fractions. As neither the η phase nor the Zn is reported to have a distinct effect on recovery of deformed structure, the difference should be explained only by Zr addition. Zr and Al_3Zr particles are reported to lead to solute drag and Zener pinning of grain boundaries promoting continuous recrystallization and thus more homogeneous structure.

The compacts prepared from powders milled in attritor, the compacts prepared from planetary ball milled powders exhibit a homogeneous sub-microcrystalline structure with grains separated predominantly by high angle boundaries. Both TEM investigation and EBSD results document recrystallized equiaxed grains with a size in the order of few hundreds nm. This structure is the finest one among all compacts

studied in our research. The stabilizing effect of Zr can be also clearly observed. All grains in the Al7075Zr_MC_RT_8_400P compact are finer than 0.6 μm. Such a structure is even finer that that observed in an ECAP processed material of similar chemical composition [21].

As SPS led to precipitation of phases from the solid solution of milled powders, and to a recrystallization of highly deformed structure of milled powders, significant changes in the materials microhardness can be expected. The very high microhardness exceeding mostly 200 HV observed in powders milled in attritor decreased to values between 120 – 130 HV. The expected decrease in dislocation density and recrystallization process resulting in an increase in grain size can be assumed to be the reason for this drop in microhardness. These microhardness values are lower if compared to that of the compacts prepared from gas atomized powders. This result is somewhat strange from two reasons. First, the grain sizes in compacts prepared from powders milled in attitor are slightly lower than those of compacts prepared from gas atomized powders. According to the Hall-Petch relation (Eq. 8) the grain size hardening should be thus higher in the compacts prepared from powders milled in attritor. Second, XRD investigation revealed a higher content of intermetallic phases in the compact prepared from milled powders, so that, according to the theory of precipitation strengthening a higher microhardness could be expected in this material. However, the content of intermetallic phases is not the only parameter determining the strengthening effect of second phase particles. Especially the size and type of these particles has to be considered. The comparison of SEM-BSE micrographs in Figures 29, 30 and 39 reveals, that the compacts prepared from powders milled in attritor contain a higher fraction of larger second phase particles, which could have a decreased strengthening effect than the smaller ones.

In compacts prepared from the planetary ball milled powders, similar processes occurring during SPS can be expected. Consequently, a drop in microhardness compared to planetary milled powders is not surprising. Nevertheless, the microhardness values (154 and 186 HV) were significantly above those for compacts prepared from powders milled in attritor (120 – 130 HV) and even slightly above those measured for the compact from gas atomized powder (151 and 171 HV). The finer grain size, homogeneous microstructure and higher content of second phase particles should lead to these higher microhardness values.

High values of microhardness were reported for a mechanically milled and hot pressed Al-Zn-Mg-Cu(-Zr) powder, where a microhardness of 195 HV was found, independent on the alloys actual Zr content [232]. The high values of microhardness was prescribed to the very fine grain size, around 200 nm. The microhardness of a mechanically alloyed and hot pressed Al-Zn-Mg-Cu powder was reported to be 170-210 HV, which was prescribed to the samples nanocrystalline grains and to fine precipitates ranging from 50 to 400 nm [231]. However, samples porosity was reported to be above 2 vol%. An extremely high microhardness value of 288 HV was reported for a nanocrystalline grained Al7075 alloy processed by milling and hot pressing [192]. Nevertheless, the density and the powder bonding quality was not discussed although the oxide layer on Al powders surface can lead to low quality bonds, when conventional PM techniques are used without secondary processing as extrusion.

The Al7075 alloy is a heat treatable alloy containing several types of intermetallic phases which can be present in several modifications and variable composition. Without exact data on weight fraction, size and composition of each present intermetallic phase their strengthening effect cannot be evaluated using theoretical models. Other strengthening mechanisms as solid solution, dislocation, and grain boundary strengthening are also complicated to evaluate. As XRD does not show reliable information about low intensity peaks, the exact amount of alloying elements in solid solution cannot be evaluated, thus its strengthening effect cannot be quantified. Moreover, another strengthening effects cannot be evaluated for example in powders milled in attritor due to the difficulties around sample preparation. Further, from powder particles more lamellae should be prepared as one is not necessary representative for all the powders. Another problem is connected with the technique of combination of each strengthening effects. Therefore, no quantitative evaluation of strengthening effect could be performed, and only considerations about the influence of microstructural changes on resulting microhardness are given.

4.4. High temperature stability of compacts

The thermal stability of the compacts prepared from gas atomized powders was studied by annealing at 300 and 425 °C for 1 h. Annealing at the lower temperature was selected to result in overageing, annealing at the higher temperature to partially dissolve the intermetallic phases formed during SPS.

Heat treatment changed the distribution and content of second phase particles along with the phase composition of compacts. According to SEM-BSE annealing at 300 °C led to precipitation of phases, as Figure 58b show a higher density of second phase particles than Figure 58a. XRD showed, that annealing at 300 °C led to an increase in wt% of the η phase, the changes in the S phase content were within the measurements accuracy. These changes are in accordance with literature. The temperature of 300 °C is too low to dissolve the η phase as its dissolution starts around 450 °C [191]. The dissolution of the S phase starts around 470 °C after extended times [252]. The S phase normally precipitates from the solid solution, but due to the already present precipitates the concentration of solutes in solid solution is low to lead to remarkable precipitation of S phase [252].

The temperature of 300 °C corresponds to the temperature range where predominantly the stable modification of the η phase precipitates and he coarsening of this phase occurs. This heat treatment also leads to a depletion of matrix from solute atoms, which was retained in solid solution after SPS. This limits possible natural aging of compacts, especially formation of GP zones, after this heat treatment and the microhardness remains stable. These changes in the phase composition result in a large drop in microhardness (from 151 to 82 HV in the Al7075_AC compact and from 171 to 114 HV in the Al7075Zr_AC compact).

Annealing at 425 °C led to depletion of compacts from the finest second phase particles and to coarsening of others. Further, a drop in wt% of the η phase occurred. Although dissolution of this phase was reported to occur after annealing for extended aging times at 450 °C [252], a partial dissolution of the η phase was in our case detected already after 1 h of annealing at 425 °C. A nearly complete dissolution of precipitates of the η phase occurred during such annealing according to XRD measurements in the Al7075Zr_AC compact. This difference between both materials can be explained by a smaller grain size of the Zr-containing compact, as the high fraction of grain boundaries enhances diffusion processes. Annealing at 425 °C led to a slight increase of the Al_2CuMg phase content. The evolution of this phase is in accordance with literature. It is reported, that this phase is commonly observed only in states after solid solution treatment [253-255]. Moreover, temperature of 425 °C is too low to dissolve, as dissolution of this phase in the Al7055 alloy after annealing for 50 h at 470 °C was reported in [252].

The dissolution of the η phase leads to an increasing content of solutes in the Al matrix. During the following natural aging the formation of GP zones can be expected. Unfortunately, their presence cannot be verified by XRD and SEM experiments due to their expected low content and small size. An indirect evidence for their evolution can be found in the increased microhardness values measured around 1 week after quenching from the annealing temperature of 425 °C (125 HV for the Al7075_AC and 172 HV for the Al7075Zr compacts). The higher microhardness found in the Zr containing compact correlates well with the higher level of dissolution of the η phase during annealing.

The EBSD results revealed that the grain size was not modified by annealing and remained stable within the experimental error of the measurement. The grain boundary migration is thus suppressed.

The compacts prepared from milled powders were annealed only at 425 °C. The observed changes in the phase composition are similar to those observed in the compacts prepared from atomized powders. A partial dissolution of the η phase was observed in all compacts – the content of this phase was close to 2 wt%. This evolution was confirmed both by XRD measurements and by SEM investigations. The oversaturated Al matrix after quenching from the annealing temperature is a good precursor for natural ageing during the following stay at RT. Microhardness values measured after one week from quenching are generally very close to those of initial non-annealed compacts prepared form powders milled in attritor.

In compacts prepared from planetary ball milled powders the dissolution of the η phase is even more pronounced - its weight content decreased to 1.4 wt%. This effect can be caused by a finer grain size in these compacts. An increased concentration of dissolved atoms supports natural aging at RT. The microhardness measurements confirmed this expectation and values found in annealed compacts are even above those observed in non-annealed compacts. Again, the microhardness of the Zr-containing material is higher. Both finer grain size and the presence of very small Al_3Zr particles can contribute to this strengthening. The value around 200 HV belongs to the highest ones found in the Al7075-based materials.

The evolution of microhardness in all compacts can be performed in terms of second phase particles. As annealing at 425 °C led to dissolution of the η phase, the samples solute content in solid solution increased. Solid state precipitation of S phase led to a slight decrement of the solute content. Following natural aging then led to

formation of strengthening phases. As different compacts had different amount of dissolved phase and precipitates S phase, the amount of precipitated strengthening phase also differ. Therefore, samples with a lower content of S phase have a higher microhardness.

EBSD measurements revealed that the grain size of all compacts prepared from milled powders was stable and no coarsening occurred during annealing at 425 °C. Especially the mean grain size of 340 nm - found in the Al7075Zr_MC_RT_8_400P sample - is remarkable and suggests that the selected processing route is capable of preparing thermally stable Al-based materials which retain their very fine-grained structure and high strength characteristics even after exposition to high temperatures. The way to the production of so-called high temperature Al-based alloys is thus open.

Conclusions

The combination of gas atomization, mechanical milling and spark plasma sintering as consolidation method was used for the production of two Al based alloys- the Al7075 and Al7075 + 1 wt% Zr. Based on the presented experimental findings, the following main conclusions can be made:

- Gas atomization with nitrogen led to mostly spherical powder particles. The mass median size of both powders sieved down to 50 μm was slightly above 20 μm.
- The SEM investigation revealed that the microstructure of gas atomized powder particles was dependent on their size, i.e. on the solidification rate. A segregation free microstructure was found only in the smallest powder particles solidified at the fastest rate. Larger powder particles exhibited a cellular microstructure, the cells were divided mostly by continuous layers of intermetallic phases, mainly of the $Mg(Zn,Cu,Al)_2$ type. The TEM observation at higher magnification performed on the individual powder particle revealed that these layers were at some places composed of small individual second phase particles with the size below 100 nm. The cell size was inversely proportional to the powder particle size.
- In coarser gas atomized powder particles, the boundaries between cells had a high-angle character, so that the cells corresponded to grains. In some finer powder particles, the number of nucleation centres was limited and grains were composed of more cells with the same crystallographic orientation. Even single crystalline powder particles with a very fine internal cellular microstructure were observed. The distribution of grain sizes was relatively broad, the mean grain size was estimated to be around 6 μm in the Al7075 powder and around 4 μm in the Al7075 + 1 wt% Zr powder.
- The microhardness of both gas atomized powders was around 100 HV, i.e. close to the value reported for the solution treated ingot cast Al7075 alloy.
- Mechanical milling was carried out in two different mills – in an attritor and in a planetary mill. Various milling conditions (time of milling, RPM) were tested in case of milling in attritor, including cryo-milling in liquid nitrogen. Cold welding occurring during milling (including cryo-milling) was responsible for a significant increase in the size of powder particles.

- Milling altered the powders microstructure and phase composition. At the lowest milling intensity, the original cellular microstructure was partially retained. Increasing milling intensity resulted in a complete destruction of the cellular microstructure and only places with an increased content of alloying elements were observed. The intensity of diffraction peaks of second phases was strongly reduced and the weight fraction of the $Mg(Zn,Cu,Al)_2$ phase evaluated using Rietveld analysis decreased in some cases also below the detectability limit.

- In planetary ball milled powder, some coarser particles inside milled powder particles containing Ni and Ti were observed. These particles represent a contamination from the previous milling in the same milling vessel. A repeated milling in a new non-contaminated vessel resulted in a powder without these particles. The comparison of both powders confirmed that these particles did not influence the properties of the milled powders. The STEM investigation carried out on the individual milled powder particles revealed the presence of nanometer-sized particles rich on Mg and Zn located at grain boundaries in case of Al7075 alloy. No such particles were found in the lamella prepared from the Al7075Zr alloy.

- In the milled powders, it was not possible to obtain EBSD orientation maps, probably because of very small grains with a lattice distorted by milling. The only indirect information on the grain size was obtained from the evaluation of the diffraction peaks broadening. The size of crystallites (coherently diffracting domains) is between 50 and 90 nm in all milled powders. A good correlation between the crystallite size and the grain size was confirmed by TEM experiments performed on both planetary ball milled powders. These experiments revealed elongated grains with typical dimensions of 50 – 200 nm in the Al7075 powder and 20 – 100 nm in the Al7075Zr powder, i.e. both these powders are nanocrystalline.

- The microhardness of powders milled in attritor was close to 200 HV, a slight increase of microhardness was observed with increasing intensity of milling. These values are above the value reported for a peak aged ingot metallurgical counterpart (170 HV). Extremely high microhardness values of 327 and 343 HV were found in both planetary ball milled powders. No such high microhardness values were reported till now in any similar material.

- SPS at 425 °C with 80 MPa for 4 min led to nearly full density compacts from all gas atomized and milled powders. The samples porosity was below 1 vol% in all cases.

- SPS of gas atomized powders led to redistribution of second phase particles. Coarse second phase particles (around 1 μm) were formed at contact points between original powder particles. The former continuous layers of intermetallic phases in cell boundaries were replaced by chains of individual particles. Due to the short duration of exposition to elevated temperature the solutes were not able to diffuse to a long distance and new precipitates were formed at places of original continuous layers of intermetallic phases. TEM revealed also a presence of much smaller precipitates inside former cells. In the Zr containing alloy, precipitates of the metastable modification of the Al_3Zr phase were found either homogeneously distributed or arranged into a fan-shaped structure. Rietveld analysis of XRD pattern confirmed an increase in the weight fraction of the $Mg(Zn,Cu,Al)_2$ phase and also a presence of the Al_2CuMg phase.

- The EBSD experiments confirmed that SPS did not lead to grain coarsening in compacts prepared from gas atomized powders. Original powder particles are still recognisable. The presence of Zr resulted in a slightly smaller grain size and more homogeneous distribution of grain sizes. More than 90 % of grain boundaries have a high angle character in both materials and the distribution of misorientation angles resembles that for randomly oriented polycrystals.

- The microhardness of compacts prepared from gas atomized powders increased to values between 150-170 HV. The precipitation of new second phase particles is responsible for this increase.

- SPS of milled powders led to even more massive precipitation of second phase particles. Coarser particles with the size around 1 μm were formed predominantly at boundaries between original milled powder particles and at grain boundaries. One order finer precipitates were found in the grain interiors. Rietveld analysis of XRD pattern revealed the weight fraction of the $Mg(Zn,Cu,Al)_2$ phase between 3.7 and 5.7 wt%. The accelerated precipitation in comparison with SPS compacts prepared from gas atomized powders can be explained by a faster diffusion along a higher number of grain boundaries and along dislocations introduced during milling.

- Recrystallization resulting in significant grain coarsening occurred during SPS of powders milled in attritor. The grain structure is bimodal. Coarser grains with the size reaching up to 10 μm form curved strips, whereas finer, frequently sumbmicrocrystalline, grains are located between these strips. The homogeneity of grain structure increases with increasing intensity of milling. The best homogeneity was found in the Zr containing material. The mean grain sizes in SPS compacts prepared from powders milled in attritor are usually between 1 and 2 μm. In all samples, more than 90 % of HAGB was found and the distribution of misorientation angles is nearly identical with that for random orientation of grains in polycrystalline material.

- The microhardness of all SPS compacts prepared from powders milled in attritor was between 120 and 140 HV. The drop in microhardness in comparison with milled powders can be explained by a reduction in dislocation density and by a significant grain coarsening occurring during SPS.

- Very similar changes in microstructure and phase composition were found in SPS compacts prepared from planetary milled powders. Precipitates of two different size were observed - the coarser ones located at grain boundaries and the finer ones located inside grains. The grain structure of both compacts prepared from planetary ball milled powders is very homogeneous with the mean grain sizes of 0.55 μm and 0.34 μm in the Al7075 and Al7075Zr materials, respectively. This means that a submicrocrystalline structure can be prepared by the selected processing route.

- The microhardness values of 161 and 195 HV were measured in SPS compacts prepared from planetary milled Al7075 and Al7075Zr powders, respectively. These values are deeply below maximum microhardness values (above 300 HV) found in the corresponding planetary milled powders because of restoration processes occurring during SPS. However, the value found in the Zr containing compact is significantly above that reported for the peak aged ingot metallurgical counterpart, despite of the fact, that no special thermal treatment aimed at the maximum precipitation strengthening was applied. Especially the submicrocrystalline grain structure is believed to be responsible for it.

- The high temperature stability of SPS compacts prepared from gas atomized powders was tested by annealing at 300 and 425 °C for 1 hour. Annealing at 300 °C resulted in overageing accompanied by a drop of microhardness. Annealing at 425 °C

led to a partial dissolution of second phases, especially of smaller precipitates. Simultaneously a coarsening of larger particles was observed. The resulting microhardness was comparable with that of non-annealed materials. The grain size was retained during annealing at both temperatures.

- The high temperature stability of SPS compacts prepared from milled powders was tested by annealing at 425 °C for 1 hour. The microstructure development was similar to that observed in SPS compacts prepared from gas atomized powders. The stability of the grain size was observed in all these SPS compacts, e.g. the submicrocrystalline grain structure of SPS compacts prepared from planetary milled powders was retained after this thermal treatment. The microhardness of all annealed compacts is very close to that of non-annealed samples. An extraordinary high microhardness value above 200 HV was observed in the SPS compact prepared from the planetary milled Zr containing alloy. This material can be therefore depicted as a high temperature Al alloy.
- The positive influence of Zr addition to the Al7075 alloy was proved at all stages of preparation. It led to a more homogeneous and finer microstructure which mostly resulted in higher values of microhardness. This can be prescribed to the stabilizing effect either by solute drag or pinning effect.

The results of our research opened a way to so called high temperature Al alloys which would retain their high strength characteristics during exposition to high temperatures. The research should proceed in the following directions. The powders should be handled under protective atmosphere in order to suppress oxidation on their surface. Avoiding oxidation and absorption of gas molecules from air should led to higher quality compacts, not leading to voids and blistering when exposed to temperature above 450 °C. In this case the stability at temperatures above 425 °C might be tested. Larger SPS billets are necessary to prepare samples for compression and tensile tests. Furthermore, a thorough study by transmission electron microscopy of milled powders and their compacts is needed, as missing information about their exact microstructure and composition does not enable to consider the exact strengthening processes and stabilization effects.

Bibliography

[1] STACEY, M. *Aluminium Recyclability and Recycling.* Nottingham + Llundain : Cwningen Press, 2015.

[2] QUINKERTZ, R., ROMBACH, G. and LIEBIG, D. A scenario to optimise the energy demand of aluminium production depending on the recycling quota. *Resour. Conserv. Recycl.* 2001, Vol. 33, 3, pp. 217-234.

[3] MELO, M.T. Statistical analysis of metal scrap generation: the case of aluminium in Germany. *Resour. Conserv. Recycl.* 1999, Vol. 26, 2, pp. 91-113.

[4] DAVIS, J.R. *Alloying: Understanding the Basics.* Materials Park : ASM International, 2001.

[5] HUSSIN, M.A., SINHA, P.K. and DARBARI, A.S. Design and analysis of connecting rod using aluminium alloy 7068, T6511. *IJMET.* 2017, Vol. 5, 10, pp. 57-69.

[6] LIDDICOAT, P.V., LIAO, X.Z., ZHAO, Y., ZHU, Y., MURASHKIN, M.Y., LAVERNIA, E.J., VALIEV, R. Z. and RINGER, S. P. Nanostructural hierarchy increases the strength of aluminium alloys. *Nat. Commun.* 2010, Vol. 1. Article number: 63.

[7] SURYANARAYANA, C. Rapid solidification. *Mater. Sci. Technol.* 2006, pp. 57-110.

[8] LAVERNIA, E.J., AYERS, J.D. and SRIVATSAN, T.S. Rapid solidification processing with specific application to aluminium alloys. *Int. Mater. Rev.* 1992, Vol. 37, 1, pp. 1-44.

[9] LAVERNIA, E., RAI, G. and GRANT, N.J. Rapid solidification processing of 7XXX aluminium alloys: A review. *Mater. Sci. Eng.* 1986, Vol. 79, 2, pp. 211-221.

[10] GUPTA, R.K., MURTY, B.S. and BIRBILIS, N. *An Overview of High-energy Ball Milled Nanocrystalline Aluminum Alloys.* Cham : Springer International Publishing, 2017.

[11] SURYANARAYANA, C. Mechanical alloying and milling. *Prog. Mater. Sci.* 2001, Vol. 46, 1-2, pp. 1-184.

[12] IWAHASHI, Y., HORITA, Z., NEMOTO, M. and LANGDON, T.G. The process of grain refinement in equal-channel angular pressing. *Acta Mater.* 1998, Vol. 46, 9, pp. 3317-3331.

[13] ESTRIN, Y. and VINOGRADOV, A. Extreme grain refinement by severe plastic deformation: A wealth of challenging science. *Acta Mater.* 2003, Vol. 61, 3, pp. 782-817.

[14] SAHEB, N. Spark plasma and microwave sintering of Al6061 and Al2124 alloys. *Int. J. Miner. Metall. Mater.* 2013, Vol. 20, 2, pp. 152-159.

[15] SUÁREZ, M., FERNÁNDEZ, A., MENÉNDEZ, J.L., TORRECILLAS, R., KESSEL, H.U., HENNICKE, J., KIRCHNER, R. and KESSEL, T. Challenges and Opportunities for Spark Plasma Sintering: A Key Technology for a New Generation of Materials. *Sintering Applications.* s.l. : InTech, 2013, pp. 320-338.

[16] ZHAO, Y.H., LIAO, X.Z., CHENG, S., MA, E. and ZHU, Y.T. Simultaneously increasing the ductility and strength of nanostructured alloys. *Adv. Mater.* 2006, Vol. 18, 17, pp. 2280-2283.

[17] MA, K., WEN, H., HU, T., TOPPING, T.D., ISHEIM, D., SEIDMAN, D.N., LAVERNIA, E.J. and SCHOENUNG, J.M. Mechanical behavior and strengthening mechanisms in ultrafine grain precipitation-strengthened aluminum alloy. *Acta Mater.* 2014, Vol. 62, pp. 141-155.

[18] IBRAHIM, M.F., GARZA-ELIZONDO, G.H., SAMUEL, A.M. and SAMUEL, F.H. Optimizing the Heat Treatment of High-Strength 7075-Type Wrought Alloys: A Metallographic Study. *Int. J. Metalcast.* 2016, Vol. 10, 3, pp. 264-275.

[19] WEILAND, H. and CHEONG, S.W. The Role of Zirconium Additions in Recrystallization of Aluminum Alloys. *Mater. Sci. Forum.* 2007, Vols. 558-559, pp. 383-387.

[20] MÁLEK, P., ERLEBACH, J., CIESLAR, M. and KNOOP, F.M. Superplasticity in an Al-Zn-Mg-Cu-Zr alloy prepared by powder metallurgy. *Phys. Stat. Sol.* 1996, Vol. 157, 2, pp. 275-286.

[21] TURBA, K., MÁLEK, P. and CIESLAR, M. Superplasticity in a Zr and Sc modified AA7075 aluminium alloy produced by ECAP. *Kovove Mater.* 2007, Vol. 45, 3, pp. 165-170.

[22] KELLY, A. and NICHOLSON, R.B. *Strengthening methods in crystals.* Amsterdam : Elsevier, 1971.

[23] NABARRO, F.R.N. and DUESBERY, M.S. *Dislocations in Solids.* Amsterdam : Elsevier, 2002.

[24] KRATOCHVÍL, P., LUKÁČ, P. and SPRUŠIL, B. *Úvod do fyziky kovů 1.* Praha : SNTL, 1984.

[25] HAIDEMENOPOULOS, G. N. *Physical Metallurgy: Principles and Design.* Boca Raton : CRC Press, 2018.

[26] TABOR, D. *Hardness of Metals.* Oxford : The Clarendon Press, 1951.

[27] ZHANG, P., LI, S.X. and ZHANG, Z.F. General relationship between strength and hardness. *Mater. Sci. Eng. A*. 2011, Vol. 529, pp. 62-73.

[28] MITTEMEIJER, E. J. *Fundamentals of Materials Science.* Berlin : Springer, 2011.

[29] YU, H., TIEU, A.K., LU, C. and KONG C. Abnormally high residual dislocation density in pure aluminum after Al/Ti/Al laminate annealing for seven days. *Phil. Mag. Lett.* 2014, Vol. 94, 11, pp. 732-740.

[30] FRIEDEL, J. *Dislocations.* Oxford : Pergamon, 1964.

[31] FLEISCHER, R.L. Solid solution strengthening. *The strengthening in metals.* New York : Rinhold Press, 1964, pp. 93-140.

[32] LABUSCH, R. A Statistical Theory of Solid Solution Hardening. *Phys. Stat. Sol.* 1970, Vol. 41, 2, pp. 659-669.

[33] SMALLMAN, R.E. and NGAN, A.H.W. *Modern Physical Metallurgy.* Oxford : Butterworth-Heinemann, 2014.

[34] NIEH, T.G. and WADSWORTH, J. Hall–Petch relation in nanocrystalline solids. *Scr. Metall. Mater.* 1991, Vol. 25, 4, pp. 955-958.

[35] ECKERT, J., HOLZER, J.C., KRILL, C.E. and JOHNSON, W.L. Structural and thermodynamic properties of nanocrystalline fcc metals prepared by mechanical attrition. *J. Mater. Res.* 1992, Vol. 7, 7, pp. 151-1761.

[36] LIFSHITZ, I.M. and SLYOZOV, V.V. The Kinetics of Precipitation from Supersaturated Solid Solutions. *J. Phys. Chem. Solids.* 1961, Vol. 19, 1-2, pp. 35-50.

[37] WAGNER, C. Theorie der Alterung von Niederschlagen durch Umlosen. *Z. Elektrochemie.* 1961, Vol. 65, 7-8, pp. 581-591.

[38] SMALLMAN, R.E. and BISHOP, R.J. Chapter 8 - Strengthening and toughening. *Modern Physical Metallurgy and Materials Engineering.* Oxford : Butterworth-Heinemann, 1999.

[39] ANDRIEVSKI, R.A. Review of thermal stability of nanomaterials. *J. Mater. Sci.* 2014, Vol. 49, 4, pp. 1449-1460.

[40] TSCHOPP, M.A., MURDOCH, H.A., KECSKES, L.J. and DARLING, K.A. ‘‘Bulk’’ Nanocrystalline Metals: Review of the Current State of the Art and Future Opportunities for Copper and Copper Alloys. *JOM.* 2014, Vol. 66, 6, pp. 1000-1019.

[41] CHOOKAJORN, T., MURDOCH, H.A. and SCHUH, C.A. Design of Stable Nanocrystalline Alloys. *Science.* 2012, Vol. 377, 6097, pp. 951-954.

[42] SURYANARAYANA, C. and AL-AQEELI, N. Mechanically alloyed nanocomposites. *Prog. Mater. Sci.* 2013, Vol. 58, 4, pp. 383-502.

[43] KOCH, C.C., SCATTERGOOD, R.O., DARLING, K.A. and SEMONES, J.E. Stabilization of nanocrystalline grain sizes by solute additions. *J. Mater. Sci.* 2008, Vol. 43, 23-24, pp. 7264-7272.

[44] HUMPHREYS, F. and HATHERLY, M. *Recrystallization and Related Annealing Phenomena.* Oxford : Elsevier Ltd, 2004.

[45] DETOR, A.J. and SCHUH, C.A.,. Tailoring and patterning the grain size of nanocrystalline alloys. *Acta Mater.* 2007, Vol. 55, 1, pp. 371-379.

[46] THUMMLER, F. and OBERACKER, R. *Introduction to powder metallurgy.* London : The Institute of Materials, 1993.

[47] JACOBSON, L.A. and MCKITTRICK, J. Rapid solidification processing. *Mater. Sci. Eng., R.* 1994, Vol. 11, 8, pp. 355-408.

[48] CHRISTOULIS, D.K. , PANTELIS, D.I., DE DAVE-FABRÈGUE, N., BORIT, F., GUIPONT, V. and JEANDIN, M. Effect of substrate temperature and roughness on the solidification of copper plasma sprayed droplets. *Mater. Sci. Eng. A.* 2008, Vol. 485, 1-2, pp. 119-129.

[49] TONGSTI, R., DASHWOOD, R. and MCSHANE, H. Microstructure and Solidification of Al-Fe-(V, Si) Alloy Powders. *Scienceasia.* 2004, Vol. 30, pp. 33-41.

[50] LAVERNIA, E.J. and SRIVATSAN, T.S. The rapid solidification processing of materials: science, principles, technology, advances, and applications. *J. Mater. Sci.* 2010, Vol. 45, 2, pp. 287-325.

[51] OSORIO, W.R., SPINELLI, J.E., AFONSO, C.R.M., PEIXOTO, L.C. and GARCIA, A. Electrochemical corrosion behavior of gas atomized Al–Ni alloy powders. *Electrochimica Acta.* 2012, Vol. 69, pp. 371-378.

[52] MOHAMED, F.A. A dislocation model for the minimum grain size obtainable by milling. *Acta Mater.* 2003, Vol. 51, 14, pp. 4107-4119.

[53] ZHOU, F., LIAO, X.Z., ZHU Y.T., DALLEK S. and LAVERNIA E.J. Microstructural evolution during recovery and recrystallization of a nanocrystalline Al-Mg alloy prepared by cryogenic ball milling. *Acta Mater.* 2003, Vol. 51, 10, pp. 2777-2791.

[54] BELOV, N.A., AKSENOV, A.A. and ESKIN, D.G. *Iron in Aluminium Alloys: Impurity and Alloying Element.* London : CRC Press, 2002.

[55] BALÁŽ, P., GODOČÍKOVÁ, E., KRILOVÁ, L., LOBOTKA, P. and GOCK, E. Preparation of nanocrystalline materials by high-energy milling. *Mater. Sci. Eng. A.* 2004, Vol. 386, 1-2, pp. 442-446.

[56] ZHOU, F., LEE, Z., NUTT, S.R. and LAVERNIA, E.J. The influence of Sc on thermal stability of a nanocrystalline Al-Mg alloy processed by cryogenic ball milling. *Metall. Mater. Trans. A.* 2005, Vol. 36, 6, pp. 1587-1594.

[57] HUANG, B., PEREZ, R.J. and LAVERNIA, E.J. Grain growth of nanocrystalline Fe–Al alloys produced by cryomilling in liquid argon and nitrogen. *Mater. Sci. Eng. A.* 1998, Vol. 255, 1-2, pp. 124-132.

[58] TELLKAMP, V.L., LAVERNIA, E.J. and MELMED, A. Mechanical behavior and microstructure of a thermally stable bulk nanostructured Al alloy. *Metall. Mater. Trans. A.* 2001, Vol. 32, 9, pp. 2335-2343.

[59] LÜ, L. and LAI, M.O. *Mechanical Alloying.* New York : Springer Science & Business Media, 1998.

[60] AHN, B., NEWSBERY, A.P., LAVERNIA, E.J. and NUTT, S.R. Effect of degassing temperature on the microstructure of a nanocrystalline Al-Mg alloy. *Mater. Sci. Eng. A.* 2007, Vol. 463, 1-2, pp. 61-66.

[61] SASAKI, T.T., OHKUBO, T. and HONO, K. Microstructure and mechanical properties of bulk nanocrystalline Al–Fe alloy processed by mechanical alloying and spark plasma sintering. *Acta Mater.* 2009, Vol. 57, 12, pp. 3529-3538.

[62] ZHOU, F., LEE, J. and LAVERNIA, E.J. Grain growth kinetics of a mechanically milled nanocrystalline Al. *Scripta Mater.* 2001, Vol. 44, 8, pp. 2013-2017.

[63] ENAYATI, M.H. Nanocrystallization of Al Powder by Cryomilling Process. *KONA Powder Part. J.* 2017, Vol. 34, pp. 207-212.

[64] LAVERNIA, E.J., HAN, B.Q. and SCHOENUNG, J.M. Cryomilled nanostructured materials: Processing and properties. *Mater. Sci. Eng. A.* 2008, Vol. 493, 1-2, pp. 207-214.

[65] ROY, T.K., SUBRAMANIAN, C. and SURI, A.K. Pressureless sintering of boron carbide. *Ceram. Int.* 2006, Vol. 32, 3, pp. 227-233.

[66] ANGLEO, P.C., SUBRAMANIAN, R. *POWDER METALLURGY: SCIENCE, TECHNOLOGY AND APPLICATIONS.* New Delhi : PHI Learning Pvt. Ltd., 2009.

[67] ANKLEKAR, R.M., AGRAWAL, D.K. and ROY, R. Microwave sintering and mechanical properties. *Powder Metall.* 2001, Vol. 44, 4, pp. 355-362.

[68] TORRALBA, J.M., RUIZ-NAVAS, E. and FOGAGNOLO, H.B. Development of new materials by mechanical alloying. *Characterization and Control of Interfaces for High Quality Advanced Materials.* Westerville : The American Ceramic Society, 2012, pp. 207-2018.

[69] EKSI, A.K. Investigation of mechanical properties before and after sintering of cold isostatically pressed metallic powders. *Kovove Mater.* 2006, Vol. 44, 4, pp. 191-198.

[70] SHANMUGASUNDARAM, T., HEILMAIER, M., MURTY, B.S. and SARMA, V.S. On the Hall–Petch relationship in a nanostructured Al–Cu alloy. *Mater. Sci. Eng. A.* 2010, Vol. 527, 29-30, pp. 7821-7825.

[71] WAND, G., LANG, L.H., YU, W.J., HUANG, X.N. and LI, F. Influences of Hot-Isostatic-Pressing Temperature on the Microstructure, Tensile Properties and Tensile Fracture Mode of 2A12 Powder Compact. *Acta Metall. Sin. Engl.* 2016, Vol. 29, 10, pp. 963-974.

[72] HAN, B.Q., LEE, Z., WITKIN, D., NUTT, S.R. and LAVERNIA, E.J. Deformation behavior of bimodal nanostructured 5083 Al alloys. *Metall. Mater. Trans. A.* 2005, Vol. 36, 4, pp. 957-965.

[73] TANG, F., HAGIWARA, M. and SCHOENUNG J.M. Formation of coarse-grained inter-particle regions during hot isostatic pressing of nanocrystalline powder. *Scripta Mater.* 2005, Vol. 53, 6, pp. 619-624.

[74] LEE, Z., RODRIGUEZ, R., HAYES, R.W., LAVERNIA, E.J. and NUTT, S.R. Microstructural evolution and deformation of cryomilled nanocrystalline Al-Ti-Cu Alloy. *Metall. Mater. Trans. A.* 2003, Vol. 34, 7, pp. 1473-1481.

[75] YE, J., HAN, B.Q., LEE, Z., AHN, B., NUTT, S.R. and SCHOENUNG, J.M. A tri-modal aluminum based composite with super-high strength. *Scripta Mater.* 2005, Vol. 53, 5, pp. 481-486.

[76] MUNIR, Z.A. Surface oxides and sintering of metals. *Powder Metall.* 1981, Vol. 24, 4, pp. 177-180.

[77] ELDESOUKY, A., JOHNSSON, M., SVENGREN, H., ATTALLAH, M.M. and SALEM, H.G. Effect of grain size reduction of AA2124 aluminum alloy powder compacted by spark plasma sintering. *J. Alloy. Comp.* 2014, Vol. 609, pp. 215-221.

[78] GUTMANAS, E.Y. Materials with fine microstructures by advanced powder metallurgy. *Prog. Mater. Sci.* 1990, Vol. 34, 4, pp. 261-366.

[79] ORRÙ, R., LICHERI, R., LOCCI, A.M., CINCOTTI, A. and CAO, G. Consolidation/synthesis of materials by electric current activated/assisted sintering. *Mater. Sci. Eng. R.* 2009, Vol. 63, 4-6, pp. 127-287.

[80] ZHAOHUI, Z., FUCHI, W., LIN, W., SHUKUI, L. and OSAMU, S. Sintering mechanism of large-scale ultrafine-grained copper prepared by SPS method. *Mater. Lett.* 2008, Vol. 62, 24, pp. 3987-3990.

[81] GUILLON, O., GONZALEZ-JULIAN, J., DARGATZ, B., KESSEL, T., SCHIERNING, G., RATHEL, J. and HERRMANN, M. Field-assisted sintering technology/spark plasma sintering: mechanisms, materials, and technology developments. *Adv. Eng. Mater.* 2014, Vol. 16, 7, pp. 830-849.

[82] GERMAN, R.M. *Sintering Theory and Practice.* New York : Wiley, 1996.

[83] GROZA, J.R. and DOWDING, R.J. Nanoparticulate materials densification. *Nanostruct. Mater.* 1996, Vol. 7, 7, pp. 749-768.

[84] GUILLARD, F., ALLEMAND, A., LULEWICZ, J.D. and GALY J. Densification of SiC by SPS-Effects of Time, Temperature and Pressure. *J. Eur. Cera. Soc.* 2007, Vol. 27, 7, pp. 2725-2728.

[85] LIU, D., XIONG, Y., TOPPING, T.D., ZHOU, Y., HAINES, CH., PARAS, J., MARTIN, D., KAPOOR, D., SCHOENUNG, J.M. and LAVERNIA, E.J. Spark Plasma Sintering of Cryomilled Nanocrystalline Al Alloy - Part II: Influence of Processing Conditions on Densification and Properties. *Metall. Mater. Trans. A.* 2012, Vol. 43, 1, pp. 340-350.

[86] GUBICZA, J., DIRRAS, G. and RAMTANI, S. Effect of processing conditions on microstructure and mechanical behaviour of metals sintered from nanopowders. *Mater. Sci. Forum.* 2013, Vol. 729, pp. 49-54.

[87] STANCIU, L.A., KODASH, V.Y. and GROZA, J.R. Effects of Heating Rate on Densification and Grain Growth during Field-Assisted Sintering of alfaAl2O3 and MoSi2 Powders. *Metall. Mater. Trans. A.* 2001, Vol. 32, 10, pp. 2633-2638.

[88] MUNIR, Z.A., ANSELMI-TAMBURINI, U. and OHYANAGI, M. The effect of electric field and pressure on the synthesis and consolidation of materials: A review of the spark plasma sintering method. *J. Mater. Sci.* 2006, Vol. 41, 3, pp. 763-777.

[89] ZHANG, F., REICH, M., KESSLER, O. and BURKEL, E. The potential of rapid cooling spark plasma sintering for metallic materials. *Mater. Today.* 2013, Vol. 16, 5, pp. 192-197.

[90] OLEVSKY, E.A. and FROYEN, L. Impact of Thermal Diffusion on Densification During SPS. *J. Am. Ceram. Soc.* 2009, Vol. 92, 1, pp. 122-132.

[91] XIONG, Y., LIU, D., LI, Y., ZHENG, B., HAINES, C., PARAS, J., MARTIN, D., KAPOOR, D., LAVERNIA, E.J. and SCHOENUNG, J.M. Spark Plasma Sintering of Cryomilled Nanocrystalline Al Alloy - Part I: Microstructure Evolution. *Metall. Mater. Trans. A.* 2012, Vol. 43, 1, pp. 327-339.

[92] SANTANACH, J.G., WEIBEL, A., ESTOURNÈS, C., YANG, Q., LAURENT, CH. and PEIGNEY, A. Spark plasma sintering of alumina: Study of parameters, formal sintering analysis and hypotheses on the mechanism(s) involved in densification and grain growth. *Acta Mater.* 2011, Vol. 59, 4, pp. 1400-1408.

[93] ANSELMI-TAMBURINI, U. , GARAY, J. E., MUNIR, Z. A., TACCA, A., MAGLIA, F. and SPINOLO, G. Spark plasma sintering and characterization of bulk nanostructured fully stabilized zirconia: Part I. Densification studies. *J. Mater. Res.* 2004, Vol. 19, 11, pp. 3255-3262.

[94] CHEN, W., ANSELMI-TAMBURINI, U., GARAY, J.E., GROZA, J.R. and MUNIR, Z.A. Fundamental investigations on the spark plasma sintering/synthesis process: I. Effect of dc pulsing on reactivity. *Mater. Sci. Eng. A.* 2005, Vol. 394, 1-2, pp. 132-138.

[95] BERTOLINO, N., GARAY, J., ANSELMI-TAMBURINI, U. and MUNIR, Z.A. Electromigration effects in Al-Au multilayers. *Scripta Mater.* 2001, Vol. 44, 5, pp. 737-742.

[96] GUYOT, P., RAT, V., COUDERT, J. F., JAY, F., MAÎTRE, A. and PRADEILLES N. Does the Branly effect occur in spark plasma sintering? *J. Phy. D.* 2012, Vol. 45, 9. Article ID 092001.

[97] OZAKI, K., KOBAYASHI, K., NISHIO, T., MATSUMOTO, A. and SUGIYAMA, A. Sintering phenomena on initial stage in pulsed current sintering. *J. Jpn. Soc. Powder Powder Metall.* 2000, Vol. 47, 3, pp. 293-297.

[98] YANAGISAWA, O., KURAMOTO, H., MATSUGI, K. and KOMATSU, M. Observation of particle behavior in copper powder compact during pulsed electric discharge. *Mater. Sci. Eng. A.* 2003, Vol. 350, 1-2, pp. 184-189.

[99] ZHANG, Z.H., LIU, Z.F., LU,J.F., SHEN X.B., WANG, F.CH. and WANG, Y.D. The sintering mechanism in spark plasma sintering – Proof of the occurrence of spark discharge. *Scripta Mater.* 2014, Vol. 81, pp. 56-59.

[100] HULBERT, D.M., ANDERS, A., ANDERSSON, J., LAVERNIA, E.J. and MUKHERJEE, A.K. A discussion on the absence of plasma in spark plasma sintering. *Scripta Mater.* 2009, Vol. 60, 10, pp. 835-838.

[101] SHEN, Z., PENG, H. and NYGREN, M. Formidable increase in the superplasticity of ceramics in the presence of an electric field. *Adv. Mater.* 2003, Vol. 15, 12, pp. 1006-1009.

[102] YUE, M., ZHANG, J., XIAO, Y., WANG, G. and LI, T. New kind of NdFeB magnet prepared by spark plasma sintering. *IEEE Trans. Magn.* 2003, Vol. 39, 6, pp. 3551-3553.

[103] ZHANG, Z.H., WANG, F.C., LEE, S.K., LIU, Y., CHENG, J.W. and LIANG, Y. Microstructure characteristic, mechanical properties and sintering mechanism of nanocrystalline copper obtained by SPS process. *Mater. Sci. Eng. A.* 2009, Vol. 523, 1-2, pp. 134-138.

[104] DIOUF, S. and MOLINARI, A. Densification mechanisms in spark plasma sintering: Effect of particle size and pressure. *Powder Technol.* 2012, Vol. 221, pp. 220-227.

[105] CHENG, Y., CUI, Z., CHENG, L., GONG, D. and WANG, W. Effect of particle size on densification of pure magnesium during spark plasma sintering. *Adv. Powder Technol.* 2017, Vol. 28, 4, pp. 1129-1135.

[106] CHUA, A.S., BROCHU, M. and BISHOP, D.P. Spark plasma sintering of prealloyed aluminium powders. *Powder Metall.* 2015, Vol. 58, 1, pp. 51-60.

[107] BOUSNINA, M.A., OMRANI, A.D., SCHOENSTEIN, F., MADEC, P., HADDADI, H., SMIRI, L.S. and JOUINI, N. Spark plasma sintering and hot isostatic pressing of nickel nanopowders elaborated by a modified polyol process and their microstructure, magnetic and mechanical characterization. [ed.] J. Alloys Compd. *J. Alloy. Compd.* 2010, Vol. 504, 1, pp. 323-327.

[108] ZADRA, M., CASARI, F., GIRARDINI, L. and MOLINARI, A. Spark Plasma sintering of pure aluminium powder: mechanical properties and fracture analysis. *Powder Metall.* 2007, Vol. 50, 1, pp. 40-45.

[109] KELLOGG, F., MCWILLIAMS, B., SIETINS, J., GIRI, A. and CHO, K. Comparison of SPS Processing Behavior between As Atomized and Cryomilled Aluminum Alloy 5083 Powder. *Metall. Mater. Trans. A.* 2017, Vol. 48, 11, pp. 5492-5499.

[110] KELLOGG, F., MCWILLIAMS, B. and CHO, K. Effect of Current Pathways During Spark Plasma Sintering of an Aluminum Alloy Powder. *Metall. Mater. Trans. A.* 2016, Vol. 47, 12, pp. 6353-6367.

[111] KHALIL, A. Synthesis and Wear Behaviour of Aluminium 6061 Alloy Reinforced with CNT. *Master Thesis.* King Fahd University of Petroleum and Minerals, Dhahran, Saudi Arabia : s.n., 2012.

[112] NAGAE, T.,YOKOTA, M.,NOSE, M.,TOMIDA, S.,KAMIYA, T. and SAJI, S. Effects of Pulse Current on an Aluminum Powder Oxide Layer Layer During Pulse Current Pressure Sintering. *Mater. Tran.* 2002, Vol. 43, 6, pp. 1390-1397.

[113] ZOLOTOREVSKY, V.S., BELOV, N.A. AND GLAZOFF, M.V. *Casting Aluminum Alloys.* London : Elsevier, 2007.

[114] CHINH, N.Q., GUBICZA, J., CZEPPE, T., LENDVAI, J., XU, CH., VALIEV, R.Z. and LANGDON, T.G. Developing a strategy for the processing of age-hardenable alloys by ECAP at room temperature. *Mater. Sci. Eng. A.* 2009, Vol. 516, 1-2, pp. 248-252.

[115] ZHAO, Y.H., LIAO, X.Z., JIN, Z., VALIEV, R.Z. and ZHU, Y.T. Microstructures and mechanical properties of ultrafine grained 7075 Al alloy processed by ECAP and their evolutions during annealing. *Acta Mater.* 2004, Vol. 52, 15, pp. 4589-4599.

[116] NAM, C.Y., HAN, J.H., CHUNG, Y.H. and SHIN, M.C. Effect of precipitates on microstructural evolution of 7050 Al alloy sheet during equal channel angular rolling. *Mater. Sci. Eng. A.* 2003, Vol. 347, 1-2, pp. 253-257.

[117] WISKEL, J.B., NAVEL, K., HENEIN, H. and MAIRE, E. Solidification Study of Aluminum Alloys Using Impulse Atomization: Part ii. Effect of Cooling Rate on Microstructure. *The Canadian Journal of Metallurgy and Materials Science.* 2002, Vol. 41, 2, pp. 193-204.

[118] ROKNI, M.R., WIDENER, C.A. and CRAWFORD, G.A. Microstructural evolution of 7075 Al gas atomized powder and high-pressure cold sprayed deposition. *Surf. Coat. Technol.* 2014, Vol. 251, pp. 254–263.

[119] BECKER, H., DOPITA, M., STRÁSKÁ, J., MÁLEK, P., VILÉMOVÁ, M. and RAFAJA, D. Microstructure and Properties of Spark Plasma Sintered Al-Zn-Mg-Cu Alloy. *Acta. Phys. Pol. A.* 2015, Vol. 128, 4, pp. 602-605.

[120] TRIVEDI, R., JIN, F. and ANDERSON, I.E. Dynamical evolution of microstructure in finely atomized droplets of Al-Si alloys. *Acta Mater.* 2003, Vol. 51, 2, pp. 289-300.

[121] ZUNIGA, A., AJDELSZTAJN, L. and LAVERNIA, E.J. Spark plasma sintering of a nanocrystalline Al-Cu-Mg-Fe-Ni-Sc alloy. *Metall. Mater. Trans. A.* 2006, Vol. 37, 4, pp. 1343-1352.

[122] HONG, S.J., SURYANARAYANA, C. and CHUN, B.S. Size-dependent structure and properties of rapidly solidified aluminum alloy powders. *Scripta Mater.* 2001, Vol. 45, 12, pp. 1341-1347.

[123] DEVARAJ, S., SANKARAN, S. and KUMAR, R. Influence of spark plasma sintering temperature on the densification, microstructure and mechanical properties of Al-4.5 wt %Cu alloy. *Acta Metall. Sin.* 2013, Vol. 26, 6, pp. 761-771.

[124] TIAN, W., LI, S., LIU, J., YU, M. and DU, Y. Preparation of bimodal grain size 7075 aviation aluminum alloys and their corrosion properties. *Chinese J. Aeronaut.* 2017, Vol. 30, 5, pp. 1777-1788.

[125] BERGMANN, D., FRITSCHING, U. and BAUCKHAGE, K. A mathematical model for cooling and rapid solidification of molten metal droplets. *Int. J. Therm. Sci.* 2000, Vol. 39, 1, pp. 53–62.

[126] KHAN, A.S., FARROKH B. and TAKACS, L. Effect of grain refinement on mechanical properties of ball-milled bulk aluminum. *Mater. Sci. Eng. A.* 2008, Vol. 489, 1-2, pp. 77-84.

[127] OLESZAK, D. and SHINGU, P.H. Nanocrystalline metals prepared by low energy ball milling. *J. Appl. Phys.* 1996, Vol. 79, 6, pp. 2975-2980.

[128] BONETTI, E., PASQUINI, L. and SAMPAOLESI, E. The influence of grain size on the mechanical properties of nanocrystalline aluminium. *Nanostruct. Mater.* 1997, Vol. 9, 1-8, pp. 611-614.

[129] ZHOU, F., LEE, J., DALLEK, S. and LAVERNIA, E.J. High grain size stability of nanocrystalline Al prepared by mechanical attrition. *J. Mater. Res.* 2001, Vol. 16, 12, pp. 3451-3458.

[130] RANA, J.K., SIVAPRAHASAM, D., RAJU, K.S. and SARMA, V.S. Microstructure and mechanical properties of nanocrystalline high strength Al–Mg–Si (AA6061) alloy by high energy ball milling and spark plasma sintering. *Mater. Sci. Eng. A.* 2009, Vol. 527, 1-2, pp. 292-296.

[131] AZABOU, M., KHITOUNI, M. and KOLSI, A. Characterization of nanocrystalline Al-based alloy. *Mater. Charact.* 2009, Vol. 60, 6, pp. 499-505.

[132] CHOI, J.H., MOON, K.I., KIM, J.K., OH, Y.M., SUH, J.H. and KIM, S.J. Consolidation behavior of nanocrystalline Al–5at.%Ti alloys synthesized by cryogenic milling. *J. Alloy. Compd.* 2001, Vol. 315, 1-2, pp. 178-186.

[133] AKINRINLOLA, B., GAUVIN, R. and BROCHU, M. Improving the mechanical reliability of cryomilled Al-Mg alloy using a two-stage spark plasma sintering cycle. *Scripta Mater.* 2012, Vol. 66, 7, pp. 455-458.

[134] CALKA, A., KACZMAREK, W. and WILLIAMS, J. S. Extended solid solubility in ball-milled Al-Mg alloys. *J. Mater. Sci.* 1993, Vol. 28, 1, pp. 15-18.

[135] MUKHOPADHYAY, D.K., SURYANARAYANA, C. and FROES, F.H. Structural evolution in mechanically alloyed Al-Fe powders. *Metall. Mater. Trans. A.* 1995, Vol. 26, 8, pp. 1939-1946.

[136] CLARK, C.R., SURYANARAYANA, C. and FROES, F.H. [book auth.] C. Suryanarayana, C.M. Ward-Close (Eds.) F.H. Froes. *Synthesis and processing of lightweight metallic materials.* Warrendale : TMS, 1995, pp. 175-182.

[137] KIM, G.H., KIM, H.S. and KUM, D.W. Determination of titanium solubility in alpha-aluminum during high energy milling. *Scripta Mater.* 1996, Vol. 34, 3, pp. 421-428.

[138] SRINIVASARAO, B., SURYANARAYANA, C., OH-ISHI, K. and HONO, K. Microstructure and mechanical properties of Al–Zr nanocomposite materials. *Mater. Sci. Eng. A.* 2009, Vol. 518, 1-2, pp. 100-107.

[139] MENDIS, C.L., JHAWAR, H.P., SASAKI, T.T., OH-ISHI, K., SIVAPRASAD, K., FLEURY, E. and HONO, K. Mechanical properties and microstructures of Al-1Fe-(0-1)Zr bulk nano-crystalline alloy processed by mechanical alloying and spark plasma sintering. *Mater. Sci. Eng. A.* 2012, Vol. 541, pp. 152-158.

[140] PING, S.W. Developments in Premium High-Strength Powder Metallurgy Alloys by Kaiser Aluminum. [book auth.] M.E. and STARKE, E.A. FINE. *Rapidly Solidified Powder Aluminum Alloys.* Philadelphia : American Society for Testing Materials, 1986, pp. 369–380.

[141] DUDAS, J.H. and DEAN, W.A. The production of precision aluminium P/M parts. *Int. J. Powder Metall.* 1969, Vol. 5, 2, pp. 21-36.

[142] SURESH K.R, MAHENDRAN, S., KRUPASHANKARA, M.S. and AVINASH, L. Influence of Powder Composition & Morphology on Green Density for Powder Metallurgy Processes. *IJIRSET.* 2015, Vol. 4, 1, pp. 18629-18634.

[143] PRADEEP, K.G., WANDERKA, N., CHOI, P., BANHART, J., MURTY, B.S. and RAABE, D. Atomic-scale compositional characterization of a nanocrystalline AlCrCuFeNiZn high-entropy alloy using atom probe tomography. *Acta Mater.* 2013, Vol. 61, 12, pp. 155-158.

[144] LE, G.M., GODFREY, A. and HANSEN, N. Structure and strength of aluminum with sub-micrometer/micrometer grain size prepared by spark plasma sintering. *Mater. Des.* 2013, Vol. 49, pp. 360-367.

[145] SWEET, G.A., BROCHU, M., HEXEMER JR., R.L., DONALDSON, I.W. and BISHOP, D.P. Microstructure and mechanical properties of air atomized aluminum powder consolidated via spark plasma sintering. *Mater. Sci. Eng. A.* 2014, Vol. 608, pp. 273-282.

[146] XIE, G., OHASHI, O., YOSHIOKA, T., SONG, M., MITSUISHI, K., YASUDA, H., FURUYA, K. and NODA, T. Effect of Interface Behavior between Particles on

Properties of Pure Al Powder Compacts by Spark Plasma Sintering. *Mater. Trans.* 2001, Vol. 42, 9, pp. 1846-1849.

[147] KWON, H., PARK, D.H., PARK, Y., SILVAIN, J., KAWASAKI, A. and PARK, Y. Spark plasma sintering behavior of pure aluminium depending on various sintering temperatures. *Met. Mater. Int.* 2010, Vol. 16, 1, pp. 71-75.

[148] XÜ, C.Y., JIA, S.S. and CAO, Z.Y. Synthesis of Al–Mn–Ce alloy by the spark plasma sintering. *Mater. Charact.* 2005, Vol. 54, 4-5, pp. 394-398.

[149] KHALIL, A., HAKEEM, A.S. and SAHEB, N. Optimization of process parameters in spark plasma sintering Al6061 and Al2124 aluminum alloys. *Adv. Mat. Res.* 2011, Vols. 328-330, pp. 1517-1522.

[150] GUPTA, R.K., FABIJANIC, D., DORIN, T., QIU, Y., WANG, J.T. and BIRBILIS, N. Simultaneous improvement in the strength and corrosion resistance of Al via high-energy ball milling and Cr alloying. *Mater. Des.* 2015, Vol. 84, pp. 270-276.

[151] YE, J., AJDELSZTAJN, L. and SCHOENUNG, J.M. Bulk nanocrystalline aluminum 5083 alloy fabricated by a novel technique: Cryomilling and spark plasma sintering. *Metall. Mater. Trans. A.* 2006, Vol. 37, 8, pp. 2569–2579.

[152] KUBOTA, M. Properties of nano-structured pure Al produced by mechanical grinding and spark plasma sintering. *J. Alloy. Compd.* 2006, Vols. 434-435, pp. 294-297.

[153] KUBOTA, M. and WYNNE, B.P. Electron backscattering diffraction analysis of mechanically milled and spark plasma sintered pure aluminium. *Scripta Mater.* 2007, Vol. 57, 8, pp. 719-722.

[154] CHEN, H.B., TAO, K., YANG, B. and ZHANG, J.S. Nanostructured Al-Zn-Mg-Cu alloy synthesized by cryomilling and spark plasma sintering. *Trans. Nonferrous Met. Soc. China.* 2009, Vol. 19, 5, pp. 1110-1115.

[155] WANG, D. and SHEN, J. High strength aluminium alloys prepared by nanocrystallisation of amorphous powders using spark plasma sintering. *Powder Metall.* 2015, Vol. 58, 5, pp. 363-368.

[156] SASAKI, T.T., MUKAI, T. and HONO, K. A high-strength bulk nanocrystalline Al–Fe alloy processed by mechanical alloying and spark plasma sintering. *Scripta Mater.* 2007, Vol. 57, 3, pp. 189-192.

[157] NAYAK, S.S., WOLLGARTEN, M., BANHART, J., PABI, S.K. and MURTY, B.S. Nanocomposites and an extremely hard nanocrystalline intermetallic of Al–Fe alloys prepared by mechanical alloying. *Mater. Sci. Eng. A.* 2010, Vol. 527, 9, pp. 2370-2378.

[158] KOPAS, P., BLATNICKÝ, M., SÁGA, M. and VAŠK, M. Identification of mechanical properties of weld joints of AlMgSi07.F25 aluminium alloy. *METALURGIJA*. 2017, Vol. 56, 1-2, pp. 99-102.

[159] STOLYAROV, V.V., LAPOVOK, R., BRODOVA, I.G. and THOMSON, P.F. Ultrafine-grained Al-5 wt.% Fe alloy processed by ECAP with backpressure. *Mater. Sci. Eng. A*. 2003, Vol. 38, 31, pp. 159-167.

[160] GALANO, M., AUDEBERT, F., ESCORIAL, A.G., STONE, I. C. AND CANTOR, B. Nanoquasicrystalline Al-Fe-Cr-based alloys with high strength at elevated temperature. *J. Alloy. Compd.* 2010, Vol. 495, 2, pp. 372-376.

[161] FUJIKAWA, S.I. Impurity Diffusion of Scandium in Aluminum. *Def. Diff. Forum.* 1997, Vols. 143-147, pp. 115-120.

[162] DAS, S.K. and DAVIS, L.A. High Performance Aerospace Alloys via Rapid Solidification Processing. *Mater. Sci. Eng.* 1988, Vol. 98, 1, pp. 1-12.

[163] MONDOLFO, L. *Aluminium Alloys: Structure and properties.* London : Butterworth, 1999.

[164] SRINIVASAN, S., DESCH, P.B. and SCHWARTZ, R.B. Metastable phases in the Al3X (X = Ti, Zr, and Hf) intermetallic system. *Scripta Metall.* 1991, Vol. 25, 11, pp. 2513-2516.

[165] NES, E. Precipitation of the metastable cubic Al3Zr-phase in subperitectic Al-Zr alloys. *Acta Metall.* 1972, Vol. 20, 4, pp. 499-506.

[166] KNIPLING, K.E., DUNAND, D.C. and SEIDMAN, D.N. Precipitation evolution in Al–Zr and Al–Zr–Ti alloys during isothermal aging at 375–425°C. *Acta Mater.* 2008, Vol. 56, 1, pp. 114-127.

[167] ROBSON, J.D. and PRANGNELL, P.B. Dispersoid precipitation and process modelling. *Acta Mater.* 2001, Vol. 49, 4, pp. 599-613.

[168] NES, E. and BILLGAL, H. Non-equilibrium solidification of hyperperitetic Al-Zr alloys. *Acta Metall.* 1977, Vol. 25, 9, pp. 1031-1037.

[169] LI, X.M. and STARINK, M.J. Effect of compositional variations on characteristics of coarse intermetallic particles in overaged 7000 aluminium alloys. *Mater. Sci. Technol.* 2001, Vol. 17, 11, p. 1324.

[170] KAI, W., BAIQING, X., YONGAN, Z., GUOJUN, W., XIWU, L., ZHIHUI, L., SHUHUI, H. and HONGWEI, L. Microstructure Evolution of a High Zinc Containing Al-Zn-Mg-Cu Alloy during Homogenization. *Rare Metal. Mat. Eng.* 2017, Vol. 46, 4, pp. 928-934.

[171] ESKIN, D. and KATGERMAN, L. Hardening, Annealing, and Aging. [book auth.] G.E. and MACKENZIE, D.S. TOTTEN. *Handbook of Aluminum.* New York : Marcel Dekker, 2003, pp. 259-303.

[172] MARLAUD, T., DESCHAMPS, A., BLEY, F., LEFEBVRE, W. and BAROUX, B. Influence of alloy composition and heat treatment on precipitate composition in Al-Zn-Mg-Cu alloys. *Acta Mater.* 2010, Vol. 58, 1, pp. 248-260.

[173] STILLER, K., WARREN, P.J., HANSEN, V., ANGENETE, J. and GJONNES, J. Investigation of precipitation in an Al – Zn – Mg alloy after two-step ageing treatment at 100°and 150°C. *Mater. Sci. Eng. A.* 1999, Vol. 270, 1, pp. 55-63.

[174] HADJADJ, L., AMIRA, R., HAMANA, D. and MOSBAH, A. Characterization of precipitation and phase transformations in Al–Zn–Mg alloy by the differential dilatometry. *J. Alloys Compd.* 2007, Vol. 462, 1-2, pp. 279-283.

[175] BERG, L.K., GJONNES, J., HANSEN, V., LI, X.Z., KNUTSON-WEDEL, M., WATERLOO, G., SCHRYVERS, D. and WALLENBERG,R. GP-zones in Al–Zn–Mg alloys and their role in artificial aging. *Acta Mater.* 2001, Vol. 49, 17, pp. 3443-3451.

[176] QUEUDET, H., LEMONNIER, S., BARRAUD, E., GHANBAJA, J., ALLAIN, N. and GAFFET, E. Effect of heat treatments on the microstructure of an ultrafine-grained Al-Zn-Mg alloy produced by powder metallurgy. *Mater. Sci. Eng. A.* 2017, Vol. 685, pp. 71-78.

[177] SHA, G. and CEREZO, A. Early-stage precipitation in Al–Zn–Mg–Cu alloy (7050). *Acta Mater.* 2004, Vol. 52, 15, pp. 4503-4516.

[178] LI, M., YANG, Y., FENG, Z., HUANG, B., LUO, X., LOU, J. and RU, J. Precipitation sequence of η phase along low-angle grain boundaries in Al-Zn-Mg-Cu alloy during artificial aging. *Trans. Nonferrous Met. Soc. China.* 2014, Vol. 24, 7, pp. 2061-2066.

[179] LIU, J.Z., CHEN, J.H., YANG, X.B., REN, S., WU, C.L., XU, H.Y. and ZOU, J. Revisiting the precipitation sequence in Al–Zn–Mg-based alloys by high-resolution transmission electron microscopy. *Scripta Mater.* 2010, Vol. 63, 11, pp. 1061-1064.

[180] GJONNES, J. and SIMENSEN, C.J. An electron microscope investigation of the microstructure in an aluminium-zinc-magnesium alloy. *Acta Metall.* 1970, Vol. 18, 8, pp. 881-890.

[181] DEGISCHER, H.P., LACOM, W., ZAHRA, A. and ZAHRA, C.Y. Decomposition processes in an Al−5%Zn−1%Mg alloy: Part II. Electronmicroscopic investigation. *Zeitschrift fur Metallkunde.* 2008, Vol. 71, pp. 1-10.

[182] FANG, X., DU, Y., SONG, M., LI, K. and JIANG, C. Effects of Cu content on the precipitation process of Al-Zn-Mg alloys. *J. Mater. Sci.* 2012, Vol. 47, 23, pp. 8174-8187.

[183] HU, T., MA, K., TOPPING, T.D., SCHOENUNG, J.M. and LAVERNIA, E.J. Precipitation phenomena in an ultrafine-grained Al alloy. *Acta Mater.* 2013, Vol. 61, 6, pp. 2163-2178.

[184] LI, J., PENG, Z., LI, CH., JIA, Z., CHEN, W. and ZHENG, Z. Mechanical properties, corrosion behaviors and microstructures of 7075 aluminium alloy with various aging treatments. *Trans. Nonferrous Met. Soc. China.* 2008, Vol. 18, 4, pp. 755-762.

[185] TASH, M.M. and ALKAHTANI, S. Aging and Mechanical Behavior of Be-Treated 7075 Aluminum Alloys. *Int. J. Miner. Metall. Mater.* 2014, Vol. 8, 3, pp. 252-256.

[186] MISHRA, R.S. and KOMARASAMY, M. Chapter 2 - Physical Metallurgy of 7XXX Alloys. *Friction Stir Welding of High Strength 7xxx Aluminum Alloys.* s.l. : Butterworth-Heinemann, 2016, pp. 5-14.

[187] ENGDAHL, T., HANSEN, V., WARREN, P.J. and STILLER, K. Investigation of fine scale precipitates in Al-Zn-Mg alloys after various heat treatments. *Mater. Sci. Eng. A.* 2002, Vol. 327, 1, pp. 59-64.

[188] QUEUDET, H., LEMONNIER, S., BARRAUD, E., GUYON, J., GHANBAJA, J., ALLAIN, N., GAFFET, E. One-step consolidation and precipitation hardening of an ultrafine-grained Al-Zn-Mg alloy powder by Spark Plasma Sintering. *Mater. Sci. Eng. A.* 2017, Vol. 685, pp. 227-234.

[189] KAUFMAN, J.G. *Introduction to Aluminum Alloys and Tempers.* Materials Park : ASM International, 2000.

[190] BUHA J, LUMLEY R N, CROSKY A G. Secondary ageing in an aluminium alloy 7050. *Mater. Sci. Eng. A.* 2008, Vol. 492, 1-2, pp. 1-10.

[191] PARK, J.K. and ARDELL, A.J. Microstructures of the Commercial 7075 Al Alloy in the T651 and T7 Tempers. *Metall. Trans. A.* 1983, Vol. 14, 10, pp. 1957-1965.

[192] DAS, T., KARUNANITHI, R., SINHA, A., GHOSH, K.S. and BERA, S. Deformation, decomposition and hardening behavior of nano Al7075 alloy prepared by mechanical milling and hot pressing. *Adv. Powder Technol.* 2016, Vol. 27, 4, pp. 1874-1877.

[193] JOSHI, T.C., PRAKASH, U. and DABHADE, V.V. Microstructural development during hot forging of Al 7075 powder. *J. Alloy. Compd.* 2015, Vol. 639, pp. 123-130.

[194] JEYAKUMAR, M., KUMAR, S. and GUPTA, G.S. Microstructure and Properties of the Spray-Formed and Extruded 7075 Al Alloy. *Mater. Manuf. Processes.* 2010, Vol. 25, 8, pp. 777-785.

[195] DEAQUINO-LARA, R., ESTRADA-GUEL, I., HINOJOSA-RUIZ, G., FLORES-CAMPOS, R., HERRERA-RAMÍREZ, J.M. and MARTÍNEZ-SÁNCHEZ, R. Synthesis of aluminum alloy 7075-graphite composites by milling processes and hot extrusion. *J. Alloy. Compd.* 2011, Vol. 5059, 1, pp. S284-S289.

[196] SHERAFAT, Z., PAYDAR, M.H., EBRAHIMI, R. and SOHRABI, S. Mechanical properties and deformation behavior of Al/Al7075, two-phase material. *J. Alloy. Compd.* 2010, Vol. 502, 1, pp. 123-126.

[197] FLORES-CAMPOS, R., MENDOZA-RUIZ, D.C., AMÉZAGA-MADRID, P., ESTRADA-GUEL, I., MIKI-YOSHIDA, M., HERRERA-RAMÍREZ, J.M. and MARTÍNEZ-SÁNCHEZ, R. Microstructural and mechanical characterization in 7075 aluminum alloy reinforced by silver nanoparticles dispersion. *J. Alloy. Compd.* 2010, Vol. 495, 2, pp. 394-398.

[198] MOBASHERPOUR, I., TOFIGH, A.A. and EBRAHIMI, M. Effect of nano-size Al2O3 reinforcement on the mechanical behavior of synthesis 7075 aluminum alloy composites by mechanical alloying. *Mater. Chem. Phys.* 2013, Vol. 1238, 2-3, pp. 535-541.

[199] LITYNSKA-DOBRZYNSKA, L., DUTKIEWICZ, J., MAZIARZ, W. and GÓRAL, A. Microstructure of Rapidly Solidified Al-12Zn-3Mg-1.5Cu Alloy with Zr and Sc Additions. *Mater. Trans.* 2011, Vol. 52, 3, pp. 309-314.

[200] ZHANG, J.C., DING, D.Y., ZHANG, W.L., KANG, S.H., XU, X.L., GAO, Y.J., CHEN, G.Z., CHEN, W.G. and YOU, X.H. Effect of Zr addition on microstructure and properties of Al-Mn-Si-Zn-based alloy. *Trans. Nonferrous Met. Soc. China.* 2014, Vol. 24, 12, pp. 3872-3878.

[201] AIDA, T., MATSUKI, K., ADACHI, H., OSAMURA, K., KUSUI, J. and YOKOE, K. Microstructure refinement and high strain rate superplasticity of Al–Zn–Mg–Cu P/M alloy extrusions. *JILM.* 1999, Vol. 49, 8, pp. 389-394.

[202] LI, F.X., LIU, Y.Z. and YI, J.H. Microstructural evolution of gas atomized Al–Zn–Mg–Cu–Zr powders during semi-solid rolling process. *Trans. Nonferrous Met. Soc. China.* 2014, Vol. 24, 8, pp. 2475-2481.

[203] MATSUKI, K., IWAKI, M., TOKIYAWA, M. and MURAKAMI, Z. Microstructural evolution during initial stage of high-strain rate superplastic deformation in powder metallurgical 7475 Al-0.7Zr alloy. *Mater. Sci. Technol.* 1991, Vol. 7, 6, pp. 513-519.

[204] *ENERGY-DISPERSIVE X-RAY MICROANALYSIS.* Middleton : NORAN Instruments, 1999.

[205] LUKAC, F., CHRASKA, T., MOLNAROVA, O., MALEK, P. and CINERT, J. Effect of cryogenic milling on Al7075 prepared by spark plasma sintering method. *Powder Diffr.* 2017, Vol. 32, S1, pp. S221-S224.

[206] SCARDI, P., LEONI, M., and DELHEZ, R. Line broadening analysis using integral breadth methods: a critical review. *J. Appl. Crystallogr.* 2004, Vol. 37, 3, pp. 381-390.

[207] LEÓN-REINA, L. GARCÍA-MATÉ, M. ÁLVAREZ-PINAZO, G. SANTACRUZ, I. VALLCORBA, O. DE LA TORRE, A.G. and ARANDA, M.A. Accuracy in Rietveld quantitative phase analysis: a comparative study of strictly monochromatic Mo and Cu radiations. *J. Appl. Crystallogr.* 2016, Vol. 49, 3, pp. 722-735.

[208] Bruker AXS GmbH. TOPAS 5 User manual. 2014.

[209] MACKENZIE, J.K. Second Paper on Statistics Associated with the Random Disorientation of Cubes. *Biometrika.* 1958, Vol. 45, 1/2, pp. 229-240.

[210] WERT, J.A., PATON, N.E., HAMILTON, C.H. and MAHONEY, M. Grain-refinement in 7075 Aluminum by thermomechanical processing. *A. Met. Trans.* 1981, Vol. 12, 7, pp. 1267–1276.

[211] SHUKLA, P., MANDAL, R.K. and OJHA, S.N. Non-equilibrium solidification of undercooled droplets during atomization process. *Bull. Mater. Sci.* 2001, Vol. 24, 5, pp. 547-554.

[212] GRANT, N.J. Rapid Solidification of Metallic Particulates. *JOM.* 1983, Vol. 65, 1, pp. 20-27.

[213] YAN, M., WANG, J., SCHAFFER, G. and QIAN, M. Solidification of nitrogen-atomized Al86Ni6Y4.5Co2La1.5 metallic glass. *J. Mater. Res.* 2011, Vol. 26, 7, pp. 944-950.

[214] JONES, H. Observations on a structural transition in aluminium alloys hardened by rapid solidification. *Mater. Sci. Eng.* 1969, Vol. 5, 1, pp. 1-18.

[215] SHEN, N., TANG, Y., ZHANG, D., CHEN, L. and GUAN, S. Featureless zone in rapidly solidified aluminium alloy splats. *J. Mater. Sci. Technol.* 1993, Vol. 9, 6, pp. 464-466.

[216] TU, G.C., CHEN, I.T. and CHUNG, M.S. A study of the featureless zone in rapidly-solidified gas-atomized aluminium alloy powder. *J. Mater. Sci. Lett.* 1991, Vol. 10, 19, pp. 1125-1128.

[217] CARDOSO, K., ESCORIAL, A.G., LIEBLICH, M. and BOTTA, F.W. Amorphous and nanostructured Al–Fe–Nd powders obtained by gas atomization. *Mater. Sci. Eng. A.* 2001, Vol. 315, 1-2, pp. 89-97.

[218] AFONSO, C.R.M., SPINELLI, J.E., BOLFARINI, S., BOTTA, W.J., KIMINAMI, C.S. and GARCIA, A. Rapid solidification of an Al-5Ni alloy processed by spray forming. *Mat. Res.* 2012, Vol. 15, 5, pp. 779-785.

[219] MOLNÁROVÁ, O., MÁLEK, P., LUKÁČ, F. and CHRÁSKA, T. Spark Plasma Sintering of a Gas Atomized Al7075 Alloy: Microstructure and Properties. *Materials.* 2016, Vol. 9, 12, p. 1004.

[220] SALLER, B.D., HU, T., MA, K., KURMANAEVA, L., LAVERNIA, E.J. and SCHOENUNG, J.M. A comparative analysis of solubility, segregation, and phase formation in atomized and cryomilled Al–Fe alloy powders. *J. Mater. Sci.* 2015, Vol. 50, 13, pp. 4683-4697.

[221] BOETTINGER, W.J., BENDERSKY, L. and EARLY, J.G. An analysis of the microstructure of rapidly solidified Al-8 wt pct Fe powder. *Metall. Trans. A.* 1986, Vol. 17, 5, pp. 781-790.

[222] ZHENG, B., LIN, Y., ZHOU, Y. and LAVERNIA, E.J. Gas atomization of amorphous aluminium powder: part II. Experimental Investigation. *Metall. Mater. Trans. B.* 2009, Vol. 40, 6, pp. 995-1004.

[223] LITYNSKA-DOBRZYNSKA, L., OCHIN, P., GORAL, A., FARYNA, M. and DUTKIEWICZ J. The Microstructure of Rapidly Solidified Al-Zn-Mg-Cu Alloys with Zr Addition. *Solid State Phenom.* 2010, Vol. 163, pp. 42-45.

[224] MAHATA, A., ZAEEM, M.A. and BASKES, M.I. Understanding Homogeneous Nucleationin Solidification of Aluminum byMolecular Dynamics Simulations. *Model. Mater. Simul. SC.* 2018, Vol. 26, 2, p. 025007.

[225] ILTIS, X., ZACHARIE-AUBRUN, I., RYU, H.J., PARK, J.M., LEENAERS, A., YACOUT, A.M., KEISER, D.D., VANNI, F., STEPNIK, B., BLAY, T., TARISIEN, N., TANGUY, C. and PALANCHER, H. Microstructure of as atomized and annealed U-Mo7 particles: A SEM/EBSD study of grain growth. *J. Nucl. Mater.* 2017, Vol. 495, pp. 249-266.

[226] PANIGRAHI, S.K. and JAYAGANTHAN. Effect of ageing on microstructure and mechanical properties of bulk, cryorolled, and room temperature rolled Al 7075 alloy. *J. Alloy. Compd.* 2011, Vol. 509, 40, pp. 3208-3217.

[227] KUMAR, N. and BISWAS, K. Cryomilling: An environment friendly approach of preparation large quantity ultra refined pure aluminium nanoparticles. *J. Mater. Res. Technol.* 2017. available online, in press.

[228] ZHOU, F., NUTT, S.R., BAMPTON, C.C. and LAVERNIA E.J. Nanostructure in an Al-Mg-Sc alloy processed by low-energy ball milling at cryogenic temperature. *Metall. Mater.Trans. A.* 2003, Vol. 34, 9, pp. 1985–1992.

[229] YAZDIAN, N., KARIMZADEH, F. and TAVOOSI, M. Microstructural evolution of nanostructure 7075 aluminum alloy during isothermal annealing. *J. Alloy. Compd.* 2010, Vol. 493, 1-2, pp. 137-141.

[230] AHAMED, H. and KUMAR, V.S. A Comparative Study on the Milling Speed for the Synthesis of Nano-Structured Al 6063 Alloy Powder by Mechanical Alloying. *JMMCE.* 2011, Vol. 10, 6, pp. 507-515.

[231] AZIMI, A., SHOKUHFAR, A. and ZOLRIASATEIN, A. Nanostructured Al–Zn–Mg–Cu–Zr alloy prepared by mechanical alloying followed by hot pressing. *Mater. Sci. Eng. A.* 2014, Vol. 595, pp. 124-130.

[232] LITYŃSKA-DOBRZYŃSKA, L., DUTKIEWICZ, J., MAZIARZ, W. and GÓRAL, A. The effect of zirconium addition on microstructure and properties of ball milled and hot compacted powder of Al–12wt% Zn–3wt% Mg–1.5wt% Cu alloy. *J. Alloy. Compd.* 2011, Vol. 509, 1, pp. 304-308.

[233] TAKACS, L. and MCHENRY J.S. Temperature of the milling balls in shaker and planetary mills. *J. Mater. Sci.* 2006, Vol. 41, 16, pp. 5246-5249.

[234] HUMPHREYS, F.J., HUANG, Y., BROUGH, I.I. and HARRIS, C. Electron backscatter diffraction of grain and subgrain structures-resolution considerations. *J. Microsc.* 1999, Vol. 195, 3, pp. 212-216.

[235] TAHERI, M. L., SEBASTIAN, J., SEIDMAN, D. and ROLLETT, A. Evidence for solute drag during recrystallization of aluminum alloys. *Mater. Res. Soc. Symp. Proc.* 2005, Vol. 880, pp. 121-126.

[236] DELOGU, F. and MULAS, M. Kinetic processes and mechanisms of mechanical alloying. [book auth.] Małgorzata Sopicka-Lizer. *High Energy Ball Milling.* s.l. : Woodhead Publishing, 2010, pp. 92-110.

[237] ZHOU, F., WITKIN, D., NUTT, S.R. and LAVERNIA, E.J. Formation of nanostructure in Al produced by a low-energy ball milling at cryogenic temperature. *Mater. Sci. Eng. A.* 2004, Vols. 375-377, 1-2, pp. 917-921.

[238] SHAFEI, M.A., HOSSEINIPOUR, S.J. and RAJABI, M. Microstructural characterization of nanostructured Al-Zn-Mg-Cu alloy during mechanical alloying and subsequent annealing. *Adv. Mater. Res.* 2014, Vol. 829, pp. 57-61.

[239] FOGAGNOLO, J.B., VELASCO, F., ROBERT, M.H. and TORRALBA, J.M. Effect of mechanical alloying on the morphology, microstructure and properties of aluminium matrix composite powders. *Mater. Sci. Eng. A.* 2003, Vol. 342, 1-2, pp. 131-143.

[240] SUŚNIAK, M., PAŁKA, P. and KARWAN-BACZEWSKA, J. Influence of Milling Time on the Crystallite Size of AlSi5Cu2/SiC Composite Powder. *Arch. Metall. Mater.* 2016, Vol. 61, 2, pp. 977–980.

[241] SALEM, H.G. and SADEK, A.A. Fabrication of High Performance PM Nanocrystalline Bulk AA2124. *J. Mater. Eng. Perform.* 2010, Vol. 19, 3, pp. 356-367.

[242] XIE, G., OHASHI, O., SATO, T., YAMAGUCHI, N., SONG, M., MITSUISHI, K. and FURUYA, K. Effect of Mg on the Sintering of Al-Mg Alloy Powders by Pulse Electric-Current Sintering Process. *Mater. Trans.* 2004, Vol. 45, 3, pp. 904-909.

[243] PIELA K., BLAŽ L., SIERPINSKI Z. and FORYŠ T. Non-isothermal annealing of AA7075 aluminum alloy-structural and mechanical effects. *Arch. Metall. Mater.* 2012, Vol. 57, 3, pp. 703-709.

[244] MONDAL, C. and MUKHOPADHYAY, A.K. On the nature of T(Al2Mg3Zn3) and S(Al2CuMg) phases present in as-cast and annealed 7055 aluminum alloy. *Mater. Sci. Eng. A.* 2005, Vol. 391, 1-2, pp. 367–376.

[245] SHAERI, M.H., SHAERI, M., EBRAHIMI, M., SALEHI, M.T. and SEYYEDEIN, S. H. Effect of ECAP temperature on microstructure and mechanical properties of Al–Zn–Mg–Cu alloy. *Prog. Nat. Sci. Mater.* 182-191, Vol. 26, 2, p. 2016.

[246] LEE, Z., WITKIN, D.B., RADMILOVIC, V., LAVERNIA, E.J. and NUTT, S.R. Bimodal microstructure and deformation of cryomilled bulk nanocrystalline Al–7.5 Mg alloy. *Mater. Sci. Eng. A.* 2005, Vols. 410-411, pp. 462-467.

[247] KOIZUMI, Y., TANAKA, T., MINAMINO, Y., TSUJI, N., MIZUUCHI, K. and OHKANDA, Y. Densification and Structural Evolution in Spark Plasma Sintering Process of Mechanically Alloyed Nanocrystalline Fe-23Al-6C Powder. *Mater. Trans.* 2003, Vol. 44, 8, pp. 1604-1612.

[248] POZUELO, M., MELNYK, C., KAO, W.H. and YANG, J.M. Cryomilling and spark plasma sintering of nanocrystalline magnesium-based alloy. *J. Mater. Res.* 2011, Vol. 26, 7, pp. 904-911.

[249] ZHANG, H., HUANG. Y., NING, H., WILLIAMS, C.A., LONDON, A.J., DAWSON, K., HONG, Z., GORLEY, M.J., GROVENOR, CH.R.M., TATLOCK, G.J., ROBERTS, S.G., REECE, M.J., YAN, H. and GRANT, P.S. Processing and microstructure characterisation of oxide dispersion strengthened Fe–14Cr–0.4Ti–0.25Y2O3 ferritic steels fabricated by spark plasma sintering. *J. Nucl. Mater.* 2015, Vol. 464, pp. 61-68.

[250] HILGER, I., BOULNAT, X., HOFFMANN, J., TESTANI, C., BERGNER, F., DE CARLAN, Y., FERRARO, F. and ULBRICHT, A. Fabrication and characterization of oxide dispersion strengthened (ODS) 14Cr steels consolidated by means of hot isostatic pressing, hot extrusion and spark plasma sintering. *J. Nucl. Mater.* 2016, Vol. 472, pp. 206-214.

[251] BOULNAT, X., FABREGUE, D., PEREZ, M., MARHON, M.H. and CARLAN, Y. High-Temperature Tensile Properties of Nano-Oxide Dispersion Strengthened Ferritic Steels Produced by Mechanical Alloying and Spark Plasma Sintering. *Metall. Mater. Trans. A.* 2013, Vol. 44, 6, pp. 2461-2465.

[252] CHEN, K.H., LIU, H.W., ZHANG, Z., LI, S. and TODD, R.I. The improvement of constituent dissolution and mechanical properties of 7055 aluminum alloy by stepped heat treatments. *J. Mater. Process. Tech.* 2003, Vol. 142, 1, pp. 190-196.

[253] GHIAASIAAN, R., AMIRKHIZ, B.S. and SHANKAR, S. Quantitative metallography of precipitating and secondary phases after strengthening treatment of net shaped casting of Al-Zn-Mg-Cu (7000) alloys. *Mater. Sci. Eng. A.* 2017, Vol. 698, pp. 206-217.

[254] DENG, Y., YIN, Z.M. and CONG, F.G. Intermetallic phase evolution of 7050 aluminum alloy during homogenization. *Intermetallics.* 2012, Vol. 26, pp. 114-121.

[255] HOU, W.R., JI, W.B., ZHANG, Z.H., XIE, J.X. and CHENG, X.L. The effect of homogenization temperature on the corrosion resistance of extruded 7050 Al-alloy bars. *J. Mater. Process. Technol.* 2014, Vol. 214, 3, pp. 635-640.

List of Tables

List of Abbreviations

at% – atomic percent

b – magnitude of Burgers vector

BF – bright field

BSE – backscattered electron imaging

BTP – ball-to-powder ratio

c – solute concentration in a solid solution

c_e – the equilibrium solid solubility of alloying element

CDD – coherently diffracting domain size or crystallite size

CIP – cold isostatic pressing

CP – cold pressing

D – diffusivity of alloying elements

d – the grain size

$\langle D_f \rangle$ – the material final average grain size

DF – dark field

EBSD – electron backscatter diffraction

ECAP – equal-channel angular pressing

EDS – energy dispersive spectroscopy

f – measure of obstacle strength

$\langle f \rangle$ – the average volume fraction of spherical second phase particles

F_0 – obstacle strength

fcc – face centred cubic

FIB – focused ion beam

f_p – the volume fraction of randomly distributed spherical second phase particles

f_w – weight fraction of second phase particles

G – shear modulus

G_T – temperature gradient

HAADF – high-angle angular dark field

HAGB – high-angle grain boundary

HIP – hot isostatic pressing

HP – hot pressing

HV – microhardness

k – a constant characterizing strengthening by grain size, individual for each material

k_r – rate constant, characterizing the rate of second phase particle coarsening

L – average spacing of obstacle (solute atoms, second phase particles)

LAGB – low-angle grain boundary

LM – light microscopy

LN – liquid nitrogen

M – the grain boundary mobility

m – variable characterizing the average obstacle spacing

M_0 – the grain boundary mobility constant

N – number of dislocations in dislocation pile-up

n – variable characterizing the nature of obstacle

P – the driving force for grain growth

PCA – process control agent

PM – powder metallurgy

P_Z – pinning pressure on an unit area of grain boundary exerted by second phase particles

Q_m – the activation energy for grain boundary migration

r – the radius of grain boundary curvature

$\langle r \rangle$ – the average radius of spherical second phase particles

R – radius of obstacle

r_p – is the diameter of randomly distributed spherical second phase particles

RPM – revolutions per minute

RS – rapid solidification

$\langle R(t) \rangle$ – the average particle radius at time t

SAED – selected area electron diffraction

SE – secondary electron imaging

SEM – scanning electron microscopy

SPD – severe plastic deformation

SPS – spark plasma sintering

STEM – scanning transmission electron microscopy

t – time

TEM – transmission electron microscopy

v – velocity of grain boundary migration

vol% – volume percent

V_s – solidification velocity

w – distance around the dislocation where atomic arrangement differs from that in a perfect crystal

wt% – weight percent

XRD – X-ray diffraction

α – constant connected with the strength of actual interaction force between dislocations in a forest dislocation

α_g – a constant characterizing the dependence of materials final average grain size on average radius and volume fraction of spherical second phase particles exerting backpressure on grain boundaries

$\gamma_{\alpha\beta}$ – the particle-matrix interface energy

γ_{AF} – the anti-phase energy

γ_b – the grain boundary free energy per unit area

$\gamma_{\Delta SFE}$ – difference of stacking-fault energy in particle and matrix

δ – the relative change of lattice parameter at the particle-matrix interface

$\Delta\tau$ – strengthening effect of a given obstacle

η – the relative change of shear modulus at the particle-matrix interface

ν – Poisson ratio

ρ_f – forest dislocation density

σ – the matrix-precipitate interfacial energy

σ_0 – the contribution to yield strength from strengthening mechanisms other than from grain size

σ_y – the yield stress

σ_{UTS} – ultimate tensile strength

τ – shear stress for a single dislocation

τ_C – critical resolved shear stress

τ_f – shear stress for a dislocation forest

$\tau_{pile\text{-}up}$ – shear stress for a dislocation pile-up

τ_{PN} – Peierls-Nabarro stress